POWER LOSSES IN SPIRAL BEVEL GEARS

THOMAS ANDREW WEBB MEng

Thesis submitted to the University of Nottingham
for the degree of Doctor of Philosophy

December 2010

Abstract

This dissertation describes a numerical modelling strategy for characterising the windage of a spiral bevel gear rotating within a static shroud. The techniques employed include the use of a parametric solid model, and flow field modelling using computational fluid dynamics (CFD) software. A number of hypothetical physical alterations are made to a control system consisting of a gear and a shroud, based on those found in a Rolls-Royce aero engine.

Windage is a parasitic power loss that occurs when a gear does work on air and oil within a gas turbine internal gearbox. It leads to degradation of the oil, which wears turbo-machinery and bearing components, shortening their lives. Windage power losses also impact upon the fuel consumption of an engine, reducing its environmental credentials. The requirement of the oil is to cool and lubricate the meshing location of a pair of gears and for it to then be removed from the vicinity of the gear — preventing its re-ingestion and recirculation. The best solution to these issues of reducing windage and managing the oil is to shroud the gear effectively. Additional cooling of oil can mitigate the damage of too much heat generation, but this adds weight and expense to an engine.

A parametric model of a shrouded spiral bevel gear is created, which allows for changes to be made to single or multiple dimensions of the gear and shroud. A control volume CFD approach is used, with a single tooth of a gear modelled to reduce computational time.

Four gear size variables are tested: inner diameter, outer diameter, cone angle and module (number of teeth). Findings for air-only show that windage can be reduced by: increasing the cone angle; increasing the number of teeth; or decreasing the outer diameter. The effect of changing the inner diameter on windage was found to be complex due to the interaction of gear and shroud upon the system results, but far less significant than the outer diameter, as windage was seen to scale by this variable to the power of 4.3.

Changes to the design of the shroud are made, with a comparison of five inlet and five outlet designs. It is found that a sudden restriction at the inlet to the shroud is the most effective way of reducing single phase windage, with additional shroud features that make the flow path more tortuous also helping. The outlet of the shroud is shown to increase windage as it is opened up and permitted to be less restrictive.

A series of investigations using a Lagrangian discrete particle model (DPM) to simulate the presence of oil droplets within the system are also presented. It is shown that the destination of oil within the domain is predominantly dictated by the source location of the oil, with little sensitivity to initial velocity or size. Film modelling on the surface of the shroud, using the DPM-based film model, allows the motion of a thin layer of oil to be studied. In conjunction with the five shroud outlet designs, it is shown that a less restrictive, more open shroud outlet design will help prevent re-ingestion of oil that is present within the shrouded area of the gear.

Acknowledgements

It is right and proper to thank the individuals and organisations who have made the work within this PhD possible.

Firstly, I would like to thank Rolls-Royce Civil Aerospace for the financial and technical support that they have lent this and its associated projects. Specific mention should go to Dr. Colin Young, Marc Tittel and Adrian Jacobs for their role as technical customers

I would also like to thank my supervisors, Dr. Hervé Morvan and Dr. Carol Eastwick for their support, and their excellent mentoring and technical guidance. Dr. Graham Johnson must also be acknowledged for his input and wealth of knowledge about gear windage.

Finally, I wish to thank my family for everything before and during this PhD, and my wife Hannah for her unwavering awesomeness. My dogs, Eric and Luna, provided me with unquestioning loyalty and much needed company during the writing of this thesis, and to them I am eternally grateful. Sponsor a greyhound at `http://www.retiredgreyhounds.co.uk`.

Contents

List of Figures

List of Tables

Nomenclature

α	Inverse Prandtl number, see equation (3.40)
Δt	Timestep size [s], see equation (3.21)
$\dot{m}$	Mass-flow-rate [kg/s], see equation (3.63)
ϵ	Turbulent dispersion rate $[m^2/s^3]$, see equation (3.36)
γ	Ratio of specific heats, see equation (3.48)
Γ_ϕ	Diffusion coefficient for ϕ, see equation (3.15)
κ	von Kármán constant (= 0.4187) , see equation (3.56)
μ	Dynamic viscosity [Pa.s], see equation (3.12)
μ_t	Turbulent viscosity [Pa s], see equation (3.33)
ω	Rotational speed [rad/s], see equation (2.2)
$\overline{\overline{\tau}}$	Stress tensor, see equation (3.11)
$\overline{u}, \overline{v}, \overline{w}$	Time-averaged u, v, w velocity [m/s], see equation (3.26)
$\vec{A}$	Area Vector [m^2], see equation (3.16)
$\vec{r}$	Displacement vector from cell centre to cell face, see equation (3.18)
ρ	Density [kg/m^3], see equation (2.2)
τ_w	Wall shear stress [Pa], see equation (3.53)

$\mathbf{U}$	Vector of velocity [m/s], see equation (3.9)
inv φ_p	Involute function at pointed tip of a gear tooth, see equation (3.3)
θ_C	Cone angle [degrees], see equation (2.2)
θ_i	Polar angle of an involute, see equation (3.4)
υ	Kinematic viscosity [m^2/s], see equation (2.1)
φ_i	Transverse pressure angle of an involute curve, see equation (3.1)
A	Area [m^2], see equation (3.62)
a	Speed of sound [m/s], see equation (3.47)
C_D	Coefficient of drag, see equation (3.58)
C_M	Non-dimensional torque coefficient, see equation (2.2)
c_p	Specific heat capacity at constant pressure [J/kg K], see equation (3.50)
C_Q	Non-dimensional throughflow, see equation (2.1)
D	Diameter [m], see equation (2.5)
E	Dimensionless Droplet Impact Energy, see equation (3.65)
E	Energy [J], see equation (3.13)
F	Facewidth [m], see equation (2.5)
g	Gravitational acceleration [m/s^2], see equation (3.11)
h	Convective heat transfer coefficient [W/m^2K], see equation (3.62)
h	Enthalpy [J/kg K], see equation (3.14)
I	Identity matrix, see equation (3.12)
i, j, k	Unit vector components in x,y,z directions, see equation (3.7)
k	Thermal conductivity [W/m K], see equation (3.13)
k	Turbulent kinetic energy [J/kg], see equation (3.33)

M	Mach number, see equation (3.70)
M	Tooth module [m], see equation (2.5)
m	Mass [kg], see equation (3.62)
M_t	Turbulent Mach number, see equation (3.45)
N	Rotational speed [rpm], see equation (2.5)
P	Windage power loss [W], see equation (2.5)
p	Pressure [Pa], see equation (2.13)
p	Static pressure [Pa], see equation (3.11)
Q	Volume flow rate [m^3/s], see equation (2.1)
R	Gas law constant $= 8.31447 \times 10^3$ [J/kmol K] , see equation (3.48)
R_b	Radius of base circle of a gear tooth [m], see equation (3.1)
R_C	Cone base radius [m], see equation (2.1)
r_i	Distance to arbitrary point on involute profile [m], see equation (3.1)
Re	Reynolds number, see equation (3.58)
Re_{rot}	Rotating Reynolds number, see equation (2.3)
s	Cone to shroud clearance [m], see equation (2.4)
S_ϕ	Source term for ϕ, see equation (3.15)
S_{ij}	Mean rate of stress tensor [s^{-1}], see equation (3.43)
T	Temperature [K], see equation (3.13)
T	Torque [nm], see equation (2.2)
t	Time [s], see equation (3.10)
t_b	Transverse tooth base thickness [m], see equation (3.3)

u', v', w' Fluctuating components of u, v, w velocity about $\overline{u}, \overline{v}, \overline{w}$ [m/s], see equation (3.26)

u, v, w Velocity vectors in x,y,z directions [m/s], see equation (3.26)

U^* Non-dimensional fluid velocity, see equation (3.55)

U^T Transpose of velocityvector [m/s], see equation (3.12)

u_τ Friction velocity [m/s], see equation (3.52)

V Volume [m^3], see equation (3.16)

y^* Non-dimensional cell-wall distance, see equation (3.54)

y^+ Non-dimensional cell-wall distance, see equation (3.52)

CHAPTER 1

Introduction

1.1 Overview

This thesis describes a numerical modelling strategy for characterising the windage of a spiral bevel gear rotating within a static shroud. The techniques employed include the use of a parametric solid model, and flow field modelling using computational fluid dynamics (CFD) software. A number of hypothetical physical alterations are made to a control system consisting of a gear and a shroud, based on those found in a Rolls-Royce aero engine. This introduction will provide the background behind the problem, describe the aims that are to be achieved and finally outline the structure of the thesis.

1.2 Background

1.2.1 Gear windage in an aero engine gearbox

Windage can be defined as the wasteful work done on air by a rotating element. It is a major contributor, along with churning of oil suspended in the air, of additional heating within the internal gearbox (IGB) of an aero engine. This heating can lead to degradation of the oil, which wears turbo-machinery and bearing components, shortening their lives. Parasitic power loss impacts directly upon the specific fuel consumption (s.f.c.) of an engine, reducing its environmental

credentials and its attractiveness to airlines and airframe manufacturers. It has been shown that gear windage and churning are around 10% of the total losses for a meshing gear pair [28], but for a high power engine, this can account for megawatts of lost energy [12].

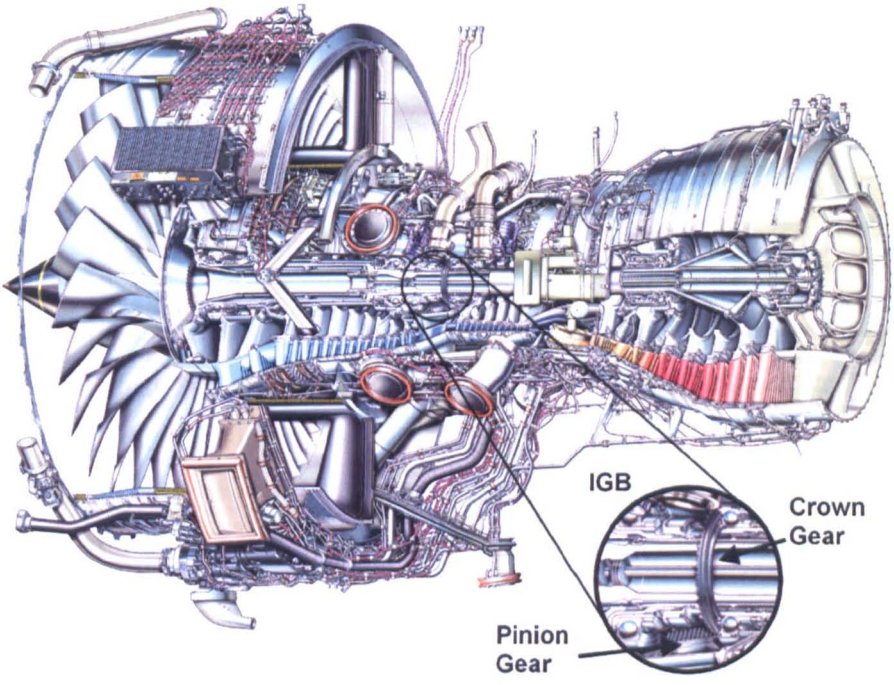

Figure 1.1: A cut-through of a Trent 500 engine, inset with detailing of the IGB [4]

The purpose of the internal gearbox is to provide power from the high pressure (H.P.) or intermediate pressure (I.P.) shaft of the engine to the ancillary equipment, such as electrical generators, through a smaller power off-take shaft, also known as a "radial drive-shaft". The exact configuration will depend upon the manufacturer and engine; however the work in this thesis is based on a Rolls-Royce Trent series three-shaft engine, which powers the ancillaries from the H.P. shaft. The power transmission path can be reversed, and the power off-take shaft used to spin the H.P. shaft in order to start the engine. The two shafts are generally at, or near, 90 degrees apart from each other, with the power off-take shaft positioned radially to the H.P. shaft's axial configuration, relative to the rest of the engine. The smaller of the two gears is generally carried on the power off-take shaft, and the larger on the H.P. shaft, due to the inner diameter of the gear

being constrained by the shaft. Figure 1.1 shows a cut-through of a Rolls-Royce Trent 500 aero engine, with an inset containing a zoomed image of the IGB. The inset shows the H.P. shaft's crown gear, and the radial drive-shaft's pinion gear.

Modern aircraft demand more electrical power from the generators than ever before. This is due to a number of factors; for example an increased quantity of electronic avionic devices for the pilots and individual audio-visual entertainment suites for passengers. In addition, the newest engines, such as the Rolls-Royce Trent 1000 and General Electric GEnx for the Boeing 787, will not use "bleed air" from the compressor stages of the engine for pressurising the cabin, but will instead use electrical compressors. The reasoning behind this is increased efficiency and improved cabin air quality, and the outcome will be further increased electrical requirements. This means that the radial off-take shaft will be transferring a higher torque, the consequence of which for gear windage is that the gears meshing between the H.P. and radial off-take shafts are increasing in outer diameter for new engine architectures, in order to safely carry the required torques.

For Rolls-Royce, reductions in wasted energy allow them to move towards meeting strategic environmental targets, such as a 50% reduction in air travel carbon dioxide emissions by 2020, compared to 2005 levels. These are the so-called "ACARE 2020" targets [14], and part of being able to achieve these is to reduce power losses in transmissions, which is where this body of work fits into the research conducted for the company. The work contained within this thesis is already used to inform and guide Rolls-Royce transmission and fluid systems engineering in creation of future engines, such as the Trent 1000, and further afield, the Trent XWB engine which will power the Airbus A350 [29].

1.2.2 Spiral bevel gear pair

The torque is transmitted between shafts in the IGB using a pair of spiral bevel gears. These have teeth which are inclined to the axis of the gear, and follow a

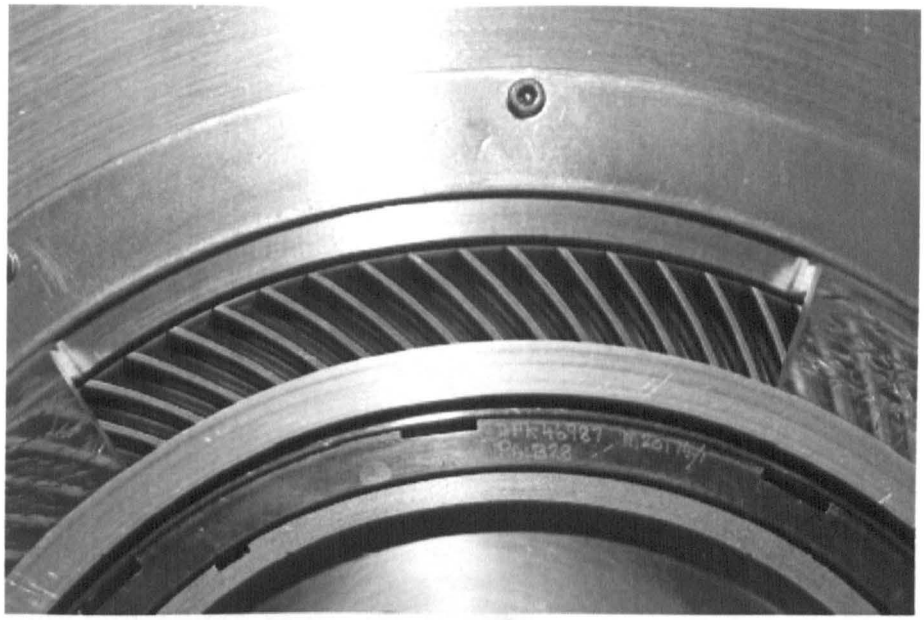

Figure 1.2: Spiral angle of the teeth viewed from front of the gear [22]

spiral profile. The spiral profile of the teeth can be seen when viewed from the front of the gear in Figure 1.2, which shows the gear partially shrouded for the experiments of Johnson *et al.* [22].

Spiral bevel gears are more expensive to produce than standard bevel gears; however, they have a few key advantages. Firstly, the teeth of the gears are constantly "in mesh", so there are always multiple teeth in contact between the two gears, which along with gradual engagement and dis-engagement of meshing teeth, means that that there is a higher contact ratio and hence a larger load carrying ability compared to the same size straight bevel gear. Secondly, the operation between the two gears is smoother than for a standard bevel gear, meaning shocks to the transmission are reduced. In particular, the enhanced load carrying capability of a spiral bevel gear is attractive to aero engine manufacturers, as for a given space within the IGB, a spiral bevel gear can safely transfer more torque than any other type of gear. They have the disadvantage of being noisier than standard bevel gears, due to the sliding action of the teeth over each other as they travel through mesh [40].

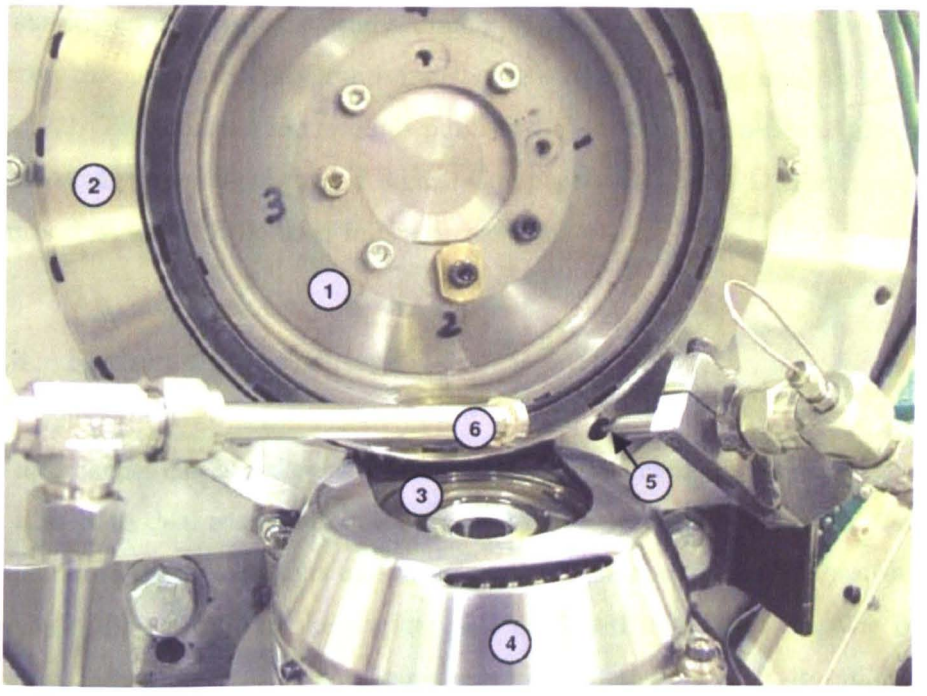

Figure 1.3: Shrouded crown and pinion gear. 1 - Crown gear, 2 - Crown shroud, 3 - Pinion gear, 4 - Pinion shroud, 5 - Pinion lubrication oil jet, 6 - Mesh lubrication oil jet.

1.2.3 Shrouding

There are a number of different shroud shapes that have been applied to aero engine internal gearboxes, and due to the complexity of designing and certifying an engine, will have been based on the current knowledge two to three years or so before entering service.

Figure 1.3 shows the shrouded crown and pinion gears from the experimental work of Johnson *et al.* [22]. Marked on the diagram are a number of components which are identified within the figure's caption. The relative size of the crown and pinion gears can be observed, along with the shrouds for both of the gears.

The work of Johnson *et al.* [22, 23] and Rapley [33, 34, 36] has respectively shown experimentally and computationally that there can be large variations in the effectiveness between shrouds, and that care must be taken to consider the motion and distribution of lubricating oil between shroud and gear. Rapley

[33] conducted a parametric study looking at the effect of changing the spacing between the gear and the shroud and focused on two designs used by Johnson *et al.* [23]. Thus far, no-one else has published a study into a series of alternate, yet physically possible shroud designs. Computational Fluid Dynamics (CFD) permits this, and will be used in the present dissertation.

1.2.4 Reduction of windage

Two approaches can be taken with gear windage by an aero engine manufacturer. The first is to deal with the consequences by increasing the cooling of the hot oil with more heat exchangers and more advanced oil management, however this involves adding weight to the engine, plus increased initial and ongoing costs. This also poses the risk of not being able to cool the entire IGB sufficiently, resulting in localised "hot-spots" and subsequent oil degradation.

The second approach is to address the windage by preventing it from occurring in the first place by shrouding the rotating gears in a way that prevents them from pumping and churning the air and oil. This is an attractive approach as it is lighter than increased oil cooling, and reduces maintenance overheads. Although the science of windage has been researched since at least the 1980s [9, 10], it has been only within the previous decade with the work of Winfree [50], Johnson *et al.* [22, 23], Rapley [33, 34, 36] and others [3, 11, 13] that the body of knowledge has increased dramatically.

The most recent work has shown that shrouding a gear needs to be done precisely and carefully, with some shrouds being little more effective than none at all [33]. This thesis aims to take the current field of knowledge further by looking into the mechanisms and physics involved in gear windage, and how these can be applied to reducing the power losses. It will do this by looking at the gear itself and also the shroud, and considering the two as closely linked in a system.

In addition to looking at single phase windage, it is important to also consider

the impact of oil within the system. Johnson *et al.* [22] have shown that the air and oil contributions to windage can be calculated separately, but as changes to the air component of windage will affect the motion of oil, they cannot be considered as mutually exclusive components. This thesis will also explore the impact of oil management, and the link of oil velocity and destination within the system to the core air flow.

1.3 Aims and objectives

The aims of this thesis can be summarised as follows:

1. To extend the CFD methodology of Rapley [33] and produce a computational parametric model of shrouded spiral bevel gear.
2. To characterise the effects which cause and can mitigate windage of a shrouded spiral bevel gear, using computational fluid dynamics software.
3. To apply engineering analysis and logic to form a series of conclusions which will aid designers trying to reduce the windage of a rotating spiral bevel gear, while accounting for oil management.

In order to achieve the aims above, a series of specific objectives have been formulated and these are:

1. Characterise the effect upon single-phase windage of four size variables of a spiral bevel gear. The variables are inner diameter, outer diameter, cone angle and module (number of teeth).
2. Investigate a series of alternative inlet and outlet geometries to see their impact upon single-phase windage.
3. Introduce oil droplets into the domain to replicate ingestion of an oil-laden atmosphere, or shedding of droplets off the rotating gear. The destination of droplets will be investigated.

4. Simulate a film created from the droplets striking the shroud, and establish whether the current CFD capabilities can qualitatively replicate the flows seen experimentally.

5. Investigate whether the design of the shroud at the outlet has a positive impact at reducing the recirculation and re-ingestion of oil into the gear.

1.4 Structure

This chapter has provided the background to the problem, and the aims and objectives that will be used to solve it. Chapter 2 reviews the current state of literature in the field of gear windage. The chapter is divided into gears of increasing complexity, starting at spur gears and ending at spiral bevel gears, and each of these sections is sub-divided into experimental and computational work. It will be seen that although a lot of work has been done into studying the effects on windage of changing the space between the gear and the shroud, very little research has been conducted into the mechanisms of gear windage, and the associated pressure losses and gains throughout the system.

Chapter 3 contains the methodology used for solving the problems in this thesis. It starts by detailing the creation of a parametric solid model of a shrouded spiral bevel gear, and the meshing techniques used to model the domain. A detailed discussion of the numerics behind finite-volume computational fluid dynamics is given, along with justification for the models chosen, and the reasons why they benefit the accuracy of the solution. The chapter concludes by verifying the results of the simulations are independent of the mesh density, and then validates the results against the experimental work of Johnson *et al.* [23]. The methodology contains material that was published at ASME Turbo-Expo 2010 [46].

Chapter 4 is the first of the three results chapters, and is a parametric study looking at the effect of four gear variables on single phase (air only) windage.

These variables are the inner and outer diameter of the gear, the cone angle and the number of teeth on the gear. This chapter uses the validated results of a "control" gear as a baseline case and extends the concept of Johnson *et al.* [23] of using a centrifugal fan as an analogy of a shrouded spiral bevel gear. This approach splits the domain into three parts: a pressure loss through the inlet to the shroud; a pressure rise across the face of the gear (through the gear teeth); and a final pressure loss at the outlet of the shroud. This chapter shows that some alterations to the gear necessitate an alteration to the shroud, and this produces a complex interactive and often conflicting change to the pressure losses and gains. This chapter also contains some material that was published at ASME Turbo-Expo 2010 [46].

Chapter 5 looks at the effect of the shroud geometry on single phase windage. There has been some previous work, in particular by Rapley [33] looking at the spacing between the shroud and the gear; however, this has been based around a small number of physical shrouds which were used in the experiments of Johnson *et al.* [23]. The work in this chapter will differ from all previous work by looking at a series of hypothetical designs at the inlet and outlet of the shroud. It has been shown by Johnson *et al.* that a restrictive inlet is the most important part of reducing single phase windage; however, mechanical constraints mean that there are physical limitations to how close the static shroud and rotating gear or shaft can get to each other (due to centrifugal expansion of rotating elements). The designs at the inlet all have the same distance between shroud and gear, and instead look at different lengths of the inlet channel, whether a "nose" is necessary, and if the shroud at the inlet can be as simple as a bent piece of flat metal, with no additional physical features. Finally, this chapter looks at a number of outlet designs, ranging from the "control" system's restrictive 1.5mm gap with gutter, to a design which effectively provides no restriction at all, just allowing the flow from the gear teeth to be ejected straight into the chamber behind the gear. The purpose of this is to see whether a less restrictive outlet which would affect the single phase windage adversely could compensate for this by allowing oil between the shroud and gear to be ejected into the rear chamber

and not be re-ingested by the gear — which would lead to overall lower power losses.

Chapter 6 expands on the work of the two previous results chapters by studying the effect of a secondary phase of oil. This chapter will start by using a discrete phase model to simulate oil droplets as particles, "overlaid" on the single phase solution, with both able to exchange momentum with each other. There has been some experimental work looking at what the presence of oil does to windage [22], but only very little computational work [3]. Qualitative comparisons to the work of Johnson *et al.* [22] will be made. Initially, the droplets will be terminated on impact with any surface, and the location of their termination noted. This will provide information as to whether and where oil will collect in various parts of the domain, or whether areas will be untouched — which could lead to overheating. Subsequently, film modelling on the surface of the shroud will be switched on, in conjunction with the discrete phase model, to see whether the CFD software is capable of simulating the movement of a film on its surface. A number of different injection velocity conditions and droplet size distributions will be studied in order to parametrise the effects that are seen in an engine. Finally, this chapter will extend this two-phase methodology to some of the shroud outlet designs tested in Chapter 5. The aim of doing this is twofold: firstly to see if the flow field from the single phase simulations can be used to pre-judge where oil droplets are likely to be dispersed; and secondly to establish if the shroud outlet shape can be used to prevent oil being re-ingested back into the rotating gear, which as shown by Johnson *et al.* [22], is a parasitic power loss that gets progressively worse at increasing oil flow rates. Some of the work in this chapter was published at the 2010 ASME conference on Engineering Systems Design Analysis [44].

Chapter 7 is the final chapter and summarises the findings of the previous chapters, and provides a number of conclusions which can aid transmission designers looking at the effect of both the gear and shroud upon one- and two-phase windage. These conclusions will consider the engineering and physical limitations of designing aero engine transmissions, and therefore will be real and applicable to future engines. This chapter also highlights the novelty of the work within the

thesis, and its contribution to science.

CHAPTER 2

Literature review

2.1 Overview

The aim of this chapter is to study the current state of knowledge in the field of gear windage, with an emphasis on spiral bevel gears. Section 2.2 will firstly describe the different types of losses within a gear set in a gas turbine internal gear box (IGB), and their relative impacts on the total loss. Literature will then be reviewed on the following three topics: rotating cones (Section 2.3), rotating spur gears (Section 2.4) and rotating spiral bevel gears (Section 2.5). This allows a complete picture to be built up — firstly the underlying physics, subsequently adding the increasing physical complexity of a spiral bevel gear.

This thesis describes a methodology and results for windage on a number of shrouded spiral bevel gears, and uses computational fluid dynamics (CFD) software to analyse numerical data and flow field. As a consequence, in each of the sections of this literature review, there will be two subsections. The first will look at experimental results and analysis, and the second will look at computational work that has been conducted. This will allow the relevance of the physical phenomena studied experimentally to be placed in a computational context, which will have clear advantages for the work reported later in the thesis.

2.2 Types of losses in a gearbox

Within a meshing gear system, there are a number of different sources of power loss. The percentages next to each loss refer to their relative contribution to overall losses as reported in Lord [28]:

- Bearing losses are the losses experienced in bearings that support the gear shafts. (50%)
- Meshing losses occur at the point where two gears contact each other when transmitting power. The magnitude of these losses is dependent upon the type and size of the gear. (40%)
- Churning losses occur when a gear accelerates a lubricating medium, incurring an energy cost.
- Windage losses are the losses in a gear assembly caused by the drag of the gear when it is running in air or an air-oil mix. This can be considered analogous to the air resistance that any body, such as a car, experiences when moving through air. This component of loss will be the primary focus of this thesis. (Churning and windage share 10%)

2.3 Rotating cones

Work that has been undertaken in the past on windage of spur gears has broken down the principles involved by first considering a blank disk or cylinder. As this body of work focusses on spiral bevel gears, the analogy to the blank disk or cylinder in this case is a smooth cone. The relevence of this to the work in this thesis is that the the work conducted on cones has focussed on the effect of a throughflow on the flow structures [35, 55], and the effect of a throughflow is important on the windage of a spiral bevel gear.

2.3.1 Experimental

Yamada and Ito [53–55] conducted a number of experiments using a rotating cone inside a static shroud. The aim was to characterise the effect upon friction of the spacing between cone and shroud, culminating in a paper studying the effects of a superposed throughflow on the frictional resistance of a rotating cone [55].

The apparatus used consisted of a stationary conical shroud with a small inlet at the apex to allow fluid (water) to be pumped through. The cone is held parallel within the shroud, and the non dimensional ratio of shroud clearance to base radius of the cone (s/R_C) varied from 0.008 to 0.16. Three cones with different cone vertex angles were used with identically angled shrouds for each case.

Yamada and Ito used two non-dimensional parameters to characterise the results. The first is a non-dimensional throughflow, C_Q which defines the axial flow of water through the cone in terms of the base radius of the cone (R_C) and kinematic viscosity (v) of the fluid.

$$C_q = \frac{Q}{R_C v}. \tag{2.1}$$

The second parameter is a moment coefficient, C_M, defined by

$$C_M = T \frac{sin\left(\frac{\theta_C}{2}\right)}{\frac{1}{2}\rho\omega^2 R_C^5}. \tag{2.2}$$

Five different values of C_Q were investigated by Yamada and Ito: 0, 750, 1500, 3000 & 6000. A rotational Reynolds number, Re_{rot} was also defined and is given by Equation 2.3.

$$Re_{\text{rot}} = \frac{R_C^2 \omega}{\upsilon}. \tag{2.3}$$

Three different flow regimes were identified, which are more visible for some combinations of throughflow rate and shroud gap than in others; the three regimes were most obvious in experiments with small shroud spacing and small (not zero) throughflow rates. The first region is one with an inversely proportional relationship between C_M and Re_{rot}, with C_M decreasing as Re_{rot} increases, typically extending up to Re_{rot} of 1×10^5. This region is laminar, and vortices are not thought to be present. For C_Q values of 750 and 1500 this laminar regime exists to higher values of Re_{rot} compared to when there was no throughflow. This was thought to be due to the throughflow suppressing the formation of "Taylor-type" vortices.

The second mode of flow is a transitional region between the laminar region and a fully turbulent one. The point at which this transitional regime starts is dependent upon the cone vertex angle, θ_C and C_Q. When it occurs, C_M increases rapidly with Re_{rot} and this continues until the third, fully turbulent region is reached.

In the final regime, there is a non-proportional relationship between C_M and Re_{rot}, with the reduction of C_M decreasing as Re_{rot} increases. Yamada and Ito postulated that Taylor-type vortices are also suppressed in this regime when there is a throughflow but only as long as the gap-radius ratio (s/R_C) is small.

Yamada and Ito found that at higher values of (s/R_C) the change from laminar to transitional flow occurs at lower values of Re_{rot}, which they termed the critical Reynolds number, $(Re_{\text{rot}})_c$. They found that if the shroud clearance, s was

used as the characteristic length to define the Reynolds number (Equation 2.4), then the values of $Re_{\mathrm{rot},s}$ that transition occurs is almost totally independent of (s/R_C),

$$Re_{\mathrm{rot},s} = \frac{R_C \omega s}{\upsilon}. \tag{2.4}$$

Yamada and Ito also studied the effect of clearance ratio (s/R_C) on C_M, and found that at higher values of Re_{rot}, there is little difference on C_M with changing clearance ratio, therefore a conclusion can be drawn that it is the viscous forces resulting from the rotation of the cone rather than from the throughflow that are dominating the moment on the cone.

2.3.2 Computational

Rapley [35] conducted a series of 2D and 3D simulations using Computational Fluid Dynamics (CFD) with the same experimental set-up as Yamada and Ito [55]. A number of turbulence models were used: $k-\epsilon$ RNG, $k-\omega$ SST and Reynolds Stress Model (RSM). The former two are both two-equation turbulence models, the latter is a seven-equation model and hence has increased complexity [41]. Turbulence modelling is explored in detail in Section 3.4.8 in the Methodology chapter.

Rapley found that for cases where there was no throughflow and the cone vertex angle, $\theta_C = 90°$, both the RNG and SST models with a two-dimensional mesh showed good agreement with the experimental results. This was not the case when $\theta_C = 120°$ with the RNG model over-predicting by between 33 - 70% and the SST model over-predicting by 16 - 67%.

When a throughflow was present in the physical experiments there was a transitional region between laminar and turbulent flows. The two dimensional Reynolds Averaged Navier Stokes (RANS) CFD simulations conducted by Rapley were un-

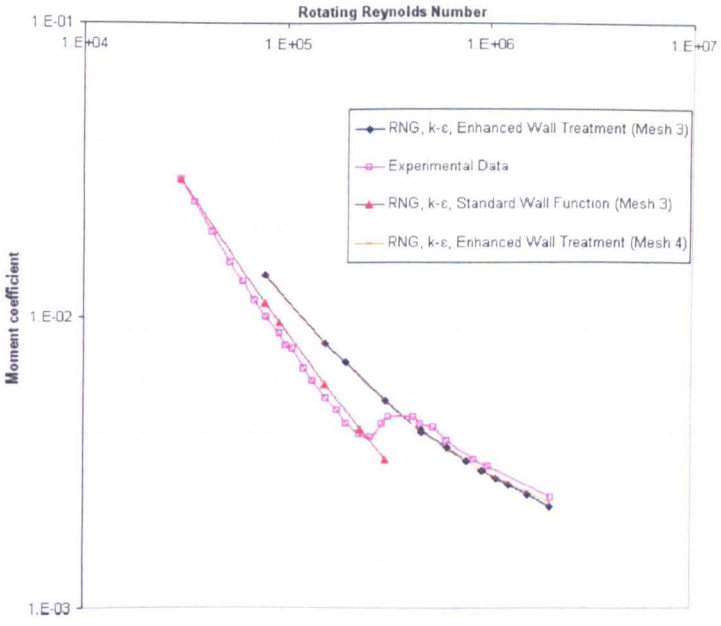

Figure 2.1: Moment coefficient (C_M) versus rotating Reynolds number (Re_{rot}), vertex angle of $\theta_C = 90°$, gap-radius ratio of $(s/R_C) = 0.008$, non-dimensional throughflow (C_Q)=1500 [35]

able to replicate this at all. Good agreement could be found between any of the turbulence models and one part of the flow regime: laminar or turbulent, but no model was close in agreement for both sections — ignoring the transient phase in the middle. This is seen in Figure 2.1 , which shows Yamada and Ito's experimental data compared with Rapley's. In all the two dimensional CFD cases shown, an RNG turbulence model has been used, with either a standard wall treatment [41] or a propriety enhanced wall treatment created by FLUENT, the CFD software used [19], but without use of any transition correlation. The enhanced wall treatment only gave close results in the turbulent region, and the standard wall function was only accurate in the laminar region before the transitional phase. Due to the difference in grid density for each wall treatment, this implies a level of grid dependence of the results.

Rapley concluded that two-dimensional modelling was unable to resolve the flow field accurately enough. He subsequently tried two three-dimensional meshes: the first a six degree wedge of 1.343 million cells with periodic boundaries; the second a full 360° model with 1.8 million cells. Whilst both improved upon

the qualitative performance of the two-dimensional meshes, neither made any difference in the transitional phase. It was clear from visualisations that the flow was non-axisymmetric so a complete three-dimensional mesh was necessary.

Rapley did not perform any transient solutions — all of his were steady state. The formation and motion of turbulent structures inside the domain during the transitional phase will by nature be a transient process accounting for a complex and still poorly understood turbulence event, so it is unsurprising that the steady state RANS-based simulations were unable to accurately reflect the experimental results.

The relevance of the papers reported in this section to the work conducted in this thesis is clear, as it forms the basis of the work done by Rapley *et al.* [33, 34, 36] into preliminary investigations of the windage on rotating spiral bevel gears. That body of work is reported in Section 2.5.2, and was used to directly feed into the methodology used for the original work in this thesis.

2.4 Spur gears

This project focuses on spiral bevel gears, as these are the predominant form of transmitting power within a gas turbine Internal Gear Box (IGB); however, there is very little literature available dealing with the windage of these gears, so it is necessary to start with a look at work that has been conducted into spur gears.

An excellent overview of the state of the literature in 2008 is written by Eastwick and Johnson [12], and much of the work reviewed from this point onwards is also found in that reference. This section, and the following Section 2.5 on spiral bevel gears go into a greater level of detail than in the work of Eastwick and Johnson, in an effort to highlight the importance of the relevant material to the work conducted within this thesis.

2.4.1 Experimental

The first systematic work done into studying the effect of windage on spur gears was done by P. H. Dawson [9, 10]. Dawson's aim was to investigate the windage relationship between gear speed, size, geometry and shrouding [9]. He used a smooth disk to simulate the sides of a spur gear, smooth drums to simulate a gear with no teeth, and a selection of thirty-seven spur gears with root diameters from 300-1160mm, face widths from 32-187mm and tooth modules from 2-24mm. Windage power loss was found to be proportional to the speed of the gear raised to the power of 2.9.

Dawson's experiments showed that for a large gear of 760mm root diameter, the power loss for the total gear (including sides) increased linearly with increasing gear tooth module; however, for a smaller gear with 300mm root diameter, the increase in gear windage increased at a higher rate. From these findings it was seen that for a large gear, over 90% of the windage losses is due to the teeth when compared with the smooth drum alone. It was found that by varying root diameter and keeping a constant module and facewidth that windage was proportional to the diameter to the power of 2.9.

The investigations into changing facewidth[1] led to some interesting conclusions. He found that there was a non-linear relationship between increasing facewidth and power loss from the gear - as the facewidth increased, the power loss increased at a rate that was smaller than linear. For a few tooth heights along the face from either end, the gear acts as a centrifugal fan, drawing air in axially and ejecting it radially and tangentially from the gear. As this effect is 4-5 times higher per unit length at the edge of the gear than at the centre of the gear face, an increasing gear facewidth would consequently not lead to the windage increasing at the same rate. In response to this, paper washers were placed at the end of the teeth in order to prevent air being drawn in axially. It was found that by doing this a reduction in windage losses of 22-44% could be produced. Preventing a gear from doing work on air is a concept that can be applied to all

[1]The facewidth of a spur gear is the length of the teeth in an axial direction

shapes and types of gear, as seen in the next section on spiral bevel gears.

Dawson did some elementary work on shrouding a large spur gear. The maximum reduction in windage he achieved was a 66% reduction using a smooth surround with rough side walls. A criticism of the shrouding that Dawson undertook is that the distances between the gear and the shroud were generally quite large, being 15 to 30mm which is significantly larger than mechanically possible, and indeed probable in a gas turbine gearbox.

In a second appendix to his paper, Dawson introduced an empirical formula shown in Equation 2.5, based on the graphs he created. It gave a good approximation to the results he had obtained, although he stated that it should only be used in the limited region of testing he had done.

$$P = N^{2.9}\left(0.16D^{3.9} + D^{2.9}F^{0.75}M^{1.15}\right) \times 10^{-20}\phi\lambda, \tag{2.5}$$

where P is the windage power loss, N is the rotational speed in rpm, D is the diameter, F is the facewidth and M is the tooth module. ϕ is an unknown function of the effective density of an oil laden atmosphere ($\phi = 1$ for oil free atmosphere) and λ is a function representing the effect of the gear case.

Dawson [10] continued his work on windage losses on high speed gears, and followed up his first paper with a second that better expressed the windage on spur gears in terms of non-dimensioned coefficients. He introduced a non-dimensional coefficient, C,

$$C = C''\left[Re/\left(5 \times 10^5\right)\right]^{\alpha}, \tag{2.6}$$

where C'' is a constant shape factor, and is equal to the value of C at a Reynolds number of 5×10^5. Dawson provided a graph from which values of C'' could be read for different shapes of gears running in free space. From his experiments, α

was found to be equal to -0.15.

Using this non-dimensionalised relationship and because of an increased quantity of results, some of the constants found in his previous paper were changed slightly to give an updated equation for power loss as shown by,

$$P = 1.12 \times 10^{-8} C'' \rho N^{2.95} D^{4.7} \upsilon^{0.15} \lambda. \tag{2.7}$$

λ is the same as in Equation 2.5, and it can be seen that the facewidth is now enveloped within the shape parameter. The equation clearly shows that the power scales very heavily with increasing root diameter. The value of $D^{4.7}$ matches well with the "back-of-the-envelope" consensus amongst gear designers that power losses scale with $\sim D^5$. Additionally, this value is close to the value of 4.32 found in Section 4.3.2 that looks at the outer diameter of a spiral bevel gear.

Lord [28] conducted some experimentation on spur gears, studying the effect of changing the module (the number of teeth for a fixed diameter), facewidth length and diameter of the gear. He found that the facewidth made the smallest difference to the windage power losses, which is in line with the findings of Dawson [9] reported earlier. Lord found that the radius and module had a larger impact upon the size of the windage power loss. He tested a range of modules[2] from 1-5 mm and found that the minimum windage was for gears with the smallest module, and the largest for those with a module of 4mm. This leads to the potential conclusion that the decreasing number of teeth of a gear with a larger module would at some point (in this case at a module of 5mm) start to outweigh the increase in per-tooth windage from the larger teeth. However, as module sizes of over 5mm were not tested, this conclusion was not made in the literature due to a lack of additional data.

Diab *et al.* [11] also presented some experimental results, and additional numerical analysis into a set of unshrouded spur gears, ranging in size from 144 to

[2]A smaller module means that a gear of a fixed diameter will have a larger number of smaller sized teeth

288mm pitch diameter. The facewidth of the spur gears was set as either 30 or 60mm and the module as 4 or 6mm. The results they established experimentally were broadly in line with those found by Dawson [9] and the empirical correlation in Equation 2.7. Diab *et al.* created two further methods of calculating the windage on the spur gear. Firstly they used dimensional analysis to create an empirical expression that used "...dimensionless terms representative of fluid flows and gear geometry." Secondly, a model of fluid flows and circulations on a rotating disk and gear sides plus teeth was created, leading to a "quasi-analytical power loss formulae". Both methods compared well with the experimental results, but the second, analytical method was judged to be most appropriate as it considered the fluid flow phenomena directly.

2.4.2 Computational

Al-shibl *et al.* [2] conducted a two-dimensional computational fluid dynamics study into the effects of windage on a single spur gear rotating in air. A two-dimensional model was used with a RSM turbulence model, running steady state, isothermal and incompressible. His study focused on the tip to shroud clearance, and also investigated the effects of adding a chamfer onto the edge of the teeth. Comparison was made with the work carried out by Lord [28], and modification of the gear tip geometries to allow comparison to Dawson's work [9, 10].

In order to reduce the computational costs of running an entire gear, a two-dimensional two-tooth slice (3.6°) of the gear was simulated with rotationally periodic boundaries. The spacing between the toplands[3] of the teeth and the shroud was variable, as this was the primary variable being investigated. Non-dimensional shroud spacing was used, defined as the ratio of clearance to gear pitch circle diameter. Values ranged from 0.005 to 0.05, which equates to shroud spacing of 1 to 10mm. The gear speed ranged from 5,000 to 20,000rpm.

[3]The topland of a tooth is the surface on the tip of the tooth, furthest from the axis

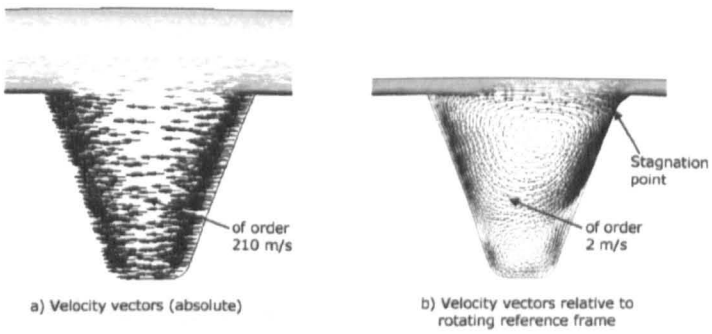

Figure 2.2: Flow structure in tooth valley of spur gear [2]

Al-Shibl's results for torque matched closely with Lord's at lower speeds, whilst at higher speeds such as 17,000rpm, a difference of 14 per cent was seen. It was apparent from the calculations that the power loss from the sides of the gears was significant. It was concluded that a fully three-dimensional model would be necessary to remove dependence on the side correlation used.

Al-Shibl was able to produce detailed graphics of the flow structures within the teeth valleys, and found secondary flows at speeds 2-4 orders of magnitude lower than the primary (rotational) flow speed, as shown in Figure 2.2. As a consequence of these flows, a stagnation point on one side of the tooth caused the difference in pressure from the other side, which leads to the retarding torque on the gear and hence power loss. This pressure difference was the largest contributor to the power loss — at 20,000rpm and a shroud spacing of 1mm, the pressure losses were 489W, and the viscous losses only 33W.

A small investigation of the effect on shroud spacing was undertaken and although limited, did find a close correlation between the computational predictions and the experimental data for shrouds of 1mm clearance, but at larger clearances the link was poorer.

These bodies of work have a clear relevance to the work reported within this thesis. The experimental work by Dawson was the first published scientific attempt to quantify gear windage, and hence provides an excellent historical perspective, whilst also providing useful conclusions. The computational work takes this

further by formulating solution strategies into modelling gear windage, and providing insight into the flow regimes present within the teeth, and this information can be directly fed into the techniques used for meshing and simulating a spiral bevel gear.

2.5 Spiral bevel gears

There is little available literature available in the field of windage of spiral bevel gears, and much of what has been done experimentally and computationally was completed at the University of Nottingham. A spiral bevel gear forms the basis for the work within this thesis, therefore, it is important to assess the work that has been carried out previously. This section will once again split the work into experimental and computational subsections.

2.5.1 Experimental

Winfree [50] conducted a series of experiments on a spiral bevel gear in an attempt to better isolate individual gear windage effects. The objective of his work was to measure the windage on a high speed spiral bevel gear with a variety of shrouds, and establish a series of design rules for shroud design.

The experimental setup consisted of a Plexiglas casing supported by a steel frame, in which sat a 15 inch hard urethane spiral bevel gear attached to a motor. The gear could run up to 6,500rpm and have oil sprayed on to it while running to replicate gearbox conditions. The apparatus is shown in Figure 2.3 . It is worth noting that in comparison to the spiral bevel gear found inside a gas turbine IGB, the one Winfree used was around 30% larger in size, but only ran at 50% of the speed and therefore is more comparable to that found in a helicopter gearbox.

Winfree, being based in the United States, used imperial units for his calculations, and established the horsepower of the motor using the current and voltage drawn

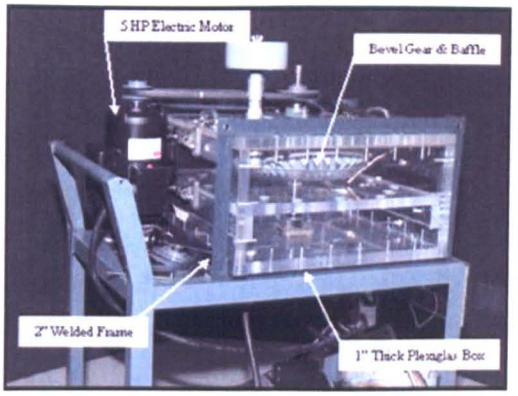

Figure 2.3: Apparatus used by Winfree [50]

and a constant to convert from Watts to horsepower. There is no mention in his paper of there having been any attempt made to quantify the system losses of the bearing and pulleys; consequently, it is difficult to know whether the horsepower calculated is just for the gear and shroud being tested, or for the whole system. Equation 2.8 is the calculated horsepower, Pw_1, established from the voltage, V and current, I drawn from the motor,

$$Pw_1 = \frac{VI}{745.7}. \tag{2.8}$$

A windage correction factor was introduced, which is a system efficiency correction for an oily atmosphere or increased density within the gearbox. It is effectively a ratio between his calculated power and the industry standard for horsepower, Pw_2, as given by Dudley's gear handbook [40] which is shown below in Equation 2.9 in which N, D & F are all specified in imperial units.

$$Pw_2 = \frac{N^3 D^5 F^{0.7}}{10^{17}}. \tag{2.9}$$

Combining Equations 2.8 and 2.9 gives the windage correction factor, C_f,

$$C_f = \frac{VI \times 10^{17}}{745.7 N^3 D^5 F^{0.7}}. \tag{2.10}$$

The figures used for Pw_2 are only approximations and lead to questions as to the validity of the windage correction factor; however, the values obtained by Winfree provide a useful set of data for designers when it comes to better estimating the windage likely to be seen in their own gearboxes.

Winfree found, much like Dawson before him, that by covering the inlet and outlets to the tooth valleys, a large reduction in power loss can occur — 79.3% when running dry, and 70.7% with 5 gallons/minute of oil being sprayed on the gear. This was while running at 4000rpm. This reduction is 2-4 times the reduction of that seen by Dawson and can most likely be attributed to two factors: firstly, the bevel gears pump fluid more than spur gears, so there is a larger scope for reducing the pumping and hence windage power losses by taping the ends of the teeth. Secondly, the gears used by Dawson were a lot larger than the ones used by Winfree, so taping the ends of these larger spur gears would leave large areas of facewidth unaffected by the taping. The spiral bevel gears that Winfree used have a far smaller facewidth to tooth height ratio, so the effects of taping the ends of the teeth would proportionally stretch further along the face of the gear. Using visualisations, Winfree concluded that just preventing the gear from pumping is not sufficient when there is a second phase involved, and that it is also necessary to vent away any trapped lubricant in the gear teeth. Unblocking the outlets of the teeth reduced the windage for the case with a lubricating fluid present, compared to when both inlet and outlet were blocked. This is an important conclusion, which is addressed in Chapter 6 with regards to the design of the outlet of a shroud.

Winfree established that the direction of rotation has little or no effect on the windage of a gear, the difference between an unshrouded dry gear clockwise and counter-clockwise was only 2.5% and for a shrouded gear with 5gal/minute water was -0.88%, and should be considered negligible in both cases.

There was also an attempt to see if there was an optimum distance that a shroud should be from the gear teeth. Winfree conducted a number of tests on shrouds with differing shroud-gear spacing, all of which had no holes in them. The con-

clusion that he drew was that restricting the inlet is the optimum solution and that keeping the shroud as close to the face of the gear is detrimental, as it is not possible in two-phase flows to vent away the lubricant properly. Visualisations showed that lubricant was drawn around the shroud climbing upwards and increasing in speed until it reached the gear speed at around 90° from the out-of-mesh lubricating jet. Winfree stated that "Logic would lead one to believe that exit holes belong in the first 90 degrees of the baffle". This statement led to the formation of a series of tests using geometrically identical shrouds, except for a differing number and configuration of holes within the first 90 degrees from the out-of-mesh lubricating jet. Using the results gathered from this testing Winfree formed an optimised shroud, which had inlet, face and outlet clearances of 0.05", 0.2" & 0.25" respectively and a single hole at a 45° location. A reduction in windage of 63.2% was found over the baseline case when running with lubrication.

At the University of Nottingham, there has recently been a program of experimental research into the windage power loss from a shrouded spiral bevel gear [22, 23]. The first paper of Johnson *et al.* involved a series of experiments on a single gear, and both unshrouded or shrouded it was concluded that it acted like a centrifugal fan [23]. Consequently, this led them to suggest that fan design approaches could be used to inform gear and shroud design to help reduce windage losses.

A test rig was designed and assembled to allow bi-directional rotation of the gear, which was tested in three configurations:

- Unshrouded
- Shrouded with no control of mass flow rate through the system — so called "natural" condition
- Shrouded with prescribed mass flow rate, with the air conditioned by a "bullet" section in the air delivery pipe.

Johnson *et al.* characterised the windage power loss in a non-dimensional form as torque coefficient, C_M,

$$C_M = \frac{T}{\frac{1}{2}\rho r^5 \omega^2}. \tag{2.11}$$

For the unshrouded case, a number of points were noted. Firstly, the C_M curves were similar in shape and constant over most of the speed range, rising slightly at higher speeds. The conclusion was that the measured windage torques scaled approximately with the square of speed. The second point was that the torque required to rotate the gear clockwise was higher than that needed to rotate the gear anti-clockwise. It was suggested that when rotating clockwise, the gear acts like a backward curved centrifugal fan — where both the leading and trailing edges of the gear teeth are inclined away from the flow. This is the usual case for most fan impeller blades [5], as by having the fan blade edges inclined away from the direction of rotation, flow separation in the blade passages is reduced. Consequently, if the gear is rotating in the opposite sense it is to be expected that the flow may be separating within the gear teeth passages, which in turn reduces the windage power loss due to a reduction in pumping of air. In effect, the result is a statement that in order to reduce the windage power losses for a spiral bevel gear, it is worth exploring fan design practice to create as ineffective a centrifugal fan as possible to reduce parasitic pumping of the air.

In the shrouded case with "natural" air mass flow rate, there was no prescribed air flow through the system — the quantity of air flow is determined by what the shrouded gear would naturally pump given the static pressure difference between inlet and outlet of the shroud, which was zero Pascals in this case. This case is effectively the same as the unshrouded case (in terms of boundary conditions) and allows the effect of the shroud to be determined. It was found that the shroud reduced the windage power loss by up to 75% for a clockwise rotation, which was the rotational direction that had the largest reduction. Secondly, the shroud reduced the windage power loss's dependence on the rotational direction

— both clockwise and anti-clockwise directions had very similar windage power loss values at all speeds when shrouded. Johnson *et al.* stated that a centrifugal fan would predict a C_M trend that was independent of speed, and this was roughly observed for both unshrouded and shrouded gears indicating that as expected, a spiral bevel gear operates in a similar manner to a centrifugal fan.

Several findings were noted when the mass flow rate through the system was prescribed: firstly, C_M increases with increasing mass flow rate; secondly, for a given mass flow rate, C_M is typically less for the clockwise direction. Through looking at static and dynamic pressure comparisons, two observations were made:

- When rotating clockwise - which is analogous to an impeller with backward curved (BC) blades -the gear generated higher static pressures than when rotating counter-clockwise, which is analogous to an impeller with forward curved (FC) blades.
- Higher shroud outlet dynamic pressures are generated for anti-clockwise rotation of the gear (like FC impeller blades) than for clockwise (BC) rotation.

For a dynamically similar set of fans operating at the same point on the performance curve, there are a series of laws which relate the performance variables of pressure, air flow & power to the fan parameters of speed, impeller diameter & air density. The testing in the experiments conducted by Johnson *et al.* was done with a single gear with identical air densities. As only the gear speed was changed, it is possible to reduce the fan similarity laws to the following three equations,

$$\frac{Q_a}{Q_b} = \frac{\omega_a}{\omega_b}, \tag{2.12}$$

$$\frac{p_a}{p_b} = \left(\frac{\omega_a}{\omega_b}\right)^2, \tag{2.13}$$

$$\frac{P_a}{P_b} = \left(\frac{\omega_a}{\omega_b}\right)^3 \text{ or } \frac{T_a}{T_b} = \left(\frac{\omega_a}{\omega_b}\right)^2 \text{ or } \frac{C_{M,a}}{C_{M,b}} = 1. \tag{2.14}$$

Using Equations 2.12, 2.13 & 2.14, Johnson *et al.* scaled the results from the gear running at 15,000 rpm down to the experimental results of 8,203 and 3,000 rpm. It was found that the pressure rise across the gear face scaled well, with a very close match to the experimental results — confirming that the gear was acting in the same manner as a centrifugal fan [1]. It was noted that the pressure scaled as equally well for clockwise gear rotation as for anticlockwise rotation, despite the potential for large amounts of flow separation between the gear teeth when rotating anticlockwise; consequently, it was concluded that flow separation was not a dominant factor determining performance. C_M was not found to scale well, but this was determined to be due to poor characterisation of the assumed losses of the gearbox.

When characterising the performance of a fan, it is useful to plot static pressure and air flow against each other in a non-dimensional form, as given by flow coefficient φ, Equation 2.15, and static pressure coefficient ψ_s shown in Equation 2.16.

$$\varphi = \frac{Q}{\omega D^3}, \tag{2.15}$$

$$\psi_s = \frac{p}{\rho\omega^2 D^2}. \tag{2.16}$$

Using these non-dimensional equations, the performance trends of typical BC and FC centrifugal fans can be compared with that of a shrouded gear. What was found was that although the gear acted as a fan, its performance was greatly reduced when compared to either type of centrifugal fan — a good thing when it is considered that this means less power is being used transferring energy from

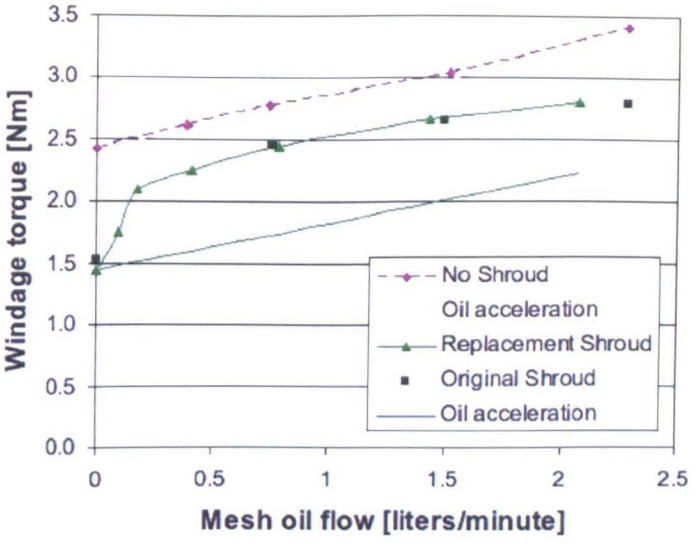

Figure 2.4: A graph of gear windage versus mesh oil flow rate at 12500rpm [22]

the gear to the air.

Johnson *et al.* were able to alter the shroud design, which was done in order to see if windage power losses could be reduced by restricting the air flow through the system — a key way in reducing power losses. It was concluded from the experimentation that a shroud with a restrictive outlet and inlet was far better at reducing windage than a shroud which had a more open free-flowing fluid passage. This was in line with the single phase findings of Winfree [50].

The second paper from Johnson *et al.* [22] expanded upon the work done previously by introducing oil as a lubricating medium. When the gear was unshrouded, an increasing amount of oil being injected onto the gear led to an increased torque above the single phase windage. This could be closely calculated using an oil acceleration relationship as given by Equation 2.17,

$$T_{\text{oil}} = m_{\text{oil}} \omega r_{\text{gear}}^2. \tag{2.17}$$

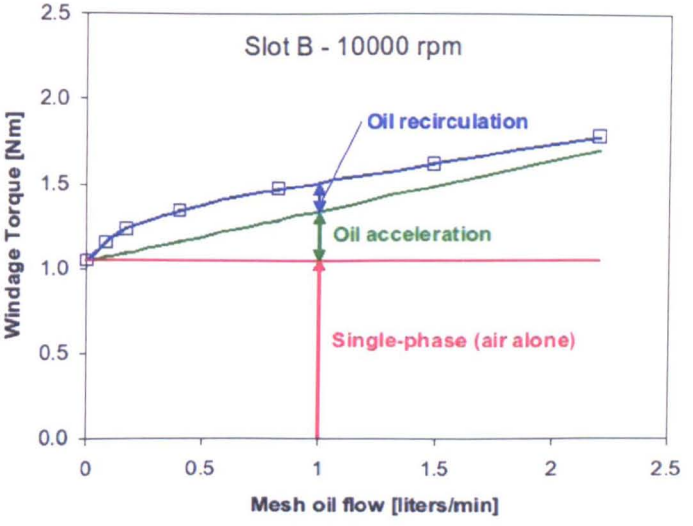

Figure 2.5: Breakdown of terms that determine windage torque level [22]

When the gear was shrouded it was seen that as soon as a small amount of oil was added the effects of shrouding were almost completely nullified, as shown in Figure 2.4 in which the green line for windage torque is at almost the same level as the unshrouded gear after only a small oil flow is introduced. Visualisations showed that trapped oil was moving along the underside of the shroud towards the centre of the gear owing to a toroidal vortex between the gear and shroud. This oil is constantly recirculated, incurring a heavy energy cost. A number of slots in new shrouds were created to identify an optimal location of a slot in order to allow oil to escape from between shroud and gear, hence reducing oil recirculation. The two best cases were similar as they allowed the oil to escape very soon after injection onto the gear and were designated slots "A" and "B". Slot "A" started 17° round from the oil jet and extended 26° and slot "B" started 5° round from the jet and extended a further 61°. It was seen that the further round from the oil jet that the slot started, the higher the total windage — which leads to the conclusion that recirculation of the oil is important and should be reduced.

Figure 2.5 shows for a typical slot – slot "B" – how total windage torque (indicated by the blue line) changes with increasing oil flow, and how it can be formulated from three components: single phase windage (red line); oil acceleration (green

Parameter	Value
Number of teeth	91
Outer radius	133.5 mm
Module	2.92 mm

Table 2.1: Geometric data for Farrall gear

line) which was also given in Equation 2.17; and the oil recirculation component which is the component most affected by the position and size of the slots.

This work is very useful, as the geometries involved are close (or identical) to the ones used within this thesis for modelling gear windage of a spiral bevel gear. The work of Johnson *et al.* [22, 23] in particular is essential, as the data produced will be used for validation of the models created. Additionally, the insight into the flow regimes present, and the size of variables such as mass-flow-rate and pressure allow a meshing strategy to be formulated that can capture the important parts of the flow, as identified in the previous literature.

2.5.2 Computational

Farrall [13] conducted three-dimensional CFD experiments into the windage of a spiral bevel gear whose geometric data is shown in Table 2.1. The gear used is the same as that used by Johnson *et al.* [22, 23], Rapley *et al.* [33, 34, 36], and as the "control" gear in the work contained in this thesis.

The computational model was rotationally periodic, with two of the 91 teeth being modelled. The periodic boundaries followed the spiral angle of the gear, and pass through the valleys of the teeth. Two model sets were studied: an open (unshrouded) gear; and three shrouded models, with varying shroud distances. The gear was simulated as running at 15,000 rpm, which equates to a tip Mach speed of 0.5. Turbulence was modelled using an RSM model. Using prescribed velocities, mass flow rates were calculated and the system subsequently characterised

for mass flow rates in the range 0.1kg/s to 0.4kg/s.

In determining the characteristic curve for each gear system, Farrall *et al.* made a couple of assumptions:

- The radial pressure in the downwind chamber is negligible compared to the pressure difference generated by the rotating gear and shroud,
- At the exit of the shroud, the air expands into a chamber with a large area, and hence loses all of its dynamic pressure.

Using these two assumptions, it is stated that at the operating point for the system, the total pressure at the model inlet will equal the static pressure at the outlet of the shroud,

$$p_{\text{total}}\,(\text{inlet}) = p_{\text{static}}\,(\text{outlet})\,. \tag{2.18}$$

As there will only be two mass flow rates for a given shaft speed and a given system that this will hold true (one of which is a mass flow rate of zero kg/s), by plotting curves of mass flow rate against $p_{\text{total}}\,(\text{inlet}) = p_{\text{static}}\,(\text{outlet})$, the operating point can be determined.

Parameter	Value
Mass flow rate (kg/s)	0.31
Windage loss (kW)	5.9

Table 2.2: Losses for unshrouded gear rotating at 15,000rpm

For the simulation of the unshrouded gear, it was found that the air drawn onto the face of the gear is given a high degree of swirl only in the immediate vicinity of the gear. The area behind the gear has high swirl due to it having picked up rotation from being pumped through the gear, and due to the rotation of the back surface of the gear. The air is ejected from the teeth at the outer diameter

of the gear in an almost entirely axial direction, which is a little unexpected when the 60° cone angle of the gear is considered. The mass flow rate pumped through the gear and the associated windage is shown in Table 2.2.

The next simulations also involved an unshrouded gear, this time with an inlet dam to the gear teeth. Dawson [9, 10] and Winfree [50] both conducted experiments into inlet dams as a way of reducing the windage on spur and bevel gears respectively, with varying degrees of success. Farrall found that the inlet dam made little difference to the mass flow rate through the gear, or to the windage and these results are shown in Table 2.3 . He did find that the dam made quite significant changes to the flow field, with far larger values of swirl being imparted to the air at the lower radii near the dam.

Parameter	Value	% change from unshrouded gear
Mass flow rate (kg/s)	0.28	-9.70%
Windage loss (kW)	5.73	-2.90%

Table 2.3: Losses for unshrouded gear with gear teeth inlet dam rotating at 15,000rpm

Farrall *et al.* make the statement that the reduction in windage in this simulation is a lot lower than the experimental reduction of around 70% that Winfree found. It should be noted that in Winfree's experiments, although the gear had the inlets to the teeth taped, the gear was also shrouded with a shroud of 0.1" inlet, outlet and face clearances. This is not made clear in the Winfree paper, and consequently, Farrall's comparison is not fully valid.

The next series of simulations involved shrouding the gear with face clearances of 1.5mm, 4mm or 12mm. For the two smaller face clearances, the inlet and outlet clearances are 4mm, whereas for the 12mm shroud, the inlet and outlet clearances are 12mm. The results for the three different shrouds are shown in Table 2.4 .

As can be noted from the table of results, the shroud of clearance 1.5mm reduced

Shroud face clearance (mm)	Mass-flow-rate (kg/s)	Windage loss (kW)	Percentage windage change
1.5	0.26	5.73	-2.9%
4	0.25	5.24	-11.2%
12	0.27	5.51	-6.6%

Table 2.4: Windage losses for shrouds with various face clearances

the windage by less than the shroud of 4mm face clearance. This led to the conclusion that there is an optimum distance between the shroud and the face of the gear. He also stated that "...in all cases the reduction of windage loss is not significant." Had a smaller inlet clearance been used, in line with the findings of Winfree [50] and Dawson [9], then the windage reductions would have most likely been larger.

Rapley *et al.* extended the work of Farrall *et al.* in two papers [34, 36] which complemented the experimental work conducted by Johnson *et al.* [22, 23]. Rapley *et al.* [34] firstly studied the best techniques to use when applying CFD to modelling windage power losses from a spiral bevel gear. They used two different geometries with experimental data from Johnson *et al.* [23] as validation. The first was an unshrouded gear which ran both clockwise and anticlockwise; the second was the same gear, shrouded in the "mass-flow rate prescribed" condition. In both cases single tooth models were created with periodic boundaries, similar to those used by Farrall *et al.* For the unshrouded gear the mesh contained 800,000 cells — a necessarily large amount owing to the gear being contained within a large chamber. The mesh for the shrouded gear contained up to 2,200,000 cells. This is a very large amount given the work that has been undertaken since. Turbulence was modelled using a $k - \epsilon$ RNG model, using both standard and enhanced wall functions.

For an unshrouded gear, Rapley was able to replicate the experimental qualitative trends well, but the quantitative agreement was poorer, with the CFD

consistently under-predicting the torque. Little difference was seen between the results for standard or enhanced wall treatments, which implies that pressure effects as opposed to viscous effects are dominating within the tooth valley, and that there is fairly constant pressure gradient moving away from the wall. Rapley explains that a steady-state simulation is unable to fully resolve the flow to a steady answer, as the flow travelling through the system is clearly transient, resulting in reported moment values which were unable to settle when a steady state formulation was used. For these reasons it was decided to conduct a transient simulation in order to capture the unsteady nature of the flow within the gear tooth valley. There is not any direct comparison of results from the steady and unsteady simulations, so it is not possible to ascertain whether any additional clarity was provided beyond being able to perform Fourier analysis on the results to identify dominant frequencies for the moment, which fluctuated with advancing time. The fact that this analysis was done does indicate that a transient simulation did improve upon the results of the steady simulation.

Rapley *et al.* [36] continued their CFD analysis in a second paper which deals with how variations in shroud geometry affect the windage on a single shrouded spiral bevel gear. This is the same gear as in his previous paper.

Three components of the shroud were changed: the inlet clearance from 1.56mm to 4mm; the face clearance from 0.25mm to 1.5mm; and the outlet clearance from 2.52mm to 4mm. These clearances are marked in red in Figure 2.6, along with the boundary conditions used in the CFD simulation. A criticism of the values used for the clearances is that the variation in their sizes is large — especially for the inlet. The smallest face clearance of 0.25mm is also unreasonably small for an engine application as interference due to thermal and centrifugal expansion of the gear/shaft would likely occur. The same turbulence settings were used as for Rapley's previous paper [34], and a standard wall function was used.

The conclusions that were drawn from this work were that small changes in the geometry of the shroud can have large impacts upon the windage power loss. Concentrating only on a clockwise rotation of the gear in question (the same

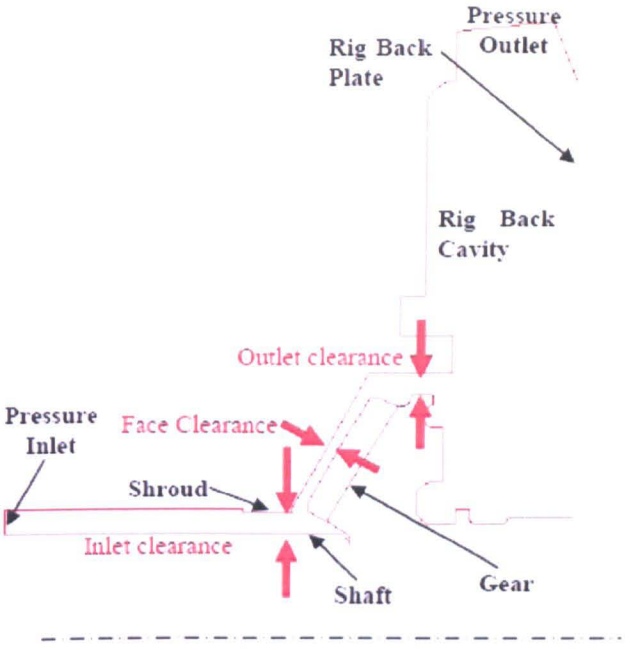

Figure 2.6: Shrouded geometry and CFD boundary conditions [36]

rotational direction as in the engine), from a baseline case of 4mm inlet clearance, 1.5mm face clearance and 4mm outlet clearance it was possible to reduce the windage by 46.7% by reducing the inlet clearance to 1.56mm. Recalling the experimental work of Johnson *et al.* [22, 23], by restricting the inlet of the shroud, the gear is prevented from being able to pump as much fluid through the system, which in turn reduces the windage power loss. Rapley *et al.* did find that by decreasing the face clearance from the baseline case to 0.25mm a 15.5% increase in torque was reported. This is once again in line with the findings of Johnson *et al.* [23] and Winfree [50] that it is possible to over-choke the flow and that there exists an optimal distance for face clearance. The work by Rapley *et al.* shows that CFD can be used to accurately predict qualitative relationships in gear windage, with a good degree of confidence of quantitative results.

Most recently, a study by Arisawa *et al.* of Kawasaki Heavy Industries [3] has used CFD to study the effect of oil churning and windage losses on aeroengine transmission gears. A difference between this work and that of Farrall [13] and Rapley [34, 36] is that the gears tested are from the external accessory gearbox,

as opposed to the internal gearbox. This means that the gears are smaller, with a maximum pitch diameter of 150mm, and rotate faster, with a maximum rotational speed of 20,000rpm. The gearbox itself contains a pair of spiral bevel gears which are used to transmit the torque from the radial driveshaft through a 90 degree angle. The gears are shrouded, and Arisawa *et al.* used three different shroud shapes, which covered less than 50% of the larger of the two gears in the gearbox.

A major difference between this study and those before, is the use of a secondary (oil) phase in the simulation. A Volume of Fluid (VOF) model was used to calculate the destination and trajectory of oil within the gearbox. When comparing the CFD simulation results to those from experimental data, the CFD was able to replicate similar trends of relative windage loss; however, there is no mention of the quantitative difference between the experimental and simulated results barring a statement saying "...the absolute values of the loss in the simulations were different from the experiments.".

There are a number of potentially serious issues with the modelling methodology used in the paper. This includes the use of incompressible governing equations, and no turbulence modelling. The pitch line velocity of the larger gear when rotating at 15,000rpm will reach over 115m/s (equivalent to around Mach 0.35), at which point compressibility effects will become important, and turbulence in the gearbox will certainly start to dominate the flow structures. Additionally, only single-order accuracy was used for discretisation of the governing equations. This truncates the length of the equations used for assessing flows between cells in the simulation, ignoring anything other than first order differentials, and consequently results in higher diffusion of flow and species than expected. Finally, the graph of power loss for the input gear versus time clearly shows that the power loss is still increasing with simulation time. This was attributed to the gearbox still filling up with oil from the beginning of the simulation, but as the oil flow rate was set significantly higher than the experiments in order to fill up faster, this leaves a number of questions as to the stability of the simulation and the averaged power values used to compare the three shrouds.

A paper by the author was published [46] that described the methodology for parametrically modelling a spiral bevel gear and simulating single phase gear windage. The paper explained the methods used, and applied the resulting model to investigate the effects of changing the number of teeth on a gear. It showed that a decreasing number of teeth results in a higher level of windage. The work in Chapters 3 and 4 builds upon the methodology and findings from that paper. Finally, a second paper [44] by the author was published that studied the destination of oil droplets released within the domain, and the work in Chapter 6 expands upon this in further detail.

2.6 Summary

This chapter has looked at a number of relevant papers in the field of gear windage. It started by looking at the basic physics behind a rotating cone, which can be thought of as a spiral bevel gear with no teeth, and also reviewed the state of computational studies into frictional resistance of a rotating, shrouded cone.

Rotating spur gears were then studied, with a number of papers looking at windage of a rotating spur gear — showing that effective shrouding, or damming of the teeth, can reduce the power losses by reducing the ability of the gear to pump air through its teeth and expel it radially or axially. A computational study that looked in detail at the flows within the valleys of the gear teeth is then reviewed.

The final section looks at the effect of shrouding upon windage of spiral bevel gears. Work conducted at the turn of the Millennium showed that shrouding a spiral bevel gear is most effective if the inlet to the shroud is heavily restricted, and that is is possible to increase windage if the shroud is too close to the face of the gear. Further work carried out at the University of Nottingham has confirmed this and taken the work further by considering the shrouded gear system as an analogy of a centrifugal fan. There has also been a program of computational

work which looked at numerically modelling the gear and shroud to conduct a parametric study into the spacing of the shroud. This work showed that CFD was capable of qualitatively replicating experimental results, but there was a quantitative difference. This section concluded with a study that used a two-phase approach to look at the impact of oil on a pair of spiral bevel gears. This study had a number of serious failings, but showed that the CFD was able to predict the relative windages of a number of shrouds.

The work reviewed in this chapter has shown a number of key conclusions: firstly, that shrouding a gear of any sort is an easy way of reducing the windage of air and churn of oil in the system, which in the context of a gas turbine will reduce heating of the oil. Secondly, CFD can be used as a way of conducting a parametric study of one or more variables of a shroud in order to assess their relative performances.

There are several gaps within the available literature which will be addressed by the work within this thesis. There is no computational work that has looked into the size and shape of the spiral bevel gear. CFD lends itself well to this work, as it is expensive to produce a physical gear, so the use of a computational model makes sense for financial and time reasons. Secondly, there have been some studies, notably Rapley [34, 36] that have looked at the distance of a shroud from the gear for a couple of designs of shroud. However, there has not been any work that has used CFD to simulate the flows of a large number of theoretical shroud shapes in an effort to directly feed into shroud design guidelines. Lastly, the use of CFD to look at the flow structures between gear and shroud when oil droplets are present has not been studied. This thesis aims to address these three separate points and unify their findings into a set of coherent conclusions which will aid future work on gear windage, and also inform future shroud and gear selection and design.

CHAPTER 3

Methodology

3.1 Introduction

This chapter describes the methodologies used to solve the simulations presented within this thesis. There are five processes involved, and each is addressed in their own section:

1. Geometry formulation, Section 3.2: This utilises Pro/Engineer [8] to create a parametric solid model of the spiral bevel gear. The walls of the chamber in which the gear sits and which form the boundaries of the simulation domain are also created within Pro/Engineer.

2. Mesh creation, Section 3.3: Meshes are created with the solid models from step one, using ANSYS ICEM CFD 12.0 [21] to produce a hexahedral mesh that enables the flow field to be solved.

3. Solution, Section 3.4: The flow field is solved using ANSYS FLUENT 12.1 [21]. This section will deal with the numerics of the solution, and justify the models chosen. It will also provide the solution strategy formulated over the course of this PhD.

4. Data analysis, Section 3.5: A number of tools are used to extract meaningful, comparable results from the solutions. These include the built-in functions and visualisation tools within FLUENT and also within ANSYS

CFD-POST [21], a post-processor that links to FLUENT. Additional numerical analysis is done within Microsoft Excel [7] and Mathsworks Matlab [20].

5. Verification (Section 3.6), and validation (Section 3.7) : In order to have confidence in the results reported elsewhere within this thesis, verification and validation of the mesh must be performed. This respectively involves checking that the mesh is not impacting upon results, and that the results accurately reflect real world experimental results.

Figure 3.1: Front view of control gear, mounted on rig

3.2 Geometry formation

3.2.1 Overview

A parametric model of a spiral bevel gear was created in Pro/Engineer Wildfire 2.0 [8], using information provided from a data sheet produced by Gleason Corp [6], a gear manufacturer. The initial model is based on a Rolls-Royce Trent 500 internal gearbox (IGB) crown gear, as used by Johnson *et al.* [22, 23], Farrall *et al.* [13] and Rapley *et al.* [33, 34, 36]. It is referred to as the "control gear" or "control system", henceforth as its results are used to compare against all

geometric variations in Chapters 4, 5 & 6. Experimental results from Johnson *et al.* [23] are used to validate the results from the simulations using the model of this gear, and this is detailed in Section 3.7. Key geometric data for this gear is given in Table 3.1. A front view of the control gear can be seen mounted on the experimental rig in Figure 3.1.

Parameter	Value
Number of teeth	91
Outer radius	133.5 mm
Module	2.92 mm

Table 3.1: Geometric data for control gear

The gear is defined within the parametric model, using sizes from the data sheet and relationships derived from the input data; for example, the module, which is defined as the pitch diameter of the gear divided by its number of teeth. This is seen in Figure 3.2, which shows a sample spur gear with the pitch diameter, and circular pitch marked on it. A spur gear is used for this example, as it is easier to follow than a spiral bevel gear when shown in 2D; however, the concepts are the same for both types of gear. The pitch circle is where the contact between meshing gears occurs, and the circular pitch is the length of the arc on the pitch circle between neighbouring teeth on a gear. The module of the gear is the pitch diameter divided by the number of teeth, and therefore represents the amount of pitch diameter per tooth. Module is an important variable, as two gears will not mesh unless their modules are the same.

The parametric model allows for automated update of the gear teeth if one or more of these values are changed. Changing a parameter such as the total number of teeth on the gear is a matter of altering the relevant number in the model and allowing the software to recalculate the gear shape. The advantage of this approach is that a computational gear can be created which is representative of a real gear, and also allows parametrisation of the effect of changing a single variable, *i.e.* creating a non-physical gear for the purposes of an investigation.

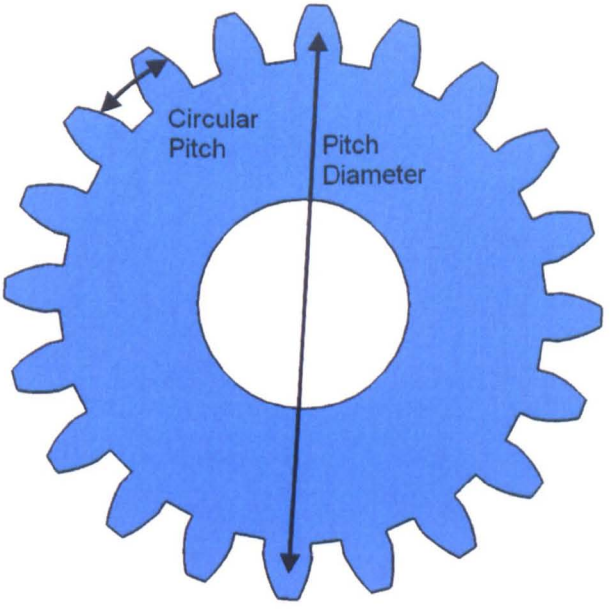

Figure 3.2: Key gear dimensions for a sample spur gear

There are limits to the extent to which a new gear can be created from the model, and these limitation should be appreciated. It is not possible, for example, to increase or decrease the number of teeth past values of around 20 above or below that of the control gear. The reason is that in the absence of a new complete set of gear geometry data from the Gleason Corporation, assumptions regarding the sizing of aspects of the gear, such as tooth height, or gear cutter radius have to be made. These assumptions are based on gear theory [40]; however, the nature of how spiral bevel gears are "generated", or "created", means they will become less appropriate the further the gear parameters deviate from the control gear. In the context of the gear cutter radius, for example, this has been kept at the constant value as used by Gleason for the Trent 500 spiral bevel gear. This cutter will have a range of facewidth sizes that it is able to cut, but a gear with a larger facewidth would generally use a cutter with a larger diameter. The relatively small changes in sizes of the gears means that assumptions like this are limited in their impact.

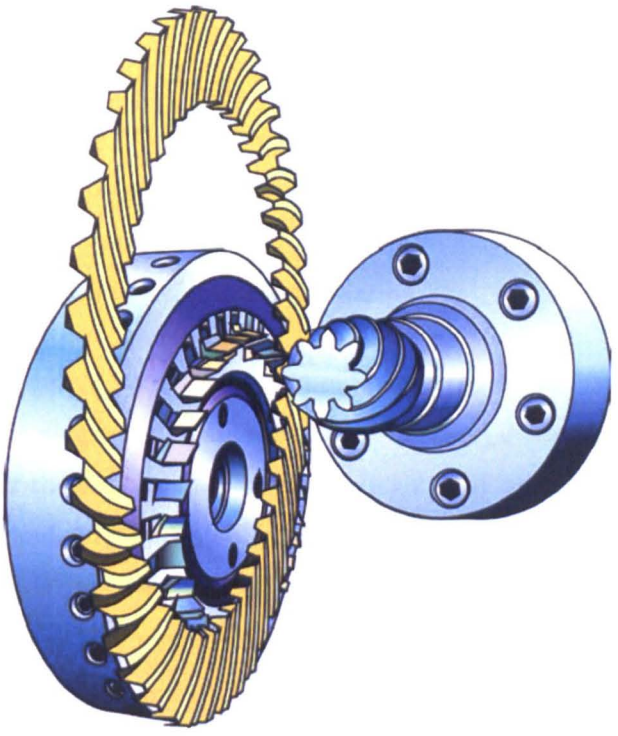

Figure 3.3: Circular cutting tool and a gear being cut. LHS in blue is the cutter,RHS is the gear being cut. The large yellow gear is the "virtual" gear which the cutter is mimicking the tooth profile of in order to cut the gear. [6]

3.2.2 Modelling of gear

The spiral bevel gear being computationally modelled is based upon one physically manufactured using a "generating" method, in which the gear teeth profile is created by a cutter that simulates the tooth of a "virtual" generating gear. This imaginary gear does not exist in reality, but represents the profile that the cutter needs to take out of the gear blank to create the tooth valley for the physical gear being manufactured. This can be illustrated in Figure 3.3, which shows the cutting of a gear on the right-hand-side of the figure by the cutter on the left-hand-side. Superimposed in yellow is the shape and size of the virtual gear, which could mesh with the gear being fabricated. Note how at the point where the gear is being cut by the cutter, the motion of the cutter blades would follow the profile of the tooth of the virtual gear. Both the cutter and the gear being manufactured rotate on their respective axes exactly as would the gear and the

imaginary generating gear (were they meshing), with rolling of each to ensure that the gear valley allows the teeth of a pinion and crown gear to mesh with each other by providing enough clearance. This method of gear cutting is quite unlike any other type of gear manufacture, and is necessary to ensure conjugate action between pinion and crown gears. Reference can be made to literature from the Gleason Corporation for further information [6].

The spiral bevel gear's teeth are commonly referred to as having an "octoid" profile due to the shape of the line of action between crown and pinion on the gear flank. This tooth shape is the spiral bevel gear analogy of a spur gear's involute curves, and they barely differ in shape. It is possible to use an external mathematical model, such as used by Li *et al.* [27] to accurately create the shape of the tooth flanks using a generating method; however it is concluded that time-consuming integration of separate models with the solid modelling software would not be an effective use of resources within this body of work.

The approach taken in this thesis is to approximate the octoid tooth profiles to that of involutes. These can be swept through a circular arc, defined by a spiral angle which creates the surfaces of the teeth, allowing a parametric model to be created in Pro/Engineer. The following section will provide an overview of the formation of an involute tooth profile.

3.2.2.1 Fundamentals of involute tooth geometry

An involute curve is often described as the shape the end of a piece of string would make if it were held taut and unwrapped from a circle around which it is curled. In spur gearing, teeth with profiles the shape of involute curves allow a pair of gears that are meshing to have a constant speed ratio between the two gears during the entire meshing cycle [40]. Figure 3.4 is a sketch that shows the line of action (marked in blue) of a pair of involute spur gears that are meshing. The line of action is the locus of contact points during meshing, and as seen in the diagram, more than one pair of teeth can be in contact at any one time. The

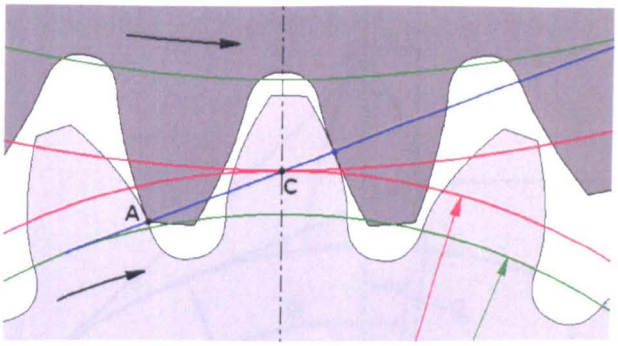

Figure 3.4: A sketch showing the engagement line of action of a pair of involute gears. Base circles of gears are marked in green, and the pitch circles marked in red. Blue is the line of action between the two gears.

line of action is the tangent to the base circles (marked in green) of both gears. Finally, the pitch circles are shown in red.

With reference to Figure 3.5, the radius to the point i on the involute profile, r_i and the constant base radius, R_b are used to define the angle φ_i, which is called the "transverse pressure angle",

$$\varphi_i = \cos^{-1}\left(\frac{R_b}{r_i}\right). \tag{3.1}$$

An involute function, *inv*, can be described by Equation 3.2,

$$\text{inv } \varphi_i = \tan \varphi_i - \varphi_i. \tag{3.2}$$

In Figure 3.5, the location of the two involute curves relative to each other is determined by the tooth thickness at its base, t_b. The angle φ_p is the angle between the centre of the tooth, where it would reach a point at p, and the position where the involute curve meets the base circle. Its involute is defined in Equation 3.3,

$$\text{inv } \varphi_p = \frac{t_b}{2R_b}. \tag{3.3}$$

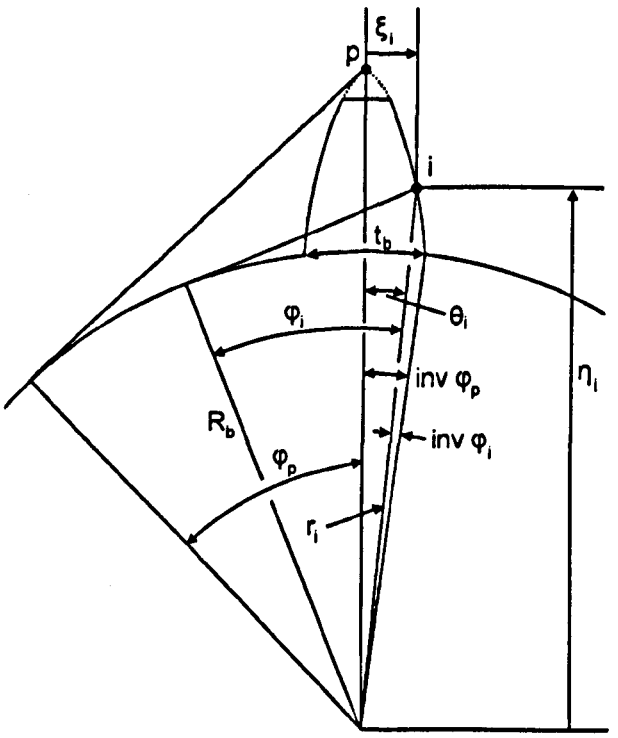

Figure 3.5: Relationships used in creating an involute curve

The parametric nature of the solid modelling program allows the coordinates of the point i, marked on Figure 3.5 to be described as the variation of polar angle θ_i. θ_i is defined by

$$\theta_i = \text{inv } \varphi_p - \text{inv } \varphi_i. \tag{3.4}$$

The coordinates of i, with respect to the centre of the gear, are therefore described by:

$$\xi_i = r_i \sin\theta_i, \tag{3.5}$$

$$\eta_i = r_i \cos\theta_i. \tag{3.6}$$

3.2.2.2 Creation of gear within Pro/Engineer

Pro/Engineer is a solid modelling program that allows for curves to be created and linked to each other using parametric relationships. For example, a line can be attached to another line, and will automatically move if the second line is moved by the user, and vice versa. The user is also able to create parametric variables and expressions that can be linked to the sizes of geometric features. A user is then able to change this variable and it to automatically update the model with the new sizes.

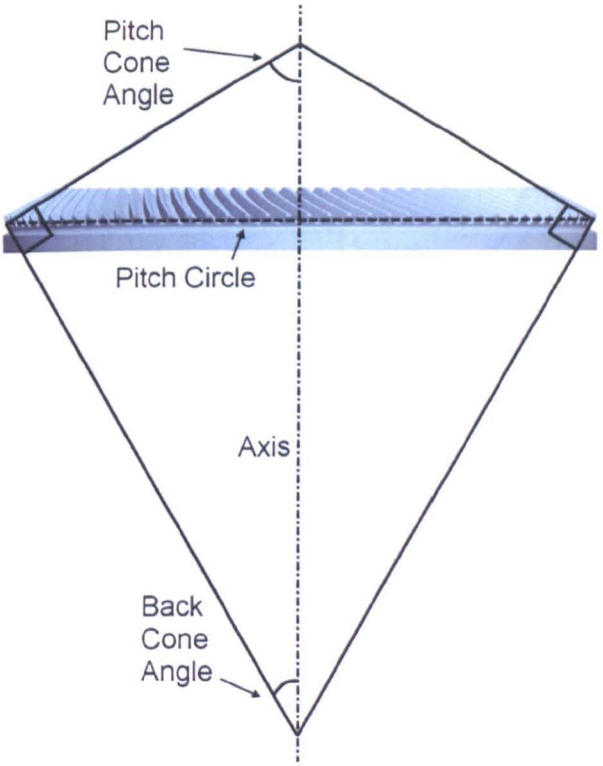

Figure 3.6: Pitch cone and back cone angles marked on a side view of the control gear

These parametric variables can also be linked to further variables, meaning that a cascade of relationships can be changed by a single number. In the context of the model presented here, changing the number of teeth involves simply changing the number in the table of dimension variables. Pro/Engineer will then create a new gear with all variables for the gear that are dependent on the number of teeth having been automatically updated. So, for example the sizes of the teeth

will have changed, but the overall pitch diameter of the gear will not have, as this is independent of the number of teeth.

Pro/Engineer allows the creation of curves using a parametric relationship, which for the surfaces of the teeth is described by Equations 3.5 and 3.6. The tooth shape is initially created at the outer diameter of the gear at an angle to the central axis called the "back-cone-angle". This angle can be seen in Figure 3.6, where the pitch cone angle is the angle between the axis and the pitch cone, and the back-cone-angle is (90° − the pitch cone angle). The pitch cone is formed by the revolution of a line that stretches from the axis to the pitch circle, around the axis, and is defined by the pitch cone angle.

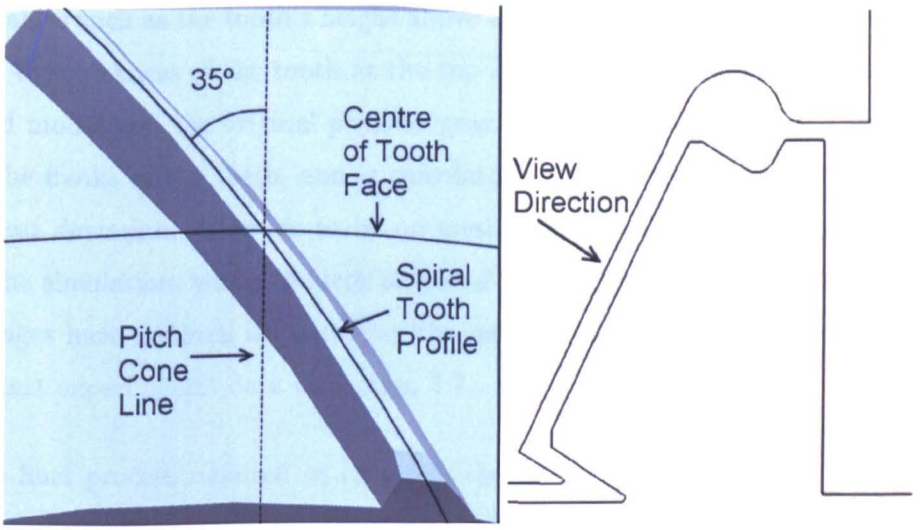

Figure 3.7: Left-hand-side is a view of the gear tooth spiral angle from the direction shown on the right-hand-side

The tooth profile created by this method is angled in such a way as that it is perpendicular to the pitch cone and also lies on the spiral angle that defines the profile of the teeth. The spiral angle is measured at a point halfway along the facewidth of the gear, and the radius is described by that of the physical cutter used to machine the gear. This can be seen in Figure 3.7 which shows the profile of a tooth when viewed from above it, and also marks the spiral angle, which for this gear, like most spiral bevel gears, is 35°.

The tooth profile is extruded along the spiral angle in Pro/Engineer, to create a solid tooth angled at the pitch cone angle. Finally, the single tooth is copied and rotated the required number of times about the axis of the gear to create a set of raw teeth that follow the correct path and size of a spiral bevel gear. Although the teeth are angled at the pitch cone angle to the axis, the teeth taper slightly, with the height of the teeth being smaller at the inner diameter of the gear — this is due to the manufacturing process used by Gleason, although some manufacturers may use non-tapered teeth [40].

The geometric assumptions in the formation of the gear, such as the shape of the gear teeth, are suitable since the difference physically is small. The key size variables such as the tooth's height above and below the height of the pitch cone and the thickness of the tooth at the top and bottom are identical between the solid model and the original physical gear. The difference lies in the curvature of the flanks of the teeth, and is calculated to be no more than 0.1mm at the largest deviation. There is to be no meshing between crown and pinion gears in the simulation, which reduces potential issues with surface interference. The changes have minimal impact upon the results as evidenced by close validation against experimental data in Section 3.7.

The final process required to complete the solid model of the gear is to finish the gear-specific shape. Section 3.2.3 details the changes made to the back of the gear when compared to the original, physical one. The detailing at the inner diameter of the gear, where it connects to the shaft must also be completed, which is relatively simple as these axisymmetric surfaces are formed from lines rotated around the central axis. The lines used to create the non-tooth elements of the gear, along with those used to created the rest of the domain (see Section 3.2.4) are linked to each other, and to the gear itself, so will automatically update when the gear is changed.

Figure 3.8.1 and Figure 3.8.2 are front views of the physical gear and the completed computational solid model respectively. The physical gear is shown with a hub and locating bolts in place, necessary to allow for attachment to the rig

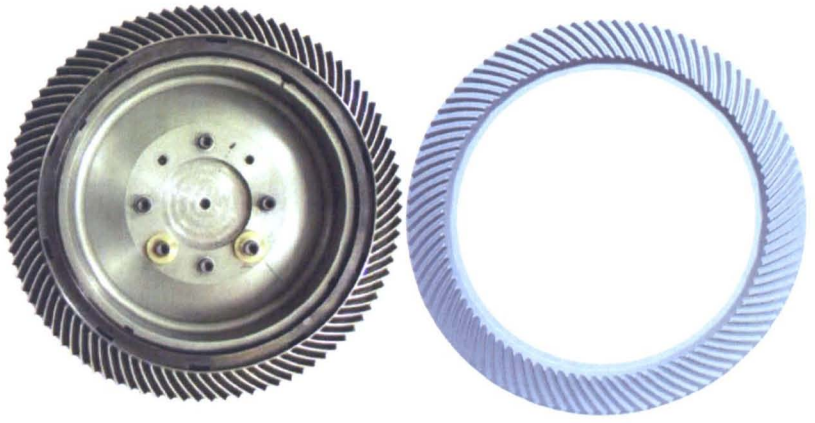

3.8.1: Physical gear **3.8.2:** Computational model

Figure 3.8: Front views of physical and computational spiral bevel crown gears

described in [23].

3.2.2.3 Terminology of the gear and shroud

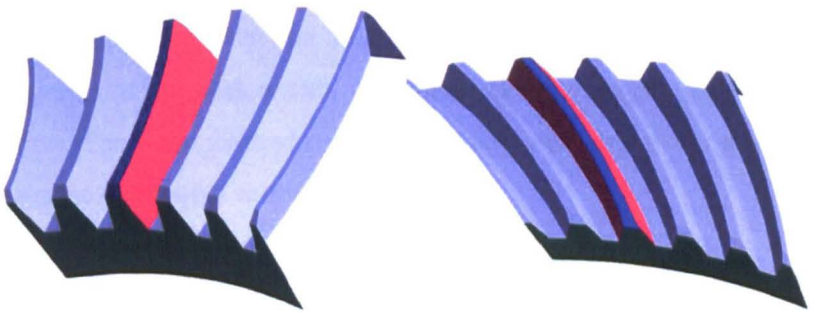

Figure 3.9: View of the gear with different parts of the gear teeth separately coloured. Green is the "front" of the gear, at the inner diameter. Red are the flanks of the gear tooth. Blue is the topland of the tooth

It can be difficult to show the shape and structure of the highly three-dimensional flows involved in gear windage, and also difficult to see the profile of the gear. Figure 3.9 shows two views of a segment of the control gear with different parts of the gear teeth coloured separately; two views are used in order to aid the reader gain perspective. The green surface is the *front* of the gear, so named as it is the first part of the gear that air flowing through the domain will hit. This surface is at the inner diameter of the gear. The red *tooth flanks* are the sides of the teeth,

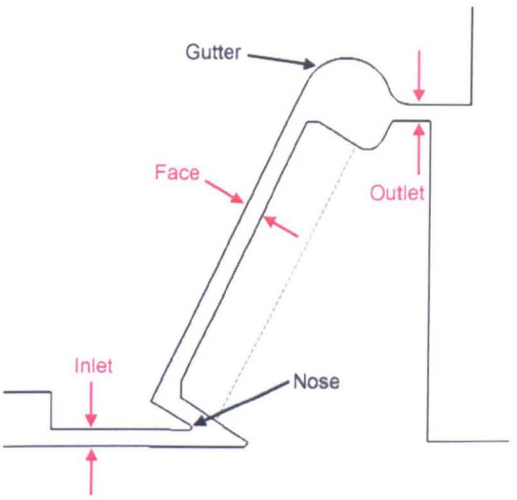

Figure 3.10: Terminology associated with the shroud

and are the surfaces that will make contact with another gear when running in mesh. The blue coloured surface is the *topland* of the gear tooth, which is often referred to as the face of the gear. This surface effectively forms the top of the gear tooth when the tooth is viewed in section. Finally, there is the *tooth valley*, which is the surface between the flanks of neighbouring teeth. The shroud used for the majority of the work within this thesis has two major components, a nose and a gutter. These are marked on Figure 3.10, which also shows where the inlet, face and outlet clearances are measured.

3.2.3 Changes to gear

The physical version of the control gear as used in a Trent 500 IGB has a number of circumferential grooves machined into the back of it, on the opposite side of the gear to the teeth. These can be seen in Figure 3.11, which shows a single tooth segment of the whole gear with a couple of grooves clearly visible. Different aero-engines have different designs of their crown gear backs, with some looking radically different from the one shown in Figure 3.11. They are primarily a weight saving method, used to reduce the moment of inertia of the spinning gear, and to also provide clearance for bearings.

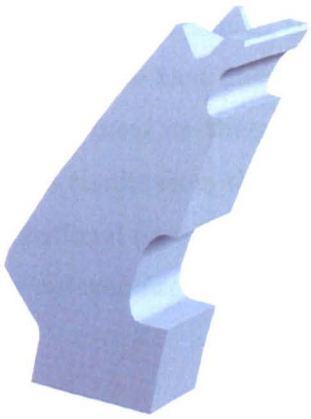

Figure 3.11: A single tooth segment of control gear showing unused grooves from physical gear

A consequence of the differing grooves between engines is that their effect on the control gear's windage would have no relevance to another engine with a different size of gear and a likely different back. As a result, it was decided that all gears modelled would have a flat back, which would both remove any windage effect of the machined grooves, and have the added advantage of reducing the complexity of the mesh in this area of the domain. The back of a single tooth-segment of the control gear can be seen in Figure 3.12, and the lack of the grooves compared to Figure 3.11 can be observed.

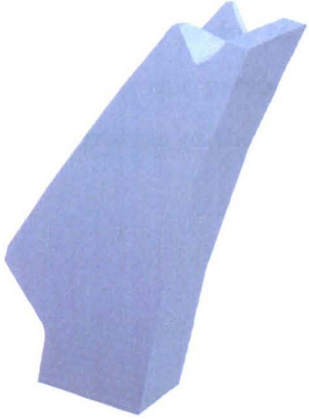

Figure 3.12: A single tooth segment of control gear showing the flattened back

The disadvantage of this decision is that validation against the experimental results for the control gear will be more difficult, as the gears are no longer like-for-like. Section 3.7.1 addresses the difference between computational and

physical gears by simulating the chamber behind the gear and the original gear back features. The results of this show that at the rotational speeds simulated, the grooved back increases the moment on the gear by 5.36%. However, as the dominant source of windage loss results from the teeth of the gear, it is felt that the benefits of reduced computational time and better comparison between gears of differing sizes outweigh the reduced accuracy of validation.

3.2.4 Domain creation

In order to run a CFD simulation, an enclosed domain must be created. To compare results with the experimental results published in [23], the chamber used in that work is also created in Pro/Engineer. A cut-through of this domain can be seen in Figure 3.13, which also shows the stub-shafts fore (coloured in red) and aft (green) of the gear (blue), onto which the gear is fixed, and that consequently rotate with it. Enclosing the gear is a shroud, and on the left of the gear is an inlet channel which conditions the air. The gear acts as a pump, with air drawn in from the left-hand-side of the figure, being ejected by the gear into the large chamber behind it, on the right-hand-side of the figure. The air then travels radially outwards (up on the figure) and exits the domain. The rear-chamber is shown truncated in the figure as due to the curvature of the periodic boundaries, it can look distorted from this perspective. The periodic boundary shape is shown in Section 3.3 on creation of the mesh.

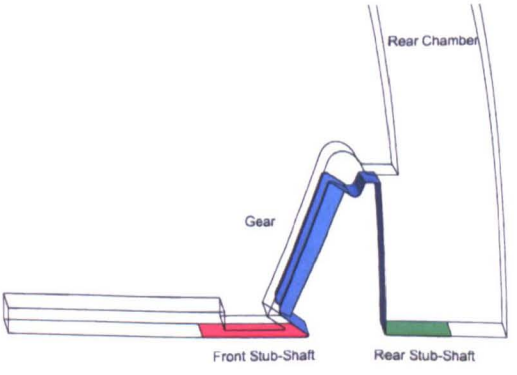

Figure 3.13: Domain, with rotating elements coloured and simplified and truncated rear chamber shown

A couple of small changes were made to the geometry in order to simplify it slightly and reduce the number of mesh cells required for the CFD simulation. The largest of these alterations is that the walls of the rear chamber, behind the gear, before the outlet, are straight when viewed tangentially. The physical gear rig has a number of circumferential features, which would require a disproportionate amount of extra cells to model given that the rear chamber should have negligible effect on results as it is a significant distance upstream of the outlet to the shroud, relative to the size of the shroud outlet radial gap. There are also features that are non-periodic such as mounting bolts used in the construction of the rig, necessitating a full 360 degree model which is not possible given the computational assets available.

There are three gear to shroud spacing dimensions used to characterise the shroud, and reference can be made to Figure 3.10:

1. Inlet clearance is the radial distance between the shroud and the shaft, and for the shroud used in the majority of the work contained in this thesis is 1.5mm.

2. Face clearance is the perpendicular distance between the top-land's of the teeth and the shroud. This is 1.76mm.

3. Outlet clearance is the radial distance between the outer radius and the shroud at the point where the flow is ejected into the chamber behind the gear. This is also 1.5mm.

The work of Rapley [33] provides an in depth study into the effect upon windage of varying these distances. These dimensions are kept constant in all of the work within this thesis, with the exception of the outlet clearance which is varied in the study on the outlet shape, Chapter 5 and in the final work in Chapter 6.

3.3 Mesh creation

The solid model from Pro/Engineer is imported as a STEP file into ICEM CFD. This imports all surfaces and edges in preparation for creation of the mesh that fills the domain. A hexahedral mesh containing around 400,000 cells for a single tooth passage is created, and captures the domain between the gear and a shroud, described as "Shroud 2"[1] in Johnson *et al.* [23]. The use of hexahedral cells with a blocking superstructure that is independent from the geometry permits a mesh to be transferred to a new gear, assuming it has a similar geometric topology to that of the control gear.

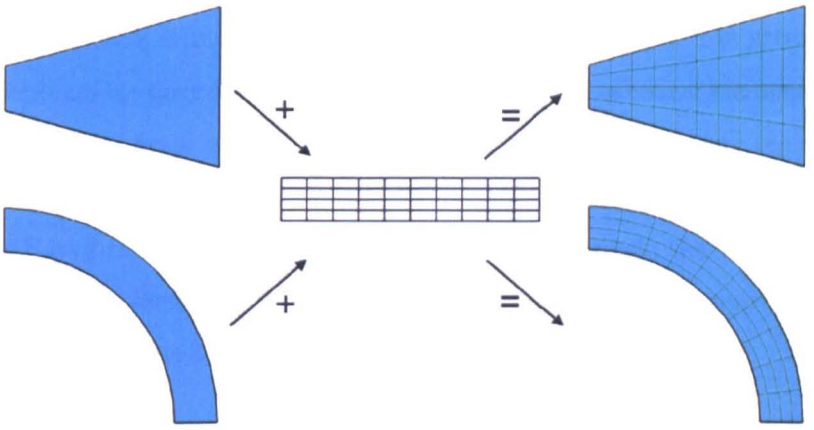

Figure 3.14: Two-dimensional sketch showing how Geometry + Blocking Structure = Mesh

Figure 3.14 demonstrates how the geometry and blocking structure are kept separate, with the blocking topology being overlaid on the geometry to create a usable mesh. This method is fast at meshing new gears when the mesh blocking structure is identical for all simulations. For instance, all spiral bevel gears simulated in this paper are identical in basic shape, therefore the blocking structure can be transferred between all gears, and constrained to the new geometry very quickly. This method used would even work on a non-spiral bevel gear as the straight teeth would not change the fundamental mesh blocking structure from the curved teeth of the spiral bevel gear. Figure 3.14 shows the simple case of a

[1]This shroud design was chosen as it was shown in the reference to be the most effective tested at reducing single phase windage

curved rectangle and an expanding rectangle, with the same blocking topology used for each of the geometries. Due to both being quadrilateral, the blocking can be used identically in two different applications, and still form coherent, usable meshes. This principle is applied to the many different sizes of spiral bevel gear and shroud shapes used in this thesis.

An alternative to using a hexahedral mesh would be to use a tetrahedral mesh to capture the domain, these are commonly referred to as "structured" and "unstructured" meshes respectively[2]. Tetrahedral meshing is convenient as it is usually faster with modern software, and it is easier and quicker to capture complex geometric shapes. However, tetrahedral cells can introduce "false-diffusion" of the solution if the mesh elements are too skewed, and this is covered in greater detail in Section 3.4.5 on discretisation. The advantage of hexahedral elements for the work within this thesis is that they offer better control in the wall region (most of the flows studied are wall-bounded) by permitting the cells to be stretched in the direction of the flow, without excessive penalty costs to the flow solution in other directions. Therefore, a reduction in the number of cells required to fill the domain can be achieved through careful mesh generation.

The mesh uses a single tooth[3] with rotationally periodic boundaries, meaning the computational time taken for each simulation is cut down considerably, and this also allows for greater mesh resolution of the single tooth for a given amount of mesh cells. There is an assumption made by doing this that the flow is periodic across a single tooth, and this is explored in greater detail in Section 3.6 on verification of the results. The periodic boundary for the entire domain follows the spiral angle of the tooth when viewed from the front of the gear, and passes through the toplands (the upper flat surface, or "face") of the gear teeth, and extends axially through the whole domain. This is shown in Figure 3.15, which shows in grey, the single tooth domain when viewed from the front of the gear.

[2]Although an unstructured mesh can have elements of any shape, most CFD software is restricted to just tetrahedral ones

[3]Multiple toothed simulations were tested in Section 3.6; however, these meshes are formed by copying and rotating the single tooth mesh

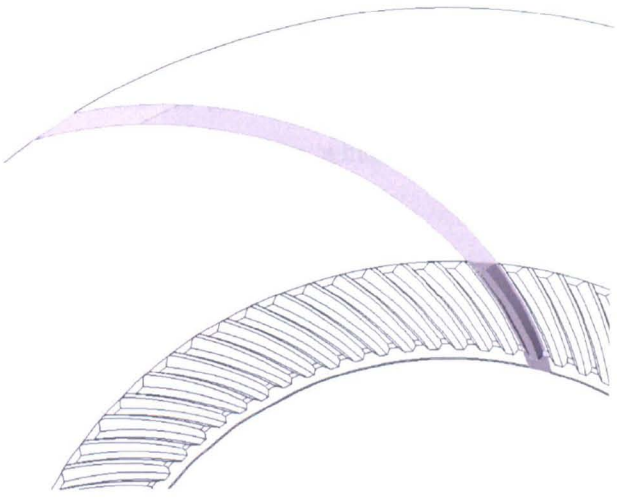

Figure 3.15: A view of the simulation domain for a single tooth, viewed from the front of the gear

Figure 3.16 shows detail of the mesh at the nose of the shroud. The purple coloured surface, closest to viewer is one of the periodic boundaries, and the yellow is of the underside of the gear tooth surfaces, viewed as if "inside" the gear itself — reference can be made to Section 3.2.2.3 which explains the shroud and gear features. The complexity of the mesh in this region is large, due to multiple changes in direction that the flow must take. The mesh can be seen to curve around the nose of the shroud in order to closely follow the air flow of the simulation, as seen by analysing the results of Rapley [33], who used a similar domain shape.

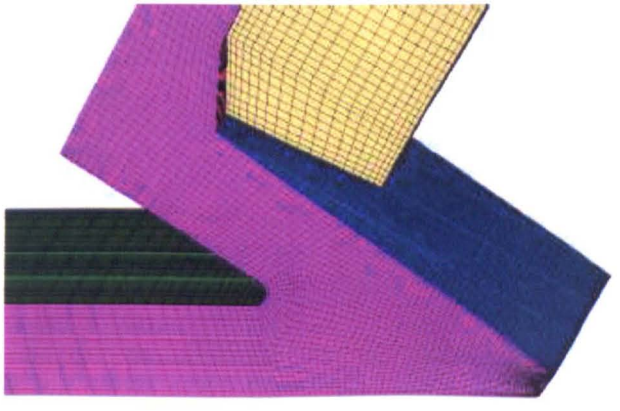

Figure 3.16: Mesh detail at the nose of the shroud

Figure 3.17 shows the mesh on the surface of the gear tooth surfaces. These are the tooth valley floor (pink), the tooth flanks (yellow and purple), the front of the gear, at the inner diameter (blue) and the topland (green and red), which is split into two by the periodic boundary, which isn't shown here.

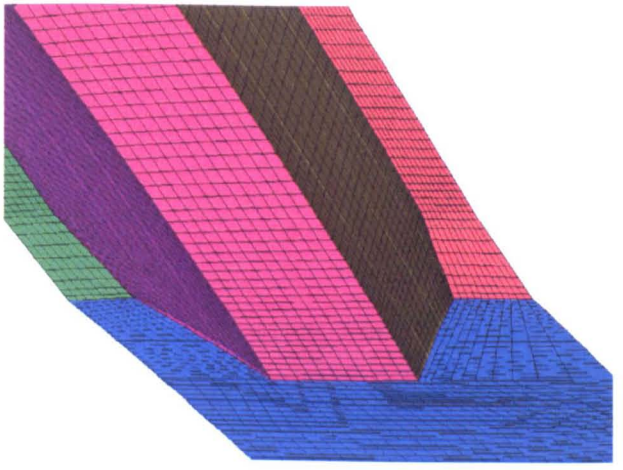

Figure 3.17: Mesh detail in the tooth valley

Figure 3.18 shows the surface mesh at the gutter of the shroud near the outlet, shown in green. The curved profile can be seen, and the mesh distribution is fairly linear and orthogonal in order to capture the complex flow field in this area.

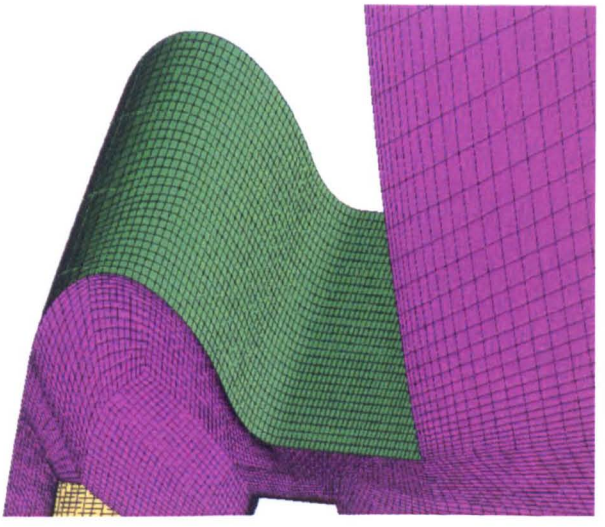

Figure 3.18: Mesh detail at the gutter of the shroud

The grid spacing at the wall is designed to have a y^+ value between 30 and 50, in line with the recommendations of the FLUENT user manual [19] when using the standard wall function; the wall functions are covered in Section 3.4.9. The aim of doing this is to capture the laminar sublayer of the flow at the wall, and its transition to more developed flow away from the wall, entirely within the first cell. The cells in the mesh have a minimum "quality" (effectively a measure of skew) of 0.5 as defined by ICEM CFD, higher than the suggested minimum of 0.4, and over 80% of the cells have a quality index between 0.9 and 1.

3.4 CFD solution

The requirement of a CFD simulation is to be able to extract meaningful, accurate information of a fluid flow problem. The information takes two forms: numerical data and graphical representation of flow. Obtaining this information is time-consuming and computationally expensive due to the complexity of fluid motion. In this body of work, a finite volume method is employed, whereby an entire flow domain is split into a number of finite volumes in which the governing equations are integrated separately.

3.4.1 Mathematical conventions

In order to reduce the number and length of the equations presented within this thesis, where applicable, equations will be written in shorthand using the nabla, or del symbol, ∇. This is defined as the partial derivative of a quantity with respect to all directions as,

$$\nabla = \frac{\partial i}{\partial x} + \frac{\partial j}{\partial y} + \frac{\partial k}{\partial z}. \tag{3.7}$$

This is used in shorthand for the gradient of a scalar quantity (ρ in this example),

$$\nabla\rho = \frac{\partial\rho}{\partial x}i + \frac{\partial\rho}{\partial y}j + \frac{\partial\rho}{\partial z}k. \tag{3.8}$$

When used in conjunction with the dot product of a vector[4], the divergence of the vector quantity is found,

$$\nabla \cdot \mathbf{U} = \frac{\partial U_x}{\partial x} + \frac{\partial U_y}{\partial y} + \frac{\partial U_z}{\partial z}. \tag{3.9}$$

3.4.2 Navier-Stokes equations

The Navier-Stokes equations describe the fundamentals of fluid motion, and are derived based on the concepts of conservation of mass, momentum and energy. They were formulated by Claude-Louis Navier and Sir George Stokes independently of each other in the 19th century. Solving these equations involves treating the fluid as a continuum, and as such, it is necessary to consider a control volume of finite size over which the concepts can be applied. The derivation of the flow field is done using a Eulerian perspective, in which the derivative of the flow field is done with respect to a fixed place in space. This can be contrasted with a Lagrangian, or convective derivation, in which a variable of a packet of fluid or solid is solved as it travels along its streamline. Both of these approaches are used in the results contained within this body of work, as the continuous, air phase is solved using Eulerian derivatives, but discrete particle modelling of oil droplets discussed later in Chapter 6 are solved with a Lagrangian perspective.

The most fundamental of the equations is conservation of mass, called the continuity equation. This is used by FLUENT as shown in Equation 3.10.

[4]Even though ∇ is not strictly a vector (it isn't commutable), this *abuse of notation* is generally accepted

$$\frac{\partial \rho}{\partial t} + \nabla \cdot (\mathbf{U}\rho) = 0. \tag{3.10}$$

Equation 3.10 is of a general form and is applicable to compressible and incompressible flows alike, but does not take into account any additional sources of mass, such as evaporation; however, this is not relevant for the work within this thesis.

Equation 3.11 below is the vector form of the general Navier-Stokes equation for momentum.

$$\frac{\partial}{\partial t}(\rho \mathbf{U}) + \nabla \cdot (\rho \mathbf{U}\mathbf{U}) = -\nabla p + \nabla \cdot (\overline{\overline{\tau}}) + \rho g + F, \tag{3.11}$$

where the stress tensor, $\overline{\overline{\tau}}$, is,

$$\overline{\overline{\tau}} = \mu \left[(\nabla \mathbf{U} + \nabla \mathbf{U}^T) - \frac{2}{3} \nabla \cdot \mathbf{U} I \right], \tag{3.12}$$

and F is additional sources of momentum[5], which for the work in this thesis would include the dispersed (second) phase, as addressed in Equation 3.63. The equations for momentum do not preserve mass, hence the continuity equation (Eqn. 3.10) is necessary.

The final governing equation necessary is energy, which in the general form used by FLUENT is

$$\frac{\partial}{\partial t}(\rho E) + \nabla \cdot (\mathbf{U}(\rho E + p)) = \nabla \cdot \left(k_{\text{eff}} \nabla T + (\overline{\overline{\tau}}_{\text{eff}} \cdot \mathbf{U}) \right) + S_h. \tag{3.13}$$

[5]Some versions of the Navier-Stokes equations include the right-hand part of Equation 3.12 in the term for momentum sources, as these influences are relatively small

E, the energy is defined as,

$$E = h - \frac{\rho}{p} + \frac{\mathbf{U}^2}{2}. \tag{3.14}$$

Both k_{eff} (the effective thermal conductivity) and $\overline{\overline{\tau}}_{\text{eff}}$ (the effective viscous dissipation) in Equation 3.13 , are dependent upon the turbulence model used, and are defined in Section 3.4.8.

S_h, in Equation 3.13, refers to energy introduced to the fluid from other sources. In the context of the simulations presented in this thesis, this will be energy from discrete particles within the fluid, which is addressed in Section 3.4.10.1.

Equation 3.11 and 3.13 are very similar, and if ϕ is used to represent their variables, both can be written as,

$$\frac{\partial \rho\phi}{\partial t} + \nabla \cdot (\rho\phi\mathbf{U}) = \nabla \cdot (\Gamma_\phi \nabla\phi) + S_\phi, \tag{3.15}$$

where Γ_ϕ is a general diffusion coefficient for ϕ, and S_ϕ is a source of ϕ. Equation 3.15 can be applied in this general form to all scalar quantities such as temperature, as it models them as,

Rate of increase of ϕ + Rate of flow out of ϕ due to convection =

Rate of increase of ϕ due to diffusion + Rate of increase of ϕ due to sources.

3.4.3 Solver

There are two different methods used by FLUENT for solving the flow field. These are the pressure-based and density-based methods. The density based approach finds the density field from the continuity equation, and subsequently uses the equation of state, $p = p(\rho, T)$, to obtain the pressure field. This method is not used for the work within this thesis for two reasons:

1. The density-based solver was historically formulated for high-speed compressible flows. The flow speeds reported within this thesis are high, yet are not large enough for compressibility effects to dominate within the domain; the maximum Mach number of the rotating gear at 12,266rpm is around 0.5. The pressure-based solver is capable of dealing with mildly compressible flows as easily as the density-based solver.

2. More importantly, there are limitations to the models that can be used within FLUENT in conjunction with the density-based solver. These include the multiphase and Volume of Fluid (VOF) models and physical velocity formulation for porous media. These three models, among others, are identified as being used in future simulations beyond the scope of this thesis, but build upon the work included in it.

As a consequence, the pressure-based solver was chosen as the default method of solving the flow field. This differs from the density-based solver as the pressure field is obtained from a pressure equation solved through manipulation of the continuity and momentum equations, and this *pressure-velocity coupling* is addressed in Section 3.4.7. A "segregated" form of the pressure-based solver is used, in which the governing equations are solved sequentially, as opposed to all at the same time — the "coupled" approach. This has the benefit of being using around half of the memory of a coupled approach because fewer variables are required to be simultaneously kept in memory. The disadvantage of the segregated method is that more iterations are generally required to attain the same level of convergence.

3.4.4 Rotating frame of reference

In order to simplify post-processing of the data from the solver, a rotating frame of reference is used for the fluid (air) in the domain. This has an effect on the input data for wall boundary conditions, so it is necessary to define what this means.

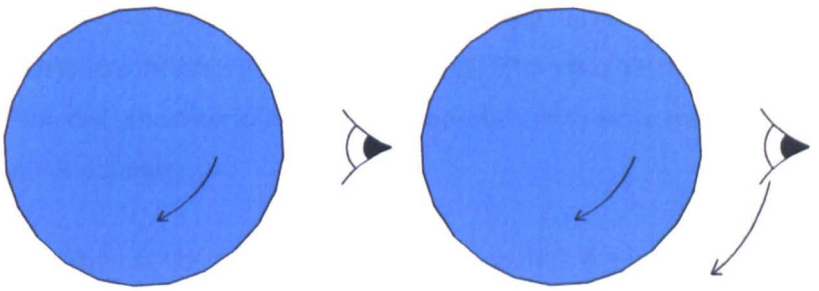

Figure 3.19: Illustration of static perspective (LHS) and rotating perspective (RHS)

If the rotating domain were to be viewed from a static position, the solution would be unsteady because of the continual passing of the teeth. Post-processing the data visually would be tricky due to the domain changing shape from the perspective of the viewer. The solution is to fix the viewer's perspective with reference to the domain, i.e. rotating at the same speed — and this describes a rotating frame of reference. This means that the appearance of the domain never changes, so it is possible to create visuals that are easier to interpret. Figure 3.19 shows the difference between the two perspective concepts. The left-hand-side of the figure has the eye stationary, designating the static perspective, while on the right-hand-side, the eye is rotating at the same speed as the circle. Both circles are rotating at the same speeds, in the same sense, so results such as pressures, velocities etc. would be identical for both methods (static and rotating frames of reference) — it is purely a tool for visualisation, and has no impact upon the solution. It does, however, involve setting up some boundary conditions slightly differently though, as explained in Section 3.4.11.1 on wall boundary conditions.

3.4.5 Spatial discretisation

FLUENT is a cell-centred control-volume CFD method. This means that the physically continuous solution is solved by modelling it as a series of continuous solutions inside multiple neighbouring cells, using a method called "discretisation". This method allows a complex flow problem to be approximated as a number of control volumes, with linkages between both neighbouring cells and the time varying solution within the cell itself. The variable data is stored at the centre of the cell; the alternative to this approach is to store data at the vertices of the control volumes.

The discretisation of the governing equations requires the introduction of a number of numerical techniques; for example with the cell-centred method, it is necessary to establish values at the faces of the control volumes. Considering the most simple example of the general transport equation for a variable ϕ (which is a scalar quantity), Equation 3.16 is the integral form of Equation 3.15 for a control volume, V.

$$\int_V \frac{\partial \rho\phi}{\partial t} dV + \oint \rho\phi \mathbf{U} d\vec{A} = \oint \Gamma_\phi \nabla\phi d\vec{A} + \int_V S_\phi dV. \tag{3.16}$$

When discretised, Equation 3.16 can be written as follows, and is applied to the individual cells,

$$\frac{\partial \rho\phi}{\partial t} V + \sum_f^{N_{\text{faces}}} \rho_f \mathbf{U}_f \phi_f \cdot \vec{A}_f = \sum_f^{N_{\text{faces}}} \Gamma_\phi \nabla\phi_f \cdot \vec{A}_f + S_\phi V. \tag{3.17}$$

In Equation 3.17 all variables with subscript f refer the value of the variable at the face of the cell, and N_{faces} is the number of faces enclosing the cell. The first term in Equation 3.17 involves discretisation of the variable with respect to time, and this is addressed in Section 3.4.6 on temporal discretisation.

One feature of Equations 3.16 and 3.17 is that compared to the general transport equation (Equation 3.15), the divergence of ϕ is not integrated over the control volume; instead the scalar field is integrated over the area of the control volume surface, or in the discretised form, summed over all the faces of the cell. This is due to the Green-Gauss theorem, alternately called the divergence theorem, which states that the volume integral of the divergence of ϕ is equal to the net flow of ϕ across the boundary of a control volume. In order to calculate the value of ϕ_f in Equation 3.17, it is necessary to use an "upwinding" scheme. This uses the cell-centre value of ϕ stored in the upstream, or "upwind" direction to interpolate a value for ϕ_f.

The upwinding scheme used for the work in this thesis is second-order, which uses a Taylor series expansion of the cell solution about the cell centroid to enhance accuracy by incorporating the gradient of the scalar. A first-order upwind scheme would not include the second-order term, and makes the simple assumption that the value at the face of the cell is the same as that at the cell centre of the upwind cell, i.e. that the value of a scalar at the centre of the cell is a cell-averaged quantity. The assumptions that this entails limits the accuracy of the solution, particularly if the gradient of the scalar across the cells is large. In second-order upwinding, ϕ_f is found by,

$$\phi_f = \phi + \nabla\phi \cdot \vec{r}, \tag{3.18}$$

where $\vec{r}$ is the displacement vector from the cell centre to the cell face centroid and $\nabla\phi$ is the gradient of ϕ in the upstream cell. In FLUENT, this gradient is evaluated using Equation 3.19.

$$\nabla\phi = \frac{1}{V}\sum \overline{\phi_f}\vec{A_f}, \tag{3.19}$$

where the face value ϕ_f is the mean of the two neighbouring cells' centroid values.

The penalty for this enhanced accuracy is that it is necessary for FLUENT to calculate $\nabla\phi$ for every cell in the domain. This entails an additional calculation, which costs time; however, the second-order upwinding scheme reduces numerical diffusion of the flow, especially on grids which have cells that are not aligned to the flow (like at certain points in the simulations in this thesis).

3.4.6 Temporal discretisation

All the simulations presented in this thesis, unless otherwise specified, are solved transiently, meaning that the solution is expected to change with respect to time. The reasons for this are threefold:

- Based on the findings of Rapley [33], convergence of a simulation is not always guaranteed when running steady-state.
- Visualisations conducted by Johnson [22], showed the turbulent and transient nature of the flow when oil was present, leading to the conclusion that this would also be the true for air-only cases.
- The quantity of simulations that are required for this thesis are not so great that computational time needs to be rationed for running transiently.

The first two points show that the flows may involve periodic transient features, such as travelling eddies, and these cannot be resolved very well with a steady-state approach. This is often the case with aerodynamics, in which the physics are best accommodated with a transient formulation which will converge more accurately and provide better mean quantities such as moments on surfaces.

With a finite-volume CFD method, it is necessary to use temporal discretisation to represent a continuous passage of time, in the exact same manner as spatial discretisation is necessary for the continuous flow field. Data is stored for the solution in a separate file for each timestep, which can dramatically increase the

amount of computer storage required. For example, a single revolution of the control gear, a total of 910 timesteps, produces over 100GB of data.

The change with time of a scalar quantity, ϕ, can be represented as,

$$\frac{\partial \phi}{\partial t} = F(\phi), \tag{3.20}$$

where $F(\phi)$ is a function which includes spatial discretisation. The first-order temporal discretisation of $F(\phi)$ can therefore be written as,

$$\frac{\phi^{n+1} - \phi^{n}}{\Delta t} = F(\phi), \tag{3.21}$$

and the second order discretisation as,

$$\frac{3\phi^{n+1} - 4\phi^{n} + \phi^{n-1}}{2\Delta t} = F(\phi), \tag{3.22}$$

where the superscript of ϕ refers to the relative position in time to the current time, ϕ^{n}, and Δt is the size of the time-step. Second order temporal discretisation is used for all transient simulations in this thesis.

FLUENT's pressure-based solver uses implicit time integration, where $F(\phi)$ is evaluated at the future time level[6] using Equation 3.23.

$$\frac{3\phi^{n+1} - 4\phi^{n} + \phi^{n-1}}{2\Delta t} = F\left(\phi^{n+1}\right), \tag{3.23}$$

Rearranging Equation 3.23, allows the future value of ϕ to be determined including the influence of neighbouring cells at time n+1 (through the function $F\left(\phi^{n+1}\right)$),

[6]Shown here using second order discretisation

$$\phi^{n+1} = \frac{2\Delta t F\left(\phi^{n+1}\right) + 4\phi^{n} - \phi^{n-1}}{3}. \tag{3.24}$$

This method can be contrasted to an explicit integration scheme where ϕ^{n+1} is only expressed in terms of current, known values; however, this scheme is not available with the pressure-based solver in FLUENT. The implicit scheme is generally found to be superior as it is unconditionally stable with respect to the timestep size.

In Section 3.6.1 the differences between a steady state and transient simulation are quantitatively and qualitatively presented.

3.4.7 Pressure-velocity coupling

It is necessary to link the momentum and continuity equations in the segregated pressure-based solver (see Section 3.4.3), because when calculating new values for velocity, the solver uses "guessed" values of pressure, usually based on the previous iteration's values (The exception is the first iteration of a simulation, when initial user defined values are used). The velocities found using this method do not enforce continuity, so a pressure correction is necessary to find an updated pressure field, which in turn can be used to correct the velocity field to conform to the continuity equation. After this step other transport equations such as energy and turbulence, and scalar quantities are calculated.

There exists a number of different algorithms used for calculating pressures and velocities within a finite volume CFD simulation. All the results presented within this thesis use the SIMPLE algorithm, which stands for Semi-Implicit Method for Pressure Linked Equations, and was first suggested by Patankar and Spalding [31]. Specific details on the method used by FLUENT to apply the SIMPLE algorithm can be found within the user guide [19]. The correction to the "guessed", or predicted, pressure is generally done in conjunction with an under-relaxation factor (URF),

$$p = p^* + \alpha p', \tag{3.25}$$

where p^* is the predicted pressure, p' is the correction to the pressure and α is the under-relaxation factor, which will lie[7] between 0 and 1. URFs are used in the other terms in the solver, and increase the stability of the calculation by preventing too great a change to a variable from one iteration to the next, although this will incur a time penalty in reaching convergence.

3.4.8 Turbulence

The flows modelled within this thesis are all high-speed, energetic and chaotic flows with high Reynolds-numbers. The result of this is that the flow is turbulent, which is where high-frequency, small-scale random fluctuations are experienced by the fluid. Resolving these directly is very computationally expensive as it is necessary with the finite-volume method to use a very fine grid that can capture the turbulent motions with a sufficient resolution, when compared to a laminar model. As such, turbulent models are used which model the effects of turbulence using various methods, some more complex than others, but all with a calculation time penalty.

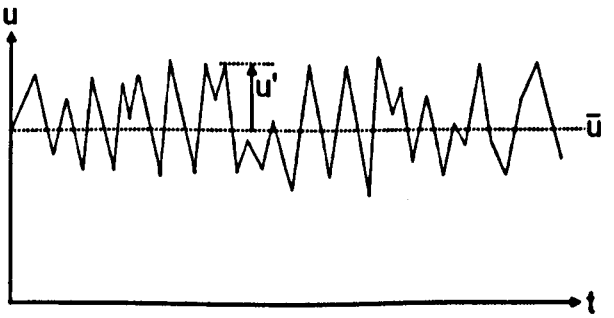

Figure 3.20: Reynolds decomposition of a variable u into a mean and fluctuating component

[7]It is possible to *over*-relax the variable by specifying a value above 1, which can greatly speed convergence although is more likely to be unstable

A turbulent flow can be characterised in terms of steady mean values, and fluctuating components. This is shown in Figure 3.20, and is represented in Equations 3.26 for a velocity and 3.27 for a scalar,

$$u = \overline{u} + u', \tag{3.26}$$

$$\phi = \overline{\phi} + \phi'. \tag{3.27}$$

The mean of the fluctuating component is by definition equal to zero,

$$\overline{\phi'} = 0. \tag{3.28}$$

The Reynolds-averaged Navier-Stokes (RANS) equations are formed by substituting decomposed variables into the Navier-Stokes equations (Equations 3.10 and 3.11). The continuity equation can therefore be written as,

$$\frac{\partial \rho}{\partial t} + \nabla \left(\overline{\mathbf{U}} \rho \right) = 0, \tag{3.29}$$

and this barely differs from Equation 3.10, the non-averaged Navier-Stokes equation for continuity due to the fact that $\overline{\nabla \mathbf{U}} = \nabla \overline{\mathbf{U}}$. The RANS momentum equations are written out in cartesian form in Equations 3.30, 3.31 & 3.32. Writing equations out in full emphasises the differences between them, and from the original Navier-Stokes equations.

$$\rho \left(\frac{\partial \overline{u}}{\partial t} + \overline{u} \frac{\partial \overline{u}}{\partial x} + \overline{v} \frac{\partial \overline{u}}{\partial y} + \overline{w} \frac{\partial \overline{u}}{\partial z} \right) = - \frac{\partial p}{\partial x} + \mu \left[\frac{\partial^2 \overline{u}}{\partial x^2} + \frac{\partial^2 \overline{u}}{\partial y^2} + \frac{\partial^2 \overline{u}}{\partial z^2} \right] - \rho \frac{\partial \overline{u'^2}}{\partial x} - \rho \frac{\partial \overline{u'v'}}{\partial y} - \rho \frac{\partial \overline{u'w'}}{\partial z}, \tag{3.30}$$

$$\rho\left(\frac{\partial\overline{v}}{\partial t}+\overline{u}\frac{\partial\overline{v}}{\partial x}+\overline{v}\frac{\partial\overline{v}}{\partial y}+\overline{w}\frac{\partial\overline{v}}{\partial z}\right)= -\frac{\partial p}{\partial y}+\mu\left[\frac{\partial^2\overline{v}}{\partial x^2}+\frac{\partial^2\overline{v}}{\partial y^2}+\frac{\partial^2\overline{v}}{\partial z^2}\right]-\rho\frac{\partial\overline{u'v'}}{\partial x}-\rho\frac{\partial\overline{v'^2}}{\partial y}-\rho\frac{\partial\overline{v'w'}}{\partial z}, \quad (3.31)$$

$$\rho\left(\frac{\partial\overline{w}}{\partial t}+\overline{u}\frac{\partial\overline{w}}{\partial x}+\overline{v}\frac{\partial\overline{w}}{\partial y}+\overline{w}\frac{\partial\overline{w}}{\partial z}\right)= -\frac{\partial p}{\partial z}+\mu\left[\frac{\partial^2\overline{w}}{\partial x^2}+\frac{\partial^2\overline{w}}{\partial y^2}+\frac{\partial^2\overline{w}}{\partial z^2}\right]-\rho\frac{\partial\overline{u'w'}}{\partial x}-\rho\frac{\partial\overline{v'w'}}{\partial y}-\rho\frac{\partial\overline{w'^2}}{\partial z}. \quad (3.32)$$

There are six terms introduced by the RANS, of the form $-\rho\overline{u_i u_j}$, and these are called the "Reynolds-Stresses". These result from the non-linearity of the averaging process, which physically is down to the interdependence of the velocity components in turbulent structures such as eddies and vortices. As a consequence, $-\rho\overline{u_i u_j}$ will be non-zero and introduces additional unknowns into the equations which must be modelled, forming the basis of turbulence modelling.

The Reynold Stress Model (RSM) approach solves the equations for each of the unknowns, plus an additional equation for the scalar dissipation rate, ϵ, typically the same equation as used in the $k-\epsilon$ model in most CFD programs, which can be seen in Section 3.4.8.2 when the RNG turbulent model is introduced. Therefore, for a three-dimensional problem, seven transport equations (and for two-dimensional problems, five transport equations) are needed to be solved. The RSM model originates from work by Launder *et al.* [24], and is the most classical form of turbulence modelling, However, solving so many equations is computationally expensive, so other models have been created which sacrifice some of the additional detail that the RSM model has — for example the anisotropy of turbulence — as captured by all the Reynolds stresses.

3.4.8.1 Boussinesq hypothesis

In order to simplify the RANS to reduce the amount of computational time required to solve them, a hypothesis is used, proposed in 1877 by Joseph Boussinesq that states the Reynolds stresses are proportional to the mean rates of deformation. It is noted in [38] among others, that paradoxically, this proposal was around 20 years before Reynolds published his work.

Boussinesq's hypothesis is most often written in the form [32],

$$-\rho\overline{u_i'u_j'} = \mu_t\left(\frac{\partial u_i}{\partial x_j} + \frac{\partial u_j}{\partial x_i}\right) - \frac{2}{3}\rho k\delta_{ij}, \tag{3.33}$$

where μ_t is the turbulent viscosity, defined by whichever turbulent model is being used. δ_{ij} is called the Kronecker delta, defined in Equation 3.34,

$$\delta_{ij} = \begin{cases} 1 & \text{if } i = j, \\ 0 & \text{if } i \neq j. \end{cases} \tag{3.34}$$

k is the turbulent kinetic energy, defined as,

$$k = \frac{1}{2}\left(\overline{u'^2} + \overline{v'^2} + \overline{w'^2}\right). \tag{3.35}$$

The disadvantage in using the Boussinesq hypothesis lies in its assumption that turbulence is isotropic — this is not always true, but for the majority of cases, particularly in industry, the potential reduction in accuracy is far outweighed by the reduction in calculation time through modelling fewer equations.

3.4.8.2 $k-\epsilon$ RNG model

All of the simulations described in this thesis use a $k-\epsilon$ RNG turbulence model. This is based on the recommendations of Rapley [33], and it is widely used in industry. The standard $k-\epsilon$ model used in FLUENT was proposed by Launder and Spalding [25, 26], and is the basis for the $k-\epsilon$ RNG model which uses Renormalisation Group (RNG) methods to create expressions for coefficients that are constant in the standard model, and also produce additional terms in the transport equations for k and ϵ. RNG analysis was first applied by Wilson [48, 49] in the context of quantum field theory, and subsequent applications to turbulent flows are summarised by Yakhot & Orszag [51], and implemented in the form below by Yakhot *et al.* [52]. In turbulence modelling, RNG methods work by eliminating the small scale motions from the governing equations (through a cascading process of substitutions) and encapsulating them in coarse expressions that are realistically modelled. As a result of these eliminations, a modified viscosity results which is introduced in Equation 3.37.

All $k-\epsilon$ variants are two-equation models. k is used in its exact form, as in Equation 3.35, whereas ϵ, the dissipation rate of turbulence is modelled based on empirical fitting. It is the form of the transport equation of ϵ that is the main difference between the various $k-\epsilon$ models.

The RNG derived transport equations for k and ϵ as used in FLUENT are shown in Equations 3.36 & 3.37 respectively.

$$\frac{\partial(\rho k)}{\partial t}+\nabla\cdot(\rho k\mathbf{U})=\nabla\cdot[\alpha_k\mu_{\text{eff}}\nabla\epsilon]+G_k+G_b-\rho\epsilon-Y_M+S_k, \qquad (3.36)$$

$$\frac{\partial(\rho\epsilon)}{\partial t}+\nabla\cdot(\rho\epsilon\mathbf{U})=\nabla\cdot[\alpha_\epsilon\mu_{\text{eff}}\nabla\epsilon]+C_{1\epsilon}\frac{\epsilon}{k}(G_k+C_{3\epsilon}G_b)-C_{2\epsilon}\rho\frac{\epsilon^2}{k}-R_\epsilon+S_\epsilon, \qquad (3.37)$$

where $\mu_{\text{eff}}=\mu+\mu_t$ is the effective viscosity. The formation of the effective

viscosity is one of the key differences between the standard and RNG forms of the $k-\epsilon$ equation, as it includes a differential equation which creates a dynamic link between the effective Reynolds number in the flow, and the viscosity. The outcome of this is that the $k-\epsilon$ RNG model is more capable of handling low Reynolds-number flows and near-wall flows than the standard model which, because of its empirical formation, is a high Reynolds-number model. In the context of the results presented in this thesis, this is advantageous because the flow is wall-bounded.

The differential relationship governing the turbulent viscosity for the RNG model in FLUENT is,

$$d\left(\frac{\rho^2 k}{\sqrt{\epsilon\mu}}\right) = 1.72\frac{\hat{v}}{\sqrt{\hat{v}^3 - 1 + C_v}}, \tag{3.38}$$

where $\hat{v} = \mu_{\text{eff}}/\mu$, and $C_v \approx 100$.

Once integrated, at large Reynolds numbers (fully turbulent flow), Equation 3.38 leads to the following expression for the turbulent viscosity, which is also the same expression used in the standard $k-\epsilon$ model,

$$\mu_t = \rho C_\mu \frac{k^2}{\epsilon}, \tag{3.39}$$

where $C_\mu = 0.0845$, as derived by the RNG theory, and this number is close to the constant value of 0.09 used by the standard model. It is this expression for turbulent viscosity which has to be fed back into the Boussinesq formulated Reynolds stresses, Equation 3.33 , necessitating the solving of both k and ϵ equations.

The inverse Prandtl numbers, α_k and α_ϵ, found in Equations 3.36 and 3.37 respectively are found using the expression in Equation 3.40, which was also formulated using RNG theory.

$$\left|\frac{\alpha - 1.3929}{\alpha_0 - 1.3929}\right|^{0.6321} \left|\frac{\alpha + 1.3929}{\alpha_0 + 2.3929}\right|^{0.3676} = \frac{\mu_{\text{mol}}}{\mu_{\text{eff}}}, \tag{3.40}$$

with μ_{mol} being the molecular viscosity, and $\alpha_0 = 1.0$.

Referring back to Equation 3.36, G_k represents the production of turbulent kinetic energy,

$$G_k = \mu_t S^2, \tag{3.41}$$

where S can be written as,

$$S \equiv \sqrt{2 S_{ij} S_{ij}}, \tag{3.42}$$

and S_{ij} is the mean rate of stress tensor,

$$S_{ij} = \frac{1}{2}\left(\frac{\partial u_i}{\partial x_j} + \frac{\partial u_j}{\partial x_i}\right). \tag{3.43}$$

This equation for turbulent production is based on the exact equation for transport of k which has been evaluated in line with the Boussinesq hypothesis. This can be seen when G_k is written in its exact form as,

$$G_k = -\rho \overline{u_i' u_j'} \frac{\partial u_j}{\partial x_i}. \tag{3.44}$$

G_b (Equation 3.36) is used when gravitational effects are modelled; however, this has not been included in the simulations presented in this paper, due to the rotational periodicity and dominance of the flow.

Y_M in Equation 3.36 accounts for the reduction in turbulent kinetic energy production through compressible dissipation. This is based upon a model proposed by Sarkar *et al.* [37], in which compressible dissipation ϵ_c, is a function of solenoidal dissipation rate ϵ and the turbulent mach number M_t, shown by,

$$\epsilon_c = \alpha_1 M_t^2 \epsilon, \tag{3.45}$$

where $\alpha_1 = 1$, found by comparing values of ϵ_c created with various values of α to results from a Direct Numerical Simulations (DNS) of a flow. Y_M as used in Fluent takes the following form,

$$Y_M = 2\rho M_t^2 \epsilon, \tag{3.46}$$

with M_t, the turbulent Mach number being,

$$M_t = \sqrt{\frac{k}{a^2}}, \tag{3.47}$$

and a, the speed of sound,

$$a \equiv \sqrt{\gamma RT}. \tag{3.48}$$

The most significant difference between the RNG variant of the $k-\epsilon$ model and the standard version is the addition of the term R_ϵ in the transport equation for ϵ (Equation 3.37), which has the effect of increasing the value of ϵ in regions of highly strained flow. This in turn increases k in those areas and leads to lower turbulent viscosities, the consequence of which is that the RNG model is able to

model flows with sensitivity to the level of the strain. This is particularly useful for the flows that are found in the simulations presented within this thesis. R_ϵ was formulated by Yakhot *et al.* [52], and is written as,

$$R_\epsilon = \frac{C_\mu \rho \eta^3 (1 - \eta/\eta_0)}{1 + \beta \eta^3} \frac{\epsilon^2}{k}, \tag{3.49}$$

where $\eta = Sk/\epsilon$, $\eta_0 = 4.38$ and $\beta = 0.012$.

One of the main issues with the RNG model is that in formulation of the strain parameter η, a modulus of the mean rate of strain $S = \sqrt{(2S_{ij}S_{ij})}$ is used. This mean rate of strain does not take into account the sign of the individual rate of strain tensors S_{ij}, the result of which is that the RNG model shows little or no improvement for contracting, accelerating flows as alluded to in [17]; however, it should be noted that these types of flows are not predominant in the models presented here.

As referred to in Section 3.4.2, the energy transport equation contains two variables whose formulation is dependent on the turbulence model employed. These are k_{eff}, the effective thermal conductivity and $\overline{\overline{\tau}}_{\text{eff}}$, the deviatoric stress tensor.

k_{eff} is calculated as,

$$k_{\text{eff}} = \alpha c_p \mu_{\text{eff}}, \tag{3.50}$$

where the effective viscosity, $\mu_{\text{eff}} = \mu + \mu_t$. α is the inverse Prandtl number, which is formulated using Equation 3.40, with the exception of α_0 which is calculated as $k/(\mu c_p)$. The effect of link between k_{eff} and the Prandtl number is that the RNG turbulent model is able to better predict heat-transfer at lower Reynolds numbers.

$\overline{\overline{\tau}}_{\text{eff}}$ is defined as,

$$\overline{\overline{\tau}}_{\text{eff}} = \left(\mu_{\text{eff}}\left[(\nabla \mathbf{U} + \nabla \mathbf{U}^T) - \frac{2}{3}\mu_{\text{eff}}\nabla \cdot \mathbf{U} I\right]\right), \tag{3.51}$$

with I being the identity matrix.

3.4.9 Wall treatments

All walls in the simulations contained in this thesis use FLUENT's standard wall function, which in turn is based upon the work of Launder and Spalding [26]. Near a wall, in the boundary layer there is a region called the viscous sublayer where viscous effects outweigh those of turbulence. In order to reduce the computational cost of running a wall-bounded simulation it is important to avoid resolving the boundary layer down to the viscous sublayer, as the first cell of a mesh that can do this should have a cell centroid y^+ value of ~ 1, where y^+ is defined as,

$$y^+ \equiv \rho u_\tau y/\mu, \tag{3.52}$$

and friction velocity[8] u_τ is,

$$u_\tau \equiv \sqrt{\frac{\tau_w}{\rho}}. \tag{3.53}$$

FLUENT uses a slightly alternative dimensionless value for y, termed y^*, which is defined in Equation 3.54. Both y^+ and y^* give very similar values at distances close to the wall [18].

[8] Also called shear velocity as it effectively rewrites a shear stress in units of velocity

$$y^* \equiv \frac{\rho C_\mu^{1/4} k_p^{1/2} y_p}{\mu}, \tag{3.54}$$

where C_μ is a constant dependent upon the turbulence model used (0.0845 for $k-\epsilon$ RNG model) and subscript p refers to the near-wall node point.

The viscous sublayer extends up to around $y^+ = 5$, hence the need in the absence of a wall function for multiple cells that are close to the wall. Outside of this region is a fully turbulent region called the log-law region that extends from $y^+ = 30$ upwards, with a buffer region blending the two.

The standard wall function greatly reduces the number of cells required by making one of two assumptions, depending on the near-cell's distance from the wall. If the cell closest to the wall is at a non-dimensional distance of $y^* < 11.225$, then,

$$U^* = y^*, \tag{3.55}$$

is applied, whereas for values of $y^* > 11.225$,

$$U^* = \frac{1}{\kappa} ln\,(Ey^*), \tag{3.56}$$

where κ is the von Kármán constant (= 0.4187), E is also an empirical constant (= 9.793), and U^* is the non-dimensional flow velocity, defined by Equation 3.57.

$$U^* = \frac{U_p C_\mu^{1/4} k_p^{1/2}}{\tau_w/\rho}, \tag{3.57}$$

where U_p is the near cell flow velocity. It is the wall functions that provide the

bridge between flow velocity and other scalar quantities found at near-cells and known values at the surface of a wall.

3.4.10 Particle injections

The simulations contained within Chapter 6 study the effect of a secondary, dispersed phase, which in the case of an aero-engine internal gear box is lubricating oil. This dispersed phase of oil is solved by tracking its motion as discrete particles, using a Lagrangian modelling approach. The particles are effectively superimposed upon the continuous phase, for which a fundamental assumption is made that the particles occupy a low volume fraction. The particles can be allowed to exchange momentum, mass, and energy with the air phase.

The Discrete Particle Model (DPM) is used to model both the oil suspended within the air, and a film forming on the surface of the shroud. The next few sections will look at the numerics behind how the DPM exchanges momentum with the primary phase. Details of the injections used to inject particles in the domain are also provided, and finally, an overview of the wall-film model.

3.4.10.1 Numerics

FLUENT predicts the trajectory of a particle by integrating the force balance on the particle, as shown in Equation 3.58, where subscript p refers to particle state variables.

$$\frac{du_p}{dt} = \frac{18\mu}{\rho_p d_p^2}\frac{C_D Re}{24}(u - u_p) + F_i. \tag{3.58}$$

In this case, Re is the relative Reynolds number and is defined as,

$$Re \equiv \frac{\rho d_p \left| u_p - u \right|}{\mu}, \tag{3.59}$$

and F_i refers to additional forces upon the particle in the i direction. These include the pressure gradient in the fluid,

$$F_i = \left(\frac{\rho}{\rho_p} \right) u_{p,i} \frac{\partial u}{\partial x_i}, \tag{3.60}$$

and the force required to accelerate the fluid surrounding the particle (the "virtual mass" force [18]), which becomes particularly important when $\rho > \rho_p$ given by,

$$F_i = \frac{1}{2} \frac{\rho}{\rho_p} \frac{d}{dt} \left(u - u_p \right). \tag{3.61}$$

Gravitational effects are not modelled for dispersed particles, due to rotational periodicity and dominance. This is the same logic that is applied to the continuous phase.

The particles used in this thesis are all defined as inert, meaning that they will not combust or evaporate and that they contain no volatile components. This assumption is appropriate given the atmospheric conditions within the IGB, and the lubricating oil used. They are, however, able to transfer heat to and from the continuous phase, and this is described in Equation 3.62, which assumes only convective heat transfer, and no radiation at the particle surface,

$$m_p c_p \frac{dT_p}{dt} = h A_p \left(T - T_p \right). \tag{3.62}$$

Where:

- m_p = mass of the particle [kg]
- c_p = specific heat capacity of the particle [J/kg K]
- h = convective heat transfer coefficient [W/m^{2}K]
- A_p = surface area of the particle [m^2]
- T = temperature of the continuous phase [K]
- T_p = temperature of the particle [K]

Equation 3.62 makes the assumption that the temperature of the particle is the same throughout, *i.e.* that conduction within its body is instantaneous. For oil droplets of the size to be injected into the domains of the simulations contained within this thesis (diameter 1 - 100 microns), this is an appropriate assumption.

All simulations reported in this thesis that use the DPM are run with two-way coupling between the primary and dispersed phases. This ensures that the motion of the particles is fed back into the continuous phase. The momentum exchange for a particle passing through a control volume is fed back into the equations for the continuum as a momentum source. This momentum change is computed as follows in FLUENT,

$$F = \sum \left(\frac{18 \mu C_D Re}{\rho_p d_p^2 24} (u_p - u) \right) \dot{m}_p \Delta t, \tag{3.63}$$

where C_D is the coefficient of drag, Re is defined in Equation 3.59, Δt is the timestep size, and $\dot{m}_p$ is the mass flow rate of particles. The value from this equation is fed back into the continuous phase's momentum equation (Equation 3.11) as a source term.

The two-way coupling is done using two continuous phase iterations per discrete phase iteration. The smaller the ratio between continuous and discrete phase iterations, the more accurate the solution will be, as the impact of particles is linked closely to the continuous phase's solution. The value of two used was found to be the smallest possible without producing excessively long simulation run times.

There is no interaction between the particles during the simulation, the particles occupy a very small volume fraction of the domain ($< 0.01\%$), and the likelihood of impact is consequently quite small. There is a time-penalty for simulating droplet collision, and the FLUENT manual does not recommend the use of the model where the droplet collision speed is high, which due to the high speed flows in the simulation (Mach numbers up to 0.5) could limit its accuracy [18].

3.4.10.2 Injection distributions

Unless otherwise specified, particles are injected with a Rosin-Rammler distribution, with a total of 20 diameter sizes, ranging from 1 to 100 micron diameter.

The Rosin-Rammler distribution makes the assumption that there is an exponential relationship between the droplet diameter, d, and the mass fraction of droplets with diameters larger than d [19]. This value is termed Y_d, and in FLUENT is defined as,

$$Y_d = e^{-(d/\overline{d})^n}, \tag{3.64}$$

where $\overline{d}$ is the mean diameter of particles for the injection, and n is the spread parameter. These values are chosen as 10 microns, and 3.5 respectively for the simulations contained within this thesis. In the absence of any experimental validation for the sizing of the droplets at any location, this is at best, an informed guess; however, as shown later in Chapter 6, there is little coupling between the motion of the droplets injected into the domain and the continuous phase,

meaning that the distribution of particles chosen doesn't have a large effect on the results, *i.e.* in the range of droplets chosen all particle distributions have a similar response.

3.4.10.3 Wall-film model

In Chapter 6, the interaction of oil droplets on the surface of the shroud is simulated by using FLUENT's film model. It is based upon the work of O'Rourke and Amsden [30], and was developed to model very thin films on the walls of cylinders of internal combustion engines, assuming that there are very small, atomised particles present. An assumption is made for this body of work that when the model is switched on, and a surface impacted by a droplet, there will be no splashing and the droplet will "stick" or "spread", and become part of the film, although FLUENT is capable of modelling this splashing. This was done because of a lack of data regarding the number of splashed droplets when a high speed particle hits a fast-moving film.

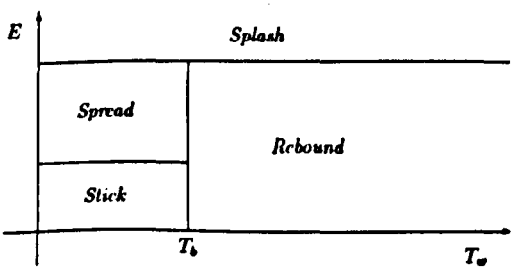

Figure 3.21: Wall Interaction criteria for droplet impact with thin-film model. T_w is wall temperature, T_b is boiling point of the droplet. [18]

Figure 3.21 shows the available options for a droplet impacting the wall. T_w is the Temperature of the wall, and T_b is the boiling point of the droplet. As the temperatures involved in the simulations reported in this thesis are well below the boiling point of the oil and as the splashing model is turned off, there are two available options for a droplet — spreading or sticking, based on the impact energy, E of the particle. This is given by,

$$E^2 = \frac{\rho_p V_r^2 D_p}{\sigma_p} \left(\frac{1}{min\,(h_0/D_p, 1) + \delta_{bl}/D_p} \right), \tag{3.65}$$

where ρ_p is the particle density, V_r is the velocity difference between wall and particle, D_p is the droplet diameter, h_0 is the film thickness and σ_p is the surface tension of the droplet. δ_{bl} is the boundary layer thickness, defined by,

$$\delta_{bl} = \frac{D_p}{\sqrt{Re_p}}, \tag{3.66}$$

where Re_p, the droplet Reynolds number is given by,

$$Re_p = \frac{\rho_p V_r D_p}{\mu_p}. \tag{3.67}$$

The boundary between sticking and spreading regimes occurs at a dimensionless droplet impact energy value of $E = 16$.

There are a number of restrictions to the applicability of the O'Rourke and Amsden particle based thin-film model. These can be summarised as the following:

- The film is less than 500 microns thick — to ensure a linear velocity profile across it
- Heat transfer from the wall is by conduction alone, and the particles are directly in contact with the wall
- The temperature of the film is below the boiling point of the liquid

Equation 3.68 shows the equation for continuity of mass within the wall film [30]. It is not necessary for FLUENT to directly solve this, as continuity is enforced automatically by the discrete particle model.

$$\frac{\partial \rho_p h_{\text{film}}}{\partial t} + \nabla_s \cdot \left[\rho_p \left(u_{\text{film}} - u_{\text{wall}}\right) h_{\text{film}}\right] = \dot{M}, \tag{3.68}$$

where h_{film} is film thickness, ∇_s is the surface gradient operator, u_{film} and u_{wall} are the film and wall velocities, and $\dot{M}$ is the mass source per unit wall area.

Equation 3.69 is the equation used for calculating the film velocity, u_{film},

$$0 = \tau_w t - \mu_p \left(\overline{T}\right) \frac{u_{\text{film}} - u_{\text{wall}}}{h_{\text{film}}/2} + \dot{P}_{\text{imp}} - \left(\dot{P}_{\text{imp}} \cdot n\right) n + \dot{M}_{\text{imp}} \left[\left(u_{\text{wall}} \cdot n\right) n - u_{\text{film}}\right], \tag{3.69}$$

where:

- τ_w = the shear stress on the gas side of the film,
- t = unit tangent to the surface in direction $u_{\text{film}} - u_{\text{wall}}$,
- μ_p = the film liquid viscosity,
- $\overline{T}$ = the film mean temperature,
- $\dot{P}_{\text{imp}}$ = the impingement pressures,
- n = the unit normal pointing away from the walls,
- $\dot{M}_{\text{imp}}$ = the impingement mass of particles hitting the wall.

The momentum of the film is determined by a balance of the shear stress on the gas-side of the film, the viscous forces resulting from film and wall motion, and the force due to droplets impinging upon the film. These models are used in Sections 6.5 in Chapter 6, where DPM droplets are allowed to form a thin film on the surface of the shroud.

3.4.11 Boundary conditions

Figure 3.22 shows the domain when viewed from the side, perpendicular to one of the periodic planes. Marked on the figure are all of the boundary conditions used for the simulations, and shown on the inset to the figure is the location of non-physical post-processing surfaces, which are addressed in Section 3.5, on data analysis.

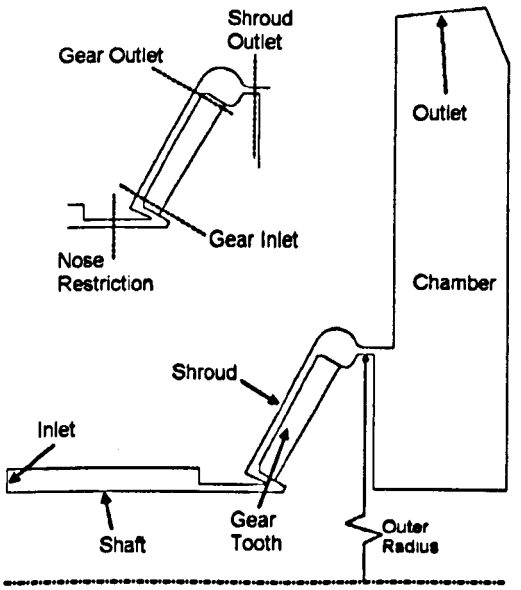

Figure 3.22: Boundary conditions, for domain, plus post-processing surfaces shown on inset

Boundary conditions are required to provide the solver with known quantities at the edges of domain — they provide suppression of the discretised transport equations beyond the boundary. For wall conditions, which make up the majority of the boundaries, it is well understood in theory and practice that the flow velocity will be zero (assuming the surface has some roughness), and therefore this provides the solver with a large amount of information that affects the results further into the domain. Each boundary condition will be addressed in turn below.

3.4.11.1 Walls

The use of a relative frame of reference for the simulations (see Section 3.4.4) means that the rotational velocities of the walls can be specified relative to the fluid. Walls which are physically rotating, such as the shafts and the gear itself are given a relative rotational velocity of zero radians per second. This means that they have the same rotational speed as the frame of reference, which in turn has been set to the same rotational speed as the physically rotating gear. Walls which are physically static, such as chamber walls and the shroud have an absolute rotational speed of zero radians per second, which means that their speed is not linked to that of the rotating frame of reference. A non-slip shear condition is used for all walls, and this ensures that the flow velocity is zero, relative to the wall's surface. Wall functions are effectively the wall boundary condition which extends into the domain, and these were covered in Section 3.4.9.

3.4.11.2 Pressure boundary conditions

All simulations use a pressure inlet boundary to prescribe appropriate conditions at the inlet to the domain. The exception to this are the cases used for validation of the control gear's mesh, as these use a mass-flow-inlet condition, covered in Section 3.4.11.3 below. When a solution uses a pressure inlet, it will be referred to as the "natural" case, with a static gauge pressure of zero pascals, following the convention of Johnson *et al.* [22, 23].

Pressure inlets are used when the pressure at the inlet to the domain is known, but conditions such as velocity or mass-flow-rate are not. They are used in areas where flow will enter the domain, although it is possible in FLUENT for flow to be allowed out of the domain at a pressure inlet — but this did not happen in any of the simulations within this thesis.

FLUENT's pressure inlet conditions require total pressure and temperature to be prescribed. The total, or stagnation pressure is constant along a streamline,

and is defined by Equation 3.70, which includes the effects of compressibility, where γ is the ratio of specific heats (c_p/c_v), M is the Mach number, and p_0 and p_s are the total and static pressures respectively.

$$p_0 = p_s \left(1 + \frac{\gamma - 1}{2} M^2\right)^{\gamma/\gamma-1} . \tag{3.70}$$

The total pressure is set at zero Pascals, relative to the operating (reference) pressure of 101,325 Pascals. This is the total pressure inside the room in which the experimental work is done [23], which will also be the total pressure at the inlet, using the logic of total pressure being equal all the way along a streamline introduced above. A result of this is that due to the flow having some velocity at the inlet (and hence the Mach number in equation 3.70 being non-zero), the static pressure will be less than zero Pascals, relative to the operating pressure. Temperature follows the same principles as pressure, and is set to 300K for all simulations.

The final quantities that need to be specified are for turbulence. This can be done by directly supplying turbulent transport values for the boundary, which for the $k - \epsilon$ RNG turbulent model would be k and ϵ. However, these values are rarely known from an experimental set-up, so can be calculated by FLUENT from turbulent intensity and hydraulic diameter values that the user enters for the boundary. The vast majority of the turbulence in the domain will be created in the area between gear and shroud, in the high shearing flow, meaning that the flow solution will be fairly independent of the turbulent quantities at the inlet [19]; however, they are still entered using sensible values to reduce dependence. Turbulent intensity is set to 1%, a low value that reflects that the flow is undeveloped. A hydraulic diameter dependent upon the simulation is used, which allows FLUENT to calculate a value for turbulent kinetic energy, k using the approximation in Equation 3.71,

$$k = \frac{3}{2}(u_{avg}I)^2, \tag{3.71}$$

where u_{avg} is the average velocity, and I is the intensity of the flow. Subsequently, the dissipation rate, ϵ can be calculated using Equation 3.72.

$$\epsilon = C_{\mu}^{3/4}\frac{k^{3/4}}{l}, \tag{3.72}$$

where, $C_{\mu} = 0.0845$ as used in Equation 3.39, derived by RNG theory, and l is the lengthscale, calculated as 0.07 times the hydraulic diameter.

All simulations use a pressure outlet as the boundary condition for the outlet to the domain. This is a condition that should be used at a point where the flow is expected to leave the system, therefore flow quantities are extrapolated from the interior cells, with the exception of the static gauge pressure, which is specified as zero Pascals. Additionally, backflow quantities are specified using the same values for temperature, turbulent intensity from the inlet conditions, and a relevant hydraulic diameter to account for the larger outlet.

3.4.11.3 Mass-flow-inlet

In Section 3.7, the response of the system to a number of different mass-flow-rates is determined. A mass-flow-inlet boundary condition is necessary to prescribe a flow rate through the system. Compressible effects are modelled for the simulations, which precludes the use of a velocity inlet condition. The user defined inputs are similar to that for the pressure inlet, with the exception of the mass-flow-rate being enforced, and the total pressure at the boundary being determined based on the solution in the interior of the domain. If the same mass-flow-rate is used as found in the "natural" case for the control gear, the exact same solution would be reached.

3.4.11.4 Periodic

The final boundary condition is the rotationally periodic boundary condition which is used for all simulations in order to reduce the amount of computation required. The reasons for doing this were covered in Section 3.3 dealing with meshing. The condition applied by FLUENT for boundary conditions is that the flow across two opposite boundaries is identical.

3.4.12 Convergence

Convergence of the simulations is monitored in two ways: the reported moment on rotating surfaces and FLUENT's scaled residuals. It is not possible to automatically stop FLUENT when a moment or force based criteria is met, therefore it must be done after a simulation is completed by analysing the moment output file. An example of the time-dependent moment on the control gear can be seen in Figure 3.23, which shows the considerable variation and multiple frequencies of the moment on the gear. Convergence of the moment is identified when the average moment on the gear doesn't change by more than 3% for each subsequent revolution of data. The first five revolutions of transient data is discarded regardless, as there are large instabilities in the moment as the change from steady-state to transient calculation occurs. Generally, the reported average moment is from the sixth to tenth revolutions inclusive.

Scaled residuals are used in order to "normalise" the sum of the residuals of the conserved variables over all the cells in the domain. This permits the same convergence criteria to be used for any simulation, regardless of the magnitude of a variable, or the number of cells. The solution is considered converged for a single time-step when the following scaled residuals are reached: continuity[9] to 10^{-4}, energy to 10^{-6}, all other quantities such as turbulence and momentum

[9]It is this variable which is the last to converge, with all other variables generally being far below their thresholds

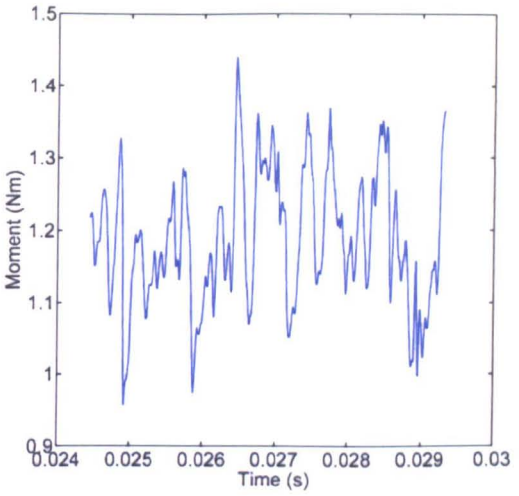

Figure 3.23: Control gear moment against time for a single revolution

to 10^{-5}. The timestep size means that this level of convergence usually takes 25-35 iterations to be reached, but computation is allowed to continue until 50 iterations if necessary.

3.4.13 Solution strategy

Using all of the solver theory described above, the following section describes the solution technique developed in order to run a complete simulation.

1. Initialisation: the matrices containing the solution have to be initialised with a first "guess" to the answer. Turbulent quantities such as k and ϵ are based on values calculated at the inlet. Static pressure is initialised with zero pascals gauge, and velocities are initialised with a radial and axial component equal to a small, non-zero value of around 2 m/s.

2. Steady-state: the best way to commence a transient calculation is by starting with a converged steady-state solution. Convergence is difficult with some steady-state solutions, such as the ones contained within this thesis, due to the imposition of forcing the single solution to one that is by nature unsteady, and this is addressed in Section 3.6.1. Nevertheless, it is possible to obtain a good initial starting point for the transient calculation, even

if poor convergence occurs. A steady-state state solution was obtained by first running a calculation at a lower rotational speed of 4000rpm, before increasing to the full 12,266rpm and running until the reported moment on the moving surfaces has stabilised. This occurs by 6000 iterations.

3. Transient calculation: the final stage is to switch to a full transient calculation. The first revolutions of data have to be discarded as the averaged moment reported on the surfaces is not initially stable, due to the development of the simulation from steady to transient with cyclic flow features. For all simulations, in order to achieve a point where the time-dependent moment has stopped changing the mean moment by more than 3% between subsequent revolutions, five revolutions of data must be discarded, and the sixth to tenth inclusive used for reporting of data used in this thesis. At the start of the sixth revolution, data-sampling within FLUENT is switched on, which enables the collection of time-averaged values for flow variables such as pressure and velocity. This aids post-processing and visualisation of these quantities. Additionally, it is at this point for simulations which use the discrete particle model that it is switched on.

3.5 Data analysis

3.5.1 Post-processing overview

The manner in which CFD simulations are post-processed is diverse, and often techniques are created which are problem specific. The highly three-dimensional and turbulent nature of the flow between the gear and shroud means that a figure showing a flow variable, such as the velocity or pressure of the air is difficult to follow and conceals important information behind physical features. Some visualisations are supplied to aid the reader's appreciation of the flow; however, as they do not provide a quantitative way of comparing simulations, their use is limited.

A number of surfaces are used for collecting data, and these are marked on Figure 3.22 in the section on boundary conditions, and are repeated for convenience here in Figure 3.24.

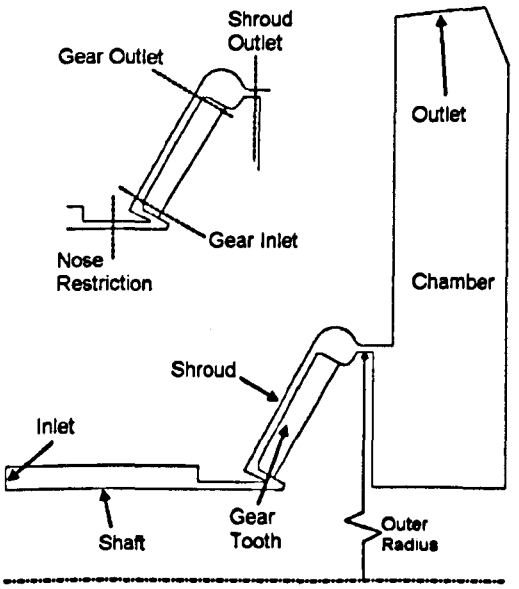

Figure 3.24: Boundary conditions, for domain, plus post-processing surfaces shown on inset

The inlet and outlet surfaces are the ones used as boundary conditions, and consequently are readily accessible for post-processing . The other surfaces marked on Figure 3.24 on the inset are non-physical and created in both FLUENT directly, or in CFD-POST, after the simulations had completed. "Nose Restriction" and "Shroud Outlet" are surfaces that are annular in shape for a whole gear, but form an annular arc for a single tooth model. They lie half-way down the nose of the shroud, and at the outlet to the shroud respectively and are iso-surfaces of constant axial coordinates. The surfaces at the inlet and outlet to the gear are conical in shape (for a whole gear), and are located at the inlet and outlet to the gear valley respectively.

3.5.2 Visual post-processing

Visualisations created for this thesis are predominantly done using CFD-POST [21], which permits non-physical surfaces to be created to aid understanding of the flow within the domain. The majority of the visualisations are done from the a perspective perpendicular to the periodic plane of the simulation. This perspective direction is marked on Figure 3.25, and concentrates on the area between shroud and gear, therefore making the back chamber appear slightly shortened; however, as this is not an area of concern for the simulations, it has limited impact upon the reader's understanding.

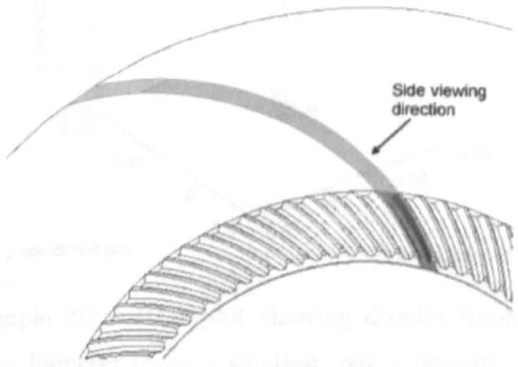

Figure 3.25: Front view of domain, with arrow making perspective used for visualisation

3.5.3 Numerical post-processing

The majority of the qualitative and analytical post-processing is done using numerical data extracted from FLUENT. This is done within Mathsworks MATLAB [20] and Microsoft Excel [7], and is correspondingly graphed to aid reader clarity.

Post-processing of the results from the discrete particle simulations requires a technique that permits the dispersion of particles that have hit the surface of the shroud to be done in a meaningful manner. Particles that hit the surface of the shroud for some of the simulations are removed from the domain and their escape

location written to file. An issue identified with FLUENT and CFD-POST is that there is no way to visualise these escape locations and the geometry at the same time. Plotting the data using a three-dimensional scatter plot of escape locations does not provide useful information, as demonstrated by Figure 3.26 which shows the results for a sample simulation, with points coloured by diameter. The plot is difficult to follow, and there is no physical, or geometric context provided to aid the viewer.

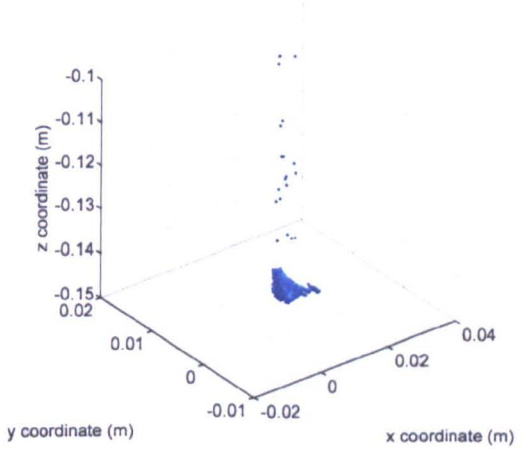

Figure 3.26: A sample 3D scatter plot showing droplet impact points on shroud. Points are coloured by diameter (blue = smallest, red = largest)

The solution identified was to create a variable that represents the distance along the shroud that a particle "escapes", measuring from the nose to the outlet — effectively unwrapping the shroud and flattening it into a 2D projection. Therefore, every location on the shroud that a particle hits can be identified by two variables: the distance along the shroud, and the azimuthal co-ordinate. This can be represented on a polar plot, where the radial distance from the centre shows the distance along the shroud, and the azimuthal co-ordinate shown as the radial angle. The results for the single tooth simulation can be copied and rotated to allow interpretation for a whole gear. This can be seen in Figure 3.27, which shows the same results from Figure 3.26, only this time using a polar plot, with the particle impact spots for a two tooth segment.

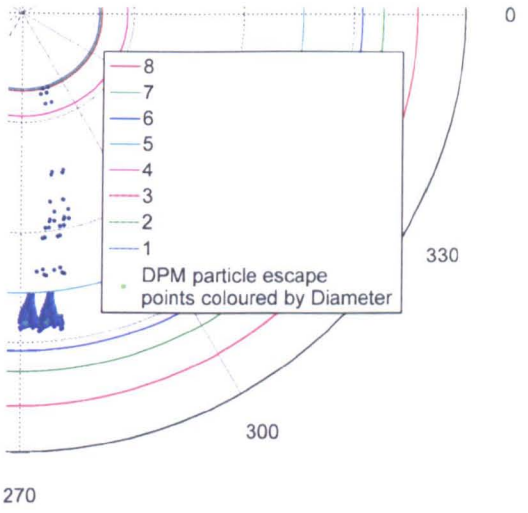

Figure 3.27: Polar plot of DPM escape points, shown for a two teeth segment

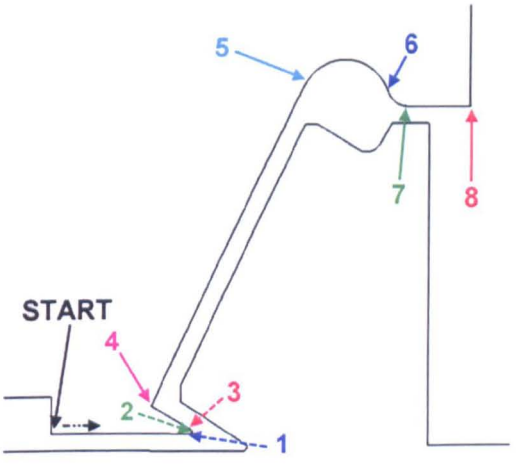

Figure 3.28: Key Shroud Features as seen in polar plots marked by colour and location

The coloured lines on the polar plot represent important geometric features of the shroud, which are marked on Figure 3.28.

The final method for visualisation of the escape locations for the discrete particles ignores the azimuthal coordinate of the particles' escape locations and instead uses a histogram to show the number of droplets hitting the shroud, with the only independent variable being the distance along the shroud. This can be seen in Figure 3.29, which shows the same set of results, as in Figures 3.26 and 3.27. The bars of the histogram can be sub-divided by a particle variable, in this case droplet diameter, which permits better comparison between different

simulations. This method is the most frequently used within this thesis, as it is clear and concise.

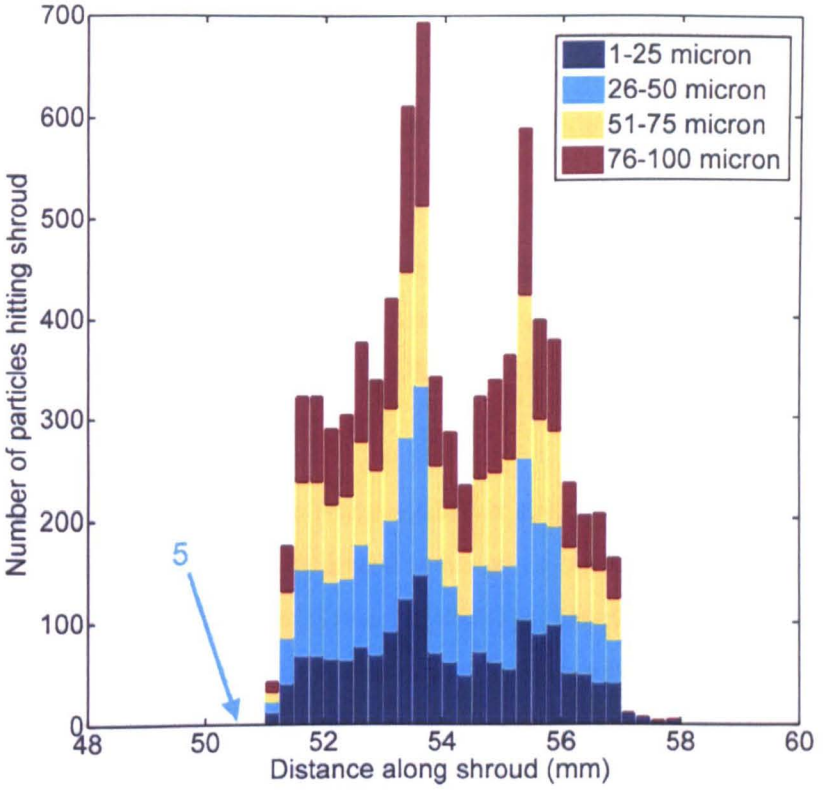

Figure 3.29: A histogram showing oil droplet escape location, coloured by diameter

3.6 Verification

3.6.1 Steady versus transient calculation

The results presented within this thesis are averaged from transient calculations. This is due to a lack of good convergence from steady-state calculations because of the natural time-dependence of the flow, which includes transient structures such as travelling vortices, being forced into a single steady solution, as detailed in Section 3.4.12.

Table 3.2 shows a number of key values comparing the results from steady-state and transient simulations. The results from the steady-state simulations are av-

	Moment (Nm)	CPU time
Steady state	1.240	3 hours
Transient	1.218	4 days

Table 3.2: Steady and transient simulation moment results for the control gear, plus CPU time

eraged over 1000 iterations, and those from the transient simulation are averaged over five revolutions. The table also provides total CPU time required to obtain the solution, based on running FLUENT with four 2.66GHz processor cores operating in parallel.

The reported moment does not differ much between steady-state and averaged transient calculation with the difference between the two being only 1.79%. However, the moment for the steady-state simulation does not stabilise to a single value, instead varying with iteration number. A sample plot of moment on rotating surfaces for the control gear against iteration number can be seen in Figure 3.30. This is a general observation for all of the simulations tested, although some have a larger difference between the steady and transient moments.

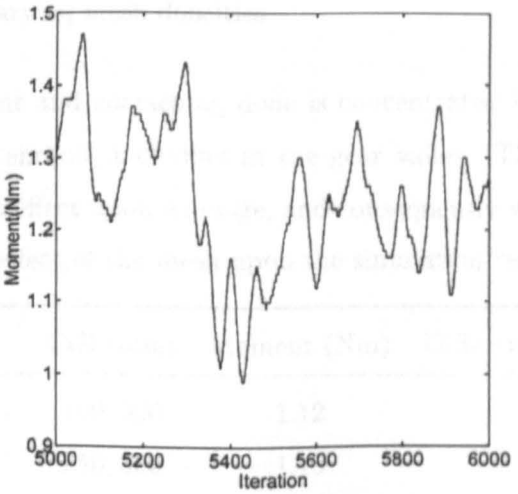

Figure 3.30: Steady state moment on rotating surfaces of control gear versus iteration number

The figure shows the large variation in the moment over relatively few iterations, and coupled with the poor convergence characteristics of the simulation this shows that the solver is attempting to fit a physically transient flow field to a single solution. As a result of this, and in order to capture transient structures such as vortices passing through the domain, simulations are to be run with transience switched on.

3.6.2 Mesh density

It is important to ensure that the mesh resolution be sufficient so as not to affect the solution too much. As the size of the cells decreases, the discretised equations tend towards the results of partial differential equations describing the flow. Computational constraints mean that the density of a mesh is limited by available processor time for a given size of problem. Modelling of aspects of the flow, such as turbulence, helps reduce the time taken to accurately solve a problem, but ultimately, a grid size must be chosen that shows mesh independence and can be run on an available computer within a reasonable timeframe. Mesh verification takes the form of comparing the results from a number of identical simulations, with varying mesh densities.

The mesh refinement and coarsening done is concentrated in the area between gear teeth and the shroud, including in the gear valley. This is the area that will have the largest effect upon windage, and consequently will provide the best indicator as to the effect of the mesh upon the simulation results.

Mesh	Cell count	Moment (Nm)	Difference from control
Very low density	180,000	1.12	−8.18%
Lower density	250,000	1.18	−3.08%
Control	400,000	1.22	-
Higher Density	480,000	1.17	−4.00%

Table 3.3: Comparison of verification meshes against control gear moment

Table 3.3 shows results for a number of simulations which used varying mesh densities, and gives a percentage difference from the control gear. All of the meshes have a moment which is smaller than the control gear's; however, as the standard deviation of the control gear's time-dependent moment is 7.0% of the mean moment, the differences for all meshes except the very low density are within one standard deviation. Figure 3.31 shows a graph of moment against time for the sixth revolution of the control gear, with the mean for the six-tenth revolutions for all the above verification cases marked on it. It shows that the average for all of the meshes except the lowest density one sits well inside the time varying moment of the control gear. The lowest density mesh's average can clearly be seen to lie outside the grouping of the other sets.

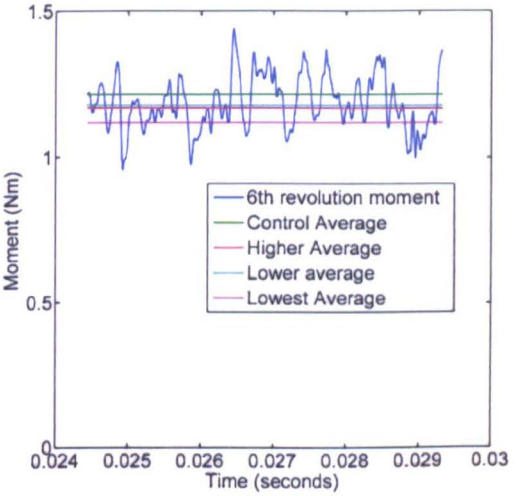

Figure 3.31: A comparison of average moments and the time-varying moment of the control gear over one revolution

3.6.3 Multiple teeth

The decision to use a single tooth of the gear, with periodic boundaries was considered in Section 3.3 on creation of the mesh. In summary, it is a desire to reduce the computational constraints of modelling an entire gear, by making an assumption that the physical flow field is the same for all neighbouring teeth. This would not be true if, for example, flow skipped teeth.

In order to test the validity of using a single tooth for the simulations contained within this thesis, a number of cases are run using multiple teeth versions of the control gear mesh, which are created by simply rotating and repeating the original single tooth mesh. These have two, three and five teeth. The results for each are shown in Table 3.4.

Gear	Moment (Nm)	Difference from control
Control	1.22	-
2 teeth	1.19	−2.24%
3 teeth	1.24	2.09%
5 teeth	1.16	−4.51%

Table 3.4: Results for all multiple teeth models, and their difference from the control gear

As can be clearly seen from the results, there is only a small difference between the results for two and three teeth models, with a slightly larger difference between the control and five-teeth model. It is unlikely that there is no effect of only modelling one tooth, however these results show that the impact is limited.

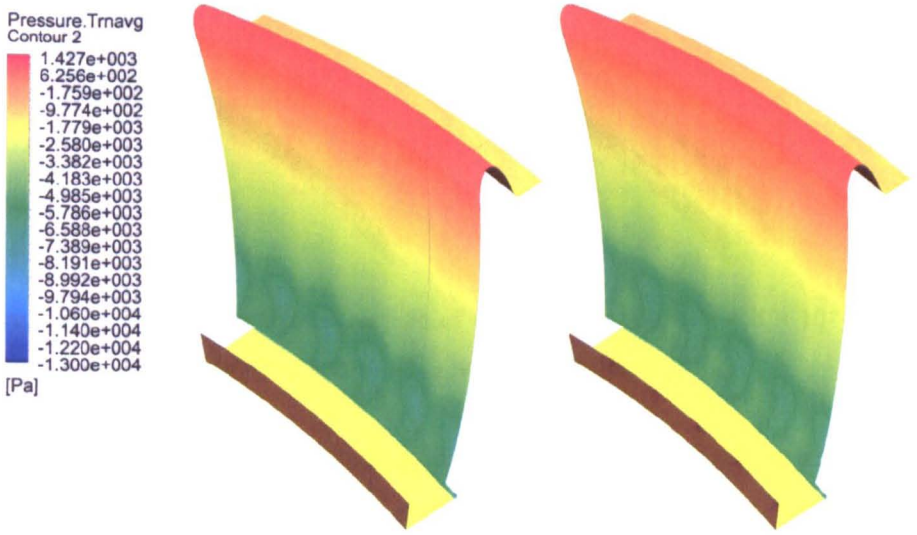

Figure 3.32: Time-averaged static pressure on surface of the shroud. LHS is single tooth result copied four times, RHS is five-tooth result

If the case of the five tooth model is studied in further detail, it is possible to see that while there are flow structures which are travelling across the surface of the shroud, the time-averaged quantities (over a number of revolutions) do not show multiple tooth periodicity. This can be seen in Figure 3.32, which shows static pressure, averaged for five revolutions, on the surface of the shroud for both the single tooth, control gear (left-hand-side) and for the five-tooth model (right-hand-side). The result for the control gear is shown copied four times to replicate the size of the five-tooth's shroud, for ease of comparison. There is a clear qualitative match between the two averaged shroud static pressures, with a linear increase with increasing diameter. There is also a patch of low pressure near the inner diameter of the shroud, and this is due to the acceleration of the flow by the teeth at this point. The quantitative match is very good also, and this gives strong confidence in the ability of the single tooth control gear to provide good time-averaged quantities, with limited impact of using periodic boundaries.

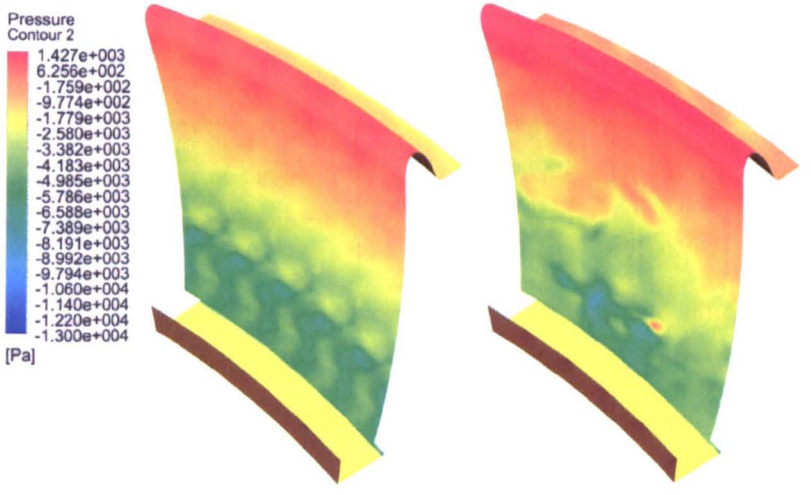

Figure 3.33: Static pressure on surface of the shroud at time = 4.8×10^{-2}s. LHS is single tooth result copied four times, RHS is five-tooth result

This can be contrasted to Figure 3.33 which shows the static pressure on the surface of the shroud at 4.8×10^{-2} seconds after the start of the simulation, corresponding to the end of the tenth revolution. This figure shows the considerable difference between the single and five-tooth models when a snapshot of the static pressure[10] is looked at. The order of magnitude of the static pressure field on the

[10]This also applies to other scalars and vectors

shroud is similar for both cases; however, the large difference in structure shows that there are clearly structures that are travelling further than a single tooth.

The majority of the moment on the rotating gear is due to the pressure forces on the flanks[11] of the teeth; 87% of the control gear's moment is a result of the flanks of the teeth. By looking at the moments on the flanks of the neighbouring teeth, it is possible to see that for the five-tooth model, there is very little variation between all of the teeth. The maximum difference for any single tooth flank from the average moment for all five flanks is only 1% of the average, with most of the flanks being within 0.5%. This indicates that there is little evidence of structures skipping teeth, as a larger variation between the flanks would then be seen.

	Positive moment flank (Nm)	Negative moment flank (Nm)
Control	0.0570	-0.0454
5 teeth	0.0558	-0.0449
Difference	-1.09%	-2.02%

Table 3.5: Comparison of moment on tooth flanks for single and five tooth gears. Results represent an average moment for the five tooth gear

Table 3.5 is a comparison of the moment on the flanks of the single toothed and five toothed models. The results represent a single tooth, so for the five tooth model is an average of all the teeth. Due to the pressure forces on the opposing sides of a tooth, one flank has a positive moment, the other has a negative one — the net difference is the 87% of the total moment mentioned previously. The table shows that there is a difference of -1.09% and -2.02% for the positive and negative moment flanks respectively, which compares favourably, demonstrating the ability of the single tooth model to replicate the averaged results of a model with more teeth, whilst cutting down on total simulation time.

[11] refer to Section 3.2.2.3 for figures showing the flanks of the teeth

3.7 Validation

All validation is done using the control gear, against the work of Johnson *et al.* [23]. This experiment matches closely with the simulations presented in this section, with a few small exceptions that have been covered before briefly, and will be explored further in this section. There are two forms of validation that will take place: firstly, a comparison of torque at given mass-flow-rates, and secondly a comparison of the static pressure profile on the surface of the shroud. These are addressed separately below.

3.7.1 Characterisation of gear system

The experimental work of Johnson *et al.* characterised the gear and restriction system by rotating the gear at a constant speed and delivering air at a prescribed flow rate. This represents conditions in an aero-engine internal gearbox, whereby the rotational speed of the shaft will be fairly constant for a set engine condition, but the pressure difference across a shroud inlet and outlet may change.

Figure 3.34 shows the air delivery system as used by Johnson *et al.* [23]. This system allowed the mass-flow-rate of the air passing through the domain between gear and shroud to be carefully controlled. For the computational simulations, the mass-flow-inlet boundary condition is used, as described in Section 3.4.11.3.

Figure 3.35 shows a graph of moment against mass-flow-rate through the domain for experimental and computational results. The CFD under-predicts moment compared to the experimental results, with a difference of around 0.2 Nm at the control gear's "natural" mass-flow-rate, which is around 14%. The trend of increasing windage torque with increasing mass-flow-rate through the system is well represented, with gradients that are within 0.8% of each other. The discrepancy between the absolute values of windage can be explained through two aspects of the physical experiment which are omitted in the computational model. Firstly,

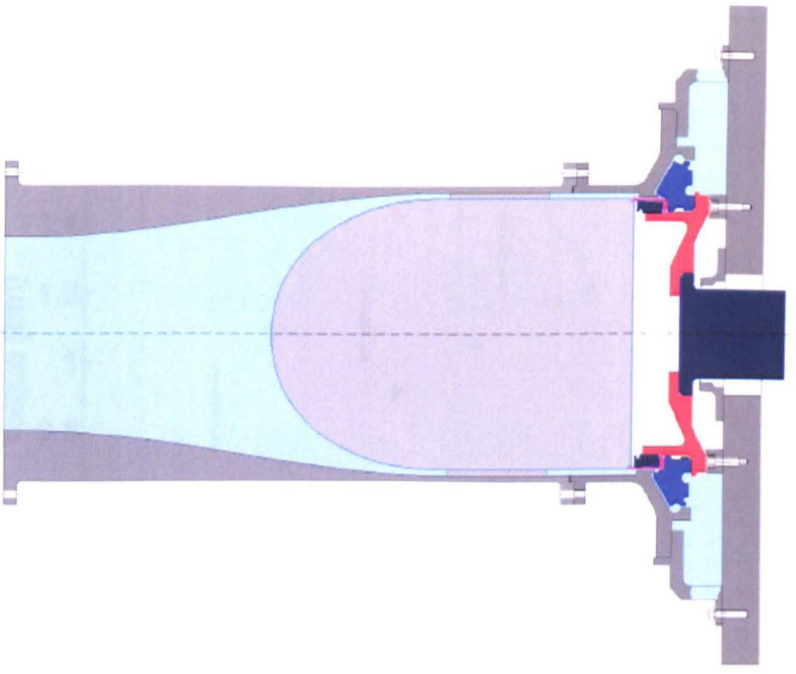

Figure 3.34: Air delivery system for experimental characterisation of gear system [23]

as addressed in Section 3.2.3, a change was made to the back of the gear, whereby the radial grooves are removed to produce a flat back. This change will reduce the viscous drag on the back of the gear. A simple 2D axi-symmetric simulation was run transiently, modelling the impact of the grooved back of the gear. This showed that the grooved back of the gear would add 0.069Nm of the 0.2Nm difference between the experimental and CFD results for the control gear. This difference would increase the control gear simulation's result by 5.36%. Figure 3.36 shows contours of tangential velocity for the simulation, which although it is two-dimensional, is shown in a three-dimensional form by CFD-POST. The inlet condition for this simulation uses data from the outlet of the shroud for the control gear one-tooth model - in order to make this simulation as relevant as possible. As the figure shows, there is a large amount of stirring of the fluid by the grooved back, which leads to the higher viscous moment experienced by the gear.

The second change, addressed in Section 3.2.2, is that the gear in the experiments was on a hub with six bolts protruding, as seen in Figure 3.8.1 (although only 4

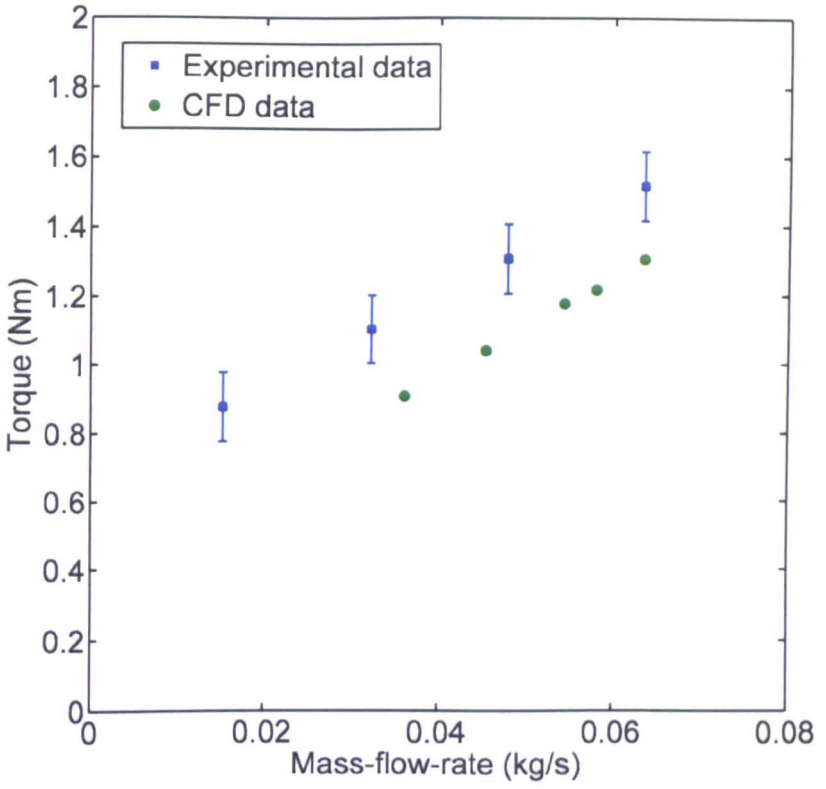

Figure 3.35: Moment against mass-flow-rate for the physical experiment and the computational gear

bolts are for mounting the hub to the rig, with the other two being for balancing the gear). This was not modelled due to the massive increase in mesh size that would entail, but would have led to the experimental results being slightly inflated due to the pressure and viscous drag.

The combination of these two factors means that the results from the CFD simulations sit within the experimental error of the results of Johnson *et al.*, and therefore, there is strong confidence in the results that are computationally obtained. Additionally, as the trend behaviour of the varying gears and shrouds used in the simulations is the key focus of this thesis, the effect of the hub and grooved back of the gear is of little interest to the results. The important aspect to get right is the response of the gear to the mass-flow-rate through the system, and the pressures experienced by the shroud.

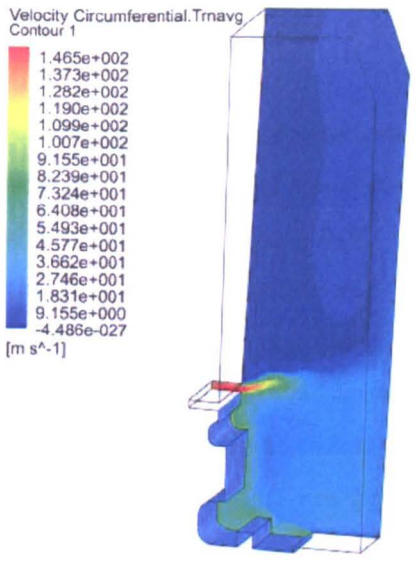

Figure 3.36: Contours of tangential velocity for grooved back of computational gear

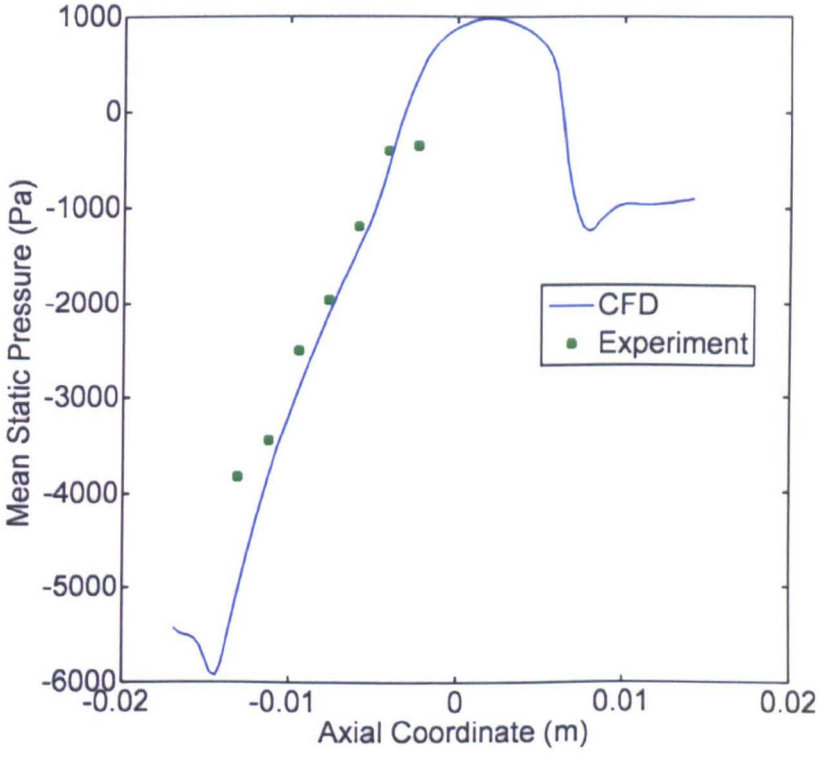

Figure 3.37: A comparison of static pressure on the shroud between CFD and experiment

3.7.2 Pressure on the shroud

One important way of ensuring that the computational model is working is to compare the static pressures on the surface of the shroud with the experimental results. This comparison can be seen in Figure 3.37, which shows the pressure profile on the surface of the shroud for both CFD and experimental results. The static pressure values from the experiment are found using four radial lines of nine pressure tappings, with the pressure averaged between them. These pressure tappings can be seen in Figure 3.38, where C to I are on the shroud, adjacent to the face of the gear. Tappings A and B are not used for comparison in Figure 3.37., as they are located a relatively significant distance upstream. The CFD static pressure values are obtained using 100 axially located circumferential bands, based on mean static pressures averaged over 5 revolutions. In the figure, an axial coordinate of zero metres corresponds to the pitch diameter of the gear.

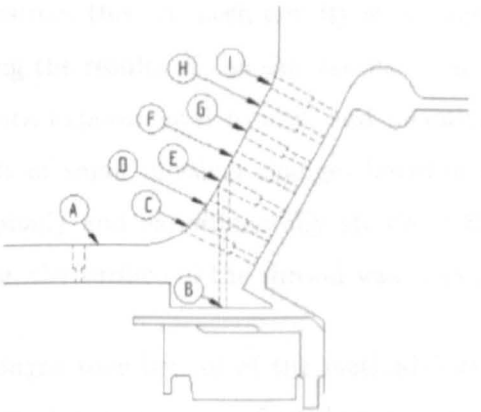

Figure 3.38: Locations of pressure tappings in experiment [23]

As can be seen, the two sets of results line up very closely with each other, with the difference being only 100 Pascals over the face of the gear. This agreement indicates the model is able to accurately predict the pressure on the gear, which is an important part of being able to investigate the influence of shroud or gear design on the windage torque.

3.8 Overview

This chapter started by looking at the formulation of the parametric solid model of the spiral bevel gear that is used in the simulations contained within the next three chapters. The meshing techniques was then outlined, as was the formation of the domain which is modelled. The numerics and justification for the CFD models chosen to simulate the domain were then explained and detail regarding the choice of turbulent model and boundary conditions provided. A modelling strategy for running the simulations was also presented in this subsection. After this, the methods used for visual and numerical post-processing of the data are explained. Finally, detailed mesh verification and validation of the model are presented. These sections showed that the use of a single tooth model, representing the whole gear, in conjunction with periodic boundary conditions, has a very limited impact upon the accuracy of the results, and the resulting decrease in simulation time justifies this. A mesh density study showed that the mesh is not adversely affecting the results of the simulations. The model matched qualitatively very well with experimental results, and quantitative differences were calculated as a result of small physical changes between the gear and domain modelled computationally and experimentally studied. Excellent validation of the pressure profile on the surface of the shroud was shown.

This chapter has brought together all of the methodology required to produce and run a simulation studying the effect of windage on a rotating, shrouded spiral bevel gear. The next three chapters will use the techniques introduced here to study the effect of changing the geometry of the gear in Chapter 4, the shape of the shroud in Chapter 5 and finally, the impact of oil on the system in Chapter 6.

CHAPTER 4

Gear parametric study

4.1 Introduction

This chapter presents results of a parametric study that looks at the effect upon windage of changing the size and shape of a spiral bevel gear that is shrouded. The aim of this is to use the techniques developed in the methodology chapter (Chapter 3), and to also establish a set of guidelines that will aid transmission designers where possible to select a spiral bevel gear that will reduce windage.

Four variables are separately investigated, and these are:

1. The outer diameter of the gear, Section 4.3. The auxiliary power transmission requirements of modern aero-engines are increasing due to more electrical demand, meaning the meshing gears in the Internal Gear Box (IGB) must be able to transmit more torque. A larger gear facewidth means more metal in contact between two gears, so therefore a higher torque can be transferred. As a result, gears are increasing in facewidth with new engine architectures. This section will look at the effect of the outer diameter on windage.

2. The inner diameter of the gear, Section 4.4. In an IGB, the inner diameter of a gear is usually determined by the size of the shaft on which it is carried. This means that an aero-engine manufacturer will only be able to use the outer diameter of the gear as a variable to increase the gear facewidth

to allow for greater torque transmission. However, in order to provide a complete picture of the impact upon windage of changing the size of the gear, this section will look at what effect the inner diameter of the gear could have, were a manufacturer able to change this dimension easily.

3. The module of the gear, Section 4.5. The torque transfer ability of a gear will be determined by the size of the teeth, and their maximum bending stresses. Module is a measure of the size of the teeth, and is defined as the amount of pitch diameter per tooth. Manufacturers have tended to use fewer, larger teeth on a gear as this reduces the shock-loading on the gears when rotating loaded at high speeds. This section will identify trends in windage with changing numbers of teeth (determined by the gear's module).

4. The pitch cone angle of the gear, Section 4.6. The pitch cone angle is used to control the angle between the shafts of the crown and pinion gears. The combined pitch cone angle of both gears when added together is the shaft angle, so there is flexibility for a manufacturer to change both in a manner that can minimise the windage power losses. This section will look at these trends.

Figure 4.1 shows these variables marked on a sample spiral bevel gear. The module is difficult to represent physically, and instead the circular pitch is shown, which is the module multiplied by π. Physically this is distance along the pitch circle between the corresponding flanks of neighbouring teeth.

In an effort to make the results suitable for a practical application, the changes that are made to all the computational gears are done to make the new model as physically realistic as possible. Each section within this chapter will detail how the changes to the gears are made, and the likely impact of any assumptions that have had to be made.

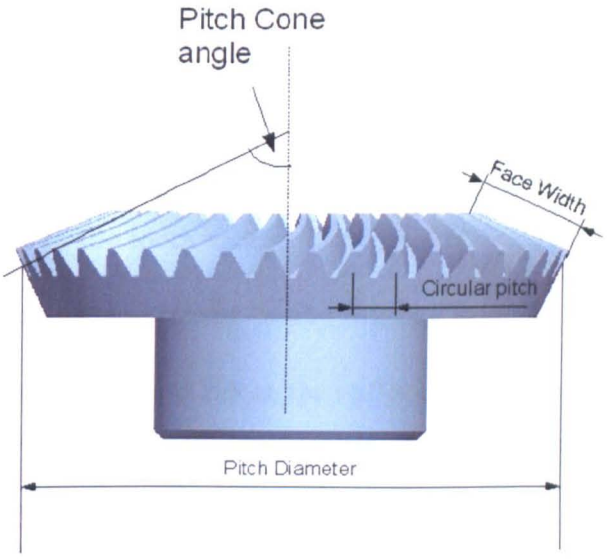

Figure 4.1: Gear Variables marked on a sample spiral bevel gear

4.2 Link to the validated control gear

This chapter will use the analogy of a centrifugal fan and system load to represent the gear and the shroud restrictions (both inlet and outlet) respectively. This approach has been taken in the past, for example by Johnson *et al.* [23], and is expanded upon in Section 2.5.1 in the literature review.

A centrifugal fan works by accelerating air radially outwards using an impeller and feeding it through a shroud, or "volute", which recovers static energy from the higher velocity of the flow [5]. The act of accelerating the flow through the impeller creates a low pressure region at its centre, through which air is forced by the higher pressure of the atmosphere at the inlet. Energy is supplied to the flow by the impeller, raising both the static pressure and the velocity of the fluid between its entry and exit. The one significant difference between a centrifugal fan and the shrouded spiral bevel gears in this case is that the fan draws air in from its centre, at a radial coordinate of zero, whereas the gears in this case only draw air in at their inner diameters — this will be considered further throughout this chapter. In the most simple form, this can be represented for the case of a rotating spiral bevel gear as in Figure 4.2, which shows the entire domain as

three separate components. Reference can be made to Figure 3.10 in Section 3.2.2.3 for guidance over the separate parts of the system.

1. A large pressure loss through the inlet of the shroud, which also includes the entrance to the tooth valley,
2. The pressure increase caused by the rotating gear,
3. The small static pressure loss at the outlet to the shroud as it is exhausted to atmospheric pressure in the chamber behind the gear.

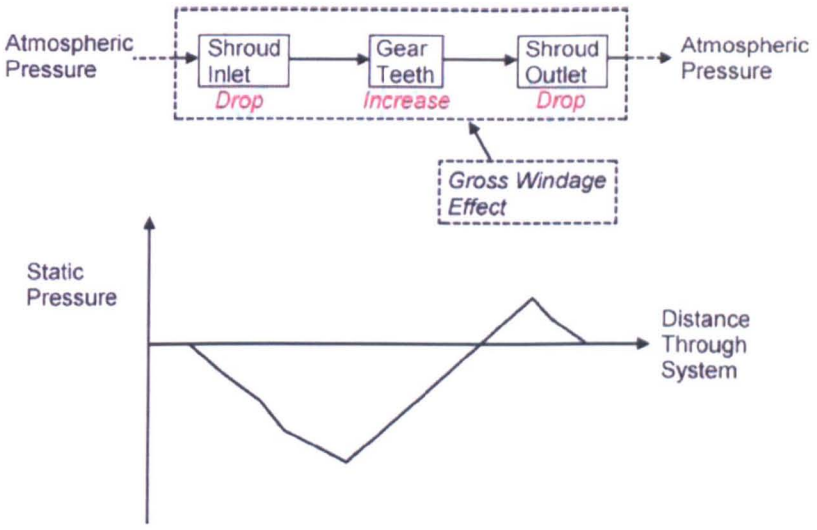

Figure 4.2: A schematic of pressure distribution throughout the domain

This figure represents a "natural" case, where the inlet and outlet static pressures represent atmospheric conditions, with the x-axis being equal to zero gauge static pressure. Also shown in the figure is the *black-box* approach of studying just the windage effect, represented by the dashed line drawn around the system components. This approach ignores the details of what is going on inside the domain, and deals with the gross windage only. This method is most appropriate in a commercial environment; however, this thesis will also look at the individual components of pressure loss and gain in the system and attempt to link their cause and effect.

In Section 3.7, in the methodology chapter, the control gear is run at a number of mass-flow-rates, but with the same rotational speed — this was to validate the model against experimental data. Due to computational time constraints, it is not possible to do this for every single gear, but the results from the control gear provide a useful benchmark against which the response of the system can be compared when the gear is changed.

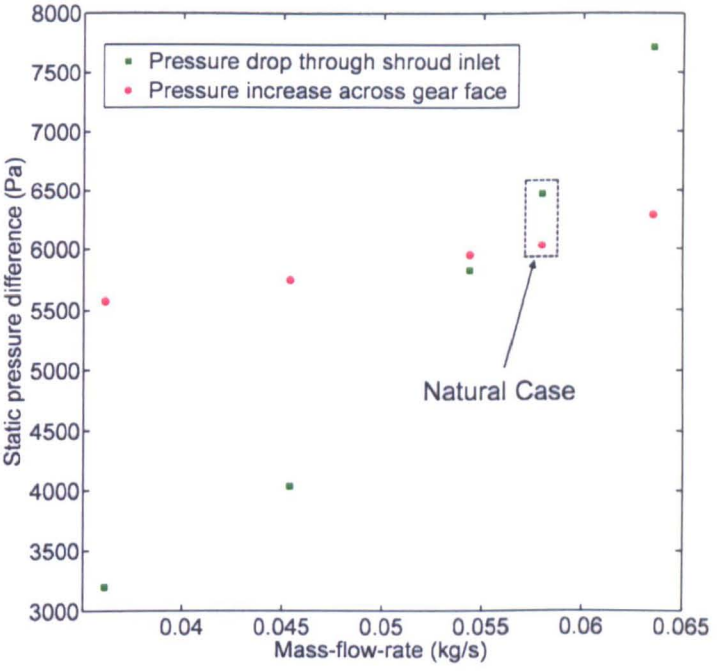

Figure 4.3: Mass-flow-rate versus static pressure drop through shroud inlet and static pressure increase across gear face for control gear

The results showed a number of things that will be relevant to the work that is covered in this chapter. Firstly, the pressure increase created by the gear is less sensitive to the mass-flow-rate through the domain than the pressure losses caused by the restrictions at the inlet and outlet of the shroud. This can be seen in Figure 4.3, which shows on the same axes, the pressure increase through the teeth of the control gear at a number of mass-flow-rates, and the corresponding pressure decrease for each case, through the inlet to the shroud[1]. The difference in gradients can be seen, and for the natural case (highlighted on the figure), the

[1]Changes in pressure as opposed to absolute value are used on the y-axis to ensure that the difference in gradients can be observed more easily

pressure losses and gains will be identical throughout the whole system — this is not quite seen in this figure as not all losses (e.g. at the shroud outlet) have been included, and the static pressure recovery as the flow is ejected into the rear chamber is also not shown. The difference between the losses and gains in the system for other cases is down to the difference between the inlet and outlet static pressures of the domain. This is representing work done by or done on the system externally. Only at the operating point is all of the work done by the gear, captured entirely by work done on the system.

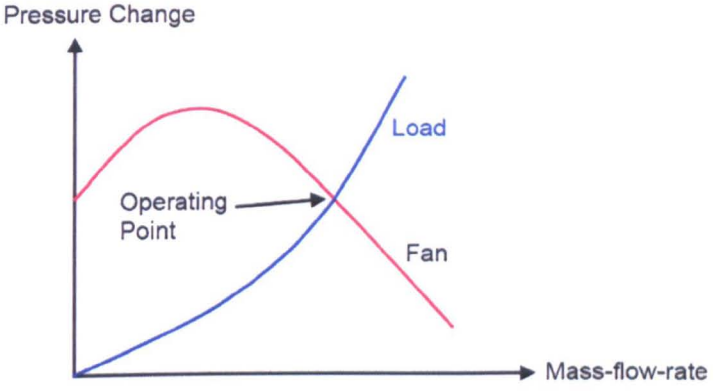

Figure 4.4: Sketch of system load and fan pressure increase with the operating point of the system marked

Figure 4.4 illustrates the operating point of a fan system. The blue line represents the pressure losses through a load, or restriction, and this can be seen to increase with mass-flow-rate. The red line represents the pressure increase that a fan can create, and in this case, has a shape that has a maximum before reducing with increasing mass-flow-rate. The point where these two lines cross is the operating point of the system as the pressures will balance throughout, and from this the mass-flow-rate that will pass through the system is identified. In other words, the work done by the fan (or gear) is entirely used to drive the flow through the restrictions in the system, and no external work is done on, or by, the system — this is the "natural" case. When a mass-flow-rate is imposed upon the system, there will be a difference between the static pressures of the load and the fan, and this represents the external work.

If one of the two parts of the system are changed, its line will shift in some way, and consequently the operating point of the system will almost certainly be different. The shallow curve of the pressure change across the gear in Figure 4.3 is typical of a backward curved (BC) centrifugal fan, to which a spiral bevel gear running in this sense has the closest physical similarity. This was seen by Johnson *et al.* [23] and provides justification to treating the gear as a centrifugal fan. By making this connection, fan theory (both design and performance) can be used to aid the analysis of the system.

The moment on the gear can be broken down into two types of losses: pressure and viscous torques. The pressure losses are the largest, and for nearly all gears tested are 4 to 5 times larger in magnitude than the viscous ones. The pressure losses predominantly come from the flanks of the gear teeth, and these are acting as the blades in our analogy to a centrifugal fan. The flanks of the teeth are the sides which transfer the torque, and are shown in Figure 3.9. Further analysis shows that the pressure torque on the teeth flanks, and the viscous torque from the gear back, and shaft account for 93.8% of the total windage on the control gear — which is a typical result for any of the gears tested, and will be explored in more detail further on within the thesis.

The results of the control gear provide an excellent comparison for the "natural" conditions of other gears as investigated in the following sections. The effect of changes made to the control gear can be observed by seeing the differences in performance of the gear/shroud system.

4.3 Outer diameter

4.3.1 Overview

The outer diameter is one of the most important variables used when choosing a gear for transmission of a large torque. As noted in the introduction to this

chapter, the inner diameter of a gear is usually restricted by the shaft on which the gear is sited. The minimum facewidth of the meshing gears is determined by the pinion, the smaller of the two meshing gears, which means that as the torque transmission requirements increase, the facewidth of both gears must increase, and this has the ultimate consequence of forcing the outer diameter of the crown gear to get larger. The crown gear is the gear that sits on the High Pressure (H.P) shaft, and the pinion is sited on the radial power off-take shaft. Both of these can be seen in Figure 1.1. New material technologies may permit the teeth to carry larger stresses, and to resonate less; however, these advances may be limited in their capacity to help in the high-speed, low-weight environment of an aero-engine.

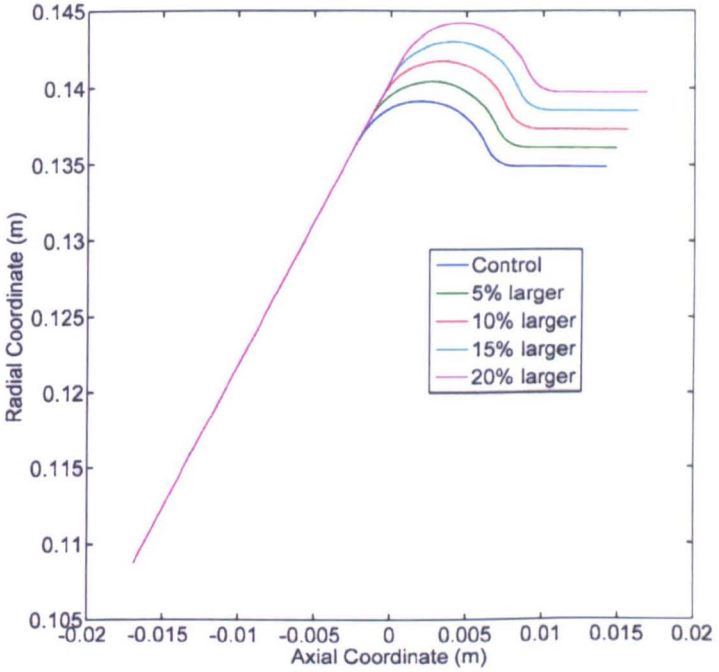

Figure 4.5: Shroud profiles of all simulations with increased facewidths radially outwards

In the work reported here, there are five gears simulated where the outer diameter is increased, including the control gear. The gears are identified by the increase in the length of their facewidth, radially outwards in 5% graduations from 5 to 20% larger than the control gear. Due to the pitch cone angle of the gear, which is 60.83°, this percentage increase does not correspond to the increase in radius

over the control gear. The profile of these gears' shrouds can be seen in Figure 4.5, which shows that the shrouds share most of their shapes, but have different lengths, and hence outer diameters. On the figure, an axial co-ordinate location of zero corresponds to the pitch circle of the control gear. The nose of the shroud is not shown, but is the same for all of the simulations.

The solid model and meshing technique allow for easy changes to the facewidth of the gear. There are two parameters which are used to control this variable, and these are the pitch diameter of the gear, and the facewidth itself. To create a gear with an identical inner diameter and increased outer diameter, the new pitch diameter and corresponding new length of the facewidth can be entered. To change the inner diameter of the gear, while keeping the outer diameter constant, the pitch diameter must be left unchanged, and only the facewidth altered — as the facewidth is measured from the pitch circle inwards.

Features such as the nose and the "gutter" at the shroud outlet are modelled automatically in Pro/Engineer as they are located in space relative to the pitch diameter and length of the facewidth of the gear, instead of having their positions described in absolute coordinates. No change in the cone angle of the gear also means that there is no change in the shape of the shroud features. The clearances between the shroud and the gear are kept identical for all of the models in line with current design policies at Rolls-Royce, and the justification for this is detailed later in Section 4.3.3.2.

The mesh is changed by adding or removing cells in the gear tooth passage, whilst keeping the mesh identical in all other locations. This is done in order to prevent cells being stretched or squashed too much and preserves the aspect ratio of cells within the gear tooth passage.

4.3.2 Windage results

This section looks at windage results and shows that the gears are all working in a similar fashion, allowing a comparison between the components in the system further on in the chapter. It is important, in addition to just looking at the "head-line" windage of the gears, to look under the surface at the structures and flow field, to make sure that by altering the gear the assumptions about the system being analogous to a centrifugal fan are still valid.

The windage moment, and mass-flow-rate though the system for all the gears tested is shown in Table 4.1. The windage is calculated as an average on all rotating surfaces of the gear (including the flat back and shaft) over five revolutions. This is detailed in Section in 3.6.1.

Gear	Windage Torque		Mass-flow-rate	
(facewith increase)	Total (Nm)	Difference (%)	kg/s	Difference (%)
Control	1.218	-	0.0579	-
5%	1.263	3.72	0.0583	0.64
10%	1.313	7.79	0.0588	1.57
15%	1.375	12.9	0.0593	2.33
20%	1.418	16.4	0.0584	0.73

Table 4.1: Windage torque and mass-flow-rate of gears with increasing outer diameter

As seen in the table, as the outer diameter of the gear increases, the windage also increases. The increase is not linear, and it can be represented as shown in Equation 4.1. The mass-flow-rates are all slightly higher than that of the control gear, however there is no particular trend.

$$\text{Windage} \propto (\text{Outer Diameter})^{4.32}. \tag{4.1}$$

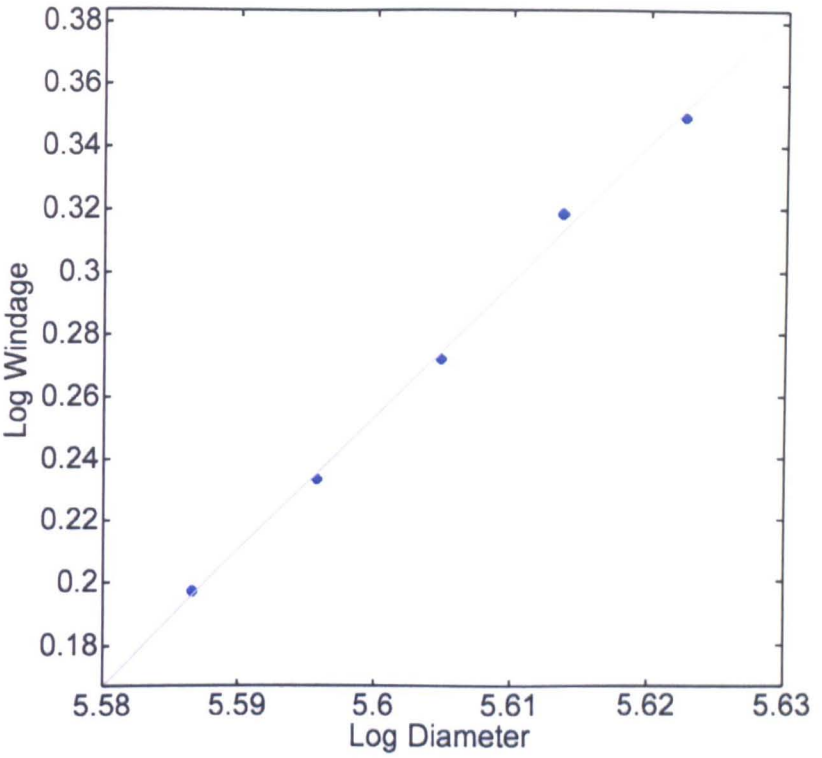

Figure 4.6: Log of windage versus log of outer diameter, with best-fit line shown

This relationship between diameter and windage fits quite closely to fan scaling theory which says that the power required by similar fans scales by the outer diameter to the power of 5 [5], and also the work of Dawson [9] who found a value of 4.7 for spur gears. Figure 4.6 shows the logarithms of outer diameter plotted against windage, and the best fit line, whose gradient is used for the scaling power. As can be seen, the fit is very close, with an R^2 coefficient of 0.997 showing the very strong positive correlation. One reason for the difference between the theoretical and computational scaling powers may be that the gears are not geometrically similar, because unlike a centrifugal fan, which draws air in from the centre (i.e. from radius = 0), the gears draw air in at a diameter of 104.5mm, and this dimension does not change, which means that the gears are not similar in shape.

Table 4.2 shows two different ratios of pressure to viscous torque. The second column is the ratio of total pressure and viscous torque – on all of the rotating surfaces. The third column is the ratio on just the flanks of the gear teeth, which

	Pressure:Viscous torque ratio	
Gear	Gear & Shafts	Gear teeth flanks only
Control	5.26	30.7
5%	5.17	31.0
10%	4.98	29.9
15%	4.51	27.4
20%	3.89	27.7

Table 4.2: Pressure to viscous torque ratio for gears & shafts, and for just gear teeth flanks

are the surfaces with the largest contribution to total windage at around 85%.

The table shows that the ratio of pressure to viscous torque on the gear reduces as it grows in outer diameter. This is due to the flat back of the gear having an increasingly larger influence upon total windage. The increase in the facewidth by 20% increases the viscous losses on the back of the gear by 126%, accounting for 8% of the total torque; however, as this part of the gear has no impact upon the flow structures between the gear and shroud, and because the shape of the gear back will be application dependent in the aero-engine, this is not an area that will be explored in this thesis. By looking at just the flanks of the gear teeth, the pressure component is by far the largest contributor to the windage, with a ratio of at least 27.7:1 for pressure and viscous moment. There is also a trend of decreasing ratio as the outer diameter of the gear increases, with the pressure being slightly less dominant.

Figure 4.7 shows the time averaged[2] static pressure on the surface of one of the tooth flanks (refer to Figure 3.9 if necessary) for the control gear and three gears with 5, 10 and 20% larger facewidths. The bottom of the figure is at the inner diameter of the teeth. The figure shows that the pressure in the tooth valley follows the exact same structure for all of gears, with a linear increase from inner

[2]Over five revolutions of the gear

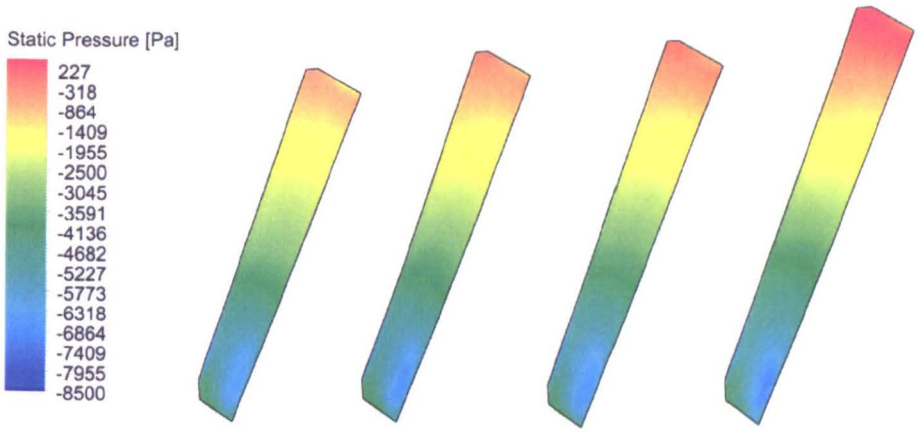

Figure 4.7: Static pressure on surface of tooth flanks of gears with increased facewidth radially outwards. (L-R) Control, 5%, 10% & 20% larger

to outer radius. The extra length of the teeth compared to the control gear allows the other cases to have higher static pressures at their outer diameters, and they continue to follow the same linear increase through the gear valley. There is a slight difference in magnitude of the lowest pressures, at the start of the gear valley, however this is due to the small difference in mass-flow-rates. The most clear similarity between the cases is that for any one location up the face of the gear, the static pressure is the same for all of the cases. This may not hold true for examples where there is a larger difference in mass-flow-rate between the cases, but gives strong credibility here that the gear teeth are all acting in the same manner when increasing the static pressure of the air.

The static pressure was chosen in this case as the time-averaged variable to demonstrate the similarity between the cases; however, any variable chosen would have shown the same trend — that the cases are near-identical up until the points where the larger diameters allow for higher pressures/velocities *etc.* to be reached.

A second aspect to look at when ensuring that the systems are acting similarly is the nature of the transient structures that are passing through the domain. Section 3.6.1 in the methodology chapter explains in detail that it is necessary to simulate the gear windage of these gears using a transient formulation that can capture the traveling eddies and structures that are in the domain. Figure 4.8 is

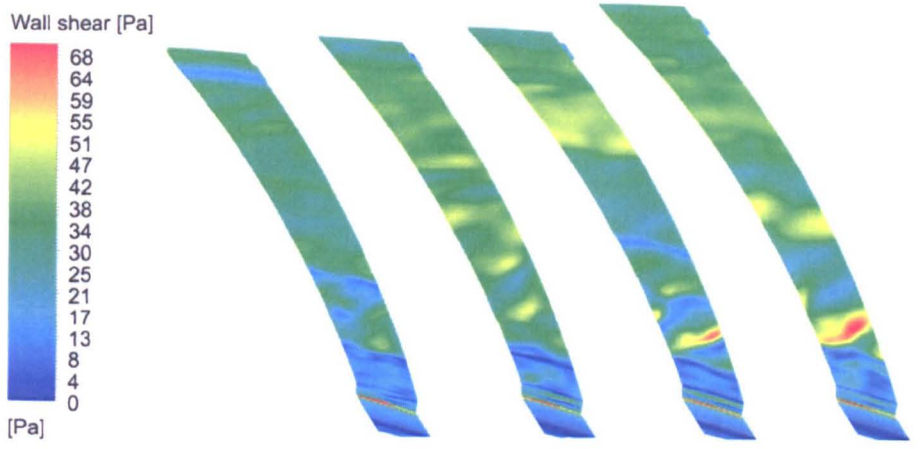

Figure 4.8: Wall shear at time = 4.8×10^{-2}s on surface of the shroud of gears with increased facewidth radially outwards. (L-R) Control, 5%, 10% & 20% larger

a snapshot at 9100 timesteps (end of 10th revolution after the simulation started) of the wall shear on the surface of the shroud. As with Figure 4.7, the control gear is on the left, and three gears with 5,10 and 20% longer facewidths go from left to right. This timestep is 4.8×10^{-2} seconds into the simulation, and by picking the same moment in time, it is unlikely that the exact same structures would be seen in the domain — mass-flow-rates and pressures are slightly different for example, which will have an impact on their formation time. What is clear from this figure is that all of the gears show similar formation of structures on the shroud; there are small regions of high shear on all of the shrouds, which correspond to eddies and vortices travelling along the surface. These areas of high shear are able to be observed as starting on the surface of the shroud at a point that corresponds to the start of the gear teeth, which is where the flow is suddenly accelerated. All of the gears here exhibit the same patterns of shedding and transient structures, for all variables investigated, meaning that they are all acting in a similar fashion when resolving the transient features, as well as the averaged quantities shown earlier.

Figure 4.9 shows the progression of transient structures across the surface of the shroud of the control gear. Similar transient structures form for all of the simulations tested in this entire thesis, but the control gear is used here as an example. Four different timesteps are chosen, with the time between each equal

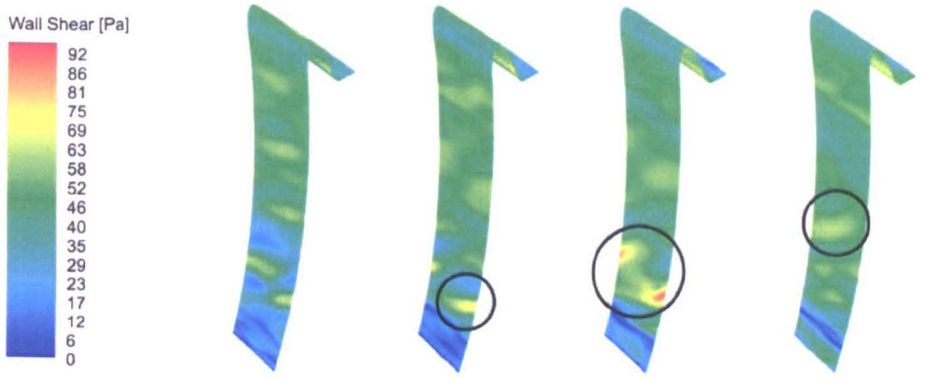

Figure 4.9: Progression of transient structures across the shroud for the control gear. Contours of wall shear, (L-R) time = 0.00962304, 0.00973044, 0.00983784, 0.00994524 seconds

to two tooth passes. One transient structure is circled, and it can be seen to both form and move up and around the shroud (because of the rotational speed of the flow), before reducing in intensity as it continues through the domain. Rapley [33] performed some FFT analysis on the frequency of the formation of the transient structures in a system like the one presented in this thesis.

4.3.3 Pressure changes in the system

The previous section has shown that the approach of looking at the spiral bevel gear as a centrifugal fan will be valid for all of the variants, and therefore this section will explore the pressure changes through the system. This approach has been used by Johnson *et al.* [23] when looking at different shrouds, and a similar approach of looking at the pressure losses through restrictive parts of the shroud and the pressure rise across the face of the gear will be used here.

Section 3.2.2 in the methodology chapter contains an explanation of the terminology of the shroud, and contains a number of figures to aid the reader. These can be consulted in conjunction with the analysis within this chapter; however, to aid the reader Figure 4.10 is a reproduction of the boundary conditions figure used within the methodology chapter, and shows the overall shape of the domain,

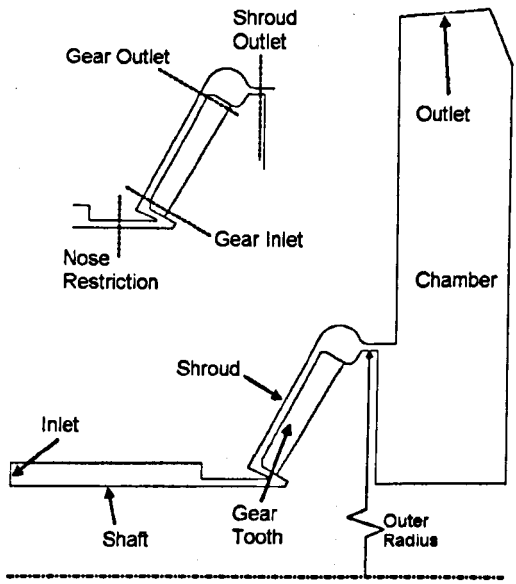

Figure 4.10: Boundary conditions, for domain, plus post-processing surfaces shown on inset

and the location of the post-processing surfaces used.

4.3.3.1 Pressure drop through shroud inlet

It has been shown repeatedly [23, 33, 50] that the restriction at the entrance to the shroud is a critical aspect when reducing gear windage. By keeping the radial gap small, there is a large pressure loss, even at low mass-flow-rates. This means that the pressure rise created by the gear is opposed by a pressure loss in the shroud which only permits a small amount of flow through the system. The consequence of this is that the gear has a smaller amount of air to pump through the domain (which also involves giving it a large component of rotational velocity), and so the effort required by the gear reduces. The exact same effect can be seen if the end of a vacuum cleaner's suction hose is covered with a hand — the motor speeds up as it suddenly is freed from the task of moving and accelerating the air that was flowing through the vacuum's fan. The pressure drop through the inlet of the shroud of the cases with a fixed inner diameter and altered outer diameter will be studied here.

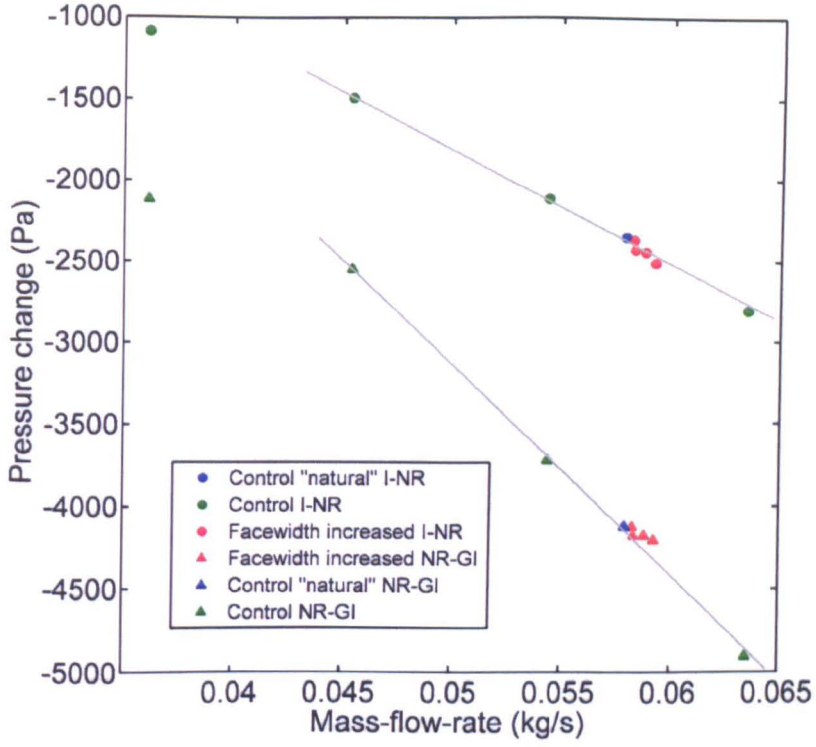

Figure 4.11: Pressure losses from Inlet (I) to Nose Restriction (NR) and NR to Gear Inlet (GI) for control gear and natural cases for increased diameter cases

The restriction of the inlet to the shroud in these simulations can be split into two seperate parts; from the Inlet (I) to the shroud Nose Restriction (NR) and then from NR to the Gear Inlet (GI). These can be seen in Figure 4.10. Figure 4.11 shows the pressure drops through these regions for the control gear and the gears with increased outer diameter. All of the gear results lie on the same line, with a linear relationship between mass-flow-rate and pressure drop, shown on the chart. This is because this part of the domain is identical in shape for all of the simulations, and would therefore respond identically to changing mass-flow-rate. The losses through this part of the shroud are explored in detail in Section 4.4.3, where changes to the inner diameter of the gears make a difference to the shape and associated pressure losses at the shroud inlet.

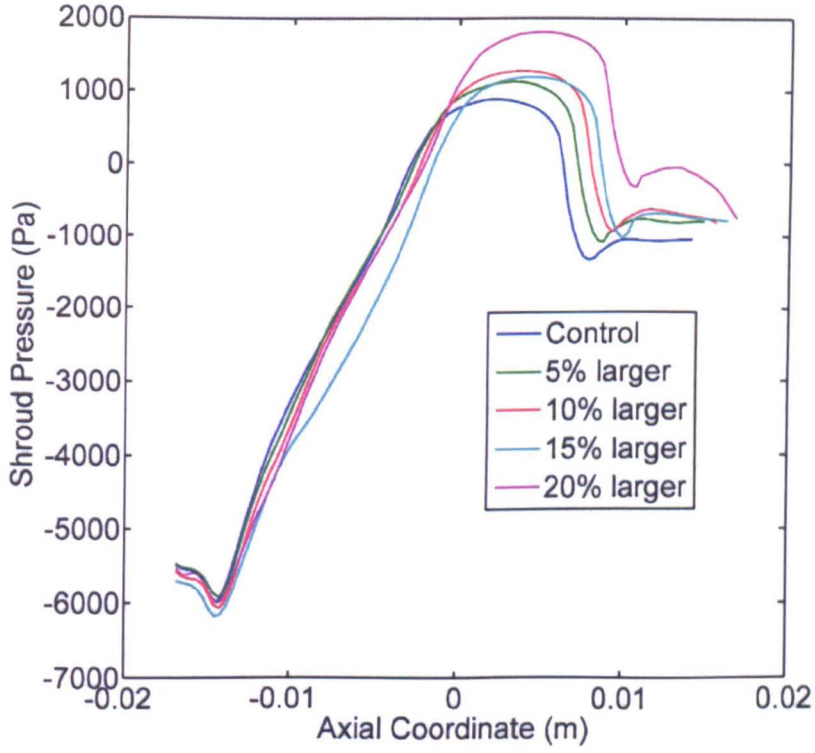

Figure 4.12: Shroud Pressure profiles for all gear variants with increased facewidth in a positive radial direction

4.3.3.2 Pressure drop through shroud outlet

Figure 4.12 shows the time-averaged pressure on the surface of the shroud for the various gears being tested in this section, which are marked on the figure. The pressure profiles have a strong similarity to the physical shape of the shroud, and the highest static pressure is reached at the outer diameter of the "gutter". This is acting in exactly the same way as the volute in a centrifugal fan, and converting the dynamic pressure of the fast moving flow ejected by the impeller (or gear in this case) into static pressure. The drop from this point to the "dip" at an axial coordinate of 0.01m is due to the flow being squeezed into the outlet of the shroud. At this point, the flow passes through the 1.5mm radial gap of the shroud outlet for around 3mm and is then ejected into the rear chamber.

Gear	Shroud outlet area	Shroud outlet pressure drop (Pa)	
(facewidth increase)	mm^2	Original	Recalculated
Control	1265	-2213	(-2213)
5%	1276	-2208	-2180
10%	1287	- 2219	-2151
15%	1299	-2215	-2115
20%	1311	-2126	-2095

Table 4.3: Annular areas and pressure drops through shroud outlet. Recalculated pressure drop is based on the mass-flow-rate of the control gear.

The static pressure drop for all of the gears at this point are nearly identical, varying from -2126Pa to -2219Pa; however in their raw form, there is slight trend that can be identified, as seen in Table 4.3, which also shows the annular area at the outlet to the shrouds and a "recalculated" pressure drop. The purpose of this recalculated pressure drop is to allow the pressure drops through the outlets to be normalised to the same mass-flow-rate (that of the control gear), which will then highlight differences between the outlets due to their difference in sizes.

$$\dot{m} = C_D A \sqrt{2\rho\Delta P}. \tag{4.2}$$

Equation 4.2 is the incompressible form of the equation that is used to represent the mass-flow-rate $\dot{m}$, through an orifice plate. C_D is a coefficient of discharge, and A is the area of the orifice (in our case we shall use the outlet area of the shroud). For any one of the gears, the area will be constant, and the discharge coeffience and area will be assumed to also remain constant. Rearranging 4.2 and capturing all of the fixed values inside a single constant, k, we arrive at,

$$\Delta P = k\dot{m}^2. \tag{4.3}$$

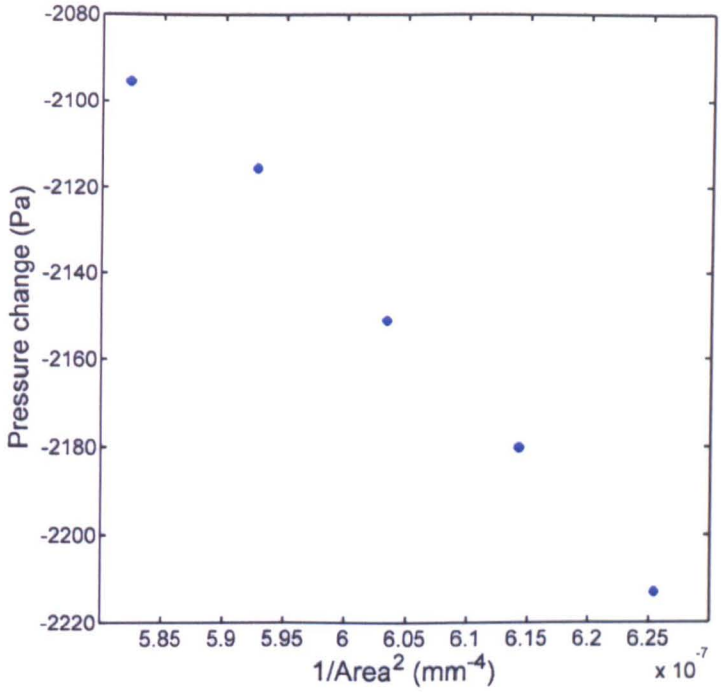

Figure 4.13: Pressure drop through the shroud outlet against inverse squared area

By calculating the k for each of the shroud outlets using the original mass-flow-rate, we can then use Equation 4.3 with the mass-flow-rate of the control gear to establish the recalculated pressure drop for each gear. This is shown in the fourth column of the table, and shows a clear trend of a smaller pressure drop as the gear gets larger. The final stage is to use these recalculated pressures to establish the effect of the area at the outlet of the shroud. Rearranging Equation 4.2 again, this time in terms of the area, A, we can show that (for a constant mass-flow-rate),

$$\Delta P \propto \frac{1}{A^2}. \tag{4.4}$$

By plotting the pressure drop against $1/A^2$, we should see a linear relationship — which is what is shown by Figure 4.13. In the figure, the pressure drop increases as the inverse of the squared area gets larger, or alternatively, as the area gets smaller. This is an interesting conclusion, as due to the radial distance between shroud and gear being fixed at 1.5mm, the annular area at the outlet will increase

with a larger outer diameter and therefore making it easier for the flow to exit the shroud. In the example of these results, this would be at least part of the reason behind the increase in windage as the outer diameter increases — the shroud restrictiveness decreases.

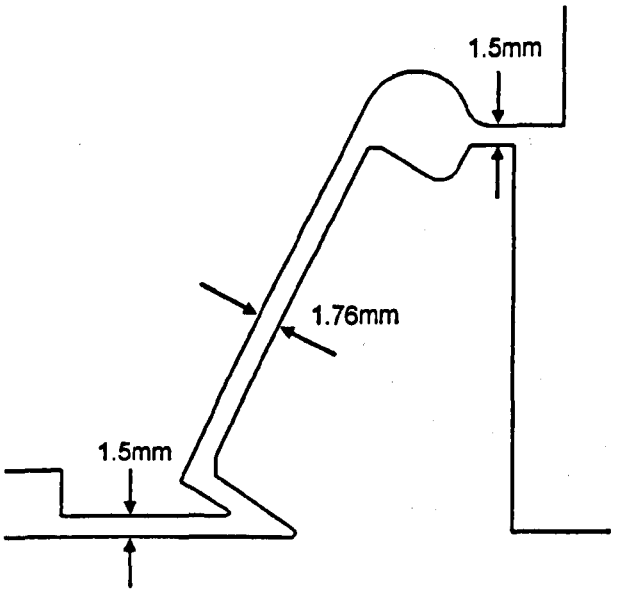

Figure 4.14: Shroud inlet, face and outlet clearances for all simulations

The decision to keep the clearance at the exit to the shroud constant for all models is based on engineering practice used in industry to ensure that centrifugal expansion of the gear spinning at high speed doesn't result in it rubbing on the shroud. This is done by keeping to an absolute minimum radial clearance of 1.5mm in these cases, as seen in Figure 4.14. In order to make sure the results in this thesis are as applicable for industry as possible, it was decided to keep the gap constant, instead of keeping the annular area constant for all the gears.

The effect of the annular area at the outlet to the shroud has been studied in the past by Rapley [33], and he concluded that although it made an appreciable reduction to the windage when it is tightened, the impact of restricting the inlet of the shroud was larger. Rapley showed that his tightest outlet of 2.52mm could reduce windage by up to 6% compared to the average of his results tested, but as all of his outlets were significantly larger than the 1.5mm being used in this chapter, it is difficult to say conclusively that the same results would apply in

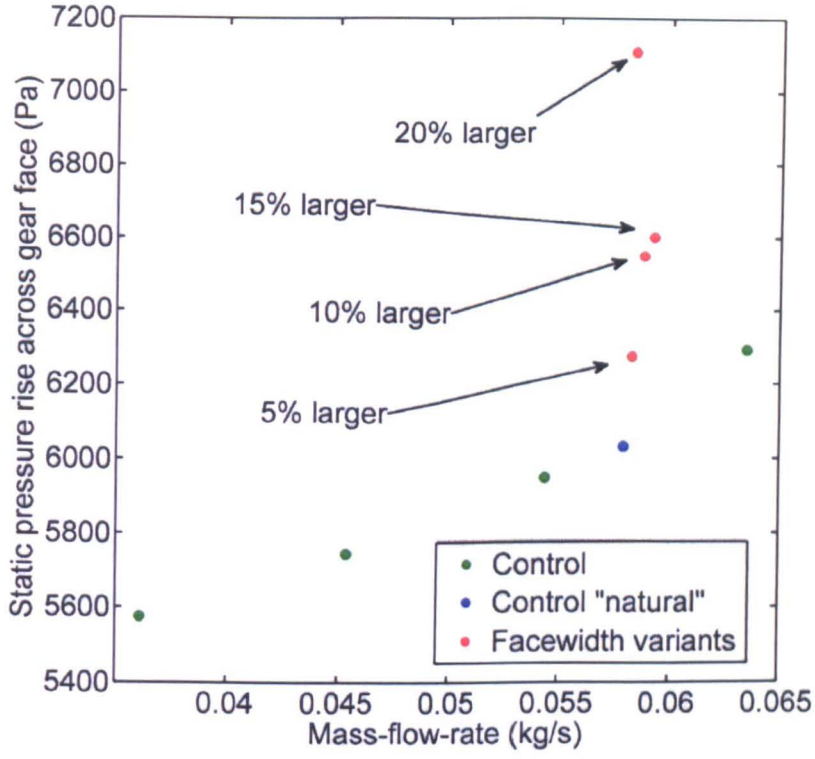

Figure 4.15: Static pressure rise across gear against mass-flow-rate through the system for the control gear and the gears with increased facewidths radially outwards

these cases. A study looking at the effect of the shape of the outlet is conducted in Section 5.3. Rapley's work was conducted using only air, and although his conclusions were valid in this context, it is likely that the presence of oil between gear and shroud would be mitigated if the outlet is able to vent the oil away swiftly, as seen by Winfree [50]. This will also be discussed in Chapters 5 and 6.

4.3.4 Static pressure rise across face of the gear

If a graph of static pressure rise across the face of the gear is plotted against the mass-flow-rate through the system, it is possible to see the deviation from the straight line of the control gear that the gears with increased outer diameter have. This is shown in Figure 4.15, which includes the results for the control gear at varying mass-flow-rates, with the "natural" case marked in blue. The small gradient of pressure rise across the control gear against mass-flow-rate matches

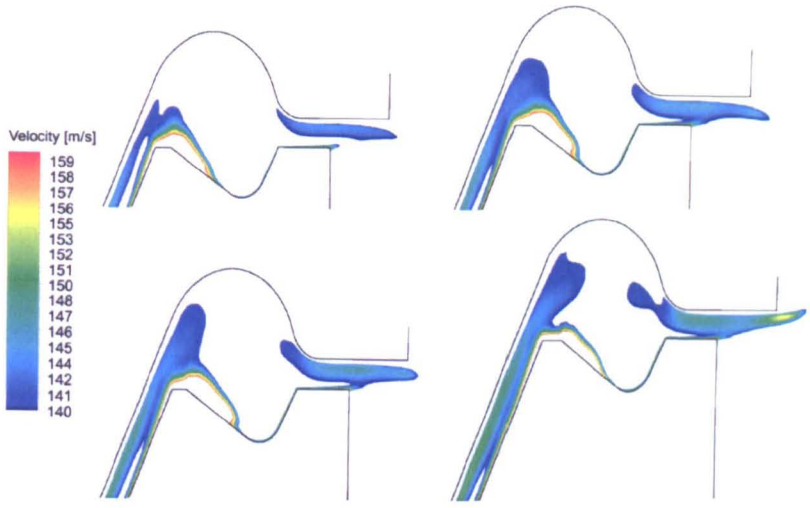

Figure 4.16: Contours of velocity at shroud outlet for gears with increased outer diameters. Clockwise from top left: Control, 5%, 20% 10% longer facewidth

well with the findings of Johnson *et al.* [23]. There is some minor deviation in the mass-flow-rates of the increased diameter gears, but the trend is that as the facewidth increases, the static pressure rise across the face of the gear increases, but the mass-flow-rate remains fairly constant in these cases. The larger pressure rise across the gear is the indication that there is more work being done by the gear on the air, which is consequently why the windage is larger.

It is well known, through fan scaling laws, that the power required to drive a centrifugal fan scales with the diameter to the power of five [5]. This is due to the increase in velocity that a larger outer diameter needs to impart to the flow. This increase in kinetic energy scales with the velocity squared, which, since the velocity scales linearly with the diameter results in the large dependence upon the outer diameter of the gear. The increase in velocity at the outer diameter can be seen in Figure 4.16, which shows clockwise from top left, the control gear and gears with 5, 20 & 20% longer facewidths. The contours of velocity are clipped between 140 and 160 m/s to emphasise the differences between the cases. There is a trend of increased velocity as the outer diameter increases, which since the mass-flow-rates are very similar, is due to the rotational component of the velocity. This increased velocity causes the gear to do more work on the air, and consequently this manifests itself as a higher windage power loss.

4.3.5 Conclusions

This section has shown that the outer diameter has a large impact upon the single phase gear windage. The first section showed that the gears were all acting in the same manner, with both time-averaged and instantaneous visualisations showing similar flow structures and patterns. Analysis of the static pressure drop through the inlet showed that the losses through this part of the system were linear with increasing mass-flow-rate, which due to the the identical geometry at this location is not a surprise. The annular area at the outlet of the shroud scales with increasing outer diameter, and consequently, the pressure drop at a comparable mass-flow-rate is smaller. Studying the effect of the increased outer diameter of the gear has shown that the additional face length creates a larger pressure rise when compared to the control gear, and this is due to larger component of tangential velocity at the increased outer diameter.

As seen in the findings above, changing the gear can have an impact upon the shroud geometry in such a way that the pressure restriction of the system is affected. This is an important conclusion, because it means that if the system is modelled as a one-dimensional series of losses in order to estimate mass-flow-rates and windage losses, as seen in the top half of Figure 4.2, it is not possible to change one part of the model without being sure that it will not affect other parts of the system. For the examples seen in this section, the outer diameter affects the restriction at the outlet to the shroud; however, the next section will show that changing the inner diameter of the gear affects the restriction at the inlet to the shroud, at its nose. This part of the system has the greatest losses, compared to the outlet — so its impact upon the windage results is also larger.

4.4 Inner diameter

4.4.1 Overview

The inner diameter of a gear is usually constrained by the shaft on which it is fixed, which for the IGB of a Rolls-Royce Trent series engine is the high pressure (H.P.) shaft. This shaft has the largest diameter in the engine as it rotates around the low- and intermediate-pressure shafts. As a consequence, transmission designers have limited scope for changing this part of the gear. Nevertheless, the use of CFD allows an investigation into the effect upon windage of changing this part of the gear, which may inform designers in the future.

Four gears with an altered inner diameter were tested, two with a smaller inner diameter, and two with a larger inner diameter, when compared to the control gear. The gears are identified by the alteration to the length of their facewidths, in the same manner as the gears which had their outer diameters changed. The manner in which the changes are implemented using the solid model is explained in the overview section of the outer diameter, Section 4.3.1.

4.4.2 Windage results

The windage losses for all these simulations, along with the mass-flow-rates through the system are shown in Table 4.4.

As seen in the table, the trends are less obvious than those for with a changed outer diameter. Of all the results, only the gear with a facewidth which is 20% smaller shows a clear deviation away from the result of the control gear. Also shown in the table are the mass-flow-rates through the domain for all the simulations. Unlike the previous set of results (for the gears with increased outer diameters) there is a significant amount of deviation between all the cases here, which means that it is not possible to directly compare the pressure losses and gains through various parts of the systems. Computational constraints mean

	Windage		Mass-flow-rate	
Gear facewidth	Total (Nm)	Difference (%)	Total (kg/s)	Difference (%)
Control	1.218	-	0.0579	-
10% smaller	1.222	0.34%	0.0565	-2.52%
20% smaller	1.143	-6.16%	0.0520	-10.24%
20% larger	1.211	-0.57%	0.0542	-6.49%
40% larger	1.206	-0.97%	0.0504	-13.08%

Table 4.4: Windage losses and mass-flow-rates for all gears with the inner diameter altered

that a full system characterisation for each gear has not been conducted. However, the "natural" conditions used for these simulations most closely reflect the conditions used in the experimentation of Johnson *et al.* [23], and this approach was shown to be valid in that work.

It is clear from these results that changing the inner diameter of the gear does not have as large an effect upon windage as changing the outer diameter. In those cases, as seen in Section 4.3.2, a change of 20% in facewidth length outwards increased windage by 16.4%, something which is not seen in these cases for a change of similar magnitude at the inner diameter. However, much like those simulations, there is a deviation away from the control gear's windage response when the mass-flow-rate is varied.

Table 4.5 breaks down the windage moment on just the teeth of the gears into pressure and viscous components. This removes the influence of the gear back and the shafts, which provide much of the viscous contribution. It can be seen that there is a trend of increasing viscous moment with increasing facewidth length, even with the differences in mass-flow-rate between the cases. The trend for the pressure moment is not clear; all the cases have a lower value than the control gear, ranging from less than 1% to just over 8.5%.

	Pressure Moment		Viscous Moment	
Gear facewidth	(Nm)	Difference (%)	Nm	Difference (%)
Control	1.023	-	0.045	-
10% smaller	1.017	-0.66%	0.042	-5.81%
20% smaller	0.936	-8.52%	0.043	-5.90%
20% larger	0.990	-3.23%	0.050	12.6%
40% larger	0.954	-6.80%	0.070	56.0%

Table 4.5: Windage losses for gear teeth only, broken down by contribution for all gears with the inner diameter altered

Figure 4.17 shows a plot of mass-flow-rate versus torque for the control gear (with the "natural" condition marked), and the gears with their inner diameters changed. The individual gears are identified by the change to the length in their facewidth compared to the control gear, in order to highlight their deviation from the control gear's curve. It can be seen that the gears that have had their inner diameters changed by the most, lie furthest from the control gear, with the gear that has a facewidth 40% larger inwards (and hence a smaller inner diameter) showing around 0.05Nm more torque than the control gear has at a comparable mass-flow-rate. There is some scatter in the data, with the gear that has 20% shorter facewidth (and hence a larger inner diameter) lying near or on the control gear's curve, but typically the larger the difference in geometric change, the further from the line the points lie. This shows that the system is changing with the alterations to the size of the gear.

When inspecting the time-averaged static pressure on the surface of the gears in Figure 4.18, it can be seen that there is a linear increase along the length of the face. This was also the case for the gears with increased outer diameters (Figure 4.7), but in those cases as explained in Section 4.3.2, the difference between them was the larger outer diameter created a larger static pressure increase. These cases all have similar magnitudes of pressure increase across the lengths of the gear teeth — there is some difference, at the ends, but this will likely be

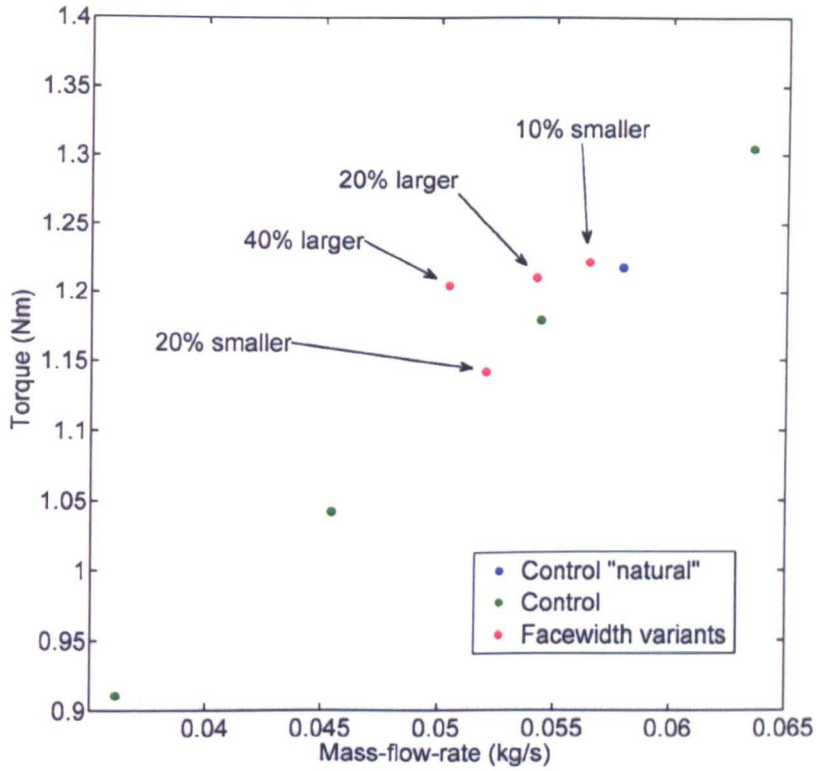

Figure 4.17: Mass-flow-rate versus torque for the control gear (red & blue for "natural" case) and gears with varying inner diameter, identified by change in facewidth length

due to time-averaged recirculations in these areas. The gear with a facewidth reduced by 10% is not shown in the figure as its result is very similar to the control gear and the gear with -20% facewidth length. The difference between the pressure rises caused by the gears will be addressed later in Section 4.4.4. Transient structures, along with other averaged quantities follow similar patterns in all cases, so the changes to the shape of the gear have not altered the way the system works, in the same way as shown in Section 4.3.2 for changes to the gear's outer diameter.

The next couple of sections will look at the pressure losses and rises through the domains of the simulations and will explore their interactions with geometric changes, because unlike the gears with an altered outer diameter, the changes made to the inner diameter affect the restrictive nature of the inlet to the shroud, which has been shown to be critical in reducing single phase windage [23, 33].

Figure 4.18: Static pressure on gear tooth flank of gears with altered inner diameters, (L-R) Control gear, -20% +20% & +40% facewidth change

4.4.3 Static pressure loss through shroud inlet

Figure 4.19 shows the pressure drop from the inlet of the domain to the shroud nose restriction. The control gear's response over a series of mass-flow-rates is shown, so that the results of the other simulations can be compared to it, as was done for the outer diameter.

This part of the shroud takes the shape of a sudden contraction of annular flow, matching the geometry of the experimental rig used by Johnson *et al.* [23], but is not found in this form in an aero-engine internal gearbox; however, as seen in Chapter 5, similar losses are found with more engine representative geometries. The radial clearance between the shaft and the shroud is fixed at 1.5mm for all cases. The logic for this at the outlet to the shroud was covered in Section 4.3.3.2, and is the same here at the inlet. This means that the annular area at the shroud's nose is not the same for each case, with it decreasing as the inner diameter is reduced. The outcome of this is the flow is contracted into a smaller area, with higher losses when the facewidth is increased.

Referring to Figure 4.19, this effect can be seen by observing the deviation of the variants away from the control gear's curve. It is reasonable given the geometric closeness between all of the simulations to assume that the inlet pressure drop curves for all gears would follow a similar trend to that of the control system - with increasing pressure drop for increasing mass-flow-rate. Therefore, for a

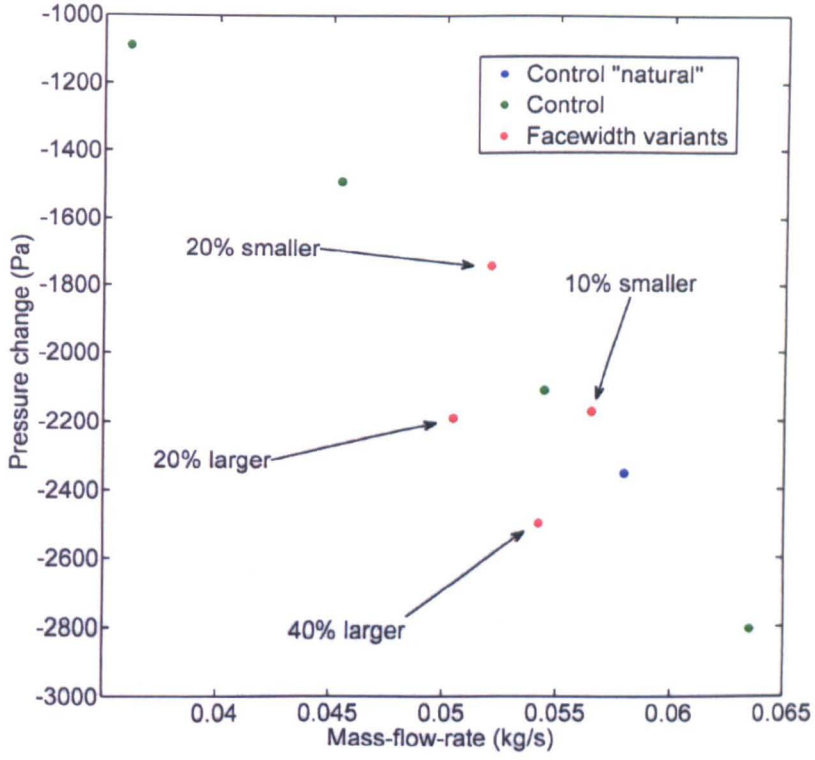

Figure 4.19: Static pressure change from domain inlet to the nose restriction of the shroud. Control gear marked in red and blue for the "natural" case. Gears with inner diameters altered are shown identified by the change to their facewidth relative to the control gear

given mass-flow-rate, a gear whose inlet creates a larger pressure drop than the control's will have a curve that lies below the control's, and vice versa. In Figure 4.19, the results for the gears with an increased inner diameter both lie above the control gear, although due to the relatively small changes in their facewidths, they are not too far away. The larger change made to the simulations with decreased inner diameters can be seen by their larger deviations from the control gear's curve, which they both lie below.

Conventional sudden-contraction theory shows that the gears with a larger inner diameter (and hence larger annular area) would have a smaller pressure loss than those with a smaller inner diameter (and hence smaller annular area). The sharp edged contraction can be observed in Figure 4.20, which shows for the control gear, contours of time-averaged static pressure when viewed from a tangential

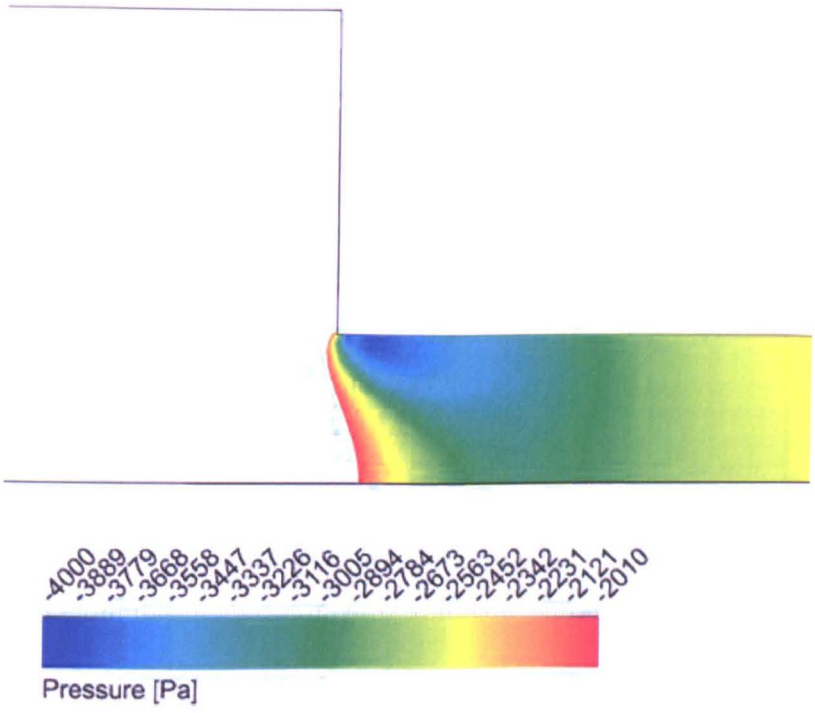

Figure 4.20: Static pressure at the entrance to the nose restriction

direction. Only the area around the contraction is shown for clarity, and the area of low pressure on the top (outer diameter) can be observed in blue. This corresponds to an area of relatively stagnant flow which restricts the area through which the axial flow can travel, even further than the physical walls of the shroud do.

The effect of the inlet contraction is studied in further detail in Section 5.2 in Chapter 5. It will be shown that the sharp edges of the sudden contraction force the flow through a vena contracta with a coefficient of discharge very close to the 0.64 value used for sharp edged orifices. Therefore, the conclusion that can be drawn from this, using orifice theory is that the pressure loss (and hence restriction to the flow) at the shroud inlet will be larger when the inlet area is smaller, which happens when the inner diameter is reduced for a fixed radial clearance between shaft and shroud. This matches well with the findings of Rapley [33] who performed a parametric study looking at the impact of changing the shroud inlet clearance for a fixed inner diameter.

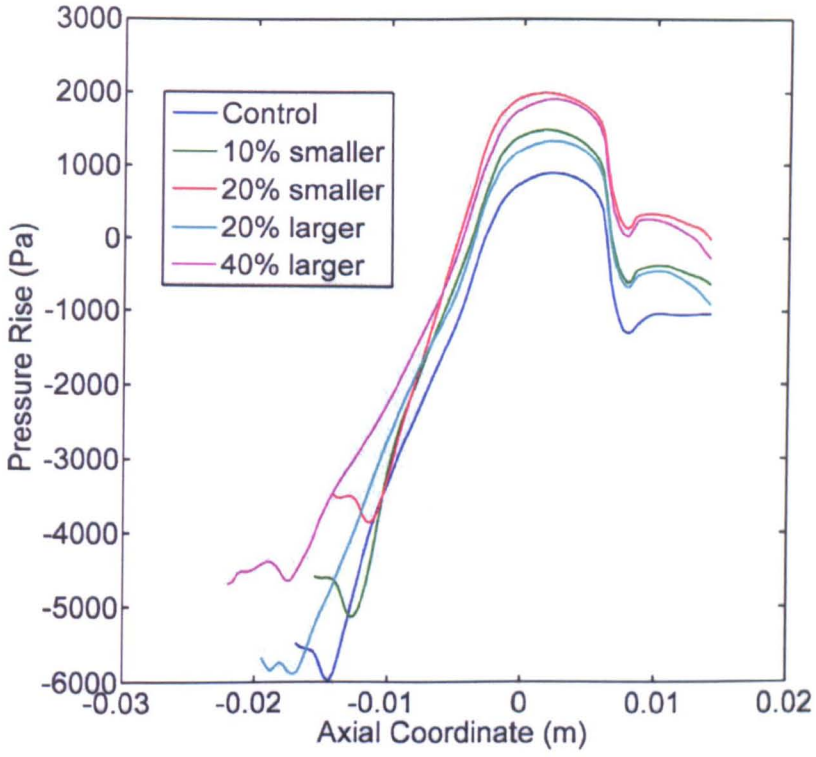

Figure 4.21: Static pressure on surface of shroud for all gears with inner diameter altered. Gears are identified by the change to facewidth length

4.4.4 Pressure rise across face of the gear

The pressure rises across the faces of all the gears follow very similar shapes to each other. Figure 4.21 shows the static pressure on the surfaces of the shrouds, after the nose. For all of the gears shown, an axial coordinate of zero meters corresponds to the location of the pitch circle.

There are a number of features of the figure which highlight differences between the gears. One of these is the small dip in static pressure near the beginning of the pressure curves, which is due to the static pressure losses caused by the flow passing by the start of the gear teeth, at the entrance to the tooth valley. In this region the flow reaches the entrance to the gear teeth with a small amount of swirl imparted to it by the shaft. It is then rapidly accelerated by the rotating gear, which produces the large static pressure loss. Differences in the behavior of the static pressure on the right-hand-side are due to differences in the mass-flow-rate

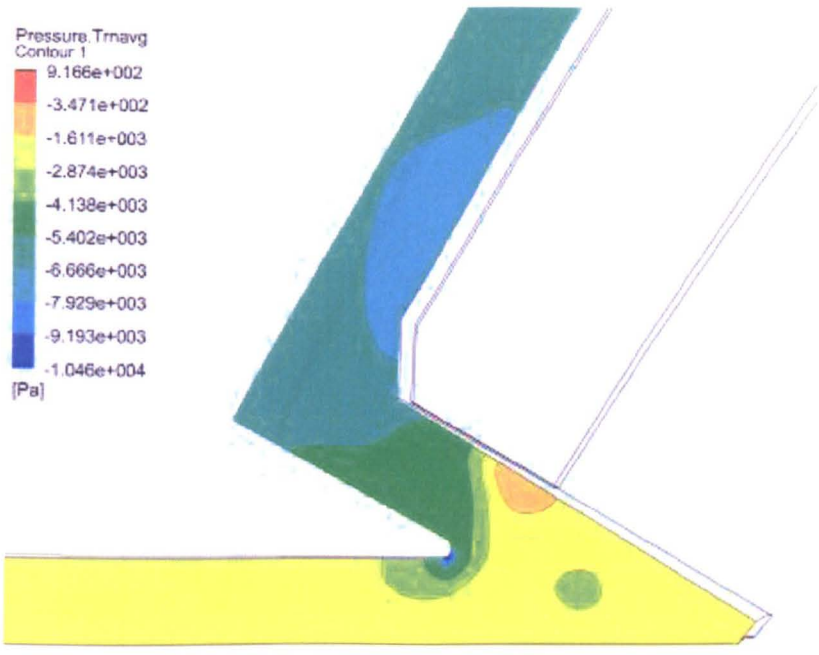

Figure 4.22: Contours of static pressure on periodic boundary of control gear

through the system, and can be observed in Figure 4.23 further on.

Figure 4.22 shows the static pressure of the flow field on one of the periodic boundaries of the control gear. This boundary passes through the centre of the topland of the tooth. The figure shows the pressure drop in the region between the tooth and the shroud, just after the point where the flow passes the entrance to the tooth valley. This pressure drop has only a very limited sensitivity to the mass-flow-rate through the system, as seen in Figure 4.23, where the control gear has "dips" in its static pressures that are weakly correlated with the mass-flow-rate. When compared to the larger difference seen for the change to inner diameter, this can be discounted as having an impact.

The conclusion that can be drawn from this is that the size of these dips is related to the change in the gear geometry, as opposed to the difference in mass-flow-rates. If Figure 4.21 is looked at in detail, it can be observed that the general trend is that the size of the dips increases as the facewidth is shortened, i.e. the gear inner diameter is increased. The sizes of the drops can certainly be grouped into smallest (gears with longer facewidth and smaller inner diameter)

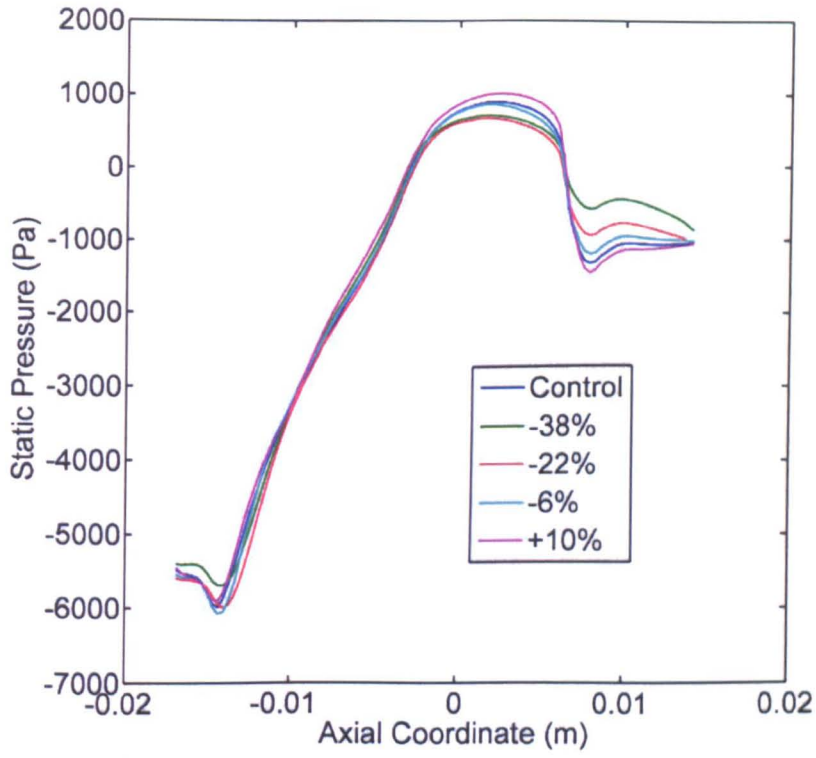

Figure 4.23: Static pressure on the surface of the shroud of the control gear at a variety of mass-flow-rates, identified by the percentage difference in mass-flow-rate from the control gear "natural" condition

and largest (gears with shorter facewidth and larger inner diameter), with the control gear sitting in between the two groups. This difference in behaviour is due to the tangential speed of the gear at the inner diameter being only related to the inner diameter, as all of the simulations are tested at the same rotational speed (12,266rpm). For a smaller inner diameter, the tangential speed will be smaller, and vice versa, with the difference in tangential velocity at the entrance to the gear tooth valley being 18.8 m/s for the largest and smallest inner diameters, which is a 15.5% difference. The impact of this upon the gear and shroud design is that areas of low pressure indicate a rapid acceleration of the flow, and this can be used by shroud designers to identify areas that may result in oil entrainment.

An interesting observation that can be made about the pressure rise across the gear face is that its gradient, seen in Figure 4.21, is dependent upon the geometry of the gear and shroud combination at the inlet. For the gears with

a shorter facewidth, there is a higher gradient, and vice-versa for those with a longer facewidth. This cannot be attributed to the differences in mass-flow-rate either, as Figure 4.23 shows that the mass-flow-rate has no impact upon the gradient. This result can be explained by generalising the system as an inlet to the shroud where the velocity of the flow is very low (around 20 m/s, and axially dominant) and an exit where the flow is rotationally dominant, and due to the identical outer diameters and rotational speeds, approximately the same at 140 m/s. Consequently, all gears have accelerated the flow from similar low speeds to similar high speeds. The gears with a shorter facewidth need to do this over a shorter distance, so will have a larger gradient of static pressure, and the opposite is true for those gears with a longer facewidth. This leads to an interesting conclusion that pre-swirling the flow would reduce the work that has to be done by the gear, and this is addressed further on in Section 5.3 in Chapter 5. This conclusion also sheds some light on the reason for why the gear with -20% facewidth length has a higher mass-flow-rate through its system than the gear with +40% length, yet it has a lower pressure component of windage. The -20% length gear has a higher amount of swirl at the nose of the gear, with an average of 28m/s, compared to 24m/s for the gear with +40% facewidth. This is due to their differences in inner diameter — their shafts will have different tangential velocities, which cause the difference in swirling of the flow. The smaller gear effectively has to do less work on the flow to get it up to the 140m/s tangential velocity at the outlet to the gear. Therefore, it could be suggested that preswirling with the shaft is an "efficient" way of reducing windage — even when the viscous component of moment of the shaft is included in the total system windage. Future work for engine geometries could therefore look at methods of pre-swirling the flow before it reaches the gear in an effort to reduce total power losses in the gearbox.

Figure 4.24 shows contours of velocity magnitude on the periodic boundary of four gears, which illustrates this point. The gear in the bottom right of the figure has a larger outer diameter than the others, as its facewidth has been increased by 20% radially outwards and was used in Section 4.3 earlier in this chapter. The

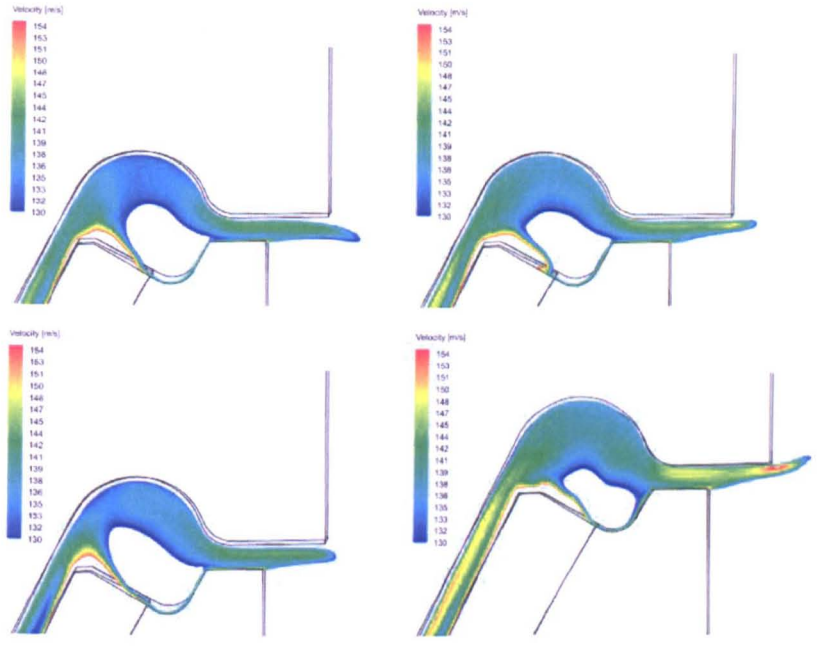

Figure 4.24: Contours of velocity at shroud outlet. Clockwise from top left: Control gear; Facewidth increased 20% at inner diameter; Facewidth increased 20% at outer diameter; Facewidth reduced 20% at inner diameter

other three gears are the control gear, and two gears with facewidths 20% longer or shorter at the inner diameter of the gear. For all of these three gears the flow at the outlet to the shroud, where it is most restrictive, is travelling at around 140m/s, whereas for the gear with the larger outer diameter has flow which is travelling around 10m/s faster.

4.4.5 Conclusions

The conclusion that can be drawn from this is that the length of the facewidth will have a fairly negligable impact upon windage torque when the outer diameter is constrained to a fixed value. It has been seen that the difference in pre-swirling the flow with the shaft, before the air reaches the gear, can reduce the windage by reducing the amount of work that the gear itself needs to do on the air. This has led to the conclusion that overall windage may be reduced if the balance of swirling is biased towards the shaft, rather than the gear. The differences

in mass-flow-rate, and deviation from the control gear's characteristic curves is caused primarily by changes to the restrictive nature of the shroud inlet, caused by changes to the inner diameter of the gear. It would seem from the results presented in this section that the length of the facewidth itself is less important than the shroud inlet design, which has been repeatedly shown to be of critical importance[23, 33, 50] to reducing single phase windage.

4.5 Module

4.5.1 Overview

The module controls the number of teeth that a gear of a certain pitch diameter has. It can be interpreted as the "amount of pitch diameter per tooth", represented as,

$$\text{Module} = \text{Pitch diameter/Number of teeth.} \tag{4.5}$$

Module is measured in mm, and one of the requirements for two gears to be able to mesh is for them to share an identical module. Module is a uniquely metric measure of comparing gears, with the preferred imperial method being *circular pitch*, which is just the module multiplied by π, and represents the length along the pitch circle between corresponding flanks of neighbouring teeth.

The maximum load rating of a gear is dependent upon many geometric features of the gear, and the properties of the materials from which is it formed. The design of the gear teeth, such as undercutting the tooth[3] at its base, also play a role in limiting the maximum bending stress that tooth can endure. There are a number of correlations which can be used for estimation of the maximum load that a gear tooth can be placed under, and some of these can be found

[3]Undercutting is where the tooth is thinned at its base to allow clearance for the tip of a meshing gear's tooth

within literature such as in [40], along with more modern approaches such as computational finite element analysis of the stresses within a gear tooth [16]. In the most basic form, a tooth can be thought of as a cantilevered beam, with an oblique load being applied. The maximum bending stress is related to the width of the teeth, hence an easy way of increasing the maximum load that a gear can take is to use a smaller number of larger teeth. This is the approach taken within the aero-space industry where the use of gears with a larger number of teeth also reduces "shock loading", which is where the gear and the lubricants on the oil are submitted to very high loads and pressures, which can squeeze the lubricant out from the the meshing teeth, leading to increased wear rates and early failure.

The consequence of these factors is that the importance of being able to transmit the mechanical torque without short or long-term gear failure may be higher than the desire to reduce windage through changing the number of teeth on a gear. This section will investigate the implications upon windage, in cases where a designer has a degree of freedom of this variable.

For a pair of gears with identical pitch diameters, if one of the pair has a smaller number of teeth, those teeth will be larger than on the other gear. The width of the teeth on the pitch circle can be larger as there is more space available per tooth, and consequently, the teeth can be made taller without fear of them breaking while meshing. The computational model reflects these physical changes, and not only makes the smaller number of teeth wider, but also taller. This is done using relationships found within literature [40] and maintains the ratio in heights between the addendum and dedendum. These are the distances from the pitch circle to the top of the tooth, and the bottom of the tooth respectively. The addendum will always be smaller than the dedendum, as the additional clearance permits the rotating tooth to avoid striking the tooth valley.

These changes are based upon sound gear theory; however, there is always the possibility that a physical spiral bevel gear would be created with a slightly different tooth height from that calculated within this thesis. This could be due to new materials which can be used for a gear, or alternative manufacturing pro-

cesses. However, any differences would be small, and therefore the assumptions that have been made can be considered to be valid for the results presented in this section.

4.5.2 Windage results

	Whole gear windage		Per tooth windage	
Number of teeth	(Nm)	Difference (%)	($\times 10^{-2}$ Nm)	Difference (%)
80	1.303	+7.00	1.629	+21.71
85	1.265	+3.85	1.488	+11.18
91 (Control)	1.218	-	1.338	-
100	1.145	-5.97	1.115	-14.43
110	1.052	-13.63	0.956	-28.55

Table 4.6: Windage losses for all gears with the module changed

Table 4.6 shows results from changing the number of teeth on the gear. The results are broken down into two parts: firstly, the results for the whole gear are shown, and secondly the windage per tooth is given. The trend for both of these measures is that the windage reduces when a gear has a larger number of teeth. Figure 4.25 shows the total windage for each gear plotted against the number of teeth. It shows that there is a linear relationship between the two variables, with R^2 of the linear trend line being equal to 0.998, a very strong correlation. It should be stressed that this linear relationship may only apply over small ranges of teeth numbers; however, the numbers of teeth tested are representative of the range likely to be used for a gas turbine IGB crown gear.

Using the gear with 110 teeth as an example, the windage per tooth is 28.55% less than the control gear; however, due to it having 21% more teeth, the effect is total windage that is only 16.62% lower, as seen in Table 4.6. The conclusion that can be drawn from this is that windage can be reduced by using a gear with a larger number of teeth — this is effectively due to the gear tending towards a smooth

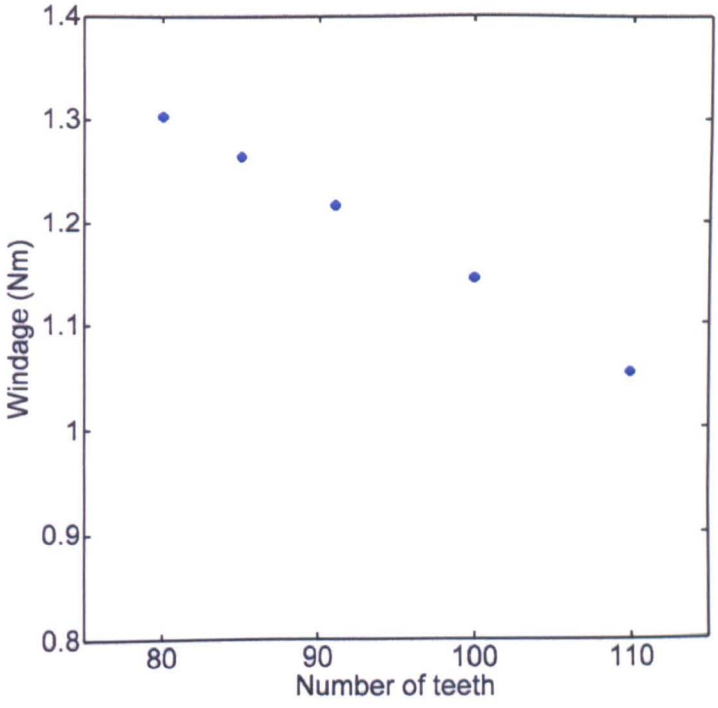

Figure 4.25: Windage of gears with varying numbers of teeth

cone, with smaller teeth. A gear designer would generally be constrained by the mechanical torque transmission requirements of the gear, but where possible, the maximum number of permissible teeth to safely carry a load would reduce single phase windage.

	Moment Totals			
Teeth	Pressure (Nm)	Viscous (Nm)	Ratio	Shaft & Gear back
80	1.251	0.234	5.41	0.141
85	1.140	0.214	5.32	0.135
91 (Control)	1.023	0.195	5.26	0.119
100	0.857	0.185	4.64	0.108
110	0.686	0.184	3.73	0.096

Table 4.7: Pressure and viscous moments for the gears with varying modules

The ratio of viscous to pressure windage losses changes heavily with the number of teeth of the gear. Table 4.7 shows a breakdown of the moment on the gears,

along with the pressure to viscous moment ratio. The viscous losses are less sensitive to the amount of teeth; the 80 toothed gear has viscous losses that are 26% higher than that of the 110 tooth gear, and this due to the teeth being larger (with a greater surface area) and the mass-flow-rate through the gear tooth valley being greater. This can be contrasted to the pressure losses which are 82% higher for the 80 tooth gear than for one with 110 teeth, which as detailed in Section 4.2 are predominantly due to the flanks of the teeth. The final column in the table is the total windage due to the shaft and back of the gear, which are identical in size for all of the simulations. It can be seen that there is a trend of increasing moment with decreasing number of teeth, which is due to the larger mass-flow-rates. The moment on these surfaces is 46% higher for the 80 tooth gear than the 110, and the mass-flow-rate is 22% higher, which indicates that although the contribution to the total moment isn't particularly significant, it does scale heavily with the mass-flow-rate.

4.5.3 Static pressure loss through shroud inlet

Figure 4.26 shows the static pressure loss through the inlet of the shroud for all the cases with varying numbers of teeth, and the control gear's results at varying mass-flow-rates. There is a clear deviation from the control gear's curve with all of the gears (which are all in "natural" condition) having a similar static pressure drop to the control gear's natural condition, even at mass-flow-rates that for the control gear would greatly alter the static pressure loss.

The reason for this is that the change in the gear has altered the loss profile at the inlet to the shroud — most notably at the entrance to the teeth. When compared to the control gear's curve, the gears with a smaller number of teeth have a smaller pressure drop, and vice versa. The 80 tooth model has an entrance to the gear valley that is 21% larger than the 100 toothed gear. This increased area will be less restrictive for the air that is passing through the system, and consequently the static pressure drop will be less. This is an example of a change in the gear affecting the losses in the system to a large degree, and this will affect

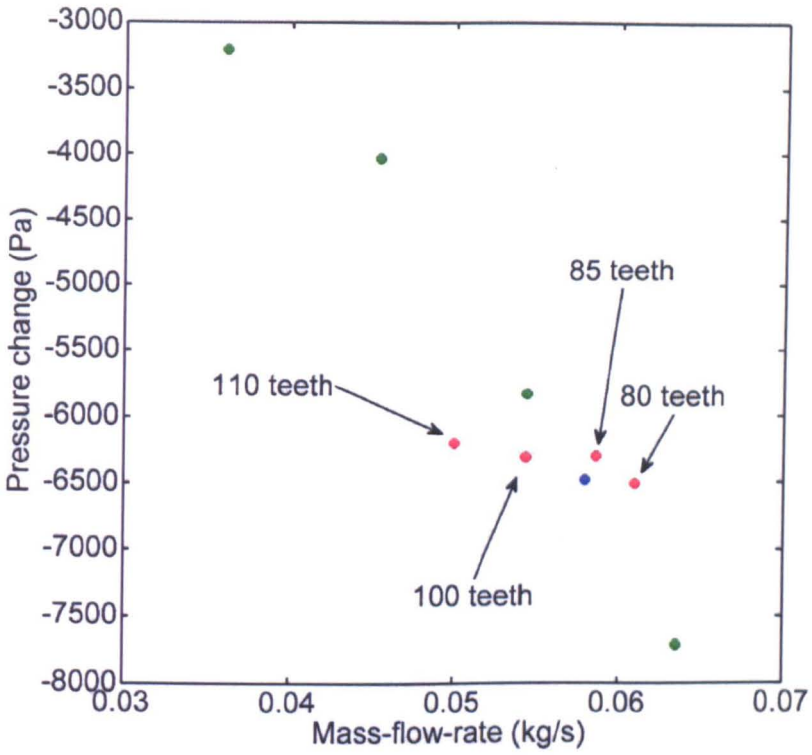

Figure 4.26: Static pressure losses from domain inlet to gear tooth valley for cases with varying numbers of teeth

the ability of the gear to draw air through the system, which incurs an energy cost, thereby contributing to windage.

A conclusion that can be drawn from this is that it is important to consider the pressure losses for the whole system, which includes those for the gear as well as the shroud. The difference between these inlets is only the size of the gear teeth entrances, so therefore these can be seen to be having an effect on the pressure loss through the whole inlet area. Therefore, care must be taken in the future when changing a gear, as it cannot be assumed that the pressure losses at the inlet will be the same just because the inlet to the shroud has not been altered.

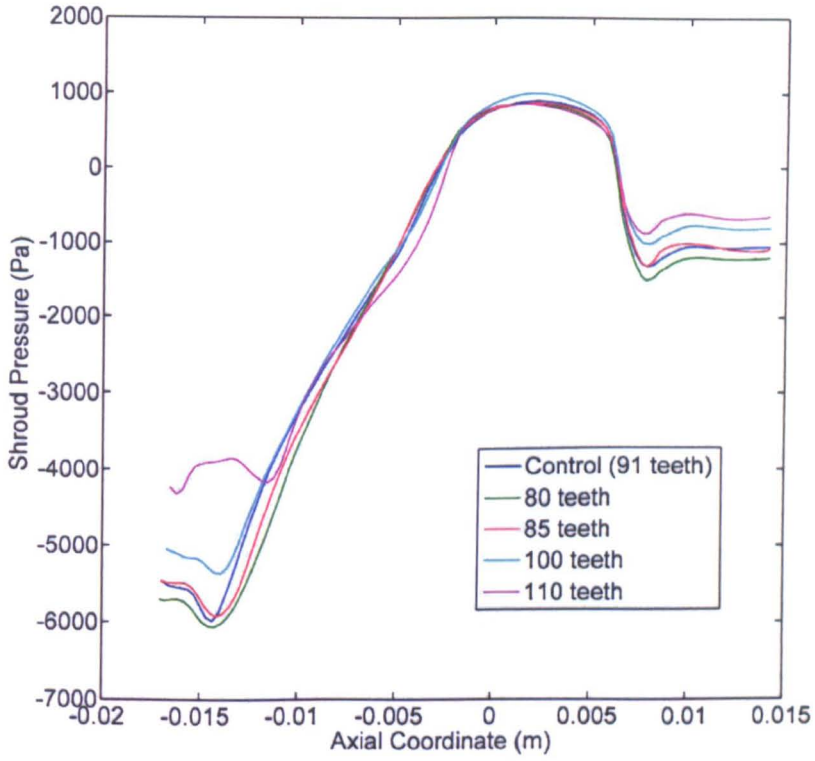

Figure 4.27: Static pressure on the surface of the shroud for gears with varying numbers of teeth

4.5.4 Static pressure increase across gear face

Figure 4.27 shows the static pressure on the surface of the shroud for all of the gears which have had their modules changed. It can be seen that for the majority of the shroud, all of the gears have a similar static pressure along their faces. There is a difference between the static pressure of the gear with 110 teeth and the others at the smallest axial coordinates, which corresponds to the area of the shroud just after the nose. The results from Figure 4.26 showed that the drop to the gear inlet was around 6000 Pascals for the 110 teeth gear and this is an area averaged using a surface that passes all the way into the gear tooth valley. The value at the same area of the shroud, but on its surface, seen on Figure 4.27 is -4000 Pa, which is one third larger. This is due to the area of low static pressure being more confined to the area inside the tooth valley, as opposed to "spilling" out over the top of the teeth because of large recirculations

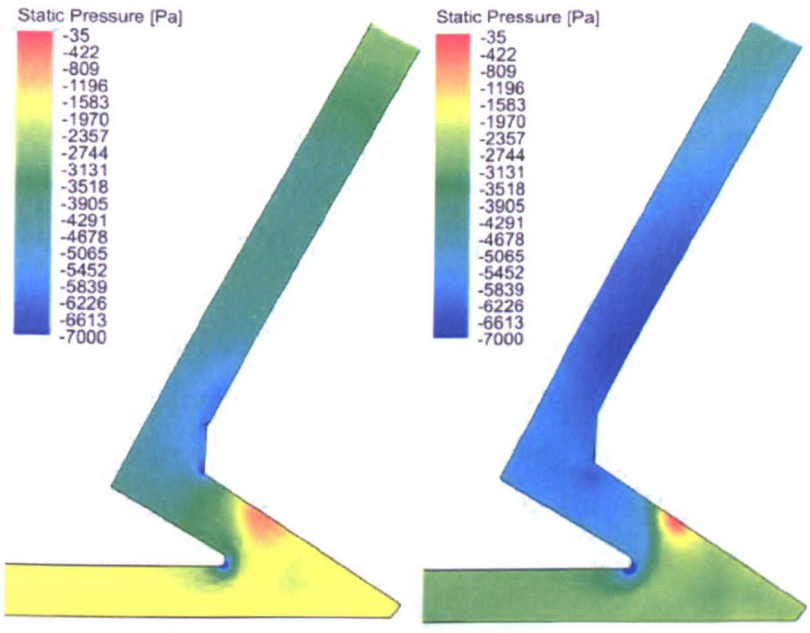

Figure 4.28: Static pressure on the periodic boundary of the 110 (LHS) and 80 (RHS) toothed models

in the flow in this region. This can be seen in Figure 4.28, which shows on a plane that bisects the teeth, the blue area of low pressure that is visible between the gear tooth and the shroud for the 80 tooth model, but not for the one with 110 teeth.

It can be seen from Figure 4.27 that the gradient of the pressure increase across the face of the gears is the same for all of the simulations. This compares to the non-similar gradients in the cases with a changed inner diameter, Section 4.4.4, which were attributed to there being differing radial distances available to accelerate the flow from the slow speeds of the inlet to the high swirling speeds of the outlet. The similar gradients in this case lend further credibility to this theory as all of these gears have the same length of facewidth, so are all accelerating the air through the same distance, *i.e.* from low inlet speeds of 10-20m/s up to high rotational speeds of 140m/s. The energy that the gear has to put into a unit of fluid will be the same — the difference lies in the amount of fluid that the gear does it to.

4.5.5 Conclusions

This section has shown that there is a strong, positive correlation between decreasing the number of teeth and the increase in gear windage. The reason for this can be split into two parts:

1. There are smaller static pressure losses through the inlet, up to the gear tooth valley entrance for a gear with a smaller number of teeth. This was shown in Figure 4.26, in which it could be seen that there was a significant deviation from the control gear's response. For example, the 110 tooth gear has a static pressure drop of 2000Pa more than the control gear at a comparable mass-flow-rate — found from the control gear's system response curve. This means that there is more restriction to the flow, and the gear has more resistance to pumping air flow through - which is why the actual mass-flow-rate is significantly lower for the gears with a higher number of teeth.

2. Secondly, it was shown in Section 4.5.4 that there is very little difference in the static pressure changes caused by the gear, as evidenced by very similar static pressure profiles on the shrouds in Figure 4.27. Based on the findings from changing the inner and outer diameter this is because the static pressure increase along the face of the gear is dependent only upon the outer diameter. The difference here is that the gears with a smaller number of teeth have larger volumes within the teeth valleys, and higher mass-flow-rates through the valleys, which means that more fluid has to be worked by the gear.

The combination of these two factors mean that gears with a smaller number of teeth will have a higher amount of gear windage, when running single phase. As mentioned in the overview to this section, larger teeth have mechanical advantages, so this finding shows that compromise will be necessary to reduce windage while specifying a gear that is capable of carrying a large torque.

4.6 Pitch cone angle

4.6.1 Overview

The pitch cone angle[4] of a spiral bevel gear is an important parameter available to transmission designers as the combined pitch cone angles of a pair of spiral bevel gears is equal to the angle between the shafts on which the gears are mounted. In the context of a gas turbine IGB, the radial off-take shaft – which transfers power to the ancillaries – is not necessarily mounted perpendicular to the high pressure shaft of the engine. During the design process of creating an engine, their relative angles can often be changed. The presence of the pinion and crown gears together also means that a transmission designer has the flexibility to chose a complementary pair of angles that allow the total shaft angle be the chosen value and are still able to carry a high enough mechanical torque. There is usually more flexibility for the designer for this variable, than say the module or the inner diameter of the gear.

Including the control gear, three gears with differing cone angles are modelled. These models are the most difficult to create from the parametric model, as they entail changing the shape of the shroud at both the nose and the outlet. This is due to the face of the shroud being at a new angle. The changes that are made to the gear itself are minimal, with the solid model of the gear being able to update easily with a change in pitch cone angle. The angles of the base cone and face angle of the gear teeth (i.e. how much they taper along the facewidth) are respectively kept the same absolute values above and below the pitch cone angle as the control gear. These values are 59.4 and 62 degrees for the control gear, which has a pitch cone angle of 60.83 degrees.

The changes that are made to the shroud are at the nose and the gutter to the shroud. The changes are not large, and the basic shapes of each are not altered. The difference is that the change in slope of the gear means that the angle of the

[4]Often just referred to as the cone angle

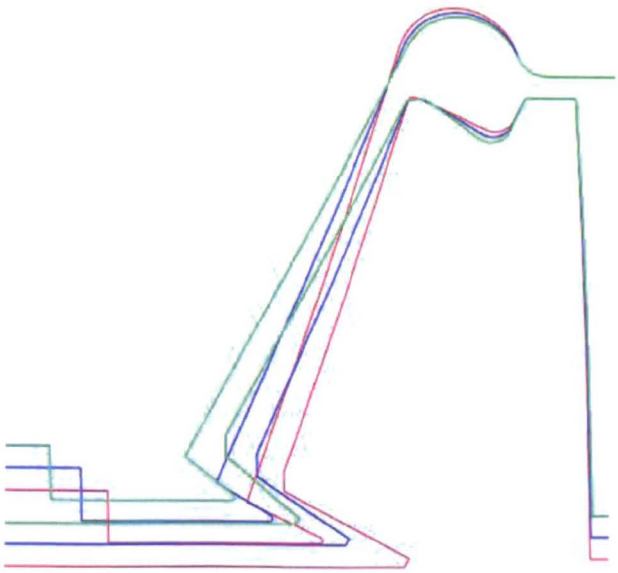

Figure 4.29: Comparison of control gear (black), 55° cone angle (green) and 66° cone angle (red)

nose must change. Figure 4.29 shows the profile of the shrouds of all three cone angle variants. The control gear is shown in blue, 55° is in green, and 66° cone angle is in red. As can clearly be seen, there is a significant difference between all three, with three major features that will affect the pressure increases and decreases through out the system. Firstly, the outer diameters of the gears is constant — the pitch diameter of the gears does not change, as this variable is independent of the pitch cone angle. This means that the radius at which the air pumped by the gear exits into the rear chamber is identical for all of the models tested in this section. The second feature is the clear difference in slope of shroud which has a minor impact upon the gutter of the shroud, but a larger impact upon the slope of the nose. When the cone angle of the gear is increased, the gear takes on a flatter appearance, and the route through which the fluid must take around the gear is more tortuous and restrictive. Lastly, due to the constant facewidth of all of the models, the inner diameter of the gears is not the same. As the pitch cone angle increases, the inner diameter of the gear gets smaller, the impact of which must be considered when dealing with the pressure losses and gains through the system.

	Windage torque		Mass-flow-rate	
Cone angle	(Nm)	Difference (%)	(kg/s)	Difference (%)
55°	1.276	+4.52	0.0605	+4.41
60.83° (Control)	1.218	-	0.0579	-
66°	1.101	-9.57	0.0496	-14.37

Table 4.8: Windage and mass-flow-rate results for gears with differing cone angles

	Torque totals		
Cone angle	Pressure (Nm)	Viscous (Nm)	Ratio
55°	1.074	0.199	5.41
60.83° (Control)	1.023	0.195	5.26
66°	0.898	0.203	4.41

Table 4.9: Windage torque, broken down by source

4.6.2 Windage results

Results for the three gears tested are shown in Table 4.8, and this shows that the gear with a larger cone angle (i.e. a flatter, more disk like gear) has a smaller windage loss.

The changes that are made to the domain when the gear's pitch cone angle is changed are the largest of all the simulations presented. It can be seen from the table of results that increasing the cone angle by just over 5 degrees reduces windage by over 9.5%. In the other direction, a reduction in cone angle of over 5 degrees increases windage by only 4.5%. These results apply within this small region of changes, which are representative of those that may be made in a gas turbine IGB. Table 4.8 also shows the results upon mass-flow-rate of changing the cone angle, and it can be seen that gears with a larger value have a smaller mass-flow-rate.

The difference in windage values is due to the change in pressure forces on the gear. Table 4.9 shows windage torque values for the gears, broken down by pressure or viscous contribution, along with the ratio of the two to each other. Viscous losses for both cases are slightly higher than for the control gear. For the gear with 66° cone angle, the viscous moment is 4.4% higher, which is due to the increased length of the back of the gear. The 55° gear has viscous losses that are 2.0% higher, and this is due to the increased mass-flow-rate in the gear tooth valley having a large impact. However, the viscous losses are 5 times smaller than the pressure losses, which are the largest contributor to the difference in total windage moment. The ratio of pressure to viscous torque reduces as the pitch cone angle gets larger, which is due to the viscous torques not reducing, whereas the pressure contribution has.

4.6.3 Pressure losses through the shroud

The impact of changing the cone angle is not limited to affecting the gear's pressure increase — there are two changes to the inlet of the shroud which affect its ability to restrict the flow through the domain. The first is that a gear with a larger cone angle has an inlet at a smaller radius compared to the control gear. This is due to the outer diameter and the facewidth of the gear being fixed. The difference between the three gears can be seen in Figure 4.29, and the change in inner radius, and hence annular area of the restriction observed. As mentioned in the section on changing the inner diameter of the gear (Section 4.3.3.2), the radial clearance at the inlet to the shroud is kept constant at 1.5mm for all of the gears tested. Table 4.10 shows the difference between annular areas for the gears.

The results show that there is a small difference between the restrictive areas at the inlet to the shrouds. The impact this has on the static pressure losses between the inlet to the domain and the restriction at the nose is seen in Figure 4.30, which again shows the control gear's results and the losses for the changed cone angles.

Cone angle	Inlet annular area (mm^2)	Difference from control (%)
55°	1008	+1.62
60.83° (Control)	992	-
66°	977	-1.52

Table 4.10: Annular areas at the inlet for gears with differing cone angles

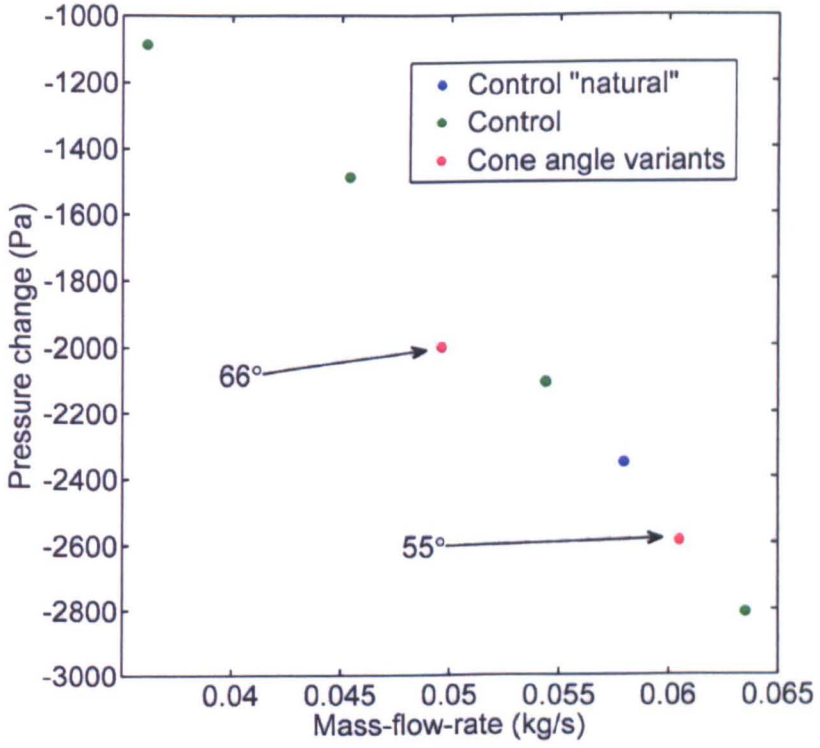

Figure 4.30: Losses between the domain inlet and the nose restriction for gears with varying cone angles

There is a small amount of deviation from the control gear's results, particularly for the gear with a 66° cone angle; however the difference is only around 200Pa at a comparable mass-flow-rate to the control. The difference for the gear with a cone angle of 55° is negligable. It is important to re-emphasise at this point that it is not the difference from the control gear's "natural" condition, but the deviation from the curve that indicates whether the inlets are acting differently.

The second change to the inlet that occurs is that the nose becomes more acute

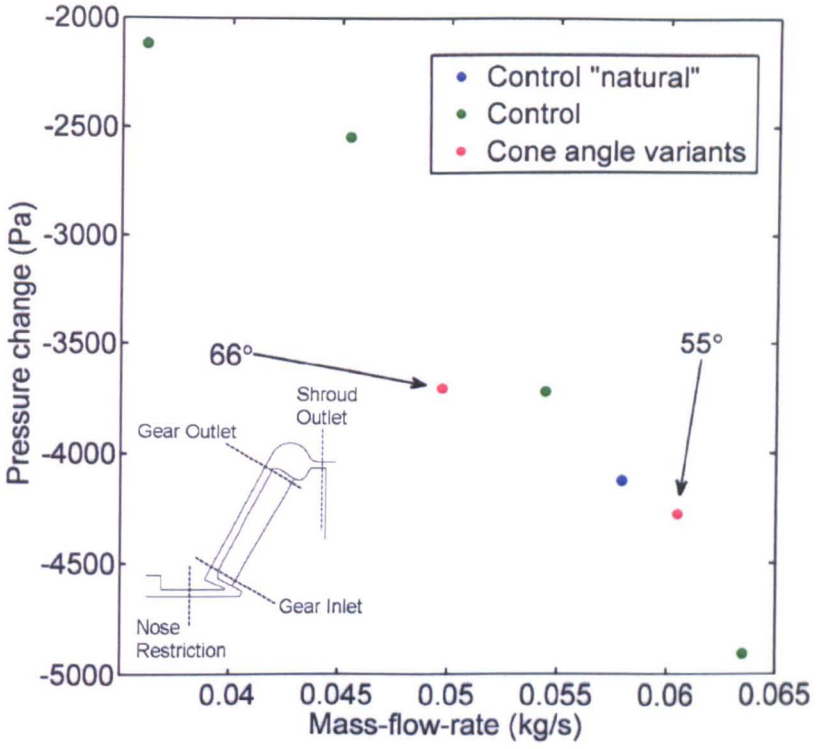

Figure 4.31: Static pressure loss from nose restriction to the gear inlet for gears with varying cone angles

with a larger cone angle, as mentioned in Section 4.6.1. This will make the route the flow takes more difficult, and introduce further static pressure losses. The change in nose shape can be observed in Figure 4.29. The difference that the shape of the nose makes is more significant than the annular area at the inlet. This is seen in Figure 4.31, which shows the static pressure loss between the nose restriction and the inlet to the gear.

The figure shows that there is a larger deviation from the control gear's curve, which is down to the difference in nose geometry. The 66° gear is showing a pressure drop that is around 1kPa larger than the control gear experiences at a similar mass-flow-rate, and although the 55° gear is showing a slightly smaller deviation from the control gear characteristic curve, it is still around 300Pa greater than that for the control gear.

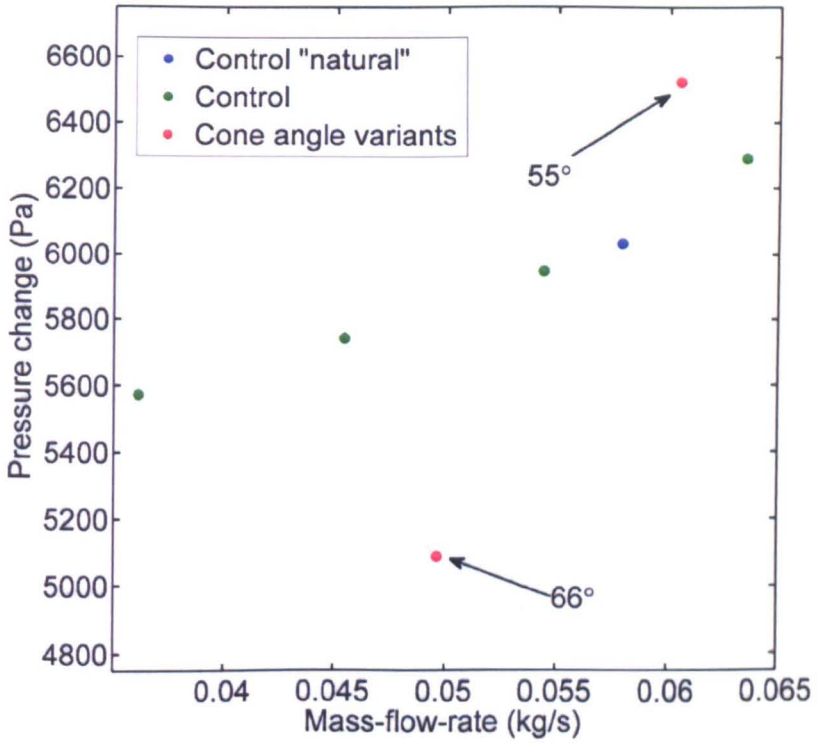

Figure 4.32: Mass-flow-rate versus static pressure increase across face for gears with varying cone angles

4.6.4 Pressure increase across face of the gear

The results seen for the pressure losses through the inlet of the shroud for the gears with altered cone angles match well with the results for windage. The more restrictive nature of the 66° gear's inlet has made it more difficult for the gear to pump air through the domain. However, this is only part of the full picture, as the alterations to the shape of the gear have also meant that the gear itself is less capable of creating as large a pressure increase over its face.

This can be seen in Figure 4.32, which shows the static pressure increase from the inlet to the outlet of the gear tooth valley. There is a clear deviation away from the control gear's characteristic curve, with the 66° gear having a lower pressure increase across the face of the gear than the control gear at a comparable mass-flow-rate, and vice versa for the gear with the smaller pitch cone angle.

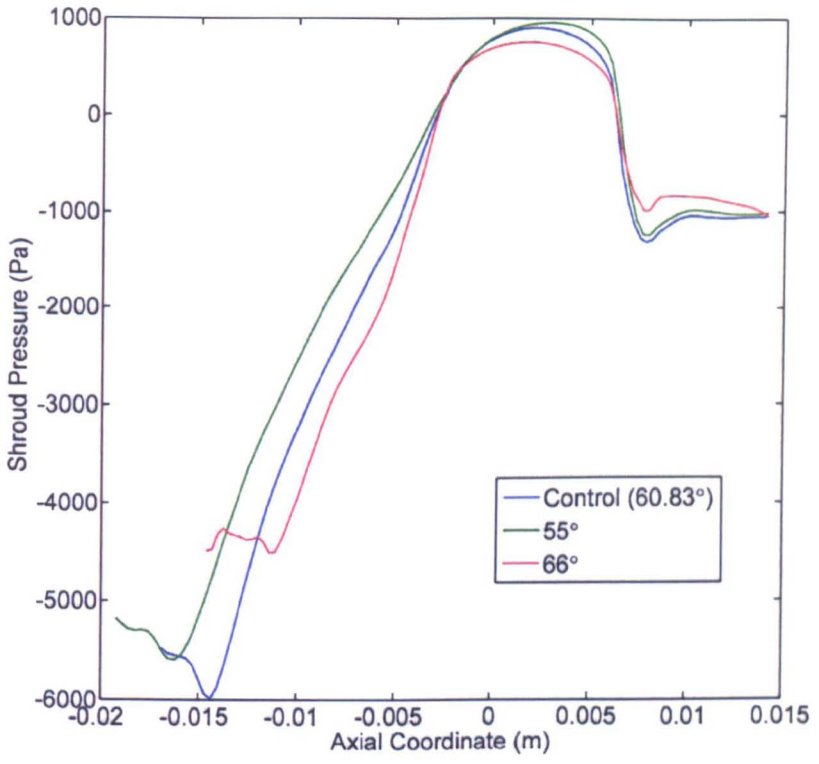

Figure 4.33: Static pressure on the surface of the shroud of gears identified by their pitch cone angles

The pressure on the surface of the shroud fits well with the findings from the previous sections. Figure 4.33 is a plot of the static pressure on the surface of the shroud of both cone angle variants, and the control gear's "natural" case. The gradients of pressure with respect to the axial coordinate are different, as they were with the cases where the inner diameter was changed; however, in this case the increase per length of facewidth is the same for all of the cases — due to the change in angle of the gear face, and the identical facewidths the 66° gear has a shorter axial length than the control, and vice versa.

A difference seen in the gear with a 66° cone angle is that the tightness of the nose has caused some flow separation. This can be seen in Figure 4.34 which shows contours of velocity for the control gear, 55° and 66° cone angle gears, going left to right. The 66° gear has an area of blue, low speed flow behind the nose, and this corresponds to an area of higher pressure, as seen in Figure 4.33 where the curve for this gear has a flatter static pressure curve at the smaller

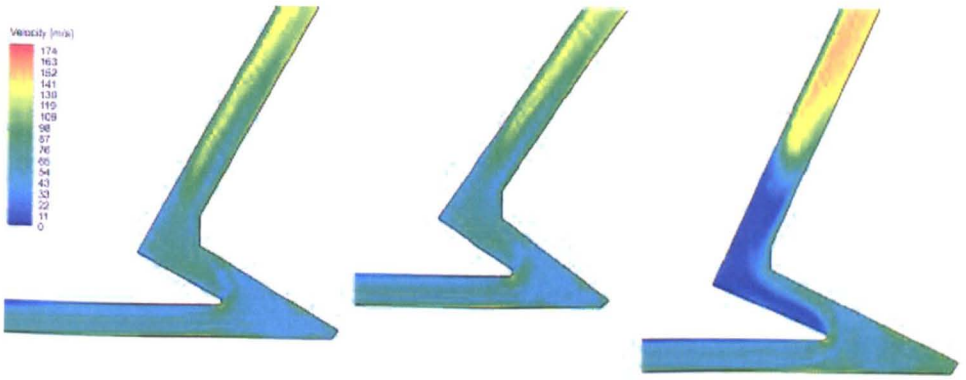

Figure 4.34: (L-R) Velocity on periodic plane of control, 55° & 66° pitch cone angle gears

axial coordinates — corresponding to the inner diameter of the shroud. This is a similar effect to the one seen for the 110 toothed gear in Section 4.5, whereby the flow is constrained in the tooth valley, and not "spilling" out over the surface of the gear at the inner diameter, where the flow enters the tooth valley. This area of stagnant flow is indicative of the inlet being more restrictive, and shows how the change to the gear has affected the whole system.

4.6.5 Conclusions

This section has shown that there is a strong correlation between the cone angle and the single phase windage. In the region tested, a smaller cone angle results in a higher windage, with the difference being due to an increase in the pressure component. The difference is mainly due to the difference in the restriction at the nose of the shroud. Changing the cone angle affects the inner diameter of the gear, however, when just this variable of the gear is changed, there is little difference to windage (Section 4.4.2). The change in the shape of the nose affects the restriction to the flow more, with the gear with a 66° cone angle requiring the flow to nearly double back upon itself, which leads to flow separation, and a higher pressure loss than the control gear at a comparable mass-flow-rate. This is a good example of the change to one component affecting another, showing the importance of considering a whole system, as opposed to a series of individual,

independent components.

4.7 Review

This chapter has shown that changes to the shape and size of the gear can have a major impact upon the single phase windage. The outer diameter was found to be a very significant factor, with windage scaling with the outer diameter raised to the power of 4.34. This is due to the gear having to do more work on the fluid trapped between the gear and the shroud because it is necessary to accelerate the flow up to higher velocities when the rotational speed is fixed. Consequently, transmission designers should minimise the outer diameter wherever possible in order to reduce the amount of energy wasted by a rotating gear.

The inner diameter had more ambiguous results, with no immediately identifiable trend, and relatively little difference between windage results. It was seen by studying the changes in the size of the annular restriction at the inlet to the shrouds, that this was causing a difference in the mass-flow-rates through the system. This has been shown in [33] to be a critical dimension in the shroud's design for reducing the windage, and the changes to the size of the gear were having a subsequent effect on the restrictive nature of the shroud. Additionally, it was seen that a higher level of pre-swirl with the shaft of gears with larger inner diameters was reducing overall windage due to the gear not having to do as much work to accelerate the flow.

The module of the gear, which controls the number of teeth the gear has, was also shown to be an important variable. The fewer teeth the gear had, the larger the windage. In these cases, the shroud restriction itself was not found to play a role, as all of the gears had the same shroud geometry. The difference was due to two factors. Firstly, there was a smaller pressure drop as the flow was accelerated into the mouth of the gear valley for a gear with a smaller number of teeth — indicating a less lossy, more free flowing inlet. The second factor was that gears with fewer, larger teeth had correspondingly larger gear tooth valleys,

which meant that the gears were pumping more flow through, and swirling it all the time. This energy has to come from the rotating gear, so results in higher windage. Where possible, a gear with a larger number of teeth should be selected to reduce single phase windage, although the mechanical torque transmission requirements may demand a gear with fewer teeth.

Finally, the pitch cone angle was analysed, and it was seen that a gear with a smaller cone angle than the control produced higher windage. This was primarily due to the restriction at the nose of the inlet being more "tortuous" for a gear with a higher cone angle, and consequently a larger pressure drop than the control gear results (at a comparable mass-flow-rate). Based on the findings of this section, a gear with a larger cone angle would be beneficial in terms of windage; however the difference would appear to be primarily down to the changes in the shroud geometry, therefore some caution would be necessary to ensure that a reduction in windage would still result with a different shroud design — *e.g.* one without a nose.

The next chapter will explore the design of the inlets and outlets of the shrouds. It will attempt to see if, for a fixed gear and radial inlet shroud clearance, the windage can be reduced with modifications to the nose of the shroud used in this chapter. A study into the effects of changing the outlet of the shroud will also be done, to ascertain the impact on single phase windage of having an outlet that is designed with a secondary (oil) phase in mind. Winfree [50] and Johnson *et al.* [22] have both suggested that there may be benefits to removing oil quickly away from a rotating gear to avoid re-ingestion. The impact upon the single phase windage of having a shroud designed to do this will therefore be investigated in Chapter 5.

CHAPTER 5

Shroud parametric study

5.1 Overview

This chapter looks at whether the shape of the shroud surrounding a spiral bevel gear can affect the single phase windage, and if so, by how much. A number of different shroud inlet and outlet designs are tested, and their effect on single phase windage quantified. For designs at the outlet, some consideration will also be made of the likely effectiveness of each at managing the flows of oil around the gear. An approach is taken whereby the effect of changing the shroud is established on the whole system, and not just looking at the effect of the shroud in isolation.

The previous chapter looked at varying the shape of the gear itself, whilst keeping the shroud as close to the same as possible to a control shape for each case. The shroud used is the same design as the one used by Johnson *et al.* [22, 23], which was shown to be a good performer, reducing the windage by up to 75% compared to no shroud, and is used as a "control" system in this chapter. The gear being tested remains the same for all cases and is the control gear as described in Chapter 3, Methodology.

The focus of this chapter is the inlet and the outlet of the shroud, and it uses a different approach for each of them in order to gather the most useful and relevant information for gear windage based shroud design.

The inlet to the shroud has been shown to be critical at reducing the overall windage, with a larger impact than the outlet [33]. Without the use of seals, and the associated rubbing that they would involve, it is difficult to get the radial distance between the rotating shaft and the static shroud to less than 1 - 1.5mm. This is due to the centrifugal expansion of the rotating elements, and a need to avoid their contact with the shroud, which could lead to metal particulate entering the oil systems, and/or frictional heating of the oil. The shroud tested in the previous chapter had a radial gap of 1.5mm at its inlet, and has been shown experimentally to be effective [23]. Section 5.2 will evaluate a number of shroud inlet designs, all with a minimum radial clearance of 1.5mm between shaft and shroud, in an effort to gauge if the length of the restrictive passage is as important as the inlet clearance.

The control shroud ("Shroud 2" in [23]) has an inlet channel which has a length of 14.4mm and a nose which undercuts the gear at its inner diameter. This shroud design is not used in an aero engine, but was created as an optimum design with no concession to expense or serviceability. The nose, although effective at reducing the windage of the gear, is a large mass that is cantilevered out over the rotating shaft, and as such may resonate and certainly will add weight and expense to the engine. Four additional shrouds will be tested which look at whether the presence of the nose is necessary to reduce windage, and if the length of the restriction is important.

The outlet to the shroud has been shown to have some importance at reducing single phase windage; however, not as much as the inlet [33]. An important feature of reducing windage when there is oil present in the system, is to make sure that the liquid phase is able to leave the area surrounding the gear as soon as possible after it has finished lubricating the gear [23, 50]. The outlet to the shroud will have an effect upon this, by either allowing oil to easily escape or by entrapping it within the confines of the gear.

In addition to the control shroud, four additional shrouds will be tested, all with different shapes at the outlet. These are tested in Section 5.3 using air only, but

the likely impact upon results when there is oil present will also be discussed.

5.2 Variation of inlet geometry

5.2.1 Introduction

The inlet is the most important part of the shroud to restrict in order to reduce single phase windage. Rapley [33] concluded that restricting the inlet to the shroud has a larger impact than restricting the outlet or face clearances; however, little attempt was made to establish why this is the case and the simulations were only run with a single phase. This was also in line with the findings of Winfree [50], who used experimentation to show that with oil present, a tight restriction and a more free-flowing outlet prevents the gear from pumping air, but allows the oil present between gear and shroud to be vented away — reducing churning. Reference can be made to Figure 3.10 in Section 3.2.2.3 for identification of the parts of the shroud.

This section will study the effect of a number of different shroud designs at the inlet. All of the shrouds have a 1.5mm radial clearance between the shaft and shroud, and for all of the simulations, the control gear is exclusively used. This study therefore complements the work done in Chapter 4, which looked at keeping the shroud design constant, while changing the gear[1].

In total, there are six shroud variants, including the control shroud, as developed and utilised by Johnson *et al.* [23]. These are shown in Figure 5.1, and on the sub-figures, a number of key dimensions are shown. The important similarity between all of the variants is that the radial inlet clearance is a minimum of 1.5mm. This means that the annular area at the inlet is the same size for all of the shrouds.

[1]Although it should be noted that the changes to the gear did involve some alterations to the dimensions of the shroud, the shape was similar for all cases

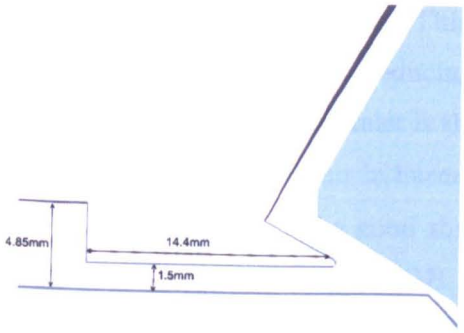

5.1.1: Control full inlet (FI)

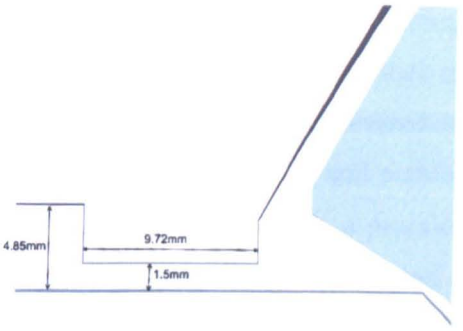

5.1.2: Full inlet, nose removed (FINR)

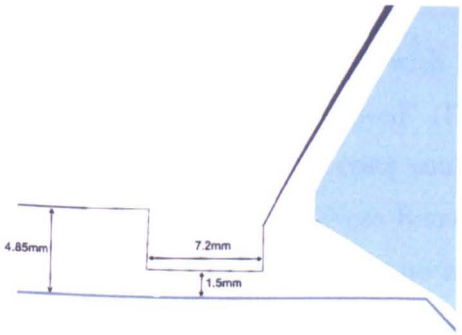

5.1.3: Half inlet, nose removed (HINR)

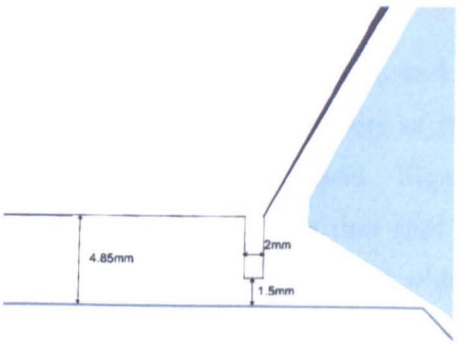

5.1.4: Vertical plate (VP)

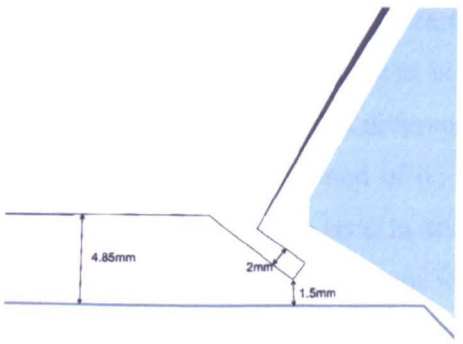

5.1.5: Inclined plate (IP)

Figure 5.1: Inlet shroud geometries

The control gear's inlet is shown in Figure 5.1.1, and has a length of 14.4mm including a large nose which undercuts the front of the gear. This shroud is called "Full Inlet" (FI) for short, and is the shroud used in Chapters 3 and 4. The purpose of the long inlet and the nose is create a tortuous route for the flow, resulting in a high pressure loss. This would reduce the mass-flow-rate through the gear for a set gear speed, reducing the work done on the air, and hence the windage. The issue with this inlet is that it involves a lot of mass cantilevered out over the gear and could result in harmonic motion during operation, and possible failure due to fatigue. It is a good shroud, but one that is limited in a practical sense for use in an aero engine IGB. Therefore, the other designs presented in Figure 5.1 are intended to establish which elements of the shroud's design are important, and which are not.

Figure 5.1.2 is the same as FI, with the exception of the nose removed, and is called "Full Inlet, Nose Removed" (FINR). The nose is a complex part of the shroud to manufacture, so costs could be reduced if it were removed. Figure 5.1.3 is termed "Half Inlet Nose Removed" and has an axial length that that is half of FI at 7.7mm, and it has no nose. Finally two designs are tested which are the most likely to be found and used, due to their simplicity of manufacture and fitting. These are Figure 5.1.5, which is a 2mm plate called "Inclined Plate" (IP) as it replicates a 2mm wide plate inclined at the same angle as the nose in FI, and Figure 5.1.4 which is the same as IP, except it is vertical (when viewed tangentially), so is called "Vertical Plate" (VP). A difference between IP and the nose of FI is that there is no rounding at the end of it; the minimum annular area only occurs at a single axial location, as seen in the figure. This is done in order to be as close as possible to a practical design for use in a gas turbine internal gearbox.

The creation of the solid models is done using Pro/Engineer [8] as described in Section 3.2, and the meshing performed as shown in Section 3.3. The differences made to the mesh are minor, as the majority of the complexity within the mesh is due to the shape of the gear teeth, so there is little additional work. The solution methodology is exactly the same as described in Section 3.4, and the simulations

	Windage		Mass-flow-rate	
Shroud	(Nm)	Difference (%)	($\times 10^{-2}$Kg/s)	Difference (%)
FI	1.218	-	5.79	-
FINR	1.257	3.23	6.71	15.9
HINR	1.294	6.29	6.78	16.9
IP	1.389	14.0	7.15	23.4
VP	1.282	5.29	6.55	13.1

Table 5.1: Windage losses and mass-flow-rates for all inlet shroud variants, with percentage difference from Full Inlet

are run in the "natural" configuration, where the mass-flow-rate through the system is determined by the balance of pressures, using pressure inlet and outlet boundary conditions.

5.2.2 Windage results

This section will look at the results for windage on the gears, and will study the differences in pressure and viscous losses. The windage and mass-flow-rate results are shown Table 5.1, and are calculated based on an average for five revolutions of the gear, which is equal to 2.4×10^{-2} seconds. These time-averaged values smooth out the impact of transient flow structures, ensuring that enough time elapses in each simulation to return accurate mean values for variables at all locations.

As the results in the table show, all of the systems have a higher level of windage than the Full Inlet control system, and a mass-flow-rate that is significantly higher. This indicates that the shrouds are not acting as effectively as FI; the removal of the nose has increased the windage by just over 3% and the shortening of the inlet in either HINR or VP has increased windage by a further few percent. The inclined plate shows a very large increase of 14% when compared to FI, which given its apparent restrictiveness is surprising, and will be explored in more detail

	Windage Moment			
Shroud	Total (Nm)	Pressure (Nm)	Viscous (Nm)	Ratio
FI	1.218	1.023	0.195	5.26
FINR	1.257	0.999	0.258	3.86
HINR	1.294	1.025	0.269	3.81
IP	1.389	1.160	0.229	5.07
VP	1.282	1.045	0.237	4.41

Table 5.2: Pressure and viscous windage moments on the gear for shroud inlet variants, and pressure:viscous ratio

in Section 5.2.5.3.

The moment is reported on the rotating surfaces of the system, which is all gear surfaces and the short shaft on which it is sited. This is the same approach that has been taken in Chapters 3 and 4.

Comparing the contribution of pressure and viscous moments on the gear, it is possible to see that their ratio changes when the shroud inlet design is changed. Table 5.2 breaks down the moment on each gear into pressure and viscous components. Compared to the Full Inlet case, there is an increase in viscous moment for all of the alternative shrouds. This is due to the increased mass-flow-rate through all of their domains. Figure 5.2 shows the time-averaged skin friction coefficient on the positive pressure side of the gear tooth[2], along with the outline of the domain to indicate the shape of the shroud inlet. This side of the gear tooth is the right-hand-side of the gear tooth, if the gear is viewed face-on. The FINR shroud is not shown due to its similarity to the HINR case. The skin friction coefficient is directly proportional to the local wall shear stress, so allows visualisation of the relative differences in viscous moment on the gear teeth. Two things can be noted from the figure: firstly, FI has the smallest skin friction coefficient, in line with the findings from Table 5.2. Secondly, the shape of the

[2]One side of a tooth has a positive pressure, the other a negative, see Rapley [33]

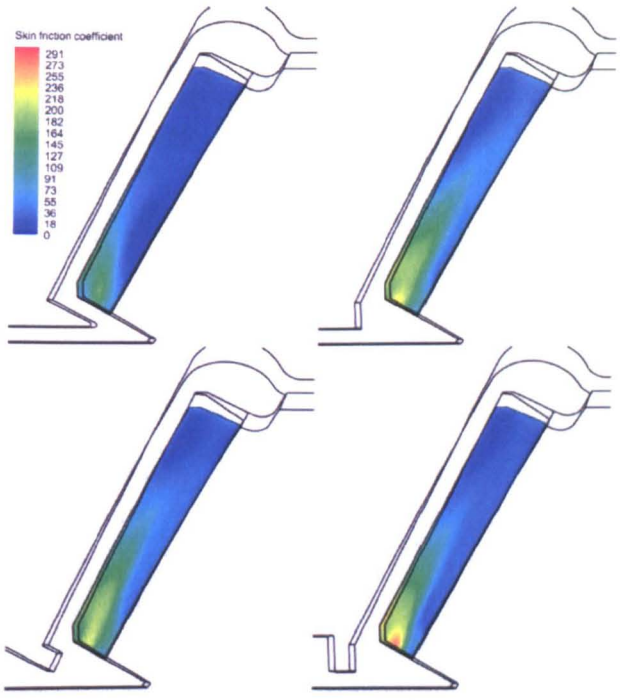

Figure 5.2: Skin friction coefficient on one tooth flank. Clockwise from top left FI, HINR, VP, IP

area of high skin friction is different for FI, appearing to not travel as far down the tooth valley, instead being jetted out of the gear tooth valley towards the shroud in a radial direction. This is probably due to the angle at which the flow reaches entrance to the tooth valley, around the nose of the shroud. These lower velocity gradients may be an indication of the gear doing less work on the flow.

The pressure moments for all of the gears, with the exception of the inclined plate(IP) are similar, being around 2% above or below the results for FI. The IP has a pressure moment which is 13.4% higher. Rapley[33] concluded that the difference in performance of shrouds with varying inlet size manifests itself mainly in a change to the pressure component of windage moment — due to it being by far the largest contributor to total windage. IP will be studied in greater detail in Section 5.2.5.3.

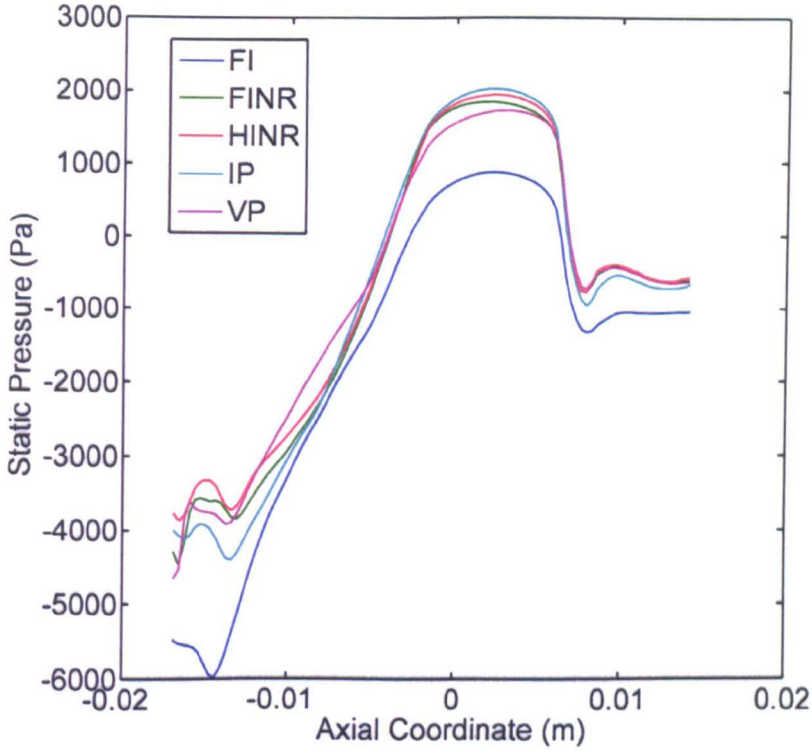

Figure 5.3: Static pressure on the surface of the shroud for all inlet variants

5.2.3 Pressure rise across gear face

The geometry for all of these cases is identical, except for the shape of the restriction at the shroud inlet; therefore it can be categorically stated that the differences in windage are due to these changes. This part of the system will be studied in this section, with a view to identifying the differences between the inlets and their respective reductions of windage.

The static pressure on the surface of the shroud is a very strong indicator of the pressure rise across the face of the gear, and allows for direct comparison between the cases. Figure 5.3 shows the static pressure on the surface of the shroud for all of the simulations. There is a clear difference between FI and the other simulations, which have around 1-1.5 kPa higher static pressure at any fixed axial position — an axial coordinate of zero corresponds to the pitch circle of the gear.

	Mass-flow-rate	Pressure Change (Pa)	
Shroud	($\times 10^{-2}$kg/s)	Gear face	Outlet
FI	5.79	6370	-2210
FINR	6.71	6150	-2620
HINR	6.29	5830	-2760
IP	7.15	6030	-2980
VP	6.55	6390	-2450

Table 5.3: Mass-flow-rate and pressure changes throughout system for shroud inlet variants

Close inspection of the magnitude of the pressure rise along the shroud allows identification of a number of common features. Table 5.3 presents results from the shrouds which gives two values to compare the simulations. The first is the pressure drop from the first part of the shroud (at the most left-hand part of the Figure 5.3) to the highest point, which corresponds to the static pressure at stagnation in the shroud gutter. This is an indication of the amount of energy that has been put into the flow by the gear. The second is the pressure change through the outlet of the gear, from the highest point of the chart to a location that corresponds to the tightest part of the shrouds' outlets, typically at the dip at around 0.008m axial location. The pressure values are established using averages of circumferential lines on the surface of the shroud, located at 100 axial locations.

There is no discernible trend with the pressure increase across the face of the gear. Given that the gears are all exactly the same, with identical shroud geometries in this area, this is is not a surprise. Referring back to Figure 4.23, which showed the static pressure on the shroud of the control system at multiple mass-flow-rates, it was shown that the pressure rise has little sensitivity to the mass-flow-rate through the system, and so this aspect does not have a large effect. The similarity of the results, and findings from the validated control gear in Section 3.7 show that all of these gears, regardless of the shroud inlet geometry all create

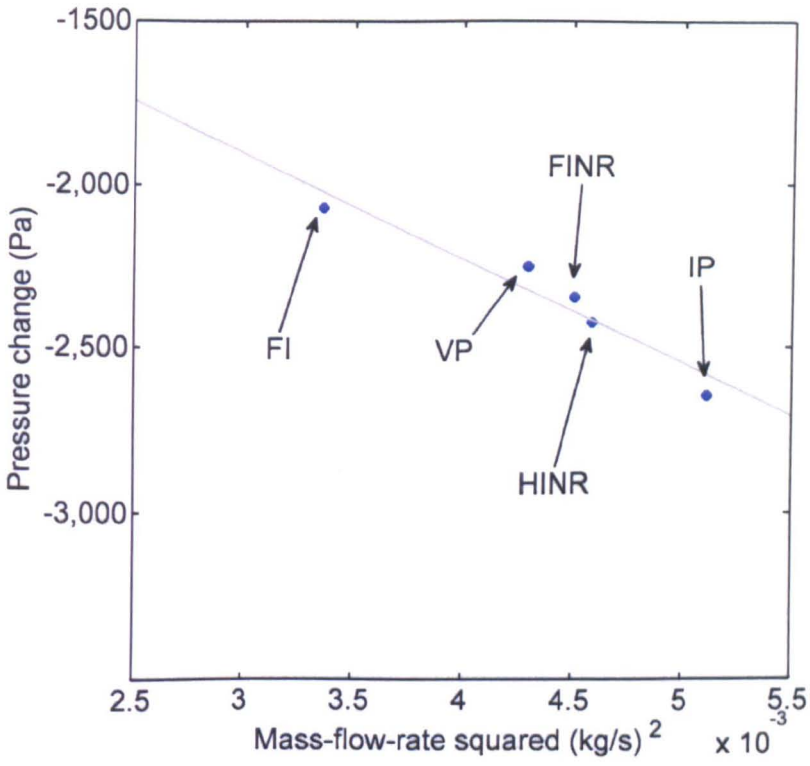

Figure 5.4: Static pressure drop through outlet of shroud for inlet variants

a similar sized pressure rise across their faces. Therefore, they can be considered to be working in the same manner.

An interesting feature of Figure 5.3 is the difference between static pressures at smaller axial coordinates, which corresponds to the part of the shroud just before the flow travels down the gear tooth valley. The difference seen is due to the change in flow structure, and this is explored in more detail in Section 5.2.5.

5.2.4 Pressure drop through shroud outlet

The fourth column in Table 5.3 is the pressure drop through the outlet to the shroud, where the flow reduces down to a 1.5mm annular area. As described in Section 4.3, this remains a constant area if the outlet is not altered and the pressure drop should be proportional to just the square of the mass-flow-rate through the outlet. Figure 5.4 is a plot for all of the shroud inlet designs showing

pressure drop through the outlet against the square of the mass-flow-rate along with a best-fit-line for the data. It can be seen that there is linear relationship, with only a small amount of scatter in the data, and the R-squared coefficient is 0.93, showing the strength of the correlation.

These results conclusively show that the gear and the outlet to the shroud are all acting in the same manner, in line with the findings from Chapter 4. Using the analogy of the fan, introduced in Section 4.2, it is now possible to rank inlets using the windage results from these simulations. The larger the windage, the worse the shroud inlet design. This may seem an obvious conclusion; however, ensuring that the other parts of the system were behaving as expected is essential to being able to categorically state this fact.

5.2.5 Pressure drop through shroud inlet

A number of studies [9, 10, 33, 50] have shown that having a restrictive shroud inlet is a critically important way of reducing single phase windage. This is due to the gear not being able to draw as much air through the system, reducing its ability to pump like a fan. The easiest way to increase the restrictiveness of a shroud is to force the air to travel through a very small area at the inlet; however in these cases, all of the minimum radial clearances are fixed at 1.5mm, and it is the changes in geometry which affect the restrictiveness of the shroud. These individual geometric aspects will be studied in turn to quantify their effect. Section 5.2.5.1 will look at the nose of the shroud, Section 5.2.5.2 the length of the restriction, and Section 5.2.5.3 will analyse the specific issues surrounding the inclined plate.

5.2.5.1 Shroud nose

The nose at the inlet to the gear is intended to make the flow path as tortuous as possible, in order to increase the pressure drop experienced by the air. It

Shroud	Pressure change (Pa)
FI	-3048
FINR	-1092
HINR	-960
IP	-2422
VP	-884

Table 5.4: Pressure change between exit to shroud inlet restriction and the gear teeth inlet

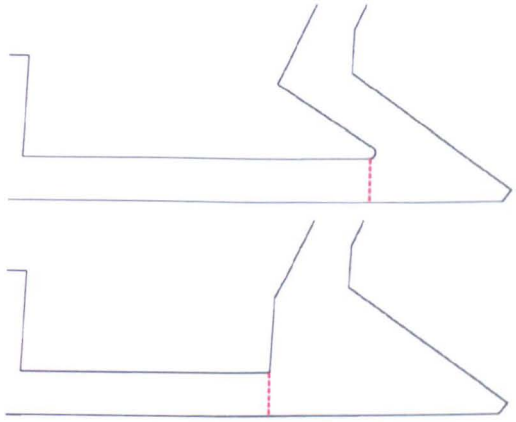

Figure 5.5: Location of surface for pressure at end of shroud inlet restriction. Full Inlet (Top) and Full Inlet Nose Removed (Bottom)

was first used by Johnson *et al.* [23], and the shrouds with a nose were shown experimentally to be best at reducing single phase gear windage. Table 5.4 shows the pressure drop between the end of the restriction at the inlet to the shroud, and the inlet to the gear tooth valley. The location of the surfaces used to determine the pressure at the end of the restrictions is shown on Figure 5.5, which shows FI and FINR as examples. The surface is located at the last axial location that the radial gap is 1.5mm, and therefore represents the static pressure as it leaves the most annularly restrictive part of the shroud. The location of the surface at the inlet to the gear tooth valley is shown in Figure 3.22. For both pressure values used to establish the pressure change, an spatial average for the plane is used, temporally averaged over five revolutions.

Table 5.4 shows that for the gears without a nose, there is a pressure drop of around 1000 Pascals, which will be due to the acceleration of the flow through the inlet to the gear teeth (which are of constant geometry for all simulations). FI is showing a pressure drop of around 3000 Pascals, which can be directly attributed to the extra length and flow passage of the nose. IP has a pressure drop of around 2400 Pascals, larger than the gears without any form of nose, but smaller than the FI. The reason for this is that there is a larger acceleration of the flow as it enters into the tooth valley, due to the IP having imparted less swirl with the shaft to the flow before it reaches the gear. This will be explored in greater detail in Section 5.2.5.3.

From these results, the additional pressure drop caused by the nose is around 2000Pa, and this can be seen in Figure 5.6, which shows averaged static pressure on the periodic plane of FI and FINR. There a difference in pressure along the restriction, but this is due to difference in mass-flow-rates; what is clear is that after the end of the restriction for FINR there is no further reduction in pressure. There is an increase at the stagnation point of the flow where it hits the gear teeth, and this can be seen as the red coloured area, but comparing this to the FI result, it can be seen that while travelling around the nose, the pressure continues to drop. The stagnation point is different in each of the cases, and can be seen to be further "up" the gear tooth for the FINR case, and this indicates that the flow from the shroud is passing more directly into the tooth valley, whereas its passage is more impeded for FI. This was also observed in Figure 5.2, where the shear on the surface of the gear tooth of the cases was seen to be directed more radially outwards and less axially for the FI, when compared to the other cases. The direction of the core air flow is marked on the figure using arrows. As expected, the nose of the shroud does a good job of reducing the flow, but it is expensive to implement in reality, hence the need for this study.

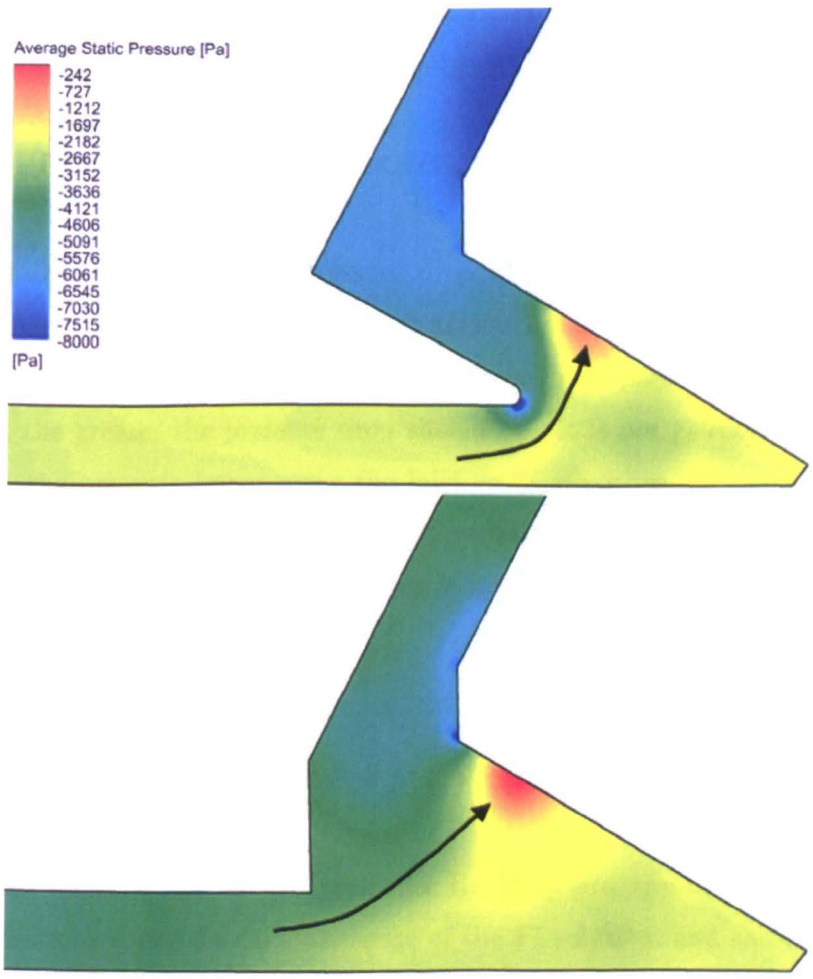

Figure 5.6: Averaged static pressure on periodic plane of Full Inlet (Top) and Full Inlet Nose Removed (Bottom). Core flow direction marked using arrows

	Pressure drop (Pa)		
Shroud	Original	Normalised	per mm
FI	-1063	-	-79
FINR	-872	-649	-67
HINR	-760	-557	-77

Table 5.5: Pressure changes per mm through inlet restriction of shroud

5.2.5.2 Pressure drop along restriction

It is possible to measure the pressure drop at the beginning and end of the restrictive passage — the lengths of which are marked in Figure 5.1. This pressure drop is due to frictional resistance of the flow through the passage. The longer the passage, the greater the pressure drop should be. It is not possible to directly compare the pressure losses along the inlet restrictions, as the simulations all have different mass-flow-rates, and hence velocities[3]. However, by using pipe flow theory, we can state that the pressure drop is proportional to the length, and to the square of the velocity [47],

$$\Delta P = f\left(L, V^2\right). \tag{5.1}$$

Using this information, we can normalise the drop pressure of the HINR and FINR solutions using the mass-flow-rate of the FI solution, and calculate their respective pressure drops per mm of length, based on just the mass-flow-rate of the FI. This effectively isolates the effect of the length of the restrictions from the mass-flow-rate. Table 5.5 shows this information, and allows us to see that the results are close to each other, with a pressure drop of between 67 and 79 Pascals per millimeter.

[3]This assumes the same density for all the present work, which is true to within 2%

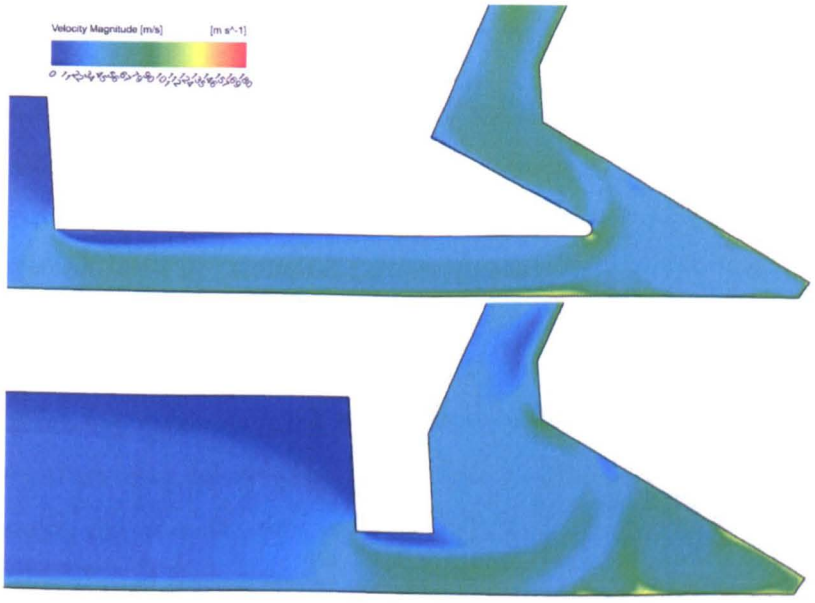

Figure 5.7: Averaged velocity magnitude on periodic plane of Full Inlet (Top) and Vertical Plate (Bottom)

The VP simulation results are not shown in this table as fully developed pipe flow is not allowed to develop along its length, so the frictional losses that cause the pressure drop will not apply. This can be seen in Figure 5.7, which compares contours of velocity magnitude for the FI (top) and VP (bottom) shrouds. It can be seen that for both cases there is a large flow separation that occurs at the contraction of the shroud, signified by an area of blue which represents low velocity flow; however for the VP case, it is clear that this does not reattach to the wall of the shroud, thereby precluding its comparison using pipe flow theory.

All of the simulations that have the sudden contraction at the inlet to the shroud show similar patterns of flow separation. The separation causes the flow to be forced through an area that is smaller than the space between the shroud and the shaft. The part of the flow where the cross section of the air-stream is smallest is called the *vena contracta*. Using the FI solution, it is possible to measure the radial location of the thinnest part of flow, and calculate the ratio of areas of the vena contracta and the physical space. The result is a ratio of 0.665, which is almost identical for all of the other simulations with the sudden contraction. This number is very close to the generally used value of 0.64 used as a coefficient

of discharge in sharp edged orifice calculations [47].

It can be seen that from this work that the length of the contraction is less important than the actual contraction itself at creating a pressure drop; by seeing that the areas of the vena-contracta are so similar for the simulations with a sudden contraction, and by noting that the typical pressure drop at the contraction is around 2,500 Pa, the additional length of even the FI's 14.4mm channel only introduces an extra 1,000Pa drop. This is why the VP results for windage are similar, given the extra length of the HINR and FINR. Therefore, for a design like these, there may be diminishing returns in reducing windage with a long inlet passage, due to extra cost and the possibility of the weight of the longer inlet causing shroud resonance.

5.2.5.3 Pressure drop through inclined plate

The Inclined Plate (IP) is a special case out of the shrouds tested, as it does not create a sudden contraction of the flow, or have any axial length to the inlet passage — the contraction down to 1.5mm radial clearance between shroud and shaft only occurs at a single axial location (see Figure 5.1.5). This has a number of implications for the pressure loss through the inlet, and also the flow structure.

Figure 5.8 shows contours of static pressure on a plane that passes through the gear tooth valley[4] for the IP (top) and VP (bottom) shrouds. It can be clearly seen that the pressure behind the restriction is far lower for the VP than for the IP, and that there will be a significant change in the flow field between the two. The restriction of the IP is not a sudden contraction — it reduces slowly, which is much more like a venturi nozzle or a funnel, and these are less lossy than orifice plates [47]. As a consequence, there is not the separation of the flow that characterises the inlets of the other simulations; so using the value of 0.665 for the coefficient of discharge is not appropriate for the IP, as its value will be higher.

[4]The flow inside the valley itself is not shown due to software visualisation limitations

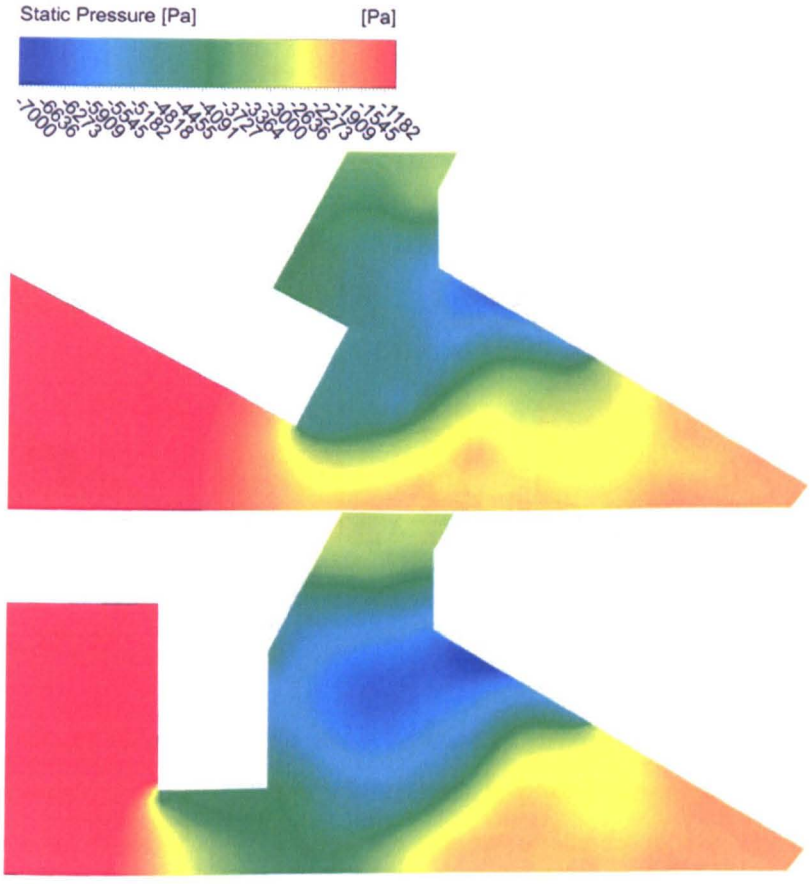

Figure 5.8: Averaged static pressure on plane that passes through tooth valley of Inclined Plate (Top) and Vertical Plate (Bottom)

There is also a difference in the amount of swirl that is imparted to the flow in the longer passages of the inlets with long axial lengths. Figure 5.9 shows contours of tangential velocity, averaged over five revolutions for four different shroud shapes. Clockwise from the top left these are FI, HINR, VP and IP. The contours of tangential velocity represent the amount of swirl that has been imparted by the gear and shaft on the air passing through the domain. The contours are coloured from 0 to 10 m/s to give better clarity, with areas of red being higher than 10 m/s and areas of dark blue representing areas that have no swirl. It can be seen that the IP simulation has the largest amount of blue, non-swirled flow at the point where the flow exits the restriction and heads towards the gear. The Full Inlet shows the opposite where there is a larger amount of swirled flow, and this has been caused by constraining the flow near the rotating

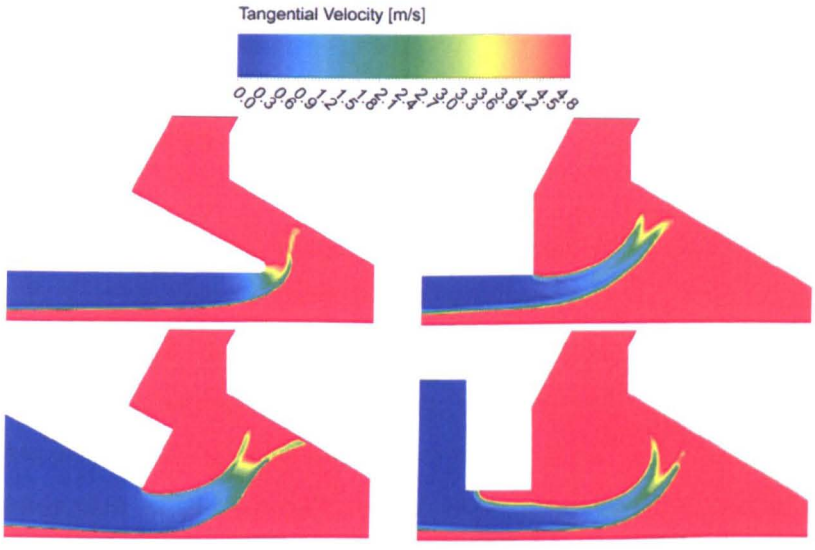

Figure 5.9: Contours of tangential velocity on periodic plane. Clockwise from top left: FI, HINR, VP, IP

shaft for longer. There is a 25% larger amount of viscous moment on the shaft in the FI simulation than in the IP case, which indicates the increased amount of work done by the shaft in this case. An interesting aspect of the VP simulation is that the separation caused by the restriction of the shroud means that there is highly swirled flow on the underside of the vertical plate, signified in red. This has come from the area of very high swirl around the gear teeth, and could have an interesting impact on the management of oil, but will not be addressed further here.

The implications for having a smaller amount of swirl is that the gear is required to do more work to accelerate the flow when it enters the gear tooth valley. This manifests itself as a higher pressure moment on the gear, which was noted in Section 5.2.2. A conclusion that can be drawn is that pre-swirling the flow in an inlet channel may be beneficial and more efficient than allowing the gear to accelerate the flow. This was also seen to be the case in Section 4.4 in Chapter 4.

5.3 Variation of outlet geometry

5.3.1 Introduction

The outlet is not as important as the inlet at reducing single phase gear windage; however, it is of key importance once oil is present in the system. Winfree [50] and Johnson *et al.* [22] have both experimented at reducing windage and churning of oil by incorporating slots into the design of the shroud. Placing a slot as soon as possible after an oil jet was found by Johnson *et al.* to be the most effective way of doing this, at the expense of an increase in single phase gear windage — the increase is proportional to the percentage of shroud uncovered by the hole.

The point of a slot in the shroud is to allow oil to escape quickly without allowing the gear to recirculate it, which incurs an unnecessary energy penalty. The same logic is applied to having a free-flowing outlet that will not trap the oil, instead venting it out to the chamber in which the shrouded gear is sitting. There is certainly a penalty in doing this, as seen in [33]; however, it is not as significant as similar sized changes at the inlet.

This section will look at the effect upon single phase windage of changing the design at the outlet to the shroud. The focus will be on the changes to the flowfield, and the likelihood of these having a positive effect upon the ability of the system to allow oil to be vented away. It was concluded by Rapley [33] that the best shroud has large re-circulations along its face, as this reduces the ability of the gear to pump air through the domain. This conclusion is only valid for single phase flows though, as it can be hypothesised that large re-circulations would cause oil to be constantly re-ingested with an associated windage cost.

Including the control system there are five outlet variations studied here, and these are shown in Figure 5.10. The outlet variants differ from the control outlet, as they do not share a common radial clearance — which is 1.5mm for the control. All of the shrouds share the exact same inlet design and clearance (1.5mm) and the same face clearance (1.76mm, which is 2mm axially). Figure 5.10.1 is the

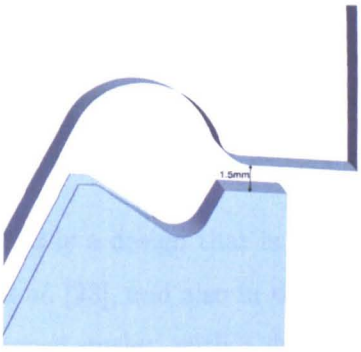

5.10.1: Control Outlet (CO)

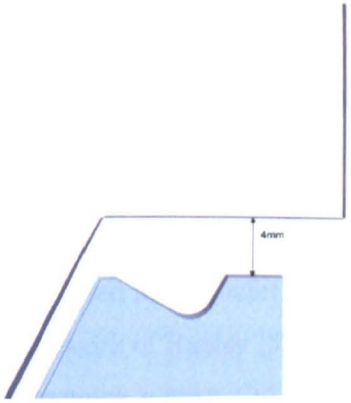

5.10.2: Flattened Outlet (FO)

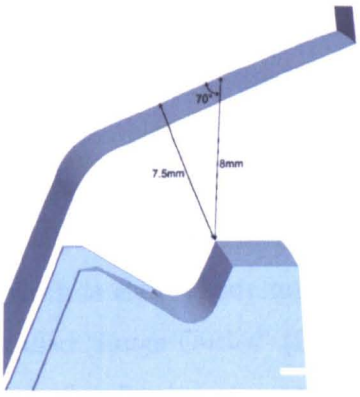

5.10.3: Medium Outlet (MO)

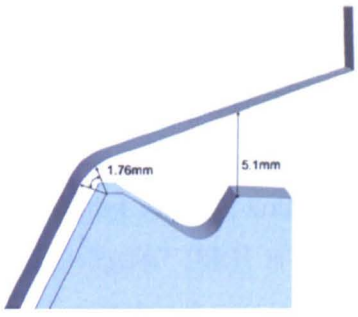

5.10.4: Hybrid Outlet (HO)

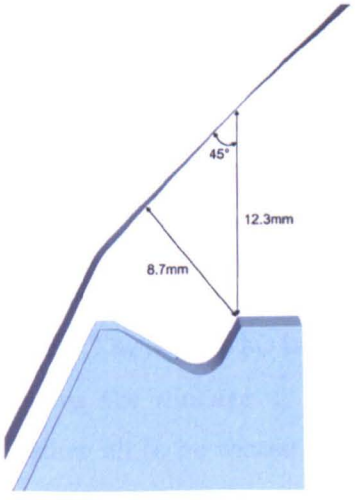

5.10.5: Large Outlet (LO)

Figure 5.10: Outlet shroud geometries

standard shroud outlet design, as used in the methodology chapter (Chapter 3) and Chapter 4 studying the effect of changing the gear, and as FI in Section 5.2 of this chapter. The purpose of the shape of the shroud, with its distinctive "gutter" is to capture oil away from the gear teeth. This shroud has been shown to have good single phase performance [23]. It is identified as the Control Outlet (CO) for ease of comparison in tables and figures.

Figure 5.10.2 is a design that is similar to that used at the oulet in the work by Johnson *et al.* [23], and also in the single phase work of Rapley [33]. This shroud has a flattened outlet, with a 4mm radial clearance betwen the outer diameter and the shroud — it is called "Flattened Outlet" (FO). This shroud has a design which is simple, and is meant to allow oil to escape away from the gear, without also taking up much space within an Internal Gearbox (IGB). Figure 5.10.5 is a shroud with a very large outlet, effectively providing no or very little restriction to the flow, meaning that the flow leaving the gear teeth is expelled into an area with a static pressure of around zero Pascals gauge[5]. The radial clearance is 12.3mm, which is eight times larger than the outlet for CO, and this shroud is therefore called "Large Outlet" (LO). "Medium Outlet" (MO) is similar to LO, as it is a very free-flowing, non-restrictive outlet, and is shown in Figure 5.10.3. This outlet is designed to take up less space than LO, and at its largest outer diameter, splits the difference between the outer diameters of CO and LO. The radial clearance between the outer diameter of the gear and the shroud is 8mm. Finally, Figure 5.10.4 shows the so-called "Hybrid Outlet" (HO), as it combines elements of the most restrictive outlets (CO and FO) and the larger, more free-flowing ones (LO and MO). The shroud is created using an outlet that is at the same angle as MO, but is slid down the face of the shroud until the minimum clearance of 1.76mm is reached[6]. The aim of this is to make the shroud restrictive around the gear tooth (reducing the windage by creating a pressure loss), but the slope of the shroud will allow oil to be vented away, preventing re-ingestion.

[5]This assumes no radial static pressure gradient

[6]This is the same clearance as between the face of the gear and the shroud

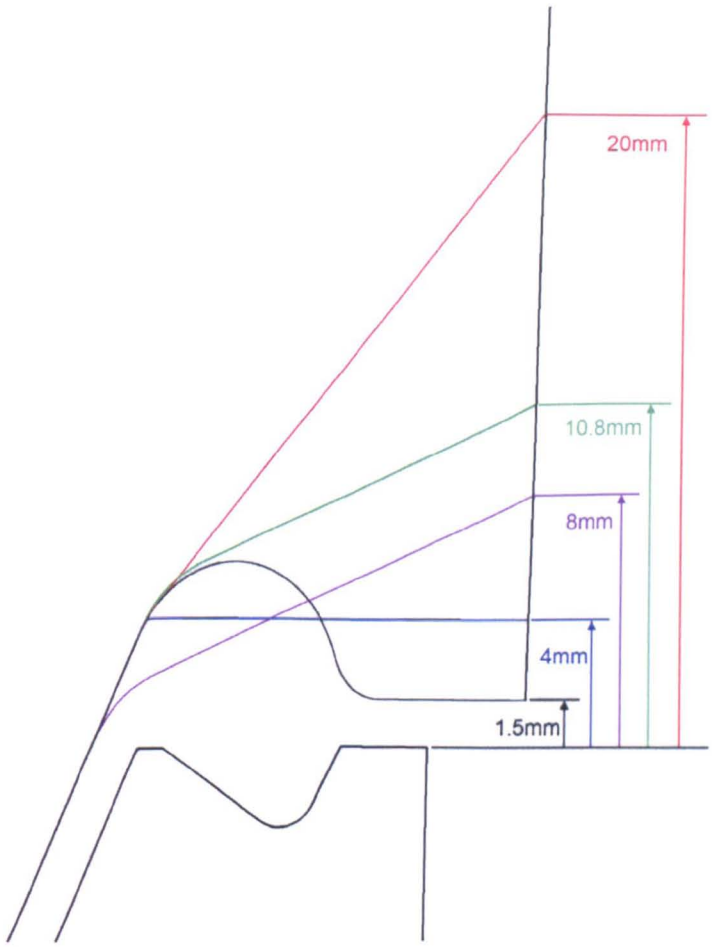

Figure 5.11: Comparison of shroud shapes at outlet. Control (Black), FO (Blue), LO (Red), MO (Green), HO (Purple)

Figure 5.11 is a comparison of the outlet shapes of the shrouds overlaid on top of each other. The shape of the control outlet is shown in black, and this colour is also used for the gear which is common to all of the domains. The flat outlet of the FO is marked in blue, and the wide openings of LO and MO can be seen in red and green respectively. The point at which they deviate from the control outlet can be seen — it was done using a tangent to the "gutter" to ensure a smooth transitional shape. Finally, HO, marked in purple shows how it is the most restrictive shroud in the vicinity of the outer diameter of the gear teeth, but still allows a large outlet for the flow to continue travelling through the domain unrestricted. The figure also shows the maximum clearances at the outlet of the shrouds, relative to the outer diameter of the gear. The changes to the domain

	Windage		Mass-flow-rate	
Shroud	(Nm)	Difference (%)	($\times 10^{-2}$ Kg/s)	Difference (%)
CO	1.218	-	5.79	-
FO	1.277	4.81	6.12	5.71
LO	1.367	12.3	6.51	12.4
MO	1.357	11.4	6.48	11.9
HO	1.319	8.32	6.42	10.7

Table 5.6: Windage losses and mass-flow-rates for all outlet shroud variants

are done within Pro/Engineer, and changes to the mesh are limited, as described in Section 5.2.1.

5.3.2 Windage results

This section will look at the windage losses and break them down in order to identify trends and differences between the dominant pressure losses and the smaller viscous losses. Table 5.6 shows the windage losses and mass-flow-rates for all of the outlet variants, with percentage differences to CO.

The control shroud outlet (CO) has the smallest single phase windage losses, with the Large Outlet (LO) having the highest losses, due to it having little or no restriction to the flow. There is a trend whereby the greater the outlet size, the larger the windage, which matches well with the findings of others [23, 33, 50] that the greater the restriction to the flow, the smaller the single phase windage. When compared to the shroud inlet variations tested in Section 5.2, the effect of changing the outlet to something that offers no restriction at all (LO) only increases the windage by half that of the Inclined Plate's increase. This demonstrates how the outlet has a smaller impact on reducing windage than the inlet.

	Windage Moment		
Shroud	Pressure (Nm)	Viscous (Nm)	Ratio
CO	1.023	0.195	5.26
FO	1.075	0.202	5.33
LO	1.150	0.217	5.30
MO	1.141	0.215	5.29
HO	1.114	0.205	5.42

Table 5.7: Pressure and viscous windage moments for shroud outlet variants

Table 5.7 breaks down the windage into pressure and viscous components. Unlike the results for the changes to the inlet of the shroud, seen in Table 5.2, there is very little change to the ratio of pressure to viscous moments. The implication of this is that the changes to the outlet have not affected the flow at the inlet, and hence the manner in which the flow is passing through the gear is the same. This can be seen visually in Figure 5.12, which shows contours of velocity at the inlets of the shrouds of four of the cases: CO, FO, LO & HO. All of the cases show the exact same flow patterns, with no difference apart from a slight difference in magnitude of the flow velocity — in line with the difference in mass-flow-rates through the domains.

If the pressure and viscous moments of just the gear teeth surfaces (the tooth flanks, toplands and the valley) are analysed, it is possible to isolate these largest components of windage from the lesser components such as the back of the gear which distort the impact of the teeth. For example the back of the gear has a high viscous moment, due to its large size, but this is fairly constant between the gears and so dominates the viscous contribution to the total windage.

Table 5.8 presents the results for all of the shroud variants tested in this chapter, using only the pressure and viscous moments from the gear teeth themselves. The top set of results is for the control system, using data from the validation of the system (Section 3.7), and also highlights the natural case used for comparison

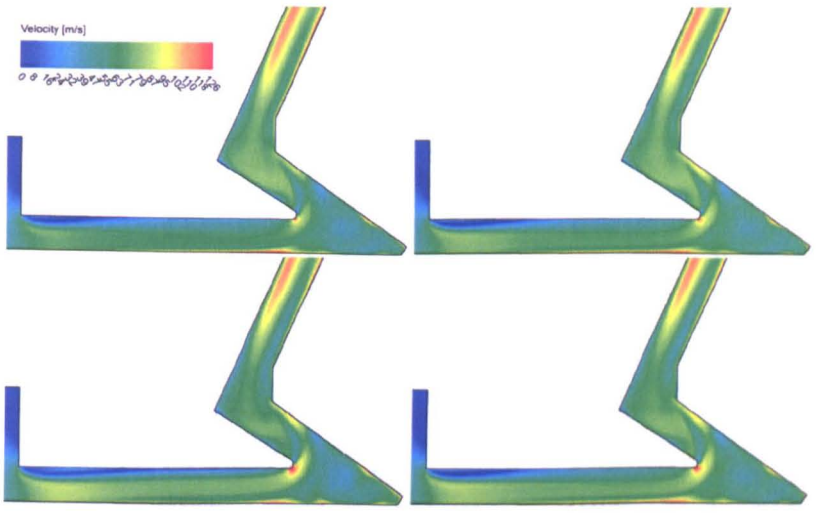

Figure 5.12: Contours of averaged total velocity on periodic plane. Clockwise from top left: CO, FO, LO, HO

in the rest of this chapter. The next two sets of results are for the shroud outlet variants and the shroud inlet variants respectively.

It is possible to see that in comparison with the data for the whole gear (Table 5.7), that the pressure component remains the same[7] and the viscous component has dropped greatly, due to the impact of the back of the gear and the shafts being removed.

All of the results for the shroud outlet variations are close, with a ratio of pressure:viscous moment between 22.9 and 24.0, with a general trend of increasing ratio with increasing mass-flow-rate and this matches the results for the control gear very well. This can be contrasted with the large difference in pressure:viscous ratio for the systems with an altered shroud inlet, where the trend for pressure moment is for it to increase with increasing mass-flow-rate, but the trend is less clear for the viscous moment. The conclusion that can be drawn from this is that the split between pressure and viscous contributions to moment is affected predominantly by the conditioning of the air as it reaches the gear, for example its swirl and flow direction. Therefore, we can say from this that changes to the outlet do not affect the effectiveness of the shroud inlet restriction, or the manner

[7]There is a difference, but it is two orders of magnitude lower than displayed in the table

	Mass-flow-rate	Windage moment of gear teeth surfaces only		
Shroud	($\times 10^{-2}$ kg/s)	Pressure (Nm)	Viscous (Nm)	Ratio
CO	3.61	0.720	0.0332	21.7
	4.53	0.857	0.0378	22.7
	5.44	0.989	0.0408	24.2
(natural)	5.79	1.023	0.0448	22.9
	6.35	1.107	0.0451	24.5
FO	6.12	1.075	0.0453	23.7
LO	6.51	1.150	0.0479	24.0
MO	6.48	1.141	0.0497	23.0
HO	6.42	1.114	0.0470	23.7
FINR	6.71	0.999	0.0810	12.3
HINR	6.77	1.025	0.0907	11.3
IP	7.15	1.160	0.0852	13.6
VP	6.55	1.045	0.0789	13.2

Table 5.8: Pressure and viscous windage moments for just the gear teeth of control outlet (at various mass-flow-rates), and results for the shroud outlet and shroud inlet variants

in which the gear experiences torque. This will be studied further in the next few sections.

5.3.3 Pressure drop through shroud inlet

As seen in Figure 5.12, there is little difference in the flow fields at the inlet of the simulations. There is a difference in the static pressure drop through the inlet area; however this is due to the difference in mass-flow-rate through the system. The response of all these systems is very close to that of the results from the validated control gear and shroud. Figure 5.13 is a plot of pressure drop from simulation domain inlet to gear tooth valley inlet, against mass-flow-rate through

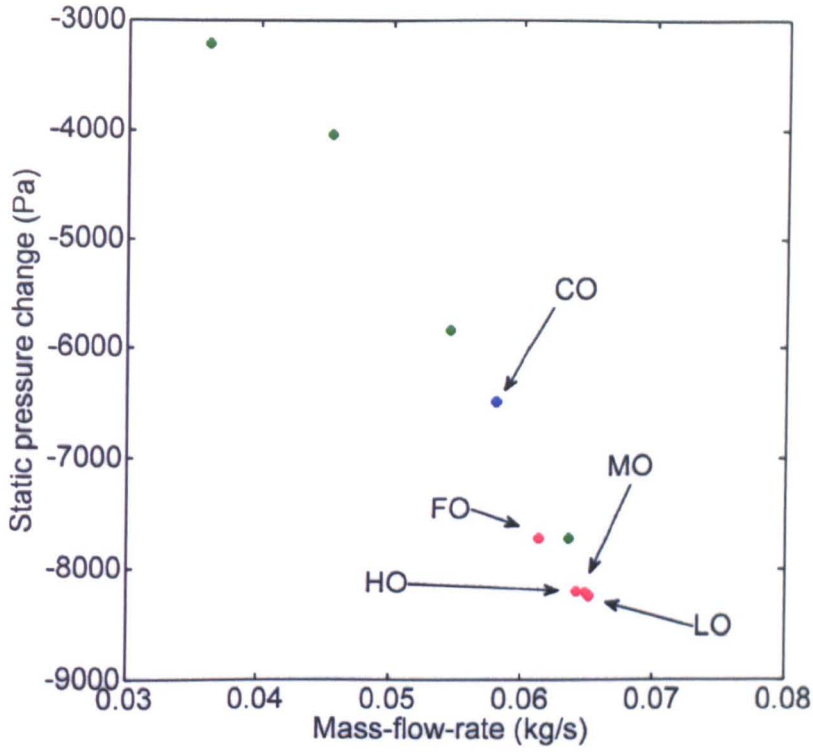

Figure 5.13: Static pressure drop between inlet of domain and inlet of gear tooth valley of shroud outlet variants. Blue is CO "natural" case, Green are CO results with varying mass-flow-rate, Red are the outlet variants, marked by shroud outlet shape

the system for all of the outlet variants (marked in red), and the Control Outlet (blue), with the results from validation of the control gear and shroud shown in green. It can be seen that the results sit very near, or on the line of the control shroud, indicating that there is very little difference in performance between the pressure drop. This is very similar to the results seen in Section 5.2.5.2, which studied the effect of changing the outer diameter of the gear. There, like here, the inlet to the shroud was identical, so the pressure drop through the shroud inlet followed the same trend as the control gear for all of the different gear sizes, with their differing mass-flow-rates.

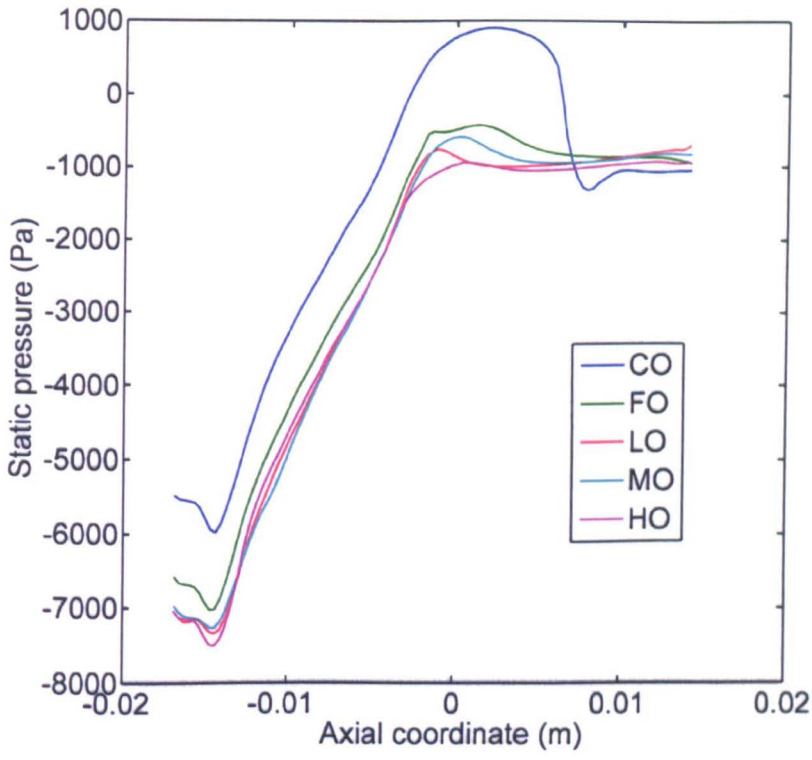

Figure 5.14: Static pressure profile on the surface of the shroud for outlet variants

5.3.4 Shroud pressure profile

The pressure profile on the surface of the shrouds is indicative of the work that is done by the gear on the air. It has been discussed earlier in this thesis in Section 4.2 that the gear and shroud act similarly to a centrifugal fan with a volute that increases the static pressure at the outlet. Reference should also be made to the shape of the shrouds in Figure 5.11.

Figure 5.14 is a plot of the static pressure under the surface of the shrouds. It can be immediately seen that there is a large difference between the shape of the Control Outlet to the others, qualitatively and quantitatively. The differences and similarities give a strong indication as to the manner in which outlet design has changed the performance characteristics of the system.

A way of measuring the pressure increase across the face of the gear is to look at the change in pressure on the surface of the shroud, in the same way as was done

Shroud	Maximum pressure increase across gear face (Pa)
CO	6370
FO	6170
LO	6300
MO	6410
HO	6120

Table 5.9: Static pressure rise along shroud of outlet variants

in Section 5.2.3. This is done using the data used to create Figure 5.14, and looks at the difference between the static pressure from the first measured point, to its highest value, before the flow is ejected into the rear chamber. These results are shown in Table 5.9, and it can be seen that there is little to no difference between the simulations, with maximum 2.4% difference from the average, and no discernable trend with mass-flow-rate or size of outlet restriction. This value is a measure of the pressure before and after the gear teeth, so therefore gives an indication into the amount of work that has been done on the air. This same trend was seen for the inlet variants and is expected given the insensitivity of the pressure rise of the gear to the mass-flow-rate as seen in Section 3.7 and by Johnson *el al.* [23].

The conclusion that can be drawn from this is that the gears all have the same work rate on the air, the difference being that the larger mass-flow-rates of the flow through some shrouds means that more energy is transferred to the air overall — hence higher windage power losses for these gears.

5.3.5 Pressure loss at outlet of shroud

Thus far it has been seen that the identical shroud inlets and gears are all acting in a very similar way, with no reason why the windage would be any different. Clearly, it is the outlet that is the reason for the difference, as it is the only part

of the domain that has been changed, but it can be said that the changes to this part have had no effect on the manner in which the rest of the system works.

Inspection of the pressure changes at the outlet, towards the right-hand-side of Figure 5.14, highlight the differences between the different shrouds. The control outlet has a large drop in static pressure as the flow is forced through a second contraction, which has a radial gap of 1.5 mm (the first contraction being the inlet to the shroud). The pressure drop is just over 2000Pa, which can be compared to the larger 6600 Pa drop through the inlet. All of the other systems, with the exception of FO have pressure drops of only a few hundred Pascals, and these can therefore be considered to be of negligible importance relative to the overall system pressure drop (including the inlet). FO has a slightly larger drop of 700 Pascals, as there is a 4mm radial restriction, which explains why it has a windage loss that lies between that of CO and the other, wider outlets (although nearer LO, MO and HO than CO).

	Total Pressure drops (Pa)	
Shroud	Original	Normalised
CO	-8692	-
FO	-8246	-7380
LO	-8487	-6721
MO	-8576	-6851
HO	-8319	-6785

Table 5.10: Pressure drops through all parts of the shroud, original and normalised to CO mass-flow-rate

Table 5.10 contains the total pressure drops for the shrouds, summed for both inlet and outlet in the second column. Using the relationship first introduced in Section 4.3.3.2 with Equation 4.3, the pressure losses for the outlet variants are "normalised" to the mass-flow-rate of the Control Outlet. This is a simple method of comparison, but allows a general ranking of total system losses using an identical mass-flow-rate for all the tested shroud outlets.

The results from the table can be interpreted as follows: the higher the normalised pressure drop, the better the shroud at restricting the flow and vice-versa. Consequently, the results show that the Control Outlet is best at restricting the flow, and thus can best reduce the amount of air being pumped through the domain, as borne out by it having the lowest mass-flow-rate and windage power loss. The shroud with the flattened outlet is worse, with a pressure loss that is 15.1% lower, and this contributes to it having windage that is 4.81% higher. The shrouds which are very open all have very similar total pressure losses, being around 22% higher than CO (and therefore less restrictive).

From the work previously presented it can be said that the best shroud to use is one that restricts the flow at the outlet as much as possible. For a single phase simulation, this is true given the cases that have been run in this section; however, once the impact of a secondary phase (oil) is considered, it may be beneficial to allow oil to leave the area of the gear as easily and quickly as possible [22, 50]. The next section will qualitatively look at the changes in the flow field caused by the alterations to the outlet of the shroud and assess their likely impact upon a second phase in the domain.

5.3.6 Flow field study

Rapley stated that the best shrouds have recirculations between the face of the gear and the shroud [33]. These recirculations act to suppress the ability of the system to pump air by effectively reducing the net mass-flow-rate through the space between gear and shroud and hence overall system. This section will look at the changes in flow-field for the different outlet cases tested, and assess the impact that changes to the shroud have made, and the likely knock-on effect for when oil is present. Comparison of the simulations will be made using visualisations and some qualitative data. This section links to Section 6.5.2 in Chapter 6.

Radial velocity can be used as an excellent indicator of how the shroud is acting, as any recirculations will be clearly visible through having a negative component

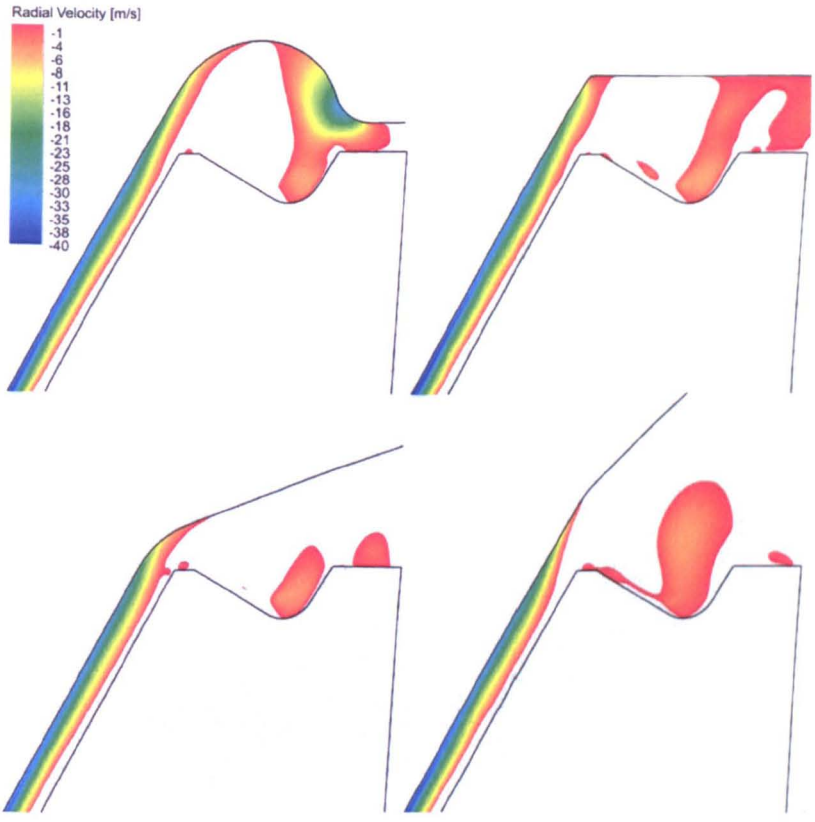

Figure 5.15: Contours of time-averaged radial velocity on periodic plane. Clockwise from top left: CO, FO, LO, HO

of radial velocity. Figure 5.15 shows contours of radial velocity between 0 and -40 m/s. Radial velocities larger than this are clipped; those smaller are not present in these areas of the systems. The structures of the negative radial velocities are similar in the space between shroud and gear face, although it can be seen that the white gap indicating a positive radial velocity is larger for the bottom two systems (HO and LO), meaning that the negative flow is larger for the CO and FO systems, although the differences are tiny (the clearance between shroud and gear is 1.76mm). This is typical of all flow variables in the region between shroud and gear face — the flow structure is remarkably similar, which is in line with the findings that the gears act in the same way when increasing the velocity and static pressure of the air. This leads to the interesting finding that the gears are acting almost entirely independently of the shroud outlet design.

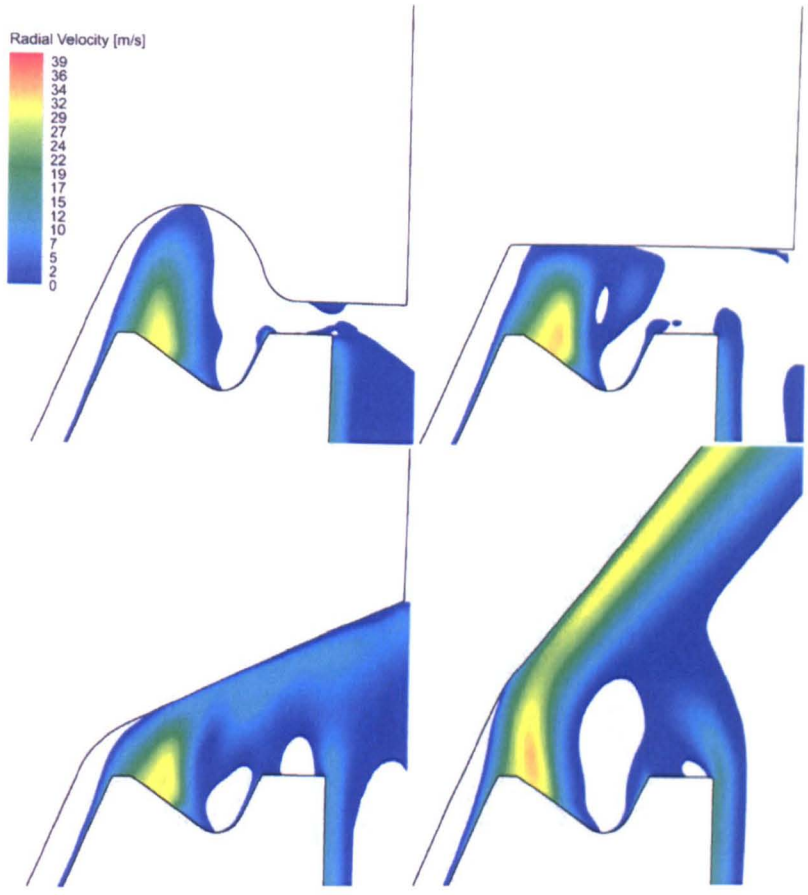

Figure 5.16: Contours of averaged radial velocity on tooth valley midsurface. Clockwise from top left: CO, FO, LO, HO

Inspection of the positive components of radial velocity allows a large difference in the structure of the flow after the gear teeth to be identified. Figure 5.16 shows time-averaged contours of radial velocity between 0 and 40m/s, and uses a plane that passes through the centre of the gear tooth valley[8], allowing the flow to be visualised as it leaves the valley of the tooth. The top two shrouds, CO and FO, have similar flow structures whereby the flow is ejected radially, but halted by the shroud, and this will cause the flow to turn through around 90° to exit the shroud into the rear chamber[9]. A similar, although less extreme version of this also occurs for the Hybrid Outlet (bottom left) and the Medium

[8]The area within the valley itself is not shown, as the surface is created by rotating the periodic boundary by half a tooth

[9]This aspect of the shroud flow causes losses and hence aids its restrictiveness

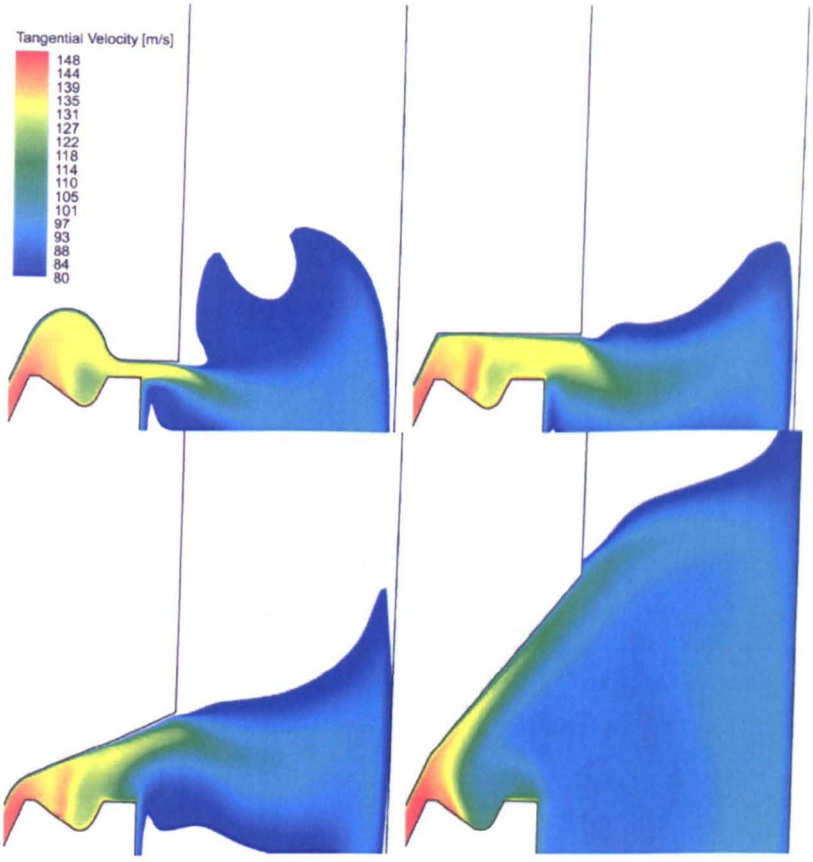

Figure 5.17: Contours of averaged tangential velocity on tooth valley midsurface. Clockwise from top left: CO, FO, LO, HO

Outlet (not shown), whereby the flow's radial trajectory is impeded slightly by the shroud, although in these cases the flow still has a radial velocity of around 15m/s, as opposed to CO and FO's near zero radial velocity. The Large Outlet is very different from the others in that the flow leaves the vicinity of the gear with a high radial velocity, up to around 30 m/s. The flow can be seen to be travelling up the surface of the shroud, and will move away from the gear very quickly, possibly highlighting its advantages at managing oil when a secondary phase is present.

Figure 5.17 is a plot that shows the averaged tangential velocity on the same plane as used in Figure 5.16. This again shows that there is a large difference in the structure of the flow between LO and the other gears. The tangential velocity of the flow leaving the valley of all of the gears is very similar, due to

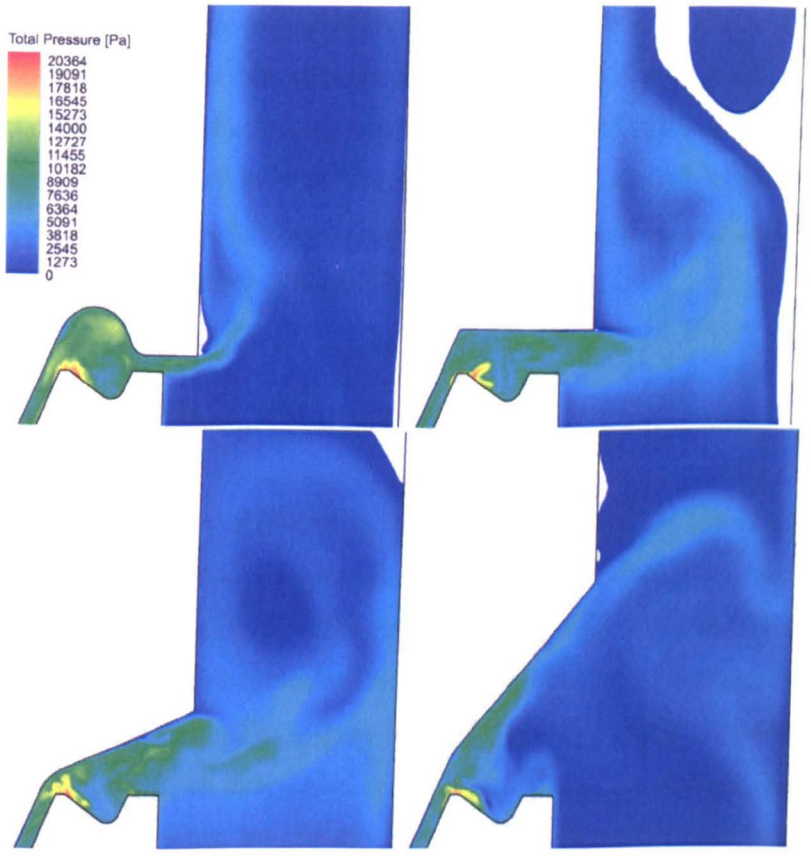

Figure 5.18: Contours of total pressure at time = 0.049s on periodic plane. Clockwise from top left: CO, FO, LO, HO

their identical rotational speeds and diameters. The freedom of the flow to travel radially outwards means that, for LO, the area of highest tangential velocity corresponds to the areas of high radial velocity on the surface of the shroud seen in Figure 5.16. The area in the immediate vicinity of the gear valley exit has a lower tangential velocity on the whole for LO, as the flow is not captured or restricted by the shroud in this area. For CO, in the top left corner, the shroud shape means that the flow has a high component of tangential velocity in the area before it is ejected into the chamber behind the gear.

FLUENT does not allow for time-averaged total-pressure to be saved within its data files; however, an instantaneous snapshot of total pressure at time = 0.049 seconds allows differences in the travelling flow structures and vortices to be looked at. Figure 5.18 shows contours of positive total pressure (relative to

gauge which is 1 atmosphere), and the unsteady nature of the flow exiting the gear can be observed. In line with the findings of tangential and radial velocity, the structures travel predominantly with the main bulk of the flow that is ejected from the gear. This is specific to the geometry of the shroud, particularly the outlet, and the rear chamber too, so the impact within an aero-engine IGB would need to be assessed on a case-by-case basis.

5.3.7 Implications of the presence of oil

One of the key objectives of changing the outlet design of the shroud is to assess whether a shroud that has a larger, and therefore less restrictive, outlet would allow oil to leave the vicinity of the gear more readily to prevent re-ingestion. The results that have been presented in this section have been carried out using a single-phase formulation only — there is no oil being modelled. However, as will be seen in Chapter 6, oil suspended within the air tends to follow the primary phase's trajectory closely, so the results from this section can inform shroud designers qualitatively when assessing the impact of oil on the system and the risk of it being trapped.

From the results in this section, it is clear that the system with the largest outlet (LO) will allow oil to be vented away from the gear, as there are large components of radial velocity. It has a windage moment that is 12.2% higher than the control shroud, so the benefits of preventing oil churn would need to outweigh the cost of increased single phase windage, and a similar conclusion would be true of the shroud with the Medium Outlet too. Johnson *et al.* [22] showed that the single phase component of windage is the largest contributor to total windage, but flooding of a chamber with oil due to poor scavenge could change this balance. The Hybrid Outlet shroud has a single phase windage moment that is 8.3% higher than the control shoud, which is better than LO or MO, and it still has relatively high radial components of velocity away from the gear (around 15 m/s), so it could well be a better overall option than one of the more free-flowing outlets. Finally, the outlet with a flat 4mm clearance

(FO) may provide the most practical option for shroud design when managing the presence of oil: it takes up a less radial space than CO due to it not having the "gutter" of CO, and has a single phase windage loss that is only 4.8% worse, while still allowing oil to escape easily. Looking at Figure 5.15, it is possible to see that there are a large component of negative radial velocity from the gutter of the shroud for CO, which may well cause pooled oil to be stripped off a film, back towards the gear, limiting its performance in a practical application.

Section 6.5.2 in Chapter 6, will simulate oil films on the surface of shrouds in order to assess how good a single phase conclusion can be, when results from a two-phase simulation are known.

5.4 Conclusions

This chapter has looked at the effect of changing the design of the inlet (Section 5.2) and the outlet (Section 5.3) on a shrouded spiral bevel gear system. The aim of doing this was to assess the impact upon windage and flow field of alterations to the system, and how these changes to the shroud geometry may have an impact upon oil management.

It has been shown that a nose of the shroud is an effective way to reduce the windage, by making the inlet to the shroud more restrictive for a flow attempting to pass through. However, the sudden contraction of the flow at the inlet down to the 1.5 mm radial clearance is the best way of reducing the windage — and the findings of Rapley [33] and Winfree [50] have shown that further reductions in windage are possible if this gap is made smaller. The length of the passage can have an effect too; the longer the passage, the higher the pressure drop and the lower the consequent windage, but consideration must be made to the mass of the shroud if a long inlet passage is used in terms of expense and resonance from the cantilevered material.

Analysis of the windage when the outlet to the shroud is changed shows a strong correlation between increasing outlet size and single phase windage. The largest shroud outlets provide a smaller restriction to the flow, and consequently allow a larger mass-flow-rate of air through the system. It was also seen that the worst shroud outlet designs affected the system single-phase windage only half as adversely as the worst shroud inlet design, thereby indicating their relative importances to the reduction of windage.

Management of oil between shroud and gear is known to be most effective if oil can escape easily [22, 50], and the work in this chapter has shown that a shroud outlet that is more open has a more defined air flow away from the gear, which could drive oil away, preventing re-ingestion. A balance between allowing oil to escape with more free-flowing shroud without impacting significantly on the single phase windage will be the best compromise, and in the context of an aero engine there will also be a limiting factor of available radial space within a gearbox.

The next chapter will expand upon the work presented in this chapter by performing a study looking at the impact of a secondary phase of oil droplets and a thin-film under the shroud. It will start off by assessing the destination of droplets released from within the domain, and advance onto modelling the formation of a thin film on the surface of the shroud and applying the techniques developed on some of the shroud outlets studied in this chapter.

CHAPTER 6

Discrete particle and thin-film modelling

6.1 Introduction

The previous two chapters have looked at the effect of changing the gear (Chapter 4) and changing the shroud design (Chapter 5) on the overall system's windage loss. The results from these have shown that it is possible to reduce gear windage by careful selection of the gear and shroud; however, all of the simulations that were conducted used only a single-phase solution methodology, ignoring a significant contributing factor of oil on the total losses of the system. This chapter will address that by assessing whether the CFD solutions currently available in software such as FLUENT can be used to model oil trapped between the gear and shroud, and whether the trajectory and velocity of the oil qualitatively matches with results from experimentation. A film on the surface of the shroud will also be modelled, in order to judge whether the software can be used to estimate locations that may be susceptible to drying out and consequent high levels of heat transfer.

The oil within the gearbox is necessary to lubricate the meshing gears and also to remove heat away from the gearbox. Degradation of the oil can occur when it is not scavenged and it gets too hot, additionally hot-spots can arise on surfaces that have dried out due to insufficient covering of oil. Therefore, it is essential

to ensure that there is enough oil in the gearbox, but not so much that it cannot be removed adequately.

Johnson *et al.* [22] and Winfree [50] both conducted a number of experiments looking at the impact of injected oil flow rates, and the influence of quantity and location of holes in the surface of the shroud. For a full review of the work that is available, see Section 2.5.1 in the literature review. Very little work has been conducted computationally, with a single study by Kawasaki Heavy Industries reviewed in Section 2.5.2.

The solution methodology is described in Section 3.4.10. A Discrete Particle Model (DPM) is used, which simulates oil as discrete particles which are influenced by and able to influence the primary phase's momentum. There is no relevant data available regarding the droplet sizes and velocities in the space between shroud and gear. This is due to the difficulty in measuring these variables experimentally with the speeds and limited space available. The DPM is a robust and well validated model as it underpins numerous industrial CFD applications, notably in combustion. This is advantageous, because in spite of a lack of validation data, the models used are established and within the limits of our assumptions. Some work has been done by Glahn *et al.* [15] on droplet generation off the rims of disks, and this will inform the data used to specify injection quantities. Section 6.2.1 provides a detailed explanation of the simulation setup.

Section 6.2 establishes the effect of droplets that are suspended in the internal gearbox (IGB) being ingested into the space between gear and shroud, with emphasis on their likely destination. Section 6.3 looks at the effect of droplet size when particles are released from the outer diameter of the gear. There are two motivations: firstly, it is a very likely location for oil to be shed; secondly, modelling a film on a surface using the DPM of O'Rourke and Amsden [30] available to the present work requires a high concentration of particles in each surface mesh cell to work effectively. The same logic is applied for looking at particles released from the toplands of the gear teeth in Section 6.4. It was felt that these locations would provide a high concentration of particles hitting the

shroud in a localised area. Lastly, Section 6.5 studies the use of the DPM based film model to simulate a film on the surface of the shroud in order to establish whether the results are physically realistic, and if so, what they can tell us about the likely destination of oil inside the domain.

6.2 Droplet releases from shroud inlet

This section looks at the destination of droplets that are ingested into the space between gear and shroud through the inlet to the shroud. The pressure drop at the inlet to the shroud is caused by the rotating gear accelerating the air, which effectively causes the higher pressure in the chamber/IGB to force air through the domain. Johnson *et al.* [22] showed experimentally that a mist will form in a similar chamber at high rotational speeds of the gear, so it is logical to assume that the IGB of an operating gas turbine will also have a suspended mist of oil within it. There are two unknown quantities which will be studied in this section — the size distribution and velocity of the particles. Logical assumptions will be made, and a parametric characterisation of the effect of changing one or both of these variables will be conducted.

The analysis takes the form of quantitative comparison of the destination of the droplets on the surface of the shroud. This is introduced in Section 3.5 in the methodology chapter, and expanded upon within this chapter. The key method is the use of a non-dimensional length that follows the profile of the shroud and allows the point at which a particle hits the shroud to be defined as the distance from the "start" of the shroud, which is marked on Figure 6.1. The figure shows a tangential view of the shroud, with key features numbered. These numbered features refer to parts of the shroud which involve a change in direction, and are marked on charts within this chapter to aid reader interpretation of histograms showing the point at which particles hit the shrouds.

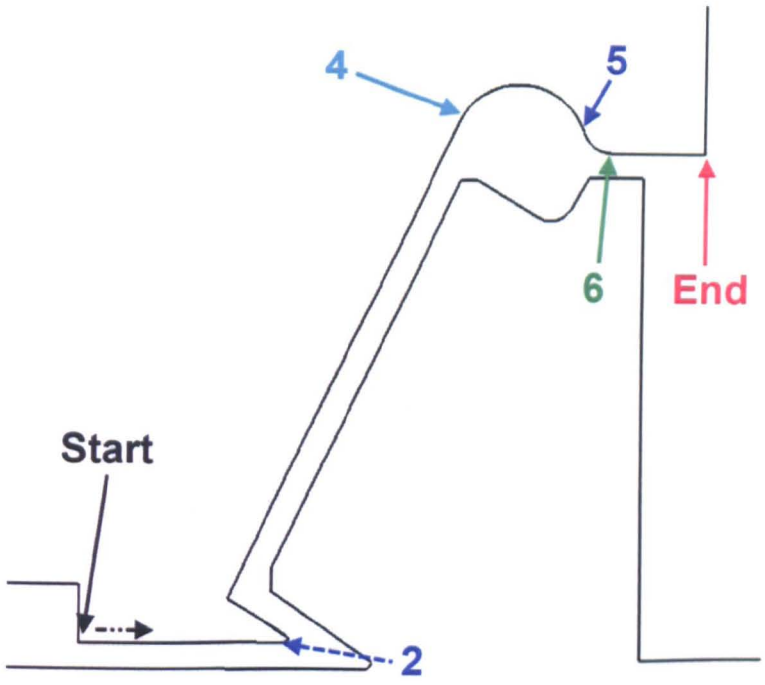

Figure 6.1: Key shroud features as seen in histograms marked by colour and location

6.2.1 Simulation setup

The injection for particles entering the the space between gear and shroud is done using the same surface used for establishing the pressure drop after the restriction of the nose (Called "Nose Restriction" in the previous two chapters). This surface is created at a point that is half way between the Start point and position 2 on Figure 6.1. The surface is annular for a whole gear, but as just a single tooth is modelled, it forms a portion of the entire annulus. The injection area is shown in dark red on Figure 6.2, which also shows the shroud in transparent yellow, with the gear in grey.

A number of different velocity profiles are tried for the injection conditions. This is in order to gauge the sensitivity of the system to a range of values. A value of zero m/s velocity for all particles is an extreme case, and is used to replicate the effect of particles instantaneously appearing in the domain and being allowed to pick up a velocity from the core air flow, with a possible lag in response for the larger ones. The other end of the spectrum is where the particles are initialised

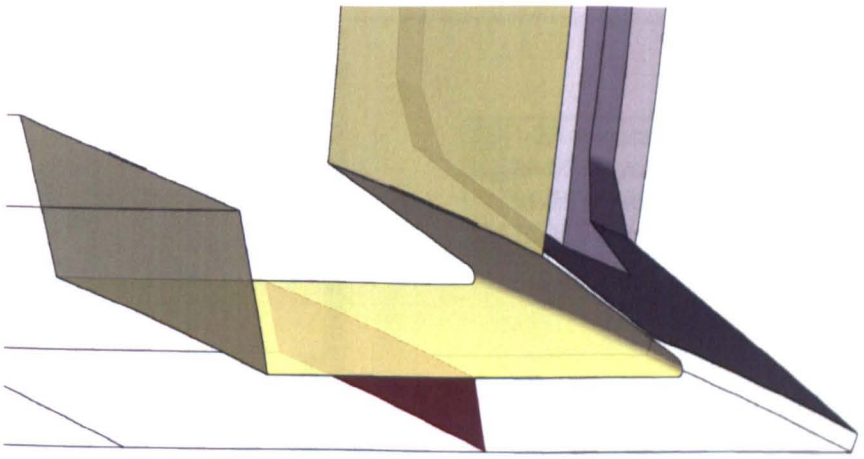

Figure 6.2: Injection location marked in red, at the inlet to the shroud marked in yellow

with a very high tangential component of velocity, equal to the maximum tip speed of the gear of 171m/s, which simulates a very high swirl within the IGB. Both of these cases are extreme, and physically unlikely, so in an effort to attempt a physical condition, "cell" velocity is used. In the absence of any knowledge on the amount of swirl at the entrance to the system and on the local oil attributes, this is necessary. This is a condition created for this thesis whereby a particle that is injected into the domain is initialised with components of velocity that are equal to the components of velocity of the air phase within its initialisation mesh cell. A user-defined-function (UDF) is created in FLUENT that automates this process and additionally allows for finer control of the component of velocity; for example the cell velocity can be used with the radial velocity set to zero. The use of the cell velocity condition ensures that particle velocities are representative of those likely to be found entering the inlet of the shroud. This is a pragmatic approach given the absence of data to use as injection conditions.

A Rosin-Rammler size distribution is also used, as detailed in Section 3.4.10.2, to charaterise the distribution of droplets at the shroud entrance. The particles range in size from 1 to 100 microns, with a mean size of 10 microns. This allows for characterisation of the system response to various particle sizes. Additionally, uniform distributions of 1 or 100 microns are used. The equivalent flow rate of the

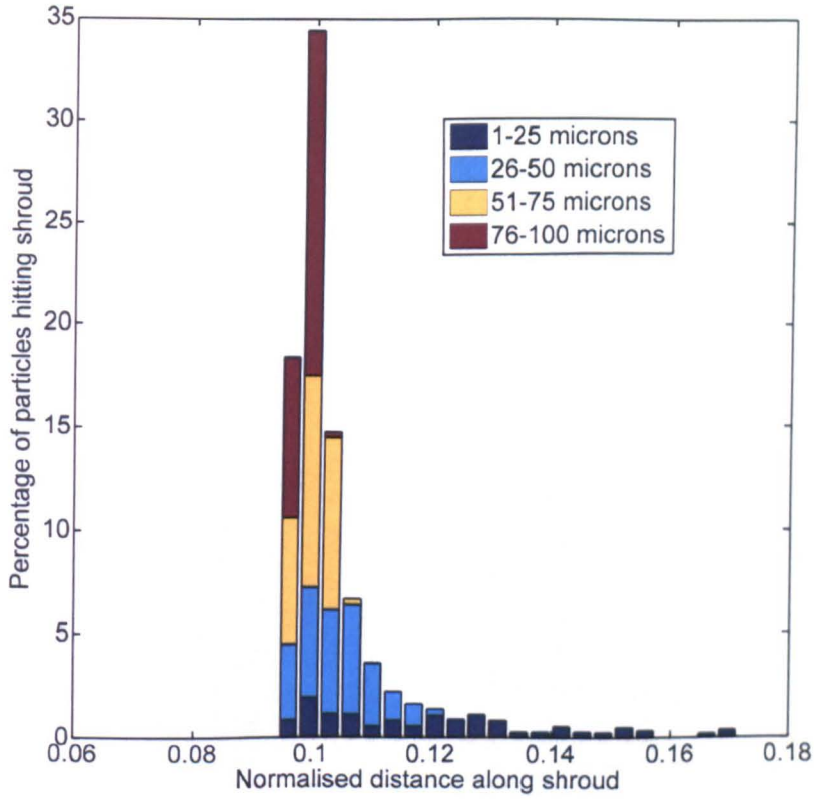

Figure 6.3: Particle distribution along shroud, coloured by size. Zero initial velocity

oil particles is 1kg/s for a whole gear, with a corresponding amount since just a single tooth is modelled. This mass of oil is used as it sits within the range tested by Johnson *et al.* [22] in their two-phase experimentation on a similar shroud and identical gear. The particles are injected with a temperature of 300K, and heat transfer is permitted between the two phases, although the relative differences in temperature are minor (maximum 20K).

6.2.2 Effect of velocity

This section will look at the effects of the injection velocity on the destinations of droplets released from the inlet of the shroud. Figure 6.3 is a histogram showing the distribution of particles released with zero initial velocity hitting the surface of the shroud. The x axis is the normalised distance along the shroud, and the injection surface (shown in Figure 6.2) is located at 0.097 Shroud Normalised

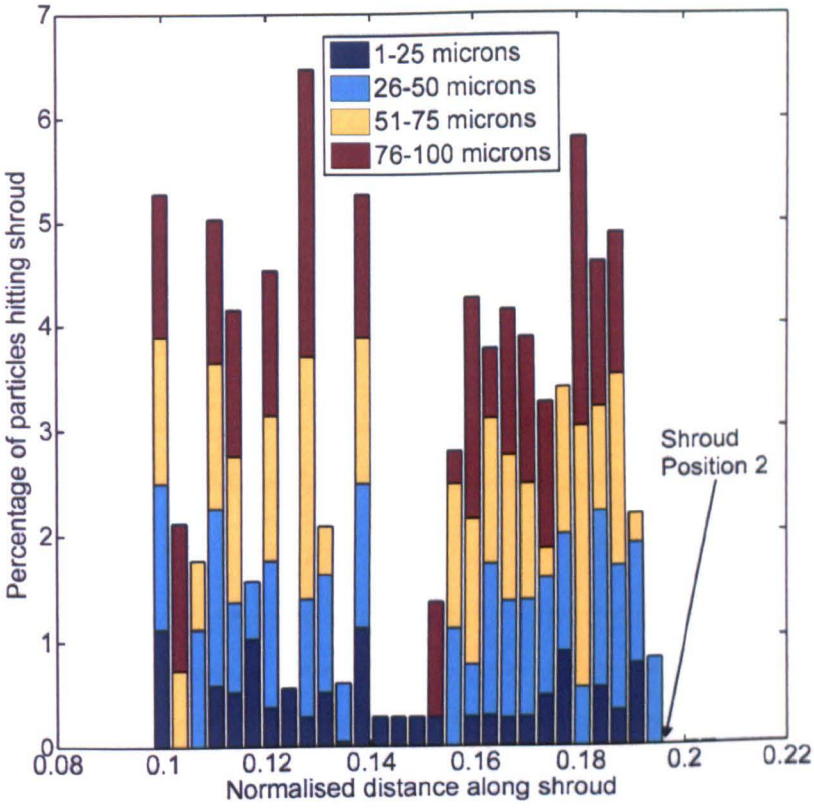

Figure 6.4: Particle distribution along shroud, coloured by size. Cell initial velocity

Distance (SND). The nose of the shroud (position 2) is at 0.197 SND, so does not feature on this chart. The particle sizes are grouped into groups each covering a 25 micron range, which allows the difference in particle destinations to be further analysed based on size.

The figure shows clearly that the particles are hitting the shroud in a very small area, just a couple of millimeters from their injection location. 84.9% of the particles released from the surface are indeed hitting the underside of the shroud's nose, travelling in a positive axial direction; no droplets have travelled backwards, towards the inlet to the simulation domain. There is clear trend of smaller particles travelling further before hitting the shroud.

Figure 6.4 shows results from the same injection, this time with the cell initial velocity condition. There is a clear difference between this and the injection shown in Figure 6.3, with a more dispersed distribution on the surface of the

shroud. The distance that the particles have travelled before striking the shroud is longer, with shroud position 2 marked on the chart. This corresponds to the nose of the shroud, where it starts to curve back on itself.

	Droplet size (Microns)			
Injection Condition	1-25	26-50	51-75	76-100
Zero initial velocity	14.64	25	25	25
Cell initial velocity	11.56	24.16	25	25

Table 6.1: Percentage of total droplets released hitting the shroud by injection and size

Although there is a difference between the distribution of the particles that have hit the shroud in the region between the injection location and the nose, ultimately the vast majority of the particles have ended up striking this area. Table 6.1 contains data of the percentage of total droplets[1] released that have hit the shroud. All but a fraction of a percentage of the particles that hit the shroud do so before the nose (shroud position 2), so this table is representative of the differences between the two simulations in this area. Both injection releases result in all of the particles above 26 microns diameter hitting the shroud. There is a difference of 3.08% in the 1-25 micron band, indicating a difference in the motion of the smallest particles. The particles that have not hit the shroud have almost all hit the front of the gear (shown in green on Figure 3.9), with a fraction of a percent having travelled further into the domain and hit the teeth of the gear.

The results from these two simulations indicate that for two very different injection conditions, the particles will hit the shroud at relatively similar areas. This is due to the air flow having a radially positive component of velocity in the area of the particles being initialised, which causes the droplets to travel outwards towards the nose. Figure 6.5 shows this using a binary contour plot on the periodic plane which ignores magnitude of the radial flow, and just shows the positive,

[1] Actually, packets of parcels. Particles of the same size released from the same spot will always take the same trajectory, so FLUENT calculates their motion once, reducing computational time

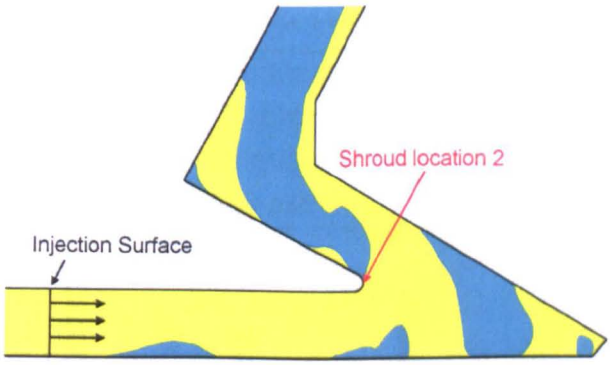

Figure 6.5: Binary contour plot of radial velocity at shroud inlet. Yellow is positive (outwards), blue negative (inwards)

outward direction in yellow and the negative, inward direction in blue. The large amount of yellow in the area of the injection indicates that the flow is radially positive, and it is this that is going to force the droplets onto the surface of the shroud — only 0.5% of the particles hit the shaft, which is a surprisingly low figure given its proximity to the injection location.

The higher dispersion of the particles initialised with cell velocity is due to them having a positive axial velocity, which allows them to travel further before being affected by the gas momentum and striking the shroud. It is possible to undertake analysis using Stokes number, St, which is a ratio of particle inertia to fluid response time. The Stokes number is defined in Equation 6.1.

$$St \equiv \frac{\rho_{\mathrm{p}} d_{\mathrm{p}}^2}{18\mu} \frac{U_0}{\delta}, \tag{6.1}$$

where U_0 is the average velocity of the flow at the inlet to the shroud, and δ is a characteristic length chosen to be the radial distance between shaft and shroud, in this case 1.5mm. Variables with a subscript of p refer to particle values. When $St > 1$, inertia of the particle is dominant over the fluid, so the particle will not follow a fluid streamline readily. The opposite is true for $St < 1$, with $St = 1$ giving an indication of the size of particle at the watershed between the two regions. A value of 3.5 microns is found to be representative of $St = 1$ using the data from the simulations presented and this fits well with the results

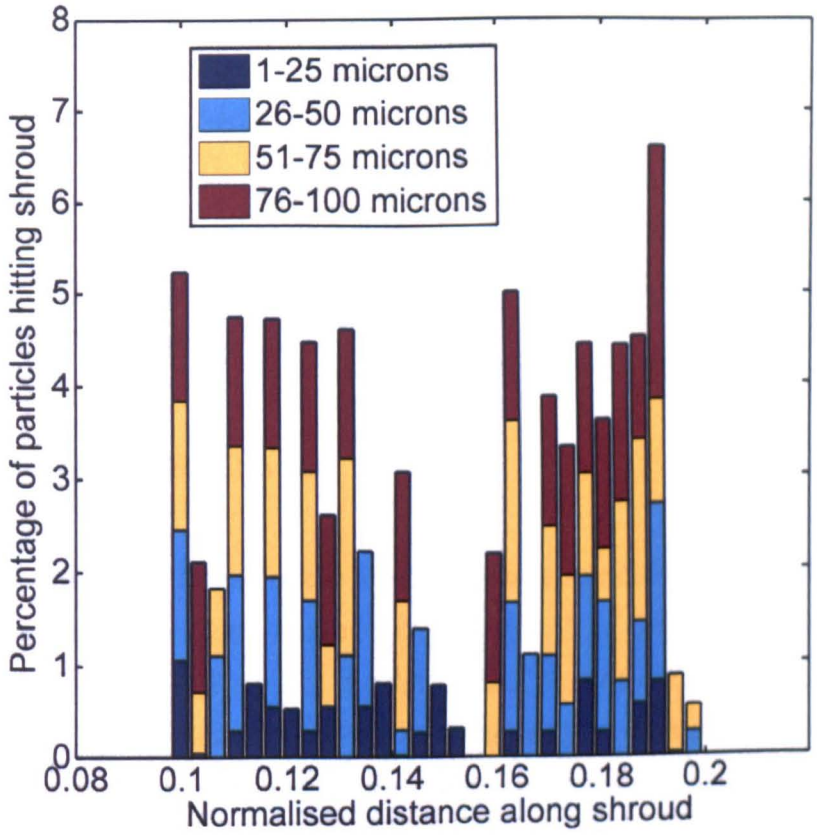

Figure 6.6: Particle distribution along shroud, coloured by size. Cell initial velocity without radial component

obtained, as it lies within the 1-25 micron band of particles that are observed to be following the flow further into the domain instead of hitting the shroud. 2.5% of all the particles released from the injection are 3.5 micron diameter or below; however, only 0.19% of the particles that have hit the shroud are at, or below, this diameter — which shows how the smaller particles are passing further into the domain.

In an attempt to identify whether the zero or cell velocity conditions are causing the particles to strike the underside of the shroud's nose, an alteration to the cell injection condition is made by simply setting the droplet's radial component of velocity to zero, while keeping the tangential and axial components. Figure 6.6 shows the results from this injection condition. It shows a similar pattern to Figure 6.4 with a dispersed collection of droplets hitting the underside of the

nose. Once again, the smallest particles have made it further into the domain than the largest ones; 94.4% of all particles over 25 microns have hit the shroud (with all particles over 75microns and 98% in the 51-75 micron band), and 40% of the smallest 1-25micron particles have also hit this area. The overwhelming end location for droplets that do not hit the shroud is the front face of the gear. This is due to the large axial velocity of the flow that fires the droplets directly at this part of the gear.

6.2.3 Particle distribution

The previous section looked at the injection velocity conditions. All of the simulations used the same Rosin-Rammler distribution. The distribution was chosen as it covered a range of sizes of droplets found to shed off a rotating disk by Glahn *et al.* [15]. The speeds of the rotating disk in that work are lower than the rotating speed of the gear used in this thesis, but it is representatively comparable, and provides a good basis for choosing the droplet sizes. This section will look at injections which are uniformly distributed, with a single size of oil droplet chosen. If a difference exists between the destinations of similar sized droplets between the Rosin-Rammler and uniform distributions, it is likely that there is a strong feedback coupling between the air flow and the oil. This feedback of momentum to the primary phase will affect the motion of the particles.

Figure 6.7 shows results from a simulation with a cell inlet velocity condition, but this time only large, 100 micron particles being released. The total flow rate of oil remains the same as the previous cases. All of the droplets that are released have hit the shroud, before the nose — this is expected given the size of the particles. There is a degree of regularity to the points at which the particles have hit the surface of the shroud, and this is due to the stratification of the particles at the injection location. The droplets are injected at the centre of each mesh cell, and the particles which have travelled the furthest along the shroud are injected closest to the shaft and have had the opportunity to move further axially. Additionally, due to the circumferential homogeneity of the flow at the injection

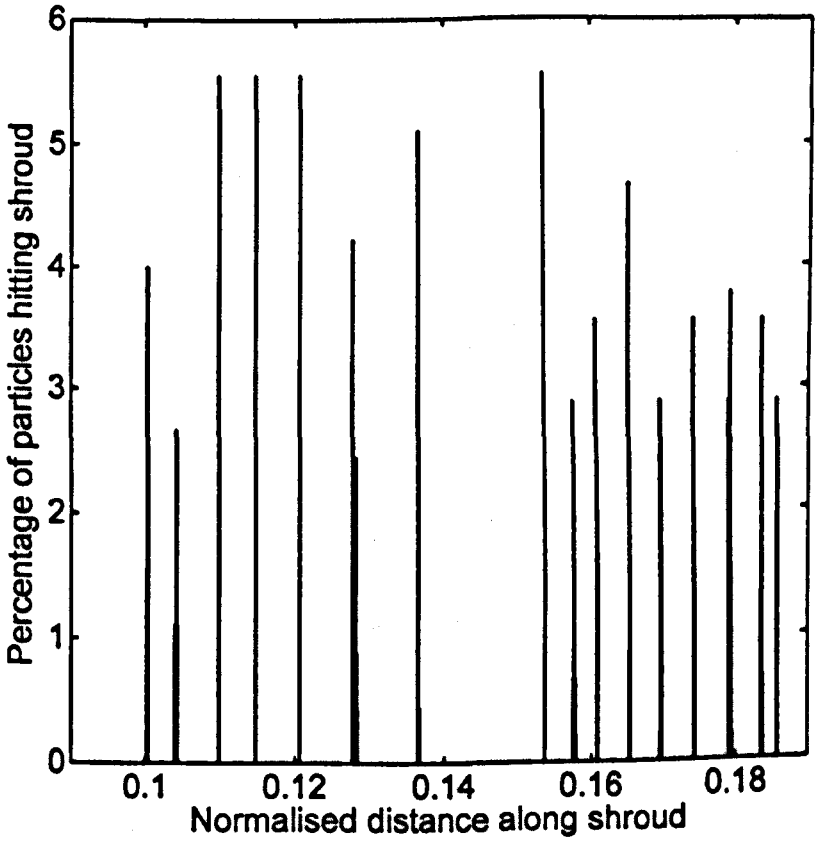

Figure 6.7: Particle distribution of 100 micron droplets along shroud. Cell initial velocity without radial component

location, droplets which are injected at one radial position tend to hit the shroud at a similar axial distance — the circumferential location of the particle only has a minor impact.

The results for the large particles match well with the findings from Section 6.2.2 in which larger particles did not make it past the nose of the shroud. A simulation using only 1 micron sized particles complements these findings by not having any particles hit the shroud at all, with them instead travelling on through the domain and predominantly hit the front of the gear and entering the gear tooth passage.

Figure 6.8 shows the progression of these particles through the first part of the domain. The subfigures are captioned based on their time after the initial injec-

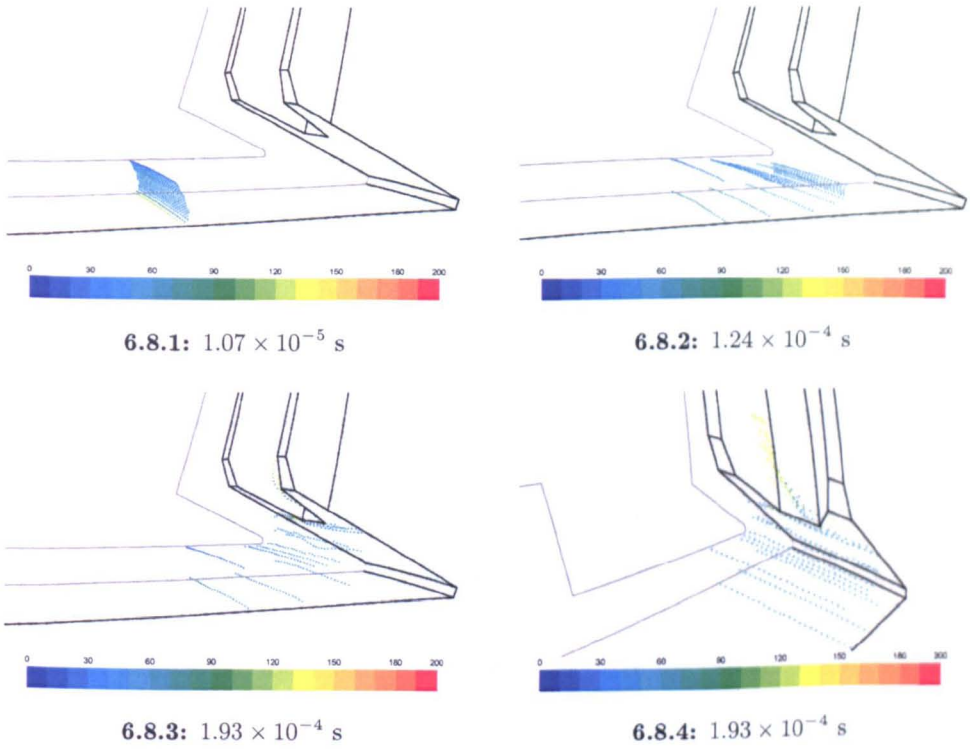

6.8.1: 1.07×10^{-5} s

6.8.2: 1.24×10^{-4} s

6.8.3: 1.93×10^{-4} s

6.8.4: 1.93×10^{-4} s

Figure 6.8: Passage of 1 micron diameter particles injected from shoud inlet with cell velocity, identified by time after injection, coloured by velocity magnitude

tion. Figure 6.8.1 is the distribution very shortly after injection, and the "sheet" of particles can be seen to travel towards the front of the gear, and their progress after 1.24×10^{-4} seconds can be seen in Figure 6.8.2. In this figure, the formation of wall-bounded flow has meant that the air in the centre of the inlet (radially) has travelled furthest, whereas the particles nearest the shroud or shaft have not. Interestingly, the particles near the shaft have the highest velocity magnitudes due to the rotational speed of the shaft. Finally, Figure 6.8.3 and Figure 6.8.4 show the same point in time, 1.93×10^{-4} s, but from two different viewpoints. There has been enough time for a lot of the particles to reach the gear, and some have terminated on the gear front, but many can be seen to be travelling up the gear tooth valley. The view in Figure 6.8.4 shows the way in which the flow enters the gear tooth valley, with it accelerating and striking the flank of the gear tooth.

6.2.4 Conclusions

The results from this section have shown that for all except the smallest particles, the majority of the droplets released hit the underside of the nose of the shroud, regardless of the injection velocity conditions for the range of particle sizes considered here (1-100 microns). The results seen here are physically realistic enough to indicate that a very fine mist in an IGB would be likely drawn in through the shroud and either hit the gear itself or pass through the domain. It may be possible to simulate this suspended oil mist using an effective density increase to represent a volume average of air and the oil. Larger droplets that strike the shroud will likely form a film at the nose. This oil will be likely stripped and ingested by the gear unless managed through effective shroud design.

The work in this section has not been able to state for certain the effect of oil ingestion at the inlet to the shroud, as there is no data available about the state of oil within a gas turbine IGB. However, it has shown that the CFD software is able to model droplet transport into the space between gear and shroud, and present data about likely destinations for droplets of different sizes.

6.3 Droplet releases from gear outer diameter

This section looks at the destination of droplets released from the outer diameter of the gear teeth. There are a few intended purposes in doing this: firstly to perform a similar parametric study as in Section 6.2 for the shroud inlet, and secondly to ascertain whether this injection location is suitable to creating a film on the surface of the shroud. Finally, this also assumes a likely scenario whereby oil sprayed at the meshing point forms a coating of oil on the gear that travels along the gear teeth and is shed off the outer diameter.

It has been shown experimentally that a film will form on the surface of the shroud. Figure 6.9 is a photo of an experiment carried out by Johnson *et al.* [22] which highlights this, albeit for a set of circumstances which do not exactly

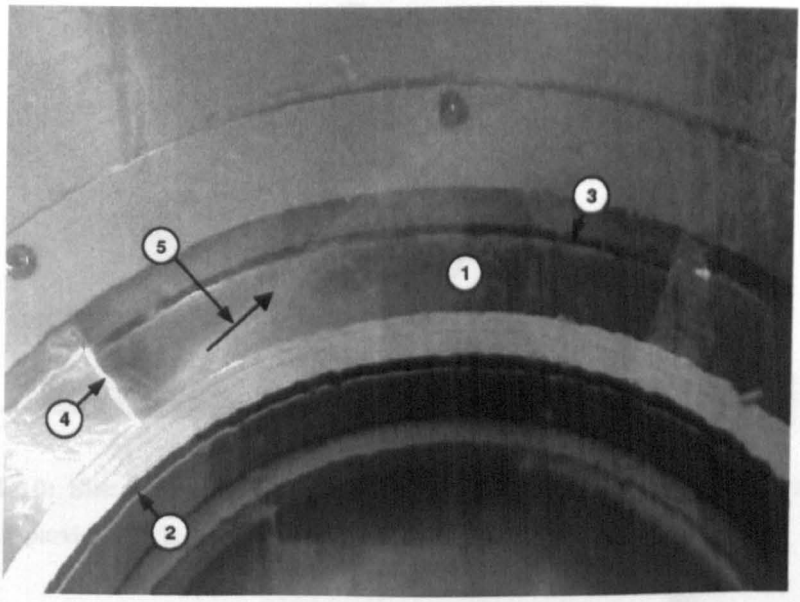

Figure 6.9: Oil leaving slotted shroud at 5000 rpm. 1: Face of crown gear; 2: Shroud inlet; 3: Shroud exit space; 4: Start of shroud slot; 5: Oil exiting the shroud [22]

match those used in this body of work. The experiment in question is a gear rotating at 5,000 rpm with a transparent shroud to enable visualisation of the oil — which gets progressively more difficult at higher rotational speeds due to the presence of oil mist. There is also a slot within the shroud, which allows oil to escape the area between shroud and gear, and it is this slot which allows the fast moving film on the surface of the shroud to be seen leaving with a large tangential velocity.

Internal work at the University of Nottingham has shown that a DPM based film demands that there is a large number of particles hitting the area of the shroud in which the film is to form. This is because the O'Rourke and Amsden [30] model used in FLUENT is inherently mesh-dependent, with the film height on the surface being determined by dividing the volume of the droplets that are "tagged" as being in the film for a cell, by that cell's surface area[2]. With an insufficient amount of particles hitting each cell, a "chequerboard" effect can be seen in the film. This is illustrated by the sketch in Figure 6.10, which shows on

[2]This model was developed for ICE injections assuming a large number of small atomised particles hitting the ICE chamber walls

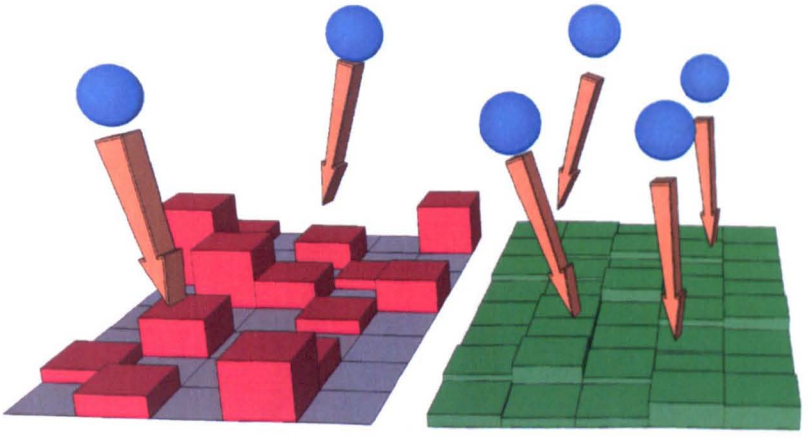

Figure 6.10: Sketch showing how a "chequerboard" style film can arise from a smaller number of particles striking a surface

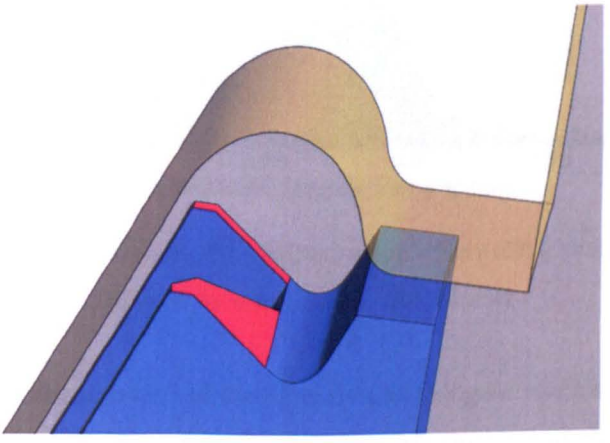

Figure 6.11: Injection location at gear outer diameter. Gear is marked in blue, shroud in yellow, periodic boundary in grey and injection surface in red.

the left-hand-side how a smaller number of particles hitting a surface mesh can result in a film with a very discontinuous height, from one cell to the next. The right-hand-side shows a more realistic film forming because of a larger number of particles per cell. A conclusion that was drawn is that the quality of the film can be affected by the number of particles hitting a wall, or by the size of the cells on the surface mesh. Therefore, the work in this section will be used to ascertain whether a sufficient amount of particles will hit the surface of the shroud when released from the outer diameter of the gear to form a good surface film.

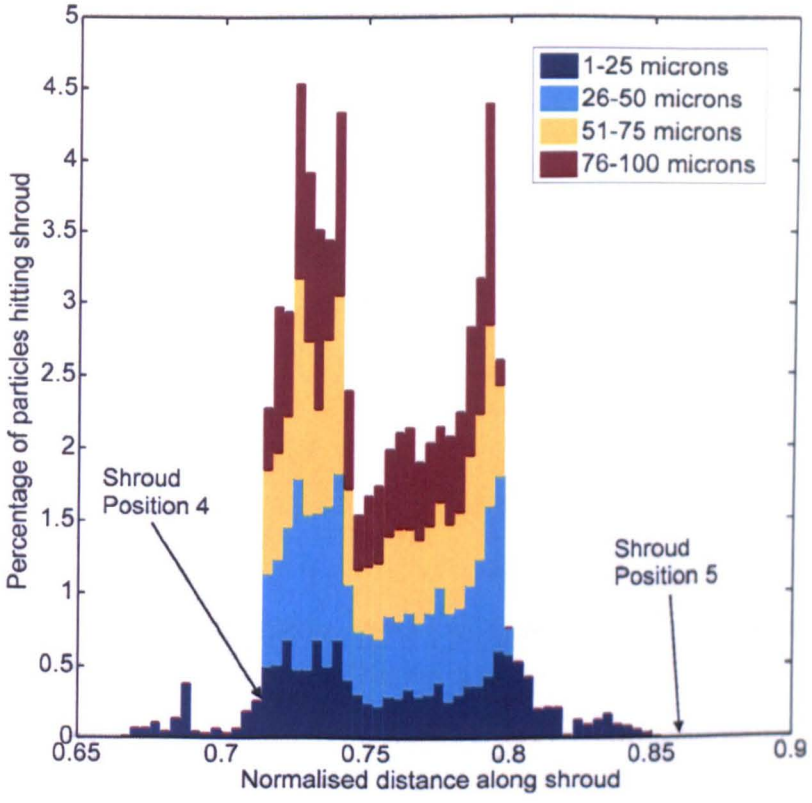

Figure 6.12: Particle distribution of 1-100 micron droplets along shroud, released from gear outer diameter and coloured by size. Zero initial velocity

Figure 6.11 shows the location of the injection at the gear teeth's outer diameter. The surface can be seen in red in the figure, with the rest of the gear shown in blue. Due to the use of periodic boundaries (one of which is marked in grey) that pass through the toplands of the teeth, the injection is split into two, although it is still treated as a single surface by FLUENT, and this will not affect the results.

6.3.1 Effect of velocity

This section looks at the destinations of droplets that are released from the outer diameter of the gear, and attempts to identify trends caused by changing the velocity of the particles when injected. It is similar to the work that was done in Section 6.2.2; however, in this case the droplets will hit the shroud near the gutter, so reference should be made once again to Figure 6.1 for identification of

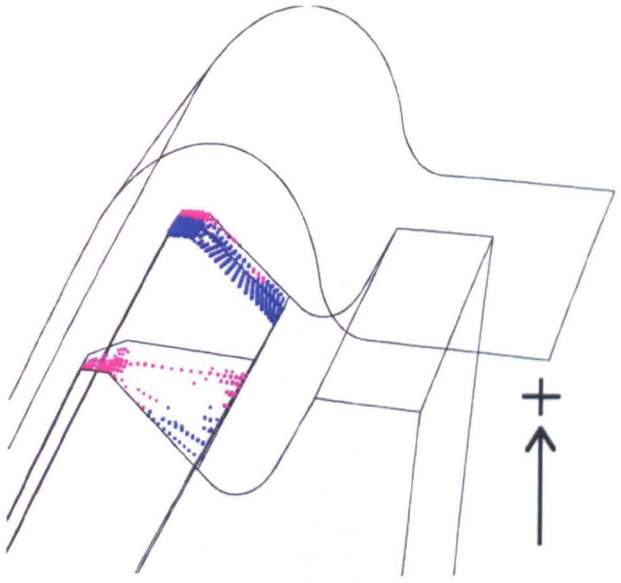

Figure 6.13: Binary plot of particles just after injection coloured by radial velocity. Blue is positive (outwards), purple is negative (inwards)

the shroud features.

Figure 6.12 shows the distribution of particles hitting the shroud having been released from the gear outer diameter with zero initial velocity. This is an unlikely initial droplet condition, as droplets will almost certainly have a high radial and tangential speed, as seen in Glahn *et al.* [15]. Nevertheless, it allows parameterisation and completeness of the effect of the initial velocity. As seen in the figure, there is a large concentration of particles, of all sizes hitting the shroud between positions four and five, which corresponds to the "gutter". The smallest particles, in the 1-25 micron band show some more dispersion, in particular in the direction of the shroud that is heading back towards the inner diameter of the gear.

An interesting aspect of the distribution seen in Figure 6.12 is the large dip its middle. This is caused by a negative component of radial velocity at some parts of the tip of the gear teeth which results in some particles proceeding to hit (and be terminated in this initial simulation) at the surface they were just released from. This can be seen in Figure 6.13 which shows the state of the particles a

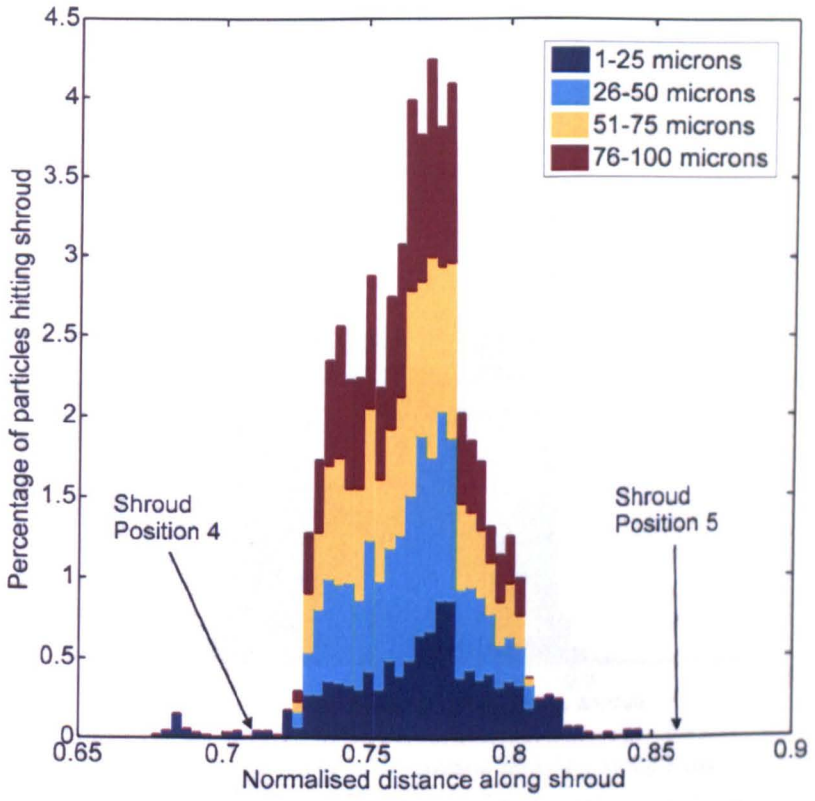

Figure 6.14: Particle distribution of 1-100 micron droplets along shroud, released from gear outer diameter and coloured by size. Cell initial velocity

couple of timesteps after release. The particles are coloured by the sign of their radial velocity only, with blue being positive (and heading towards the shroud), and purple being negative (and heading back towards the release surface). There are already gaps in the distribution where some particles have terminated almost immediately, and most of the particles which are heading outwards are doing so on the side of the gear tooth tip that is on the far side of the gear tooth valley, viewed from the figure's perspective.

Within a physical IGB, the particles that hit the gear tooth outer diameter would be very rapidly spun off the gear, so this injection condition cannot be considered representative of the situation within an engine, but by showing what happens when the particles have zero initial velocity, there is a defined boundary to the parametric investigation.

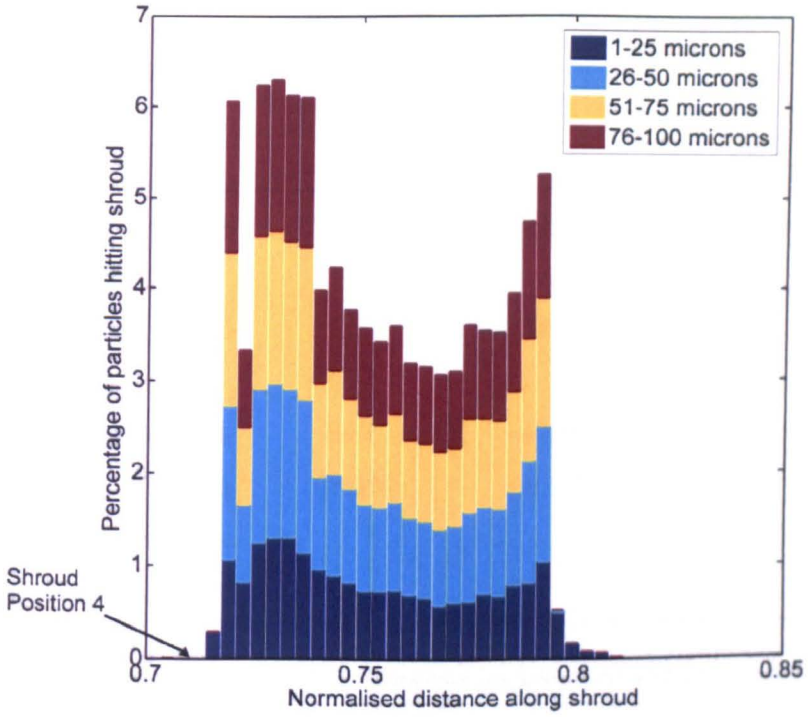

Figure 6.15: Particle distribution of 1-100 micron droplets along shroud, released from gear outer diameter and coloured by size. Initial velocity 171m/s radially

The second simulation conducted uses the "cell" boundary condition introduced in Section 6.2.1, the results of which can be seen in Figure 6.14. There is a difference in the shape of the distribution when compared to Figure 6.12, with slightly more "bunching" of the particles around a central location. There is also a slight shift of the particles to the right on the graph, which is due to the axial component of velocity in the cells causing the particles to immediately start moving through the domain, before hitting the gutter.

The final case in this section that was tested is one with a very high radial velocity; this is the opposite extreme from the case when there was zero initial velocity. The particles are injected with a radial velocity of 171m/s, which is equal to the tangential velocity at the tip of the gear at its 12,266 rpm rotational speed, representative of maximum take-off engine setting. This is the absolute maximum radial velocity that a particle could ever be given as it is spun off a gear, and in reality the figure will be only around 50% of the tangential speed as seen by Glahn *et al.* [15]. The purpose of this injection condition is to purposely force

	Injection condition		
	Zero Velocity	Cell Velocity	Radial Velocity = 171m/s
Total number of injected particles	8400	8400	8400
Number hitting injection surface	2317	3494	0
Number hitting shroud	5856	4720	8010
Percentage hitting shroud, and between 0.7 and 0.85 SND	98.5%	99.1%	99.7%

Table 6.2: Comparison of particle destinations for zero, cell and high radial velocity injection conditions

particles to head directly for the surface of the shroud, to ascertain suitability for an investigation into film modelling, and to also compare its results to those from the other cases in this section.

Figure 6.15 shows the results from this injection condition, and it is clear that the particles have dispersed less than the previous two cases. Shroud position four is marked on the graph; however, position five is just after 0.85 shroud normalised distance, outside the scale. Even with the large radial velocity involved there has been some dispersion of the smallest particles, and it would take around 1.17×10^{-4} seconds for a particle to reach the shroud, which accounts for 22 timesteps in the present simulation, so there is enough opportunity for the smallest droplets to be entrained slightly by the core air flow leaving the gear tooth valley.

A comparison of the destinations of particles for the three simulations in this section can be seen in Table 6.2, and immediately it can be seen that for all of the simulations there are some large similarities. The most striking aspect is that when the particles strike the shroud, they do so within a very small space between 0.7 and 0.85 normalised distance along the shroud, which corresponds to

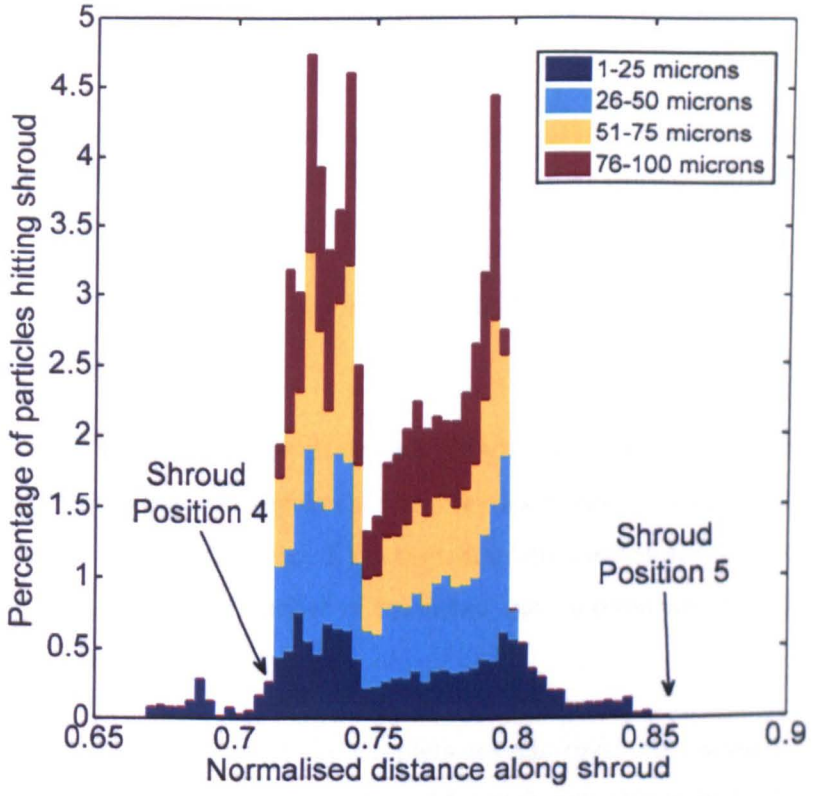

Figure 6.16: Particle distribution of 1-100 micron droplets along shroud, released from gear outer diameter and coloured by size. Zero initial velocity, turbulent dispersion modelled

the gutter of the shroud. Additionally, for all of the simulations, when particles struck the shroud outside of this small area, it was only particles in the 1-25 micron band, showing that they are more easily entrained within the flow.

6.3.2 Effect of turbulent dispersion on particle trajectories

The simulations presented within this chapter do not use a model which predicts the dispersion of the particles due to the turbulence of the flow. The effect of the turbulence on the particles in these sections is not large, due to its relative small size compared the mean velocity component of the flow. To illustrate this, Figure 6.16 shows the results of an injection with zero initial velocity and the Discrete Random Walk (DRW) model switched on. The chart can be compared to Figure

	Particles hitting shroud (%)			
	1-25	26-50	51-75	76-100
Turbulent dispersion OFF	14.6	18.2	18.4	18.5
Turbulent dispersion ON	14.9	18.4	18.4	18.4

Table 6.3: Effect of turbulent dispersion on quantities of particles hitting shroud, by size band

6.12, and their very close similarities should be noted. The DRW model works by predicting the turbulent dispersion of particles due to the instantaneous turbulent velocity fluctuations of the air. By integrating the instantaneous velocity, $u = \overline{u} + u'(t)$, for a sufficient number of particles, the randomness of turbulence on the particles can be resolved [18].

Analysis of the destination of the droplets reveals their close similarities, with the number of particles hitting the shroud for each case shown in Table 6.3. The particles are subdivided by size groupings, as in the figures, and it can be seen that the numbers are very similar to each other. The total difference in particles hitting the shroud is 0.7%, and the difference in quantities of particles hitting the injection surface is slightly larger at 3.8%.

The reason a zero velocity injection condition was chosen to compare the effect of the turbulent dispersion model was that it allows the particles to be affected by the turbulence for longer than other other cases when the particles are given an initial velocity. As shown by the results in this section, the turbulent dispersion model has very little effect upon the results, and since it can result in nonphysical results of particles collecting in areas of smaller turbulence [18], it was decided not to use the model.

6.3.3 Conclusions

This section has looked at the effect of releasing particles from the outer diameter of the gear tooth. The velocity of the particles that are injected has been shown to have an effect upon the distribution of particles hitting the shroud; however, the vast majority of them hit the shroud in a small area in the gutter of the shroud for all the inlet conditions. The gutter of the shroud (Shroud 2 in [23]) is intended to capture oil in this manner, so would appear to be working well, and the high concentration of particles hitting this relatively small area (typically around 5,000 to 6,000 for a single time-step) means that an injection from the gear outer diameter would be an ideal candidate to feed a film on the surface of the shroud. This will be conducted in Section 6.5.

This section has also shown that the turbulent dispersion model has limited effect on the trajectory taken by the particles, due to the dominance of the mean air velocity compared to the turbulent fluctuations of the flow. As a result of this, and the potential for nonphysical results, the model is not employed for future investigations.

6.4 Droplet releases from gear toplands

This section extends the work of Section 6.3 by releasing droplets from the toplands of the gear teeth, and these are shown in Figure 3.9 in Chapter 3. The toplands of the gear teeth are the surfaces on the top of the teeth and like the outer diameter, are parts of the gear where particles may be spun off due to the high rotational speeds involved. Consequently, this injection location also provides a potentially good source of particles for the formation of a thin-film on the surface of the shroud.

Figure 6.17 shows the results of injecting a distribution of particles with a high radial velocity of 171m/s from the topland of the gear tooth. This velocity condition is not physical, but is instead intended to ensure that the droplets hit

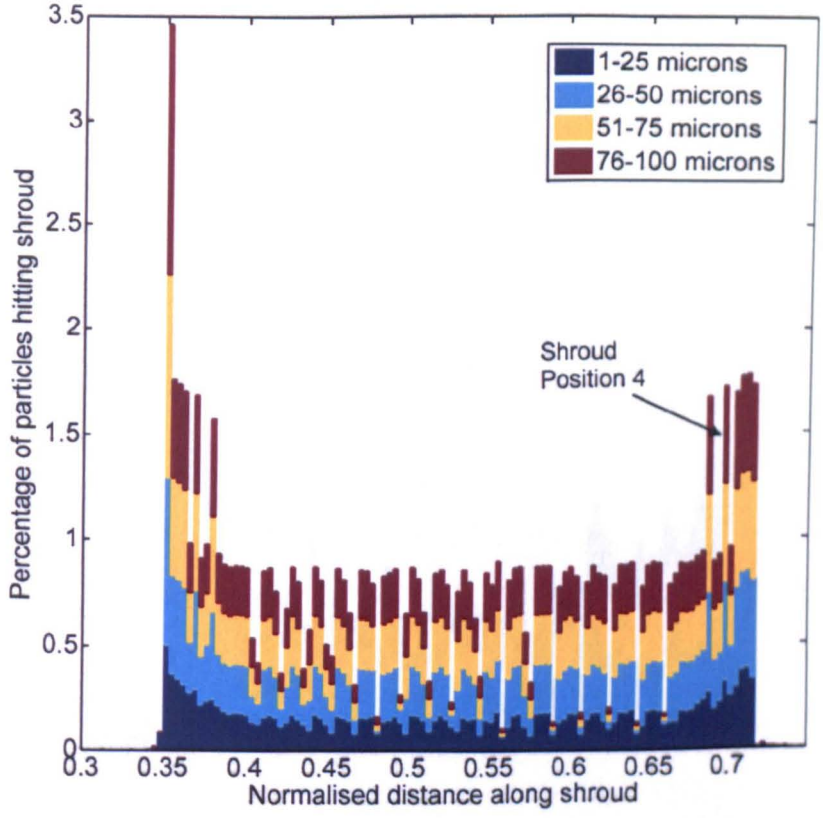

Figure 6.17: Particle distribution of 1-100 micron droplets along shroud, released from gear teeth toplands and coloured by size. Initial velocity 171m/s radially

the shroud radially outwards from their injection location. The gap between the toplands of the gear and the shroud[3] is only 1.76mm, and therefore there is very little space for a droplet to be affected by the momentum of the core airflow.

There are a number of features which are immediately identifiable in the figure. The distribution of particles is pretty constant along the length of the shroud, stretching up to shroud position four (as seen in Figure 6.1), which is the start of the gutter. There are some intermittent bars with very few particles showing up; however, this is due to a mismatch of the axial location of the bins used to create the histogram, and the cells into which they are landing. At the start and end of the distribution there are spikes, where more particles have hit the shroud, and this is due to larger numbers of particles being released at the outer and inner diameters of the topland because there is a finer mesh at this point. FLUENT

[3]The gap is 2mm when measured in an axial direction

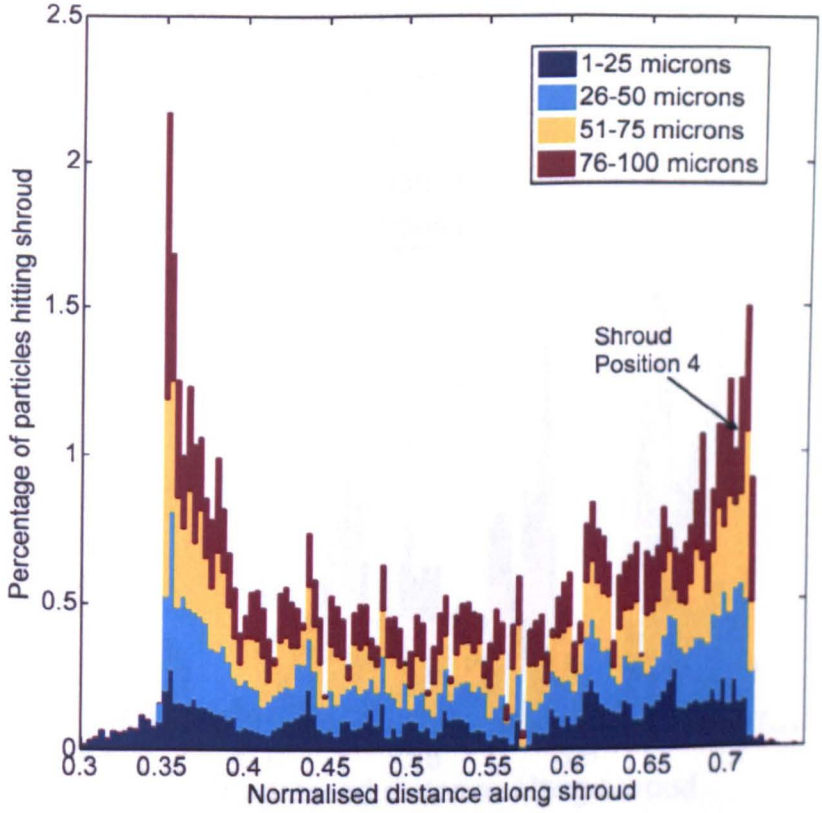

Figure 6.18: Particle distribution of 1-100 micron droplets along shroud, released from gear teeth toplands and coloured by size. Zero initial velocity

releases particles from the centres of each cell of the mesh on the injection surface, and therefore the finer mesh at the ends of the gear teeth (to capture the complex single phase flow structures) means there the amount of particles released is not uniformly distributed along the length of the gear tooth. However, this will not affect the conclusions that can be drawn from this work, due to the low coupling of momentum between particles and air seen, and the proportion of particles that aren't uniformly distributed is less than 10% of the total released.

A simulation was run with a zero initial velocity, and the results of this can be seen in Figure 6.18. There is a similarity to the simulation with a high radial injection velocity, but there is a higher dispersion of the smallest particles, signified by the blue bars. This is due to their lower inertia allowing them to be affected and carried by the air.

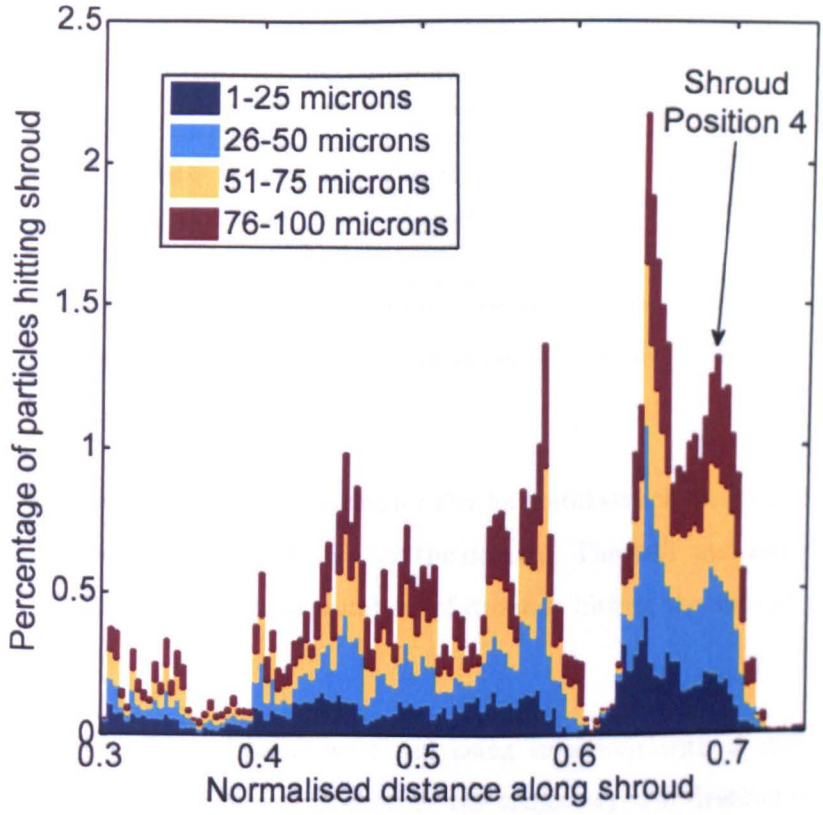

Figure 6.19: Particle distribution of 1-100 micron droplets along shroud, released from gear teeth toplands and coloured by size. Cell initial velocity

Figure 6.19 shows the results of using the "cell" initial injection condition. The axial velocity of the core air flow means that the particles have moved further up the shroud, and there is more bunching around shroud position four, which is where the gutter starts. Unlike the cases in Section 6.2 and Section 6.3, this is an example of where the injection condition (which is not uniformly or geometrically distributed) makes a more significant impact upon the destination of the oil droplets. In the absence of data about the distribution of droplets between a shroud and gear, this highlights a potential issue with this injection location, and strengthens the case for further research into the modelling of an entire gearbox.

Table 6.4 compares the destinations of droplets released from the toplands. The total number released for each case is 30240, and it can be seen that the majority of them have hit the shroud. This is clearest for the injection with high radial

	Destination	
Injection velocity	Shroud	Gear toplands
Zero	20237	9182
"Cell"	19127	10316
Radial = 171m/s	27233	1719

Table 6.4: Effect of inlet injection on destination of oil droplets released from gear topland

velocity; however some of the particles for this have still struck the initial injection surface, and also passed further through the domain. The "cell" and zero injection velocity conditions have similar numbers of droplets hitting the shroud and gear toplands.

Finally, a series of simulations were run using injections with a uniform size condition. This was to ascertain whether the trajectory and destination of the droplets would be altered if only a single size of particle is introduced into the domain. The findings were the same as those for the previous two sections in that no difference was noted, so these results are not repeated here.

6.4.1 Conclusions

This section has looked at the effect of releasing droplets off the topland of the gear teeth. This injection condition shows a lot of promise for use in film modelling, as it allows a good coverage of DPM droplets over most of the shroud, reducing the possibility of nonphysical chequerboarding of the film described in Section 6.3. It has been shown that the injection condition can make a difference to the destination of the droplets, with a lower initial velocity resulting in more particles returning to the injection surface than when there is a high radial velocity. However, as these particles would be spun back off in a physical situation, or squeezed during gear meshing, it is unlikely they would stay on the gear surface for long. Consequently, the majority of the droplets would likely end up hitting

the shroud, with a bias towards the outer diameter, regardless of the condition.

It has also been seen that the size distribution of particles does not make a difference to the destination of the droplets, with, for example, 1 micron particles taking very similar trajectories regardless of the presence of particles with different sizes included in the injection, demonstrating a low coupling of momentum between the particles and the air. The smallest particles have a low inertia due to their low masses so are more likely to be carried by the fast moving air than a larger particle which will have a higher inertia. Therefore, the smaller particles, particularly below 5 microns are seen to disperse further through the domain, and may therefore be more difficult to capture and manage than larger particles which are more likely to strike a surface.

6.5 Film modelling

This section looks at the formation of a film on the surface of the shroud. It is an extension of the work in the previous sections, as instead of terminating the DPM droplets on contact with the shroud, the particles are kept within the domain and used to form a thin-film on the wall surface.

The thin-film model is based on the work of O'Rourke and Amsden [30], and is typically used for Internal Combustion (IC) engine applications, based on large distributions of particles per surface cell [19]. It has potential for modelling the formation of a film on the surface of a shroud within a gas turbine IGB, and therefore this section will explore its potential, and whether useful conclusions for oil management can be reached. Section 3.4.10.3 in Chapter 3, Methodology, provides the numerics behind the thin-film wall model.

The model will only be utilised on the surface of the shroud, not any of the other walls within the domain, such as the chamber or the gear. The reason for this is twofold; to reduce the computation overhead of the calculation and due to a lack of a second meshing gear. Unlike the previous work on looking at the destination

of the particles, the thin-film model requires the DPM droplets to be tracked on the surface that they hit, so using a continuous injection means that the quantity of memory required to run the simulation increases with each time-step, therefore the decision to reduce the number of surfaces on which this would happen has been taken. The lack of a second, meshing gear in the simulation means that an oil film on the surface of the gear would not be physical, because it should be squeezed by the contact between the two gears, and ejected. As this will not happen in these simulations, the formation of a film on the gear surfaces will not be attempted at all. Therefore, at this early stage in development, the use of the thin-film model should be considered only for its insight into oil management on the surface of the shroud, and not a tool for predicting the total moment on the gear due to single phase windage and churn of the suspended oil.

A number of simulations have been run, with varying injection locations and shroud configurations. Section 6.5.1 explores the mechanisms for film formation on the shroud of the control gear (as used in the previous sections), and Section 6.5.2 compares the performance of the shroud outlet variants tested in Section 5.3 in Chapter 5 in an effort to determine whether they are potentially better performers when management of the oil between shroud and gear is considered.

6.5.1 Control shroud

Two injection locations are used for creating a film on the surface of the control shroud. The first is the outer diameter of the gear, and the second is the toplands of the gear teeth.

6.5.1.1 Film instigated from gear outer diameter

A large number of simulations have been run using particles injected from the outer diameter of the gear, and all of them show very similar behavior, due to the oil droplets all heading for a very similar area of the shroud in the gutter. This

Injection number	Injection Condition			
	Size distribution	Initial Velocity	Flow Rate (litre/minute)	Notes
1	Rosin-Rammler	Cell	1	10 sizes of particles
2	Rosin-Rammler	Cell	1	20 sizes of particles
3	1 micron	Cell	0.1	
4	60 micron	Cell	0.1	
5	60 micron	Cell	0.01	
6	60 micron	Cell	100	
7	1 micron	Radial = 171m/s	1	
8	1 micron	Radial = 171m/s	0.1	
9	60 micron	Radial = 171m/s	1	
10	60 micron	Radial = 171m/s	1	

Table 6.5: Film model simulations initialised from gear outer diameter

behaviour has been seen in Section 6.3, where nearly all particles would head for the same area of the shroud gutter, regardless of the injection condition tested.

Ten simulations were run, using a combination of Rosin-Rammler distributions of particles, and uniform distributions of either 1 or 60 microns. A "cell", or high radial injection velocity condition was used, with flow rates also varied to ascertain the effect of this parameter on the formation and movement of the film. Table 6.5 summarises the simulations that have been run using an injection from the outer diameter of the gear. Simulations 1 and 2 are similar, but have either 10 or 20 different sizes of particles within the Rosin-Rammler distribution respectively. Simulation 6 has a very high flow-rate of oil in order to test the effect of this on the formation of the film — this amount is considerably higher than would be expected within a physical gas turbine IGB, but shows an extreme solution for completeness.

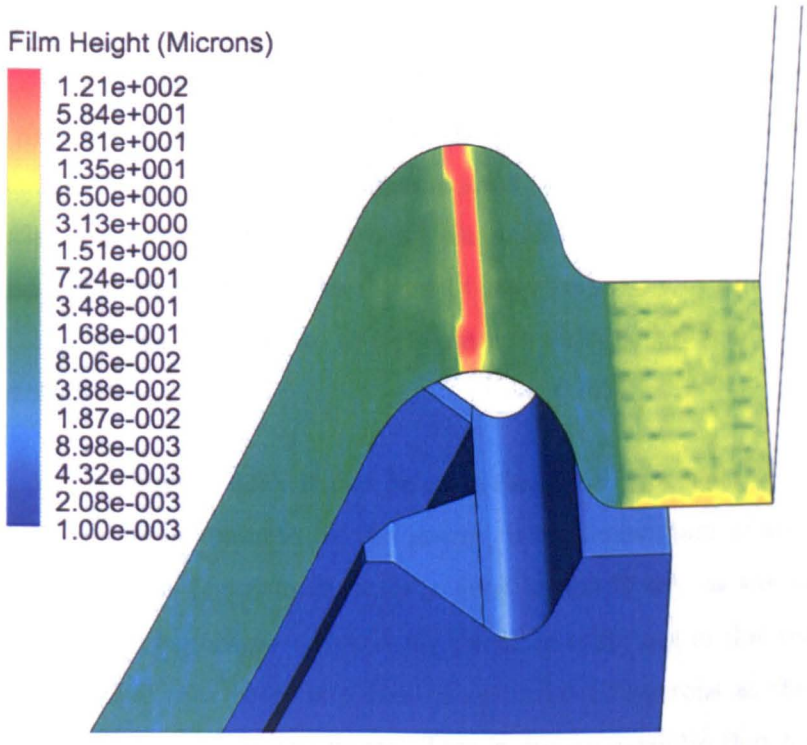

Figure 6.20: Wall-film height on shroud at time = 3.9×10^{-2}s, 60 micron particles released off gear outer diameter with radial velocity = 171m/s at 1 litre/minute flow rate

As previously stated, the simulations all show a very similar set of results, with the film becoming very thick in the region of the gutter, and extremely thin in other regions of the shroud. If the simulations are run for long enough, they all fail due to the thickness of the film exceeding the maximum allowable by FLUENT of 500 microns [18, 19]. The gutter is intended to collect oil for removal using scoops which allow it to escape at these locations, and unpublished[4] work at the University of Nottingham has shown that scoops in this location reduce windage greatly by preventing oil from being re-ingested into the gear.

Figure 6.20 shows the height of the film on the surface of the shroud for one of the simulations. The simulation uses an initial injection of 1 litre/minute oil flow, injected continuously with a radial velocity of 171m/s. The particles all have a 60 micron diameter, which is used as it is typical of the sizes seen shed

[4]At the time of writing

off a rotating disk by Glahn *et al.* [15]. There are computational advantages to using a uniform distribution, as FLUENT only has to track one "packet" of particles per cell, as opposed to a packet for each size of particle when the release distribution is made of a number of different sized particles. One packet contains the particles of a particular size released from a cell on the injection surface. As each individual particle would take the exact same trajectory in the simulation, FLUENT only needs to calculate their movement once, and this is the concept behind packets.

Referring back to Figure 6.20, it can be seen that there is a band of relatively thick film at the outer diameter of the gutter, with a maximum of around 170 microns thickness. A logarithmic scale is used in the figure, as the height of the film reduces very quickly — clearly all the oil is collecting in this very small region. Also visible that there is a film of around 6-12 microns at the exit to the shroud, seen as yellow in the figure. This is due to particles that have been suspended in the flow striking the shroud in this area as they leave the space between shroud and gear and exit into the rear chamber.

The results of releasing droplets from the outer diameter of the gear in Section 6.3 showed that the droplets were almost all hitting the shroud in the gutter region, whereas in Figure 6.20, it can be seen that there is a film that is covering the shroud towards the inner diameter of the gear. This indicates that there has been one of two things possibly happening: firstly that some particles from the injection are heading radially inwards before striking the shroud; secondly that the film itself has moved inwards due to the shear of the core air flow. Gravity is not modelled in these simulations, so this is not a factor.

Figure 6.21 shows droplets in the domain coloured by their residence time. Only 1 in 100 droplets are shown in order to reduce visual clutter; however, it can be seen that all of the droplets travelling between the gear and the shroud do so directly. There are a couple of droplets that are visible within the domain towards the outlet of the shroud but there are none that have travelled across the air flow path towards the inner diameter of the gear. Therefore, it can be

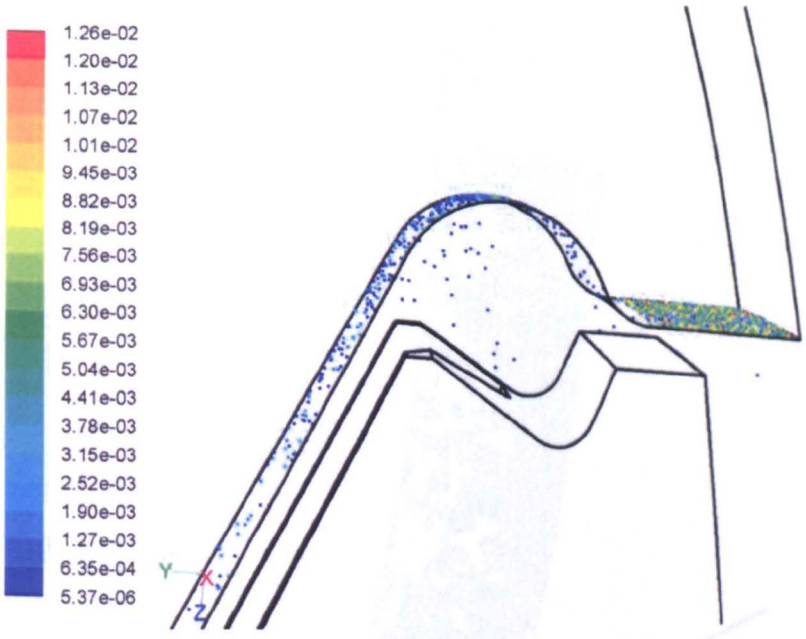

Figure 6.21: Droplets in domain, coloured by release time. 60 micron particles released off gear outer diameter with radial velocity = 171m/s at 1 litre/minute flow rate

said that the film at these points has not been formed by droplets striking the shroud, but through the film travelling down the shroud.

Figure 6.22 shows parts of the film that have a negative axial component of velocity at time = 3.91×10^{-2} seconds, which is three revolutions after the droplets were first injected into the domain. FLUENT does not store radial components of film velocity as variables — but the angle of the shroud means that a negative axial component of velocity will also mean a negative radial component, so will be used as a substitute. The equivalent film height in this region is in the order of one micron, and it can clearly be seen that there is a large amount of it which has a negative axial component of velocity, driving it towards the inner diameter. The DPM model allows the movement of droplets that are taken to be part of a film, due to the shear of the air flow over it.

The air phase has a strong negative component of radial (and axial) velocity, and this is what is causing the film to be forced down the surface of the shroud. Figure 6.23 shows contours of radial velocity on the periodic boundary of the gear, and its large magnitude can be observed — being as high as 55 m/s near

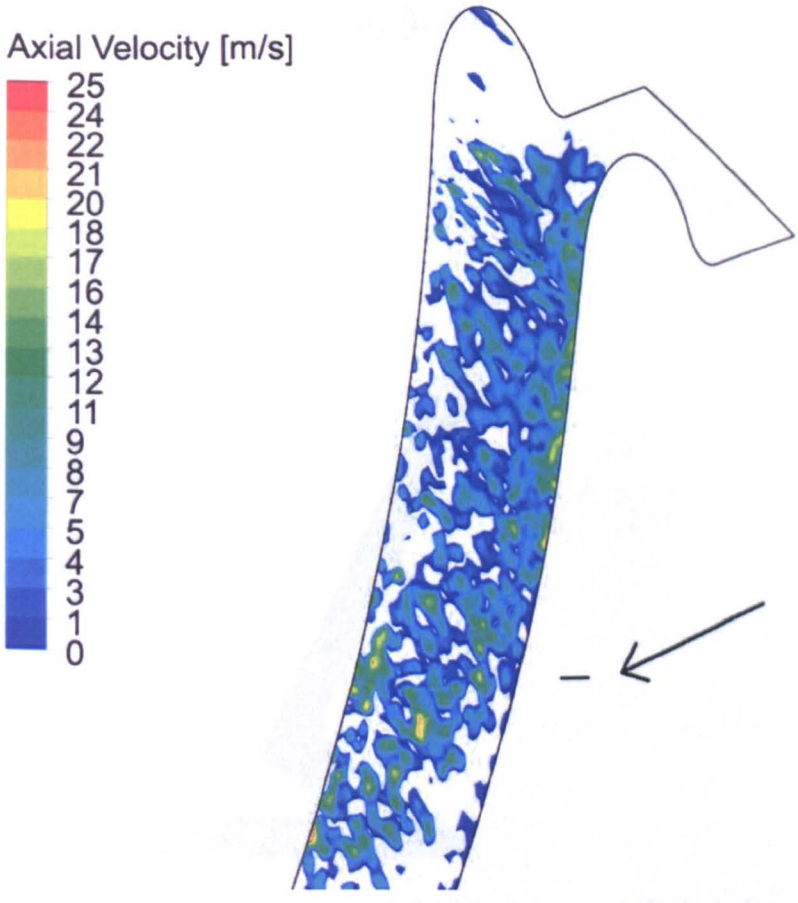

Figure 6.22: Wall-film contours of negative axial velocity at time = 3.91×10^{-2}s, 60 micron particles released off gear outer diameter with radial velocity = 171m/s at 1 litre/minute flow rate

the inner diameter, and below 20 m/s down the shroud from the outer diameter of the gear. The work conducted in Section 5.3 showed that this recirculation of flow is independent of the geometry at the outlet, so the particular shroud being used in these cases is not the primary cause for this inwards motion.

Figure 6.24 shows a picture by Johnson *et al.* [22] of an oil streak forming on the surface of the shroud of an experiment where the speed is 5000rpm. The figure shows that a streak of oil is moving towards the inner diameter of the gear, due to the recirculation of the air down the surface of the shroud causing a large amount of shear on the film. This is qualitative validation of the results seen above; however, this same behaviour was not seen by Johnson *et al.* during other

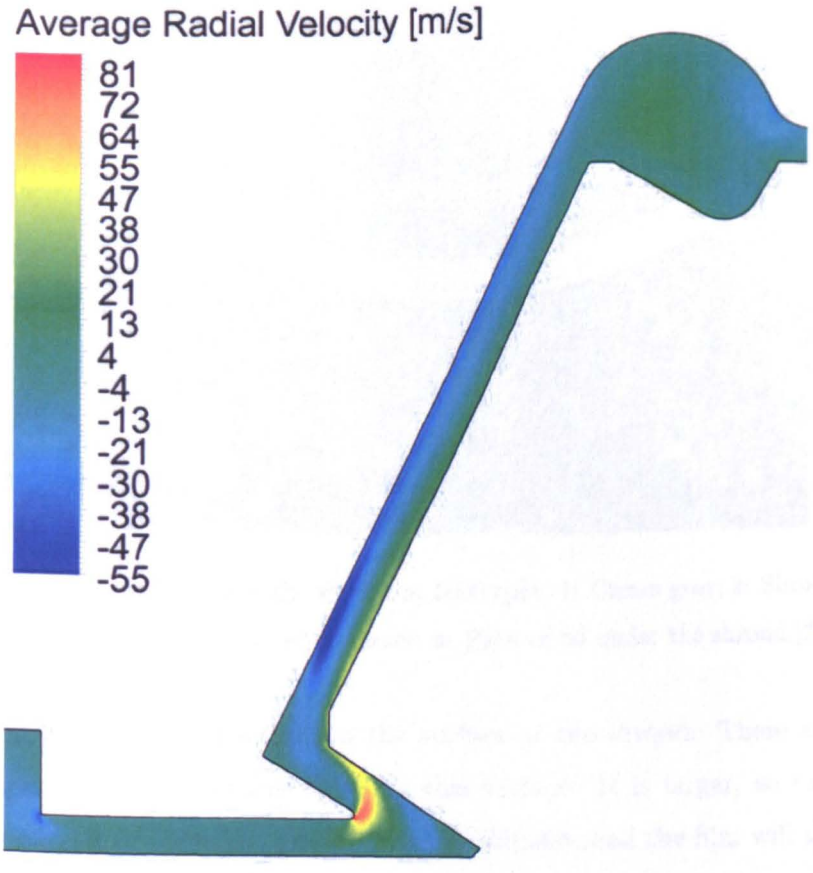

Figure 6.23: Contours of time-averaged radial velocity on periodic boundary of control gear

experiments, particularly with higher rotational speeds. The possible cause for this is that the momentum of the oil droplets hitting the shroud with a high radial velocity is exceeding the shear forces pulling them back towards the inner diameter due to the high recirculation of air.

This is seen in the next section, which looks at films formed on the shroud by droplets injection off the toplands of the gear teeth.

6.5.1.2 Film instigated from gear toplands

The work conducted in Section 6.4 showed that the toplands of the gear as a release location for the oil would also be an ideal candidate for testing the

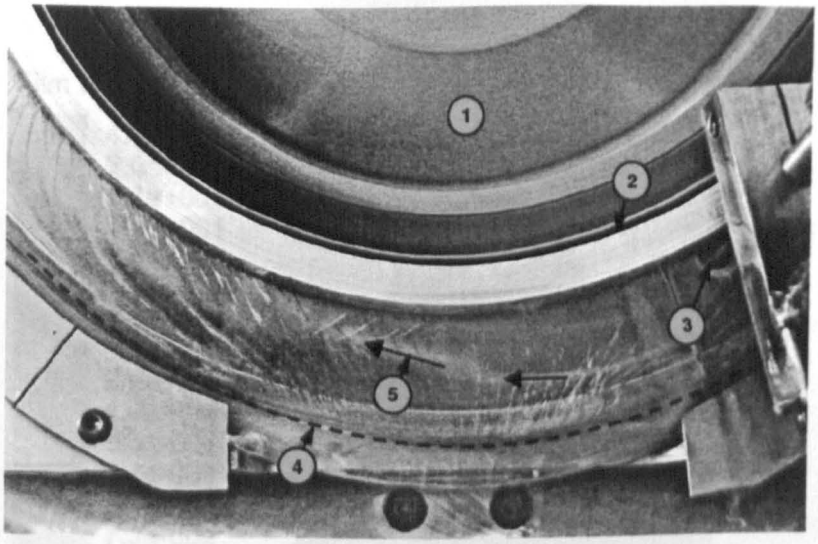

Figure 6.24: Oil streak under the shroud at 5000 rpm. 1: Crown gear; 2: Shroud inlet; 3: Into-mesh oil jet; 4: Gear outer diameter; 5: Path of oil under the shroud [22]

formation and motion of a film on the surface of the shroud. There are some advantages and disadvantages to using this surface: It is larger, so there will be more parcels of particles injected into the domain, and the film will therefore form over a larger area. However, the large number of particles also means that it is possible, after a large number of timesteps, to reach the limit of computational memory available. Similar to the releases from the outer diameter of the gear, this release is not entirely physical as it would not operate in isolation within a gas turbine internal gearbox — but it provides useful information about some of the physical effects that are likely to take place, and these can be used to inform gear and shroud design.

An interesting feature of the results for this section is that it shows that oil is once again collecting in the upper region of the shroud gutter, although it is thicker over the whole surface of the shroud when compared to the injections from the gear outer diameter. Figure 6.25 shows contours of film thickness on the shroud at time $= 4.9 \times 10^{-2}$ seconds (five revolutions after release) for a injection from the toplands of 60 microns with a 1 litre/minute flow rate. The graph uses a logarithmic scale, and it can be seen that in the gutter of the shroud the film height has gone up to around 550 microns, which is on the limit of the thin-film

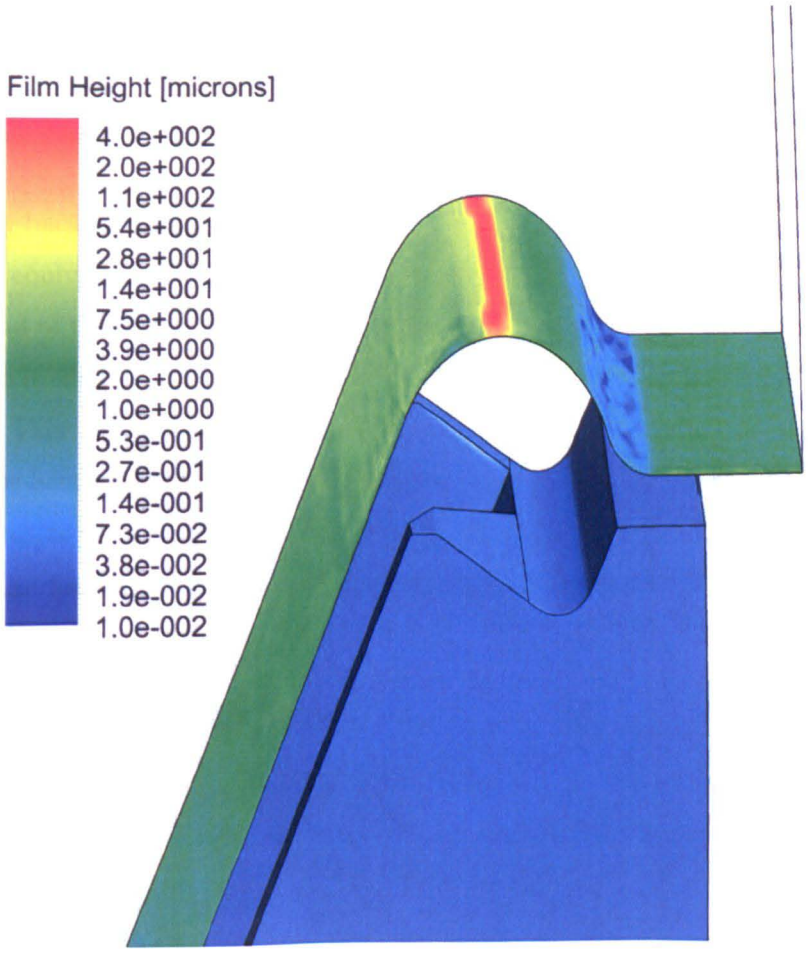

Figure 6.25: Wall-film thickness at time = 4.9×10^{-2}s, 60 micron particles released off gear toplands with cell velocity at 1 litre/minute flow rate

model available for this research. This is a typical result for any of the cases tested.

It can be seen from this, and the work in Section 6.5.1.1 that the oil thickness in the gutter of this shroud is such that it reaches 0.5mm very quickly. Some caution must be exercised as the conditions in which the oil was injected was not physical, but it is likely that oil within the space between gear and shroud would head for this location, as there is a large air flow that would drive oil towards it. Therefore, for modelling oil films forming on a shroud that captures oil in this way, the thin-film model may not be appropriate as the assumptions that it entails (and are listed in Section 3.4.10.3) will no longer be valid. Other

two-phase methods within FLUENT are not capable of modelling the droplets with enough fidelity [18], so there is scope for development of the computational code to deal with thicker films using the DPM model.

Referring back to Figure 6.25, most of the rest of the shroud has a covering of film which is equivalent to 6 and 10 microns thick, although an area can be observed at the end of the gutter, when it contracts at the outlet to the shroud where the thickness is slightly lower, being less than 1 micron thick, as signified by the blue colours. This is due to oil either collecting in the outer diameter of the shroud's gutter, or being carried through the domain — it is not tending to hit this area. At the exit to the shroud, there is a film of 6-10 microns thickness, much as was reported in Section 6.5.1.1, for results from droplets released from the gear outer diameter.

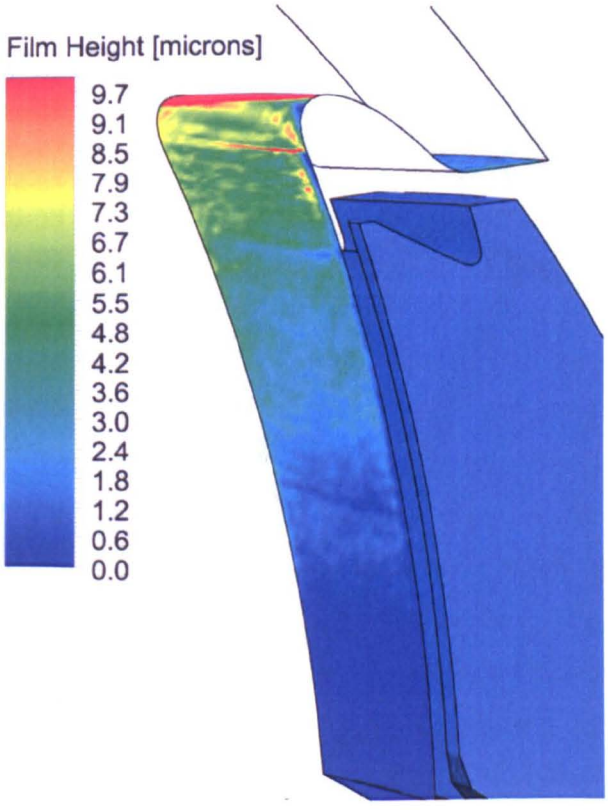

Figure 6.26: Wall-film thickness contours between 0 and 10microns at time = 4.9×10^{-2}s, 60 micron particles released off gear toplands with cell velocity at 1 litre/minute flow rate

It is possible to analyse the film on the "face" of the shroud — the part that faces the gear teeth themselves. Figure 6.26 shows contours of film height clipped between 0 and 10 microns, in order to better highlight the film in this area, without the thicker part of the film in the gutter swamping the figure's contour colouring. It can be seen that a lot of the shroud in this area is covered with a film, more so than for when particles are released from the gear outer diameter.

The film in this area is quite different in these simulations from those reported in Section 6.5.1.1. Firstly, the film has been created directly on the face of the shroud by particles hitting it from the injection. The work in Section 6.4 showed that droplets injected from the topland of the gear will hit the shroud all along its length, and this is the cause for the film being thicker than the film formed as a result of oil injected from the ends of the gear teeth, which was seen to have moved radially inwards due to the shear of the recirculating air.

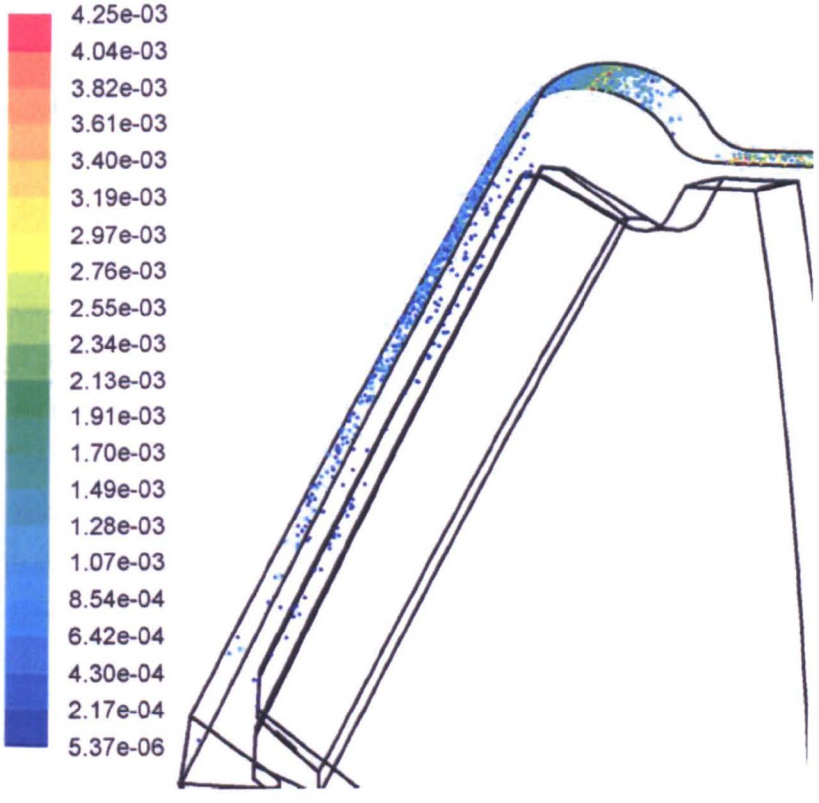

Figure 6.27: Droplets in domain, coloured by release time. 60 micron particles released off gear toplands with cell velocity at 1 litre/minute flow rate

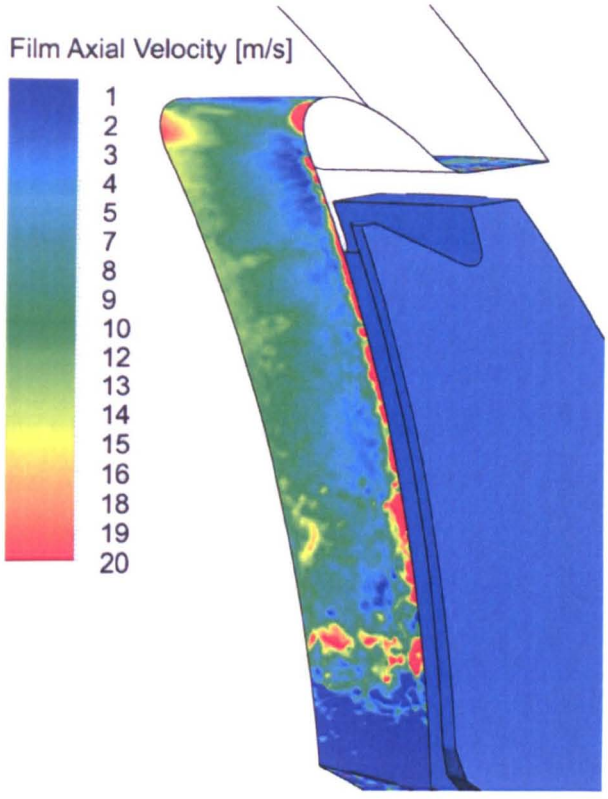

Figure 6.28: Wall-film contours of positive axial velocity at time = 4.9×10^{-2}s, 60 micron particles released off gear toplands with cell velocity at 1 litre/minute flow rate

Figure 6.27 shows the presence of droplets in the space between shroud and gear, and this can be compared with Figure 6.21 where there were none. Only 1 in 200 packets of particles are shown in this figure as there are over 1 million within the domain, so more packets are present than are visible here. Analysis of such data reveals droplets heading from the topland of the gear teeth and moving axially through the domain, and radially outwards. Some particles (not visible) have headed past the gutter of the shroud while still suspended in the air, and have made it through the exit of the shroud on the right-hand-side of the figure, and travelled further though the domain.

Figure 6.28 shows contours of positive axial velocity between 0 and 20 m/s of the film on the surface of the shroud. Once again the axial velocity is used as a substitute for the radial velocity, but as can clearly be seen, unlike the cases in Section 6.5.1.1, the film has a positive axial (and hence radial) velocity, so is

moving outwards. The air flow structure has not changed between the injection conditions, and there is still large negative radial velocities, seen in Figure 6.23, therefore it can be concluded that the momentum of the particles striking the shroud is such that the shear of the flow over the shroud is insufficient to prevent the film from moving outwards. The droplets visible in Figure 6.27 are moving with a positive radial velocity, so will strike the shroud at an angle, and this momentum is preserved as they form the film.

In Figure 6.28, the velocity is disjointed at points, with sizeable jumps between neighbouring areas. This is due to two reasons: firstly, the figure is of one time-step, so it is not a time-averaged plot of the velocities experienced by the film, and secondly, the particles that are striking the shroud and exchanging momentum do so with discrete strikes, leading to to a local value of velocity being calculated within each surface cell.

6.5.2 Shroud outlet variations

The work that has been conducted thus far in this chapter has dealt only with one shape of shroud. This shroud was used by Johnson *et al.* [22, 23] and Rapley [33], and has been shown to capture oil predominantly within its gutter, as seen in the previous sections.

This section will draw on the work of this chapter, and the work of Section 5.3 in Chapter 5 by studying the formation of a film on the surface of shrouds with different outlet shapes. It will re-examine the lessons learned for air-only simulations. It was explained in Section 5.3.7 that an outlet that was more "open" to the chamber behind the gear would likely allow oil to leave the space around the gear more readily, reducing the possibility of oil being re-ingested and churned — resulting in an energy cost.

Figure 6.29 is a repeat of Figure 5.16 from Section 5.3.6, and shows the strong component of radial velocity for the shroud with a Large Outlet (bottom right),

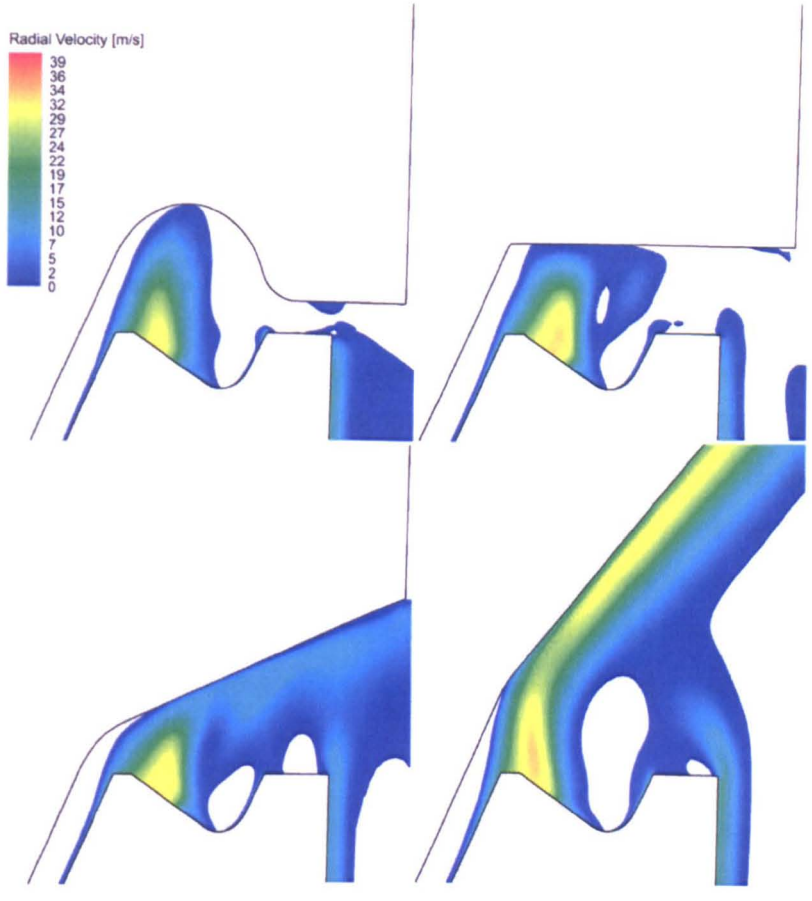

Figure 6.29: Contours of averaged radial velocity on tooth valley midsurface. Clockwise from top left: CO, FO, LO, HO

and a "Hybrid Outlet" (bottom left). It was concluded then that this would likely result in oil being swept quickly away from the vicinity of the gear. To test this, a number of simulations were created which used a release of 1 micron droplets off the toplands of the gears, modelling a film on the surface of the shroud. The simulation setups were exactly the same, and the injections started at the same time (after five revolutions of single phase running). The flow rate was 1 litre/minute of oil and a cell velocity condition was used in order to gauge how droplets suspended in the air would behave.

Referring back to the work of Section 5.3, it was shown that the systems with a larger, less restrictive outlet had a larger mass-flow-rate and windage, so these cases do not test the same set of circumstances exactly, as the impact of the

higher mass-flow-rate would be likely to move droplets away from the shroud surface with more speed. However, as this is part of the effect of the shroud outlet, all the cases are run with a "natural" condition, using pressure inlet and outlet boundaries that are set to zero gauge total and static pressure respectively (as explained in Section 3.4.11.2). By looking at each domain as a "system" as opposed to a gear and a shroud, it is easier to compare their relative performances.

Figure 6.30 shows the formation of films on the surfaces of the shrouds of four of the outlet variants. The "Medium Outlet" is not shown due to its similarity to the Large Outlet. The figures show a time one revolution after the oil has started to be injected into the domain, and use the same logarithmic scale for the thickness of the film. An early point in the film's formation is shown to allow a comparison with the same scale — after much longer the film in the gutter of the Control Outlet is so thick that it is not possible to see the detail of the other shrouds.

Already at this time, it is possible to see in Figure 6.30.1 that the film at the gutter of the shroud for the CO case is far thicker than the others, with a maximum depth of 12.5 microns. Figure 6.30.2 shows the film on FO, and this also shows a relatively thick film with a depth of 12 microns in places. The larger outlet of this shroud means that a lot of particles have been able to avoid striking the shroud and escape, but as seen in Figure 6.29, and like for CO, it has a strong core air flow that stagnates as it leaves the valley of the gear, which will probably cause a lot of the oil to hit in this area.

The films of the Large Outlet, LO (Figure 6.30.3) and the Hybrid Outlet, HO (Figure 6.30.4) both show similar trends - a far thinner film on the shroud than the other two cases. Part of this will be due to their larger air mass-flow-rates, but it is mainly due to the flow not being restricted as it leaves the vicinity of the gear, and allowing particles to travel within the core air flow away into the chamber behind the gear. In both cases, the amount of particles hitting the shroud is low enough for there to be a depth of zero at points, shown as dark blue areas. Unfortunately, it was not possible to run these simulations for long enough

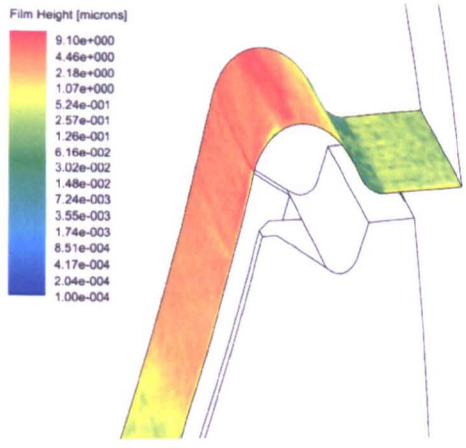

6.30.1: Control Outlet (CO)

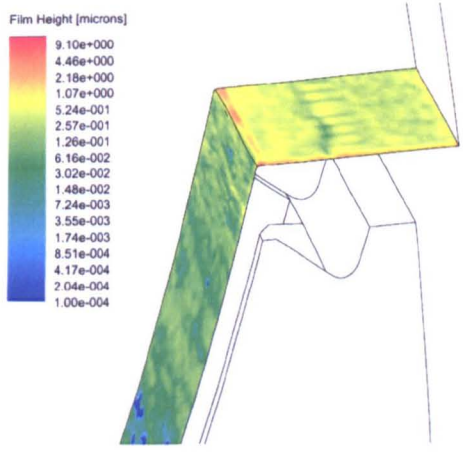

6.30.2: Flattened Outlet (FO)

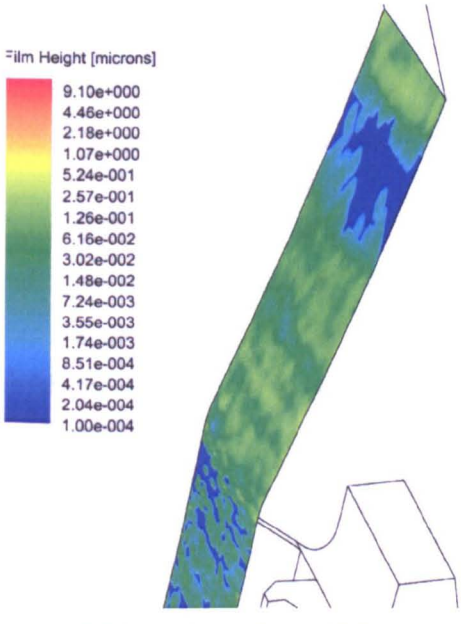

6.30.3: Large Outlet (LO)

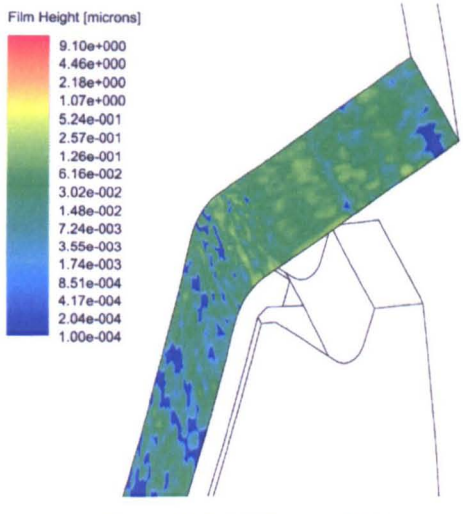

6.30.4: Hybrid Outlet (HO)

Figure 6.30: Wall film thickness on shroud of outlet variants. Time = 2.9×10^{-2} s, 1 micron particles released off gear toplands with cell velocity at 1 litre/minute flow rate

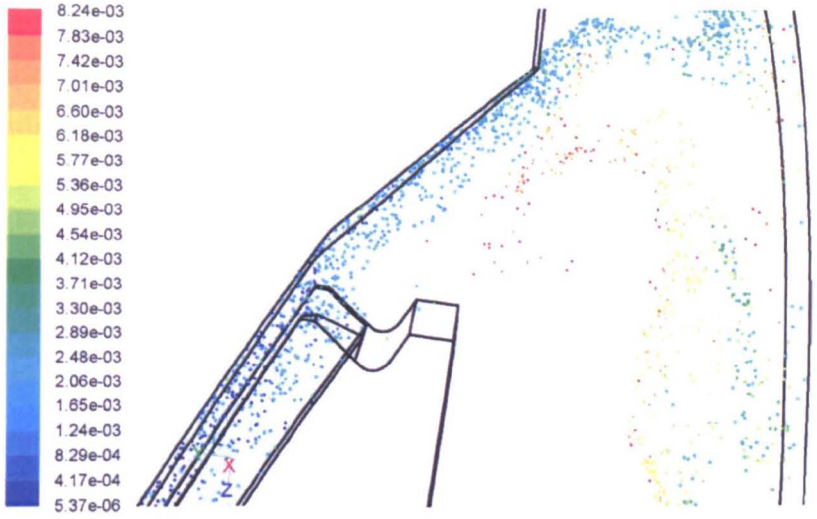

Figure 6.31: Droplets in domain for LO shroud, coloured by release time. 1 micron particles released off gear toplands with cell velocity at 1 litre/minute flow rate

to see total coverage of the surface of the shroud, as the number of particles in the domain exceeded the memory capability of the hardware; however, from the limited results obtained it can be concluded that there may be issues physically with very thin films in some areas which could result in poor cooling.

Figure 6.31 shows 1 in 200 of the droplets within the domain of LO. It can be seen that there are many droplets that are caught in the flow of the air being ejected from the gear, as seen in Figure 6.29. These are relatively young droplets, as they are bluish coloured, so it is possible to see that these have been released from the toplands and carried away into the domain without touching the shroud. The droplets on the surface of the shroud can also be seen to predominantly be blue coloured, so it can be said that this film is also quite young, and not "pooling" anywhere as was the case for the control shroud.

The same pattern is seen for the Hybrid and Medium Outlets (HO & MO), which also have strong core air flows leaving the area around the gear. The conclusion that can be drawn from this is that purely from the perspective of managing oil, it is best to have a shroud outlet shape which is not restrictive, and allows air and oil escape easily. This could, for example also take the form of slots within a shroud [22, 50]. The single phase work of Section 5.3.7 in Chapter 5 stated that

the shrouds with a larger outlet would allow oil to escape easily, and this chapter has validated that conclusion, which shows that it may be possible to judge (as a first estimate) the direction that oil suspended in the air, or in a film will take without performing a simulation using the DPM model.

6.6 Conclusions

This chapter has used the discrete particle model to simulate the presence of oil between a rotating spiral bevel gear and a static shroud. There is a lack of information, either from literature or from experimentation, providing details of the size or velocity of oil droplets present within a gas turbine internal gearbox. Therefore, a step-by-step approach has been taken, looking firstly at the destination of oil from a number of probable sources, and then building upon this by introducing a thin-film model.

The first section, Section 6.2, looked at the destination of oil droplets released from the inlet to the shroud. It was seen that the injection velocity made little difference to the point that the particles would hit a surface, with the majority of them hitting the underside of the shroud's nose. The smallest droplets, below 3.5 microns in size were shown to be most likely to follow the air through the domain, and therefore particles of this size would possibly lead to an increase in the effective density of the air and a consequent increase in windage. Although the larger particles had struck the shroud and been removed from the domain, in a physical gas turbine IGB, they would be stripped off the shroud and ingested by the gear. From these results, it can be concluded that for a shroud with a long, nose-like entrance, that most of the oil would probably hit the shroud itself and larger slugs of oil may be shed off the nose.

The next two sections, 6.3 and 6.4, released oil droplets from the outer diameter and the toplands of the gear respectively. For releases from the outer diameter of the gear, the droplets would predominantly hit the shroud, radially outwards from the injection location. This is insensitive to the initial velocity, and as such,

it can be concluded that oil shed off the outer diameter of the gear will almost certainly strike the shroud in this location.

For injections of particles from the toplands of the gear, there was a slight difference in the distribution of particles depending on the initial velocity conditions. With a high radial velocity, or zero initial velocity, the particles typically strike the shroud radially outwards from their start location, although with more dispersion of the smaller particles for the zero initial velocity condition. For a "cell" velocity condition for the injection, it was seen that there was a shift in the particles axially further through the domain, and this is due to the particles being given an axially positive component of velocity. However, for all of these cases, the oil was still hitting the shroud, and predominantly not passing through the domain. As a consequence, for the topland, and outer diameter releases, it was concluded that they were ideal candidates for creation of a film on the surface of the shroud.

Section 6.5 looked at modelling a thin film on the surface of the shroud, using the discrete particle model in FLUENT. Injections were, as mentioned above, from the outer diameter, and the toplands of the gear. It was seen for both of these cases that oil would predominantly end up pooling in the outer diameter of the shroud's "gutter". This has two implications: firstly, that oil is not being quickly removed from the area around the gear, which could result in re-ingestion, and secondly, that the thin-film model will need to be adapted to suit these thicker films (over 0.5mm height in the gutter of the shroud), or alternatives found to model situations like this in the future. It was seen that for releases of particles off the toplands of the gear, the film would move radially outwards, whereas the opposite was true for droplets released from the gear's outer diameter. There is a balance between the positive, radial momentum of the particles being transferred to the wall film, and the shear of the air flow across the film which drives the flow inwards. For the releases from the topland, the former has outweighed the latter, and vice versa for releases from the outer diameter.

Finally, a film was modelled on the surface of the shroud for a number of different

shroud outlet variants, using the shrouds tested in Section 5.3 in Chapter 5. It was found that the shrouds with a larger, free-flowing outlet allowed the air to remove the oil from the area around the gear and as such, reduced the potential of the shroud to pool oil, as was seen with the control shroud. This has two implications: firstly, that droplets suspended within the air will not be re-ingested and recirculated by the gear, which would lead to higher losses. Secondly, by preventing oil from pooling, it is less likely that oil will be stripped off a film and recirculated, or worse — the gear dipping into the oil with a consequent increase in power losses due to churning of oil.

The next chapter will summarise and form conclusions based on all of the work contained within this thesis, and will build upon those presented here, and place them within a physical context for a gas turbine transmission designer.

CHAPTER 7

Conclusions

This chapter concludes the thesis by stating what has been achieved by the work previously described, providing a series of conclusions and stating the work's contribution to science.

7.1 Statement of aims and objectives

The work presented in this thesis forms a series of computational work [13, 33] studying the effects of shroud and gear design on gear windage. The work has been carried out in parallel to a program of experimental work [22, 23], and establishes a methodology for predicting and consequently reducing the wasteful pumping and churning of oil and air by a shrouded spiral bevel gear, in the context of an aeroengine internal gearbox (IGB).

Gear windage and churning has been shown to be around 10% of the total losses within an IGB [28], and for a high power engine, this can account for megawatts of lost energy [12]. The overarching purpose of the work conducted has been to use Computational Fluid Dynamics (CFD) to reduce this proportion.

The specific aims of this thesis can be summarised as follows:

1. To extend the methodology of Rapley [33] and produce a computational parametric model of a shrouded spiral bevel gear.

2. To characterise the effects which cause and can mitigate windage of a shrouded spiral bevel gear, by using computational fluid dynamics (CFD) software.

3. To apply engineering analysis and logic to form a series of conclusions which will aid designers trying to reduce the windage of a rotating spiral bevel gear.

The specific objectives accomplished to achieve these aims were:

1. To develop a methodology to model gear windage using a parametric solid model, flexible meshing techniques and a control volume CFD approach, seen in Chapter 3.

2. To characterise the effect upon single-phase windage of four size variables of a spiral bevel gear. The variables were inner diameter, outer diameter, cone angle and module (number of teeth), as seen in Chapter 4

3. To investigate a series of alternative shroud inlet and outlet geometries to see their impact upon single-phase windage for a constant gear, seen in Chapter 5.

4. To introduce oil droplets into the domain to replicate ingestion of an oil-laden atmosphere, or shedding of droplets off the rotating gear. The destination of droplets within the gear and shroud system was investigated to aid knowledge of oil management.

5. To simulate a film created from oil droplets striking the shroud, and establishing whether the current CFD capabilities can qualitatively replicate the flows seen experimentally.

6. To investigate whether the design of the shroud at the outlet has a positive impact at reducing the recirculation and re-ingestion of oil into the gear, seen in Chapter 6.

7.2 Attainment of objectives

7.2.1 Development of methodology

Chapter 3 has presented a methodology for the creation of a parametric solid model of a spiral bevel gear using Pro/Engineer [8]. The meshing technique and topology use ANSYS ICEM CFD [21], and the numerics behind the finite volume process used to solve the simulations using FLUENT [21] are introduced.

Attention is paid to ensure that verification of the mesh is thoroughly done, firstly by performing a mesh density study, and then testing the impact of modelling just one of the teeth of a physical gear. Mesh independence was shown, and only a 4.5% difference between the values of windage for a single and five tooth model was seen, well within the variation of the time-varying moment of the gear. Time-averaged variables such as pressure showed a very close similarity, thereby justifying the use of a single tooth model.

Validation of the model against the experimental results of Johnson *et al.* [23] was undertaken, and a difference of around 14% was seen. This difference is attributed to two factors: firstly, the computational gear is modelled with a flat back, whereas the physical gear has a number of circumferential grooves machined in its back. These are not included in the CFD models as they are specific to each engine design, and due to a desire to isolate the effect upon windage of scaling them in Chapter 4, from the scaling of the teeth themselves. The second factor is that the hub on which the gear is mounted physically is not modelled in order to reduce the size of the computational mesh. Excellent validation of the static pressures on the surface of the shroud was seen, with the CFD being less than one percent different.

The work within this chapter has been presented at ASME TurboExpo 2010 [46] and presented to Rolls-Royce as a series of reports [42, 43, 45], whereby it forms a large proportion of the technology transfer from this thesis to the company.

7.2.2 Study of effect of gear shape

Chapter 4 has presented a parametric study into the effect of changing one of four size parameters of the gear: outer diameter; inner diameter; module (number of teeth); and cone angle. No changes to the design of the shroud were made; however, for some of the changes to the gear it was necessary to change the dimensions of the shroud in order to maintain identical gaps between gear/shaft and shroud. This chapter was a single phase study, looking at the effect of only air on the power losses of the gear.

From the results it was seen that the outer diameter has a large effect on loss, with the windage scaling with the outer diameter of the gear to the power of 4.3. This value is close to the oft-used "back-of-the-envelope" value of 5 employed by gear designers, and shows the importance of the outer diameter. Four gears (in addition to the control) were tested, with the gear's facewidth increasing in 5% increments at the outer diameter. The increased windage is due to a larger amount of work being done on the air that is pumped through the system. This is caused by accelerating the air to higher velocities at the outer diameter of the gear's increased radius. Consequently, wherever possible, a gear designer should have as small an outer diameter as possible, although this is not always possible due to the mechanical constraints of transmitting a large torque.

The inner diameter was shown to have a smaller effect on the windage, with no obvious trend when it is increased or decreased. Four additional gears were tested, with facewidths altered between +40% and -20% length, compared to the control gear. Gears with a smaller inner diameter have a longer facewidth, and a smaller annular area at the entrance to the shroud, which was seen to restrict the flow of air through the system, and vice versa. This could be contrasted with an opposing effect whereby the longer gears were having to accelerate the flows slightly more, due to them having a lower velocity on entering the gear teeth region. It should be stated that the inner diameter of a gear within an aeroengine gas turbine is usually constrained by the shaft on which it is mounted, so designers usually have very little scope for changing this variable.

The number of teeth on the gear was varied between 80 and 110, and it was found that a larger number of teeth would decrease the windage. The reason for this is twofold: the losses between the inlet to the domain and the gear are larger when there are more teeth. Secondly, as the number of teeth on a gear increases, the physical size of the teeth reduces, and hence they have a smaller area in the valleys between them. It was seen that the reduction in area through which the air can flow means the gear does not need to accelerate as much air, reducing the amount of work it does. The main design requirement of a gear is its torque carrying capacity, which is controlled by the teeth size; however, consideration should be made to maximising the number of teeth with a view to limiting gear windage losses.

Finally, the cone angle of the gear was found to have a significant effect within the limited data set of systems reviewed — the smaller the cone angle, the larger the windage, compared to the control gear's 60.83° cone angle. The range of cone angles tested was 55° and 66°. The difference in windage is predominantly due to the restrictiveness of the system being reduced, and the ability of the gears to create a large static pressure increase across their faces, contributing to a more "powerful" pump. The larger mass-flow-rate that results has to be accelerated by the gear, and this results in a larger moment. There is often scope for changing the cone angle for a gear designer, as the sum of the cone angles for two meshing spiral bevel gears equals the angle between their shafts, so it is possible to change both without affecting the engine configuration.

The work in this chapter is the first time that Computational Fluid Dynamics has been used to perform a study on the effect of the size and shape of a spiral bevel gear on windage, and can therefore be considered both novel, and a new contribution to science. A portion of this chapter was published at ASME TurboExpo [46].

7.2.3 Study of effect of shroud shape

Chapter 5 has looked at the effect of changing the shape of the inlet and outlet to the shroud. The original, control shroud, is based on one called "Shroud 2" by Johnson *et al.* [23], and is used exclusively throughout the rest of this thesis, with the exception of Chapter 5 and the final section of Chapter 6. This shroud has an inlet restriction of 1.5mm, with a 14.4mm long passage, and a "nose" that forces the flow to almost double back upon itself before it can reach the gear. The outlet of the shroud has a large gutter, which then contracts down to another 1.5mm radial gap. Four additional designs of shroud are each tested for the inlet and outlet.

Investigations into the inlet of the gear found that the largest component of the pressure loss (and hence resistance to the flow) is the sudden contraction down to 1.5mm. An inlet with a steady reduction down to 1.5mm was not found to be as effective, and as such this aspect of the shroud is highly recommended. Additionally, in line with the findings of Rapley [33], the inlet clearance should be made as small as possible. The length of the inlet passage was found to contribute a pressure loss of around 70 Pascals per mm (at the mass-flow-rate of the control gear), which can be compared with the total system pressure drop of over 6000 Pascals. This means that its contribution, although non-negligible, is not critical to the total system loss and therefore can be sacrificed if space for a large inlet passage is limited. The nose of the shroud was shown to contribute to around one third of the pressure drop of the control shroud's total. Therefore, where possible, this component should be implemented, but it is recognised that as it introduces a large mass cantilevered out over the gear, it may result in resonance of the shroud and possible failure due to fatigue.

The outlet of the shroud was found to have a smaller impact upon windage than the restriction of the inlet — as was also found by Rapley [33]. There was a clear trend whereby the larger the outlet, the higher the windage. An outlet which was completely open had a single phase windage that was around 12% higher than that of the control gear. It was seen that the flow structures around the gear are

almost completely independent of the outlet. As the outlet of the shroud opens up, the air being pumped through the domain is able to leave the domain without being impeded, so it was concluded that a shroud that is more free-flowing at the outlet would have advantages at managing oil, with the benefits of this possibly outweighing the single phase windage cost. The use of a discrete particle model in Chapter 6 to model a thin-film on the shrouds of these systems showed that the more open outlets did allow oil droplets to leave the vicinity of the gear more easily.

The work in this chapter is the first time that different designs of shroud have been modelled using CFD with a view to assessing their relative performances at reducing windage. Rapley [33] touched on this with a parametric study of the impact of the size of the outlet and inlet, but used the same design of shroud for his work. This chapter also considers the impact of the shape of the shroud outlet on the management of oil, which is is a novel contribution to science. This work, and the work in Chapter 4 has been as part of a shroud design guideline report [29] used by Rolls-Royce to aid the designers of the shrouded gear systems within future generations of gas turbines. It has also formed the basis of substantial technology transfer to the company, including results and computational models for running internally at Rolls-Royce.

7.2.4 Two phase flow study

Chapter 6 introduces droplets of oil into the domain using the FLUENT Discrete Particle Model (DPM). This is the first time that this model has been used for studying gear windage, and its use should be considered at a preliminary stage, as there is a lack of information about the distribution and size of oil droplets within gas turbine gearboxes. However, the DPM is a robust and well validated model as it is used extensively in combustion applications, so the results it gives are accurate, with it being well suited to parametric studies. The purpose of this chapter was to gather information about the likely destination of droplets of oil within the domain by performing a parametric study, before moving onto initial

modelling of a film on the surface of the shroud. The focus was to study the oil path with a view to optimising oil management and heat-to-oil via a better knowledge of the oil cycle, and to enhance shroud design by taking into account not just single phase gear windage, but also oil management.

The first part of Chapter 6 released particles from the inlet to the shroud, replicating ingestion of a suspended mist from the gearbox in which the gear is sited. It was found that for all but the smallest particles (below 3.5 micron in diameter), most of the oil droplets will strike the bottom of the shroud's nose, independent of the particles' initial velocities. This has potential issues for oil management, as the oil that collects here will almost certainly be shed off the nose as larger droplets straight into the path of the gear — which will incur an energy cost. The insensitivity of the destination of the oil droplets to the injection condition means that the lack of data about the state of oil and air within a gas turbine gearbox will not affect the conclusion of this section.

Oil droplets released from the outer diameter and toplands of the gear were predominantly found to strike the shroud, with only the smallest droplets travelling further through the domain. The injection velocity of the particles was found to have very limited impact on droplet destination when the particles were released from the gear outer diameter, and only a small impact when released from the gear toplands. Therefore it can be concluded that the destination of the particles is not affected strongly by the air flows within the domain, and particles will therefore head for destinations that are predominantly dependent on the location where they are introduced into the domain.

A major finding of releasing droplets from the outer diameter and toplands of the gear is that these injection locations are suited for creating a film on the surface of the shroud. This was done, and it was found that for the control shroud used, the oil predominantly collects in its gutter, to such an extent that the film cannot be considered "thin" everywhere, and the film model used in the discrete particle model is pushed beyond its limits. Clearly from an oil management point of view, this area is an ideal location to remove oil from the shroud. It was also found

in this section that the velocity and direction of travel of the film on the shroud is affected by the injection location. For injections from the outer diameter, the film formed at the gutter of the shroud, and was driven radially inwards by the shear of the air passing over it (which naturally travels in this direction due to recirculations as shown by Rapley [33]). For the injections from the toplands, the particles hit the shroud all along its face, with a positive radial component of velocity, and this momentum is sufficiently higher than the opposing shear forces of the air, meaning that it travels radially outwards — towards the gutter of the shroud.

The final section of Chapter 6 combines the work of Chapter 5 with the film modelling, and simulates the film on the surface of a number of shroud outlet variants. It was found that the wider outlets showed a thinner film, with fewer droplets hitting the shroud due to the lack of a location which causes the flow to stagnate, as the gutter in the control shroud does. These findings were in line with the conclusions from Chapter 5, and showed that it is possible to use the single phase only result to inform an initial study into the likely destination of oil, and the subsequent formation of an oil film. The conclusion of this section is that to manage the oil around the outlet of the shroud, it is better to have a more open, free-flowing path for the air to take, as this will allow the oil to be taken away from the gear, reducing the potential for recirculating it, which would incur an energy cost.

The work conducted in this chapter is the first time that the DPM model has been used to inform shroud design within gas turbine internal gearboxes. The chapter has shown that is is possible to model a secondary phase, with a view to using the information gathered to improve the management of oil, and as such has formed part of knowledge transfer to Rolls-Royce where the techniques and methodology created are informing future engine design. The presence of oil within a gear system cannot be ignored, and so increasing importance will be placed upon being able to accurately model its motion. Agreements such as "ACARE 2020" [14] to cut carbon dioxide emissions and improve efficiency will be met through improving the performance of all the engine, and this work forms

the basis for modelling the effect of air and oil upon gearbox losses — reduction of which will help Rolls-Royce meet their obligations.

7.3 Future work

The work presented in this thesis has shown that, for single phase only, it is possible to use CFD in a wide variety of ways to simulate gear windage, but it leaves a number of questions which it would be interesting to answer.

Firstly, as the computational power of workstations and High-Performance-Clusters (HPC) increase, it will be possible to regularly model more than just one tooth. In Section 3.6.3, two, three and five tooth models were used to verify the effect of only using a single tooth. These models take a very long time to run, even with a modern HPC; however, as computational tools increase in power it will eventually be possible to easily model an entire gear, which would allow any structures that cannot otherwise be resolved, to be captured and their effects analysed. It will also allow shroud features which are not periodic to be modelled — for example features located at a single circumferential location (such as oil injections and off-takes), for which a whole gear model would be necessary.

The advance in computational power will also allow meshing gears to be simulated. This was done using a 2D simulation for spur gears by Strasser [39], studying mixing of two liquid phases. It required the computational mesh to be recalculated at each timestep, so is very calculation intensive. However, the ability to do this in 3D for a pair of meshing spiral bevel gears would give huge insight into the flow structures present.

Finally, the next stage of this work is to integrate the models into a model of an entire gas turbine internal gearbox (IGB). This is essential in order to provide more physical information about the condition of the flow entering and exiting the shroud. The inlet and outlet boundary conditions used in the simulations within this thesis are based on the experimentation of Johnson *et al.* [22, 23], but

in order to better evaluate the gear windage of a spiral bevel gear in situ, a whole IGB model will permit feedback of the inlet conditions from those at the outlet. This would also be true of the introduction of further work into the presence of oil in the domain, and the formation of oil films on the surfaces.

7.4 Contribution to science

The work within this thesis has made a contribution to science, and this can be measured through the publications that have arisen from it. Chapters 3 and 4 contain work that was published at ASME Turbo Expo 2010 [46], and Chapter 6 contains work that was published at ASME ESDA 2010 [44].

The following list summarises the key findings resulting from the work contained within this thesis:

- Single phase windage scales with the outer diameter of a shrouded spiral bevel gear raised to the power of 4.3.
- The inner diameter of a spiral bevel gear has only a limited impact upon the windage.
- Within the ranges tested, increasing the number of teeth decreases single phase windage.
- Increasing the cone angle reduces windage by making flow path for air more restrictive.
- Increasing the restrictive nature of the shroud reduces system windage. A sudden contraction down to a small radial gap has the largest impact, and design features that make the flow path more tortuous are also beneficial.
- Shroud outlets that are less restrictive cause a higher system windage, but allow oil to leave the vicinity of the gear more easily.

- Discrete particle modelling of oil within the system has shown that the destination of an oil droplet within the system is primarily dependent upon the origin location of the droplets.
- Modelling a film on the surface of the shroud shows that a more open, less restrictive shroud outlet also prevents oil accumulating in one location on a shroud.

The work contained within this thesis has been disseminated extensively to Rolls-Royce in reports [42, 43, 45], and through transfer of knowledge and models. The work has also been used in formation of guidelines for shrouding spiral bevel gears within Rolls-Royce gas turbine gearboxes [29].

Bibliography

[1] *Woods Practical Guide To Fan Engineering.* Woods of Colchester Limited, Colchester, second edition, 1960.

[2] K. Al-Shibl, K. Simmons, and C. N. Eastwick. Modelling windage power loss from an enclosed spur gear. *Proceedings of the Institution of Mechanical Engineers, Part A: Journal of Power and Energy*, 221:331–341, 2007.

[3] Hidenori Arisawa, Hideyuki Imai, Motohiko Nishimura, and Tatsuhiko Goi. CFD simulation for reduction of oil churning loss and windage loss on aero-engine transmisson gears. In *ASME Turbo Expo 2009: Power for Land, Sea and Air*, Orlando, Florida, 2009. ASME.

[4] FlightLine Arts. Trent 500 cutaway. `http://www.flightlinearts.com/Portfolio/tabid/1012/Default.aspx`, 1997.

[5] Frank P. Bleier. *Fan Handbook: Selection, Application, and Design.* McGraw-Hill Inc., New York, 1998.

[6] Gleason Corporation. Rochester, USA.

[7] Microsoft Corporation. Redmond, USA.

[8] Parametric Technology Corporation. Needham, USA.

[9] P. H. Dawson. Windage loss in larger high-speed gears. *Proceedings of the Institution of Mechanical Engineers, Part A: Power and Process Engineering*, 198A(1):51–59, 1984.

[10] P. H. Dawson. High speed gear windage. *GEC Review*, 4(3):164–167, 1988.

[11] Y. Diab, F. Ville, P. Velex, and C. Changenet. Windage losses in high speed gears—preliminary experimental and theoretical results. *Journal of Mechanical Design*, 126(5):903–908, 2004.

[12] Carol N. Eastwick and Graham Johnson. Gear windage: A review. *Journal of Mechanical Design*, 130(3):034001–6, 2008.

[13] Mark Farrall, Kathy Simmons, and Stephen Hibberd. Computational investigation of the airflow through a shrouded bevel gear. In *ASME Turbo Expo: Power for Land, Sea and Air*, Reno-Tahoe, Nevada, USA, 2005. ASME.

[14] Advisory Council for Aeronautics Research in Europe. Beyond vision 2020 (towards 2050), 2010.

[15] A. Glahn, S. Busam, M. F. Blair, K. L. Allard, and S. Wittig. Droplet generation by disintegration of oil films at the rim of a rotating disk. *Journal of Engineering for Gas Turbines and Power*, 124:8, 2002.

[16] Robert Handschuh and George Bibel. Comparison of experimental and analytical tooth bending stress of aerospacespiral bevel gears. In *4th World Congress on Gearing and Power Transmission*, Paris, France, 1999. Institut des Engrenages et des Transmissions.

[17] K. Hanjalic. Advanced turbulence closure models: a view of current status and future prospects. *International Journal of Heat and Fluid Flow*, 15(3):178–203, 1994.

[18] Fluent Inc. Fluent 12 theory guide, 2009.

[19] Fluent Inc. Fluent 12 user's guide, 2009.

[20] The MathsWorks Inc. Natick, USA.

[21] ANSYS Incorporated. Canonsburg, USA.

[22] Graham Johnson, Budi Chandra, Colin Foord, and Kathy Simmons. Windage power losses from spiral bevel gears with varying oil flows and

shroud configurations. In *ASME Turbo Expo 2008: Power for Land, Sea and Air*, Berlin, 2008.

[23] Graham Johnson, Kathy Simmons, and Colin Foord. Experimental investigation into windage power loss from a shrouded spiral bevel gear. In *ASME Turbo Expo 2007: Power for Land, Sea and Air*, Montreal, Canada, 2007.

[24] B. E. Launder, G. J. Reece, and W. Rodi. Progress in the development of a reynolds-stress turbulence closure. *Journal of Fluid Mechanics Digital Archive*, 68(03):537–566, 1975.

[25] B. E. Launder and D. B. Spalding. *Lectures in Mathematical Models of Turbulence.* Academic Press, London, 1972.

[26] B. E. Launder and D. B. Spalding. The numerical computation of computational flows. *Computer Methods in Applied Mechanics and Engineering*, 3:269–289, 1974.

[27] Zhaowen Li, Yong Wang, and Deyu Xue. Modeling and simulating of spiral bevel gears based on actual cutting process. In Yong Wang, editor, *IEEE International Conference on Automation and Logistics*, pages 1694–1698, Jinan, China, 2007.

[28] Andrew Alan Lord. *An Experimental Investigation of Geometric and Oil Flow Effects on Gear Windage and Meshing Losses.* PhD, 1998.

[29] Hervé Morvan. Shroud design guidelines. Technical Report FSG 90540, Rolls-Royce Fluid Systems, 2010.

[30] P. J. O'Rourke and A. A. Amsden. A spray/wall interaction submodel for the KIVA-3 wall film model. *SAE paper 2000-01-0271*, 2000.

[31] S. V. Patankar and D. B. Spalding. A calculation procedure for heat, mass and momentum transfer in three-dimensional parabolic flows. *International Journal of Heat and Mass Transfer*, 15(10):1787–1806, 1972.

[32] Stephen. B. Pope. *Turbulent Flows.* Cambridge University Press, Cambridge, 2000.

[33] Steve Rapley. *Computational Investigation of Torque on Spiral Bevel Gears.* Phd, 2009.

[34] Steve Rapley, Carol Eastwick, and Kathy Simmons. The application of CFD to model windage power loss from a spiral bevel gear. In *ASME Turbo Expo 2007: Power for Land, Sea and Air*, Montreal, Canada, 2007.

[35] Steve Rapley, Carol Eastwick, and Kathy Simmons. Computational investigation of torque on coaxial rotating cones. Technical report, University of Nottingham, 2007.

[36] Steve Rapley, Carol Eastwick, and Kathy Simmons. Effect of variations in shroud geometry on single phase air flow over a shrouded single spiral gear. In *ASME Turbo Expo 2008: Power for Land, Sea and Air*, Berlin, 2008.

[37] S. Sarkar, G. Erlebacher, M. Y. Hussani, and H. O. Kreiss. The analysis and modeling of dilational terms in compressible turbulence. Technical Report ICASE Report 89-79, ICASE - NASA, 1989.

[38] François G. Schmitt. About boussinesq's turbulent viscosity hypothesis: historical remarks and a direct evaluation of its validity. *Comptes Rendus Mécanique*, 335(9-10):617–627, 2007.

[39] Wayne Strasser. CFD investigation of gear pump mixing using deforming/agglomerating mesh. *Journal of Fluids Engineering*, 129(4):476–484, 2007.

[40] Various. *Dudley's Gear Handbook.* McGraw-Hill Inc., New York, second edition, 1991.

[41] H K Versteeg and W Malalasekera. *An Introduction to Computational Fluid Dynamics.* Pearson Education, Harlow, second edition, 2007.

[42] Thomas Webb, Carol Eastwick, and Hervé Morvan. Gear parametric study: A computational fluid dynamics study looking at how gear design affects windage power loss. Technical Report UTC Report JF42/TW/01, University of Nottingham, 2009.

[43] Thomas Webb, Carol Eastwick, and Hervé Morvan. Shroud parametric study: A computational fluid dynamics study looking at how shroud design affects windage power loss. Technical Report UTC Report JF42/TW/02, University of Nottingham, 2009.

[44] Thomas Webb, Carol Eastwick, and Hervé Morvan. CFD modelling of gear windage losses: Two phase modelling using particle injections. In *ASME 10th Biennial Conference on Engineering Systems Design and Analysis*, Istanbul, Turkey, 2010.

[45] Thomas Webb, Carol Eastwick, and Hervé Morvan. Methodology for modelling spiral bevel gears using CFD. Technical Report UTC Report JF42/TW/03, University of Nottingham, 2010.

[46] Thomas Webb, Carol Eastwick, and Hervé Morvan. Parametric modelling of a spiral bevel gear using cfd. In *ASME Turbo Expo 2010: Power for Land, Sea and Air*, Glasgow, UK, 2010. ASME.

[47] Frank White. *Fluid Mechanics*. McGraw-Hill, New York, fifth edition, 2003.

[48] Kenneth G. Wilson. Renormalization group and critical phenomana. i. renormalization group and the kadanoff scaling picture. *Physical Review B*, 4(9):3174–3183, 1971.

[49] Kenneth G. Wilson. Renormalization group and critical phenomena. ii. phase-space cell analysis of critical behavior. *Physical Review B*, 4(9):3184–3205, 1971.

[50] Don D. Winfree. Reducing gear windage losses from high speed gears. In *ASME Power Transmission and Gearing Conference*, page 10, Baltimore, Maryland, 2000.

[51] Victor Yakhot and Steven A. Orszag. Renormalization group analysis of turbulence. i. basic theory. *Journal of Scientific Computing*, 1(1):3–51, 1986.

[52] Victor Yakhot, S Thangam, T.B. Gatski, Steven A. Orszag, and C.G. Speziale. Development of turbuence models for shear flows by a double ex-

pansion technique. Technical Report ICASE Report 91-65, ICASE - NASA, 1991.

[53] Y. Yamada and M. Ito. Frictional resistance of enclosed rotating cones. 1. frictional moment and observation of flow with a smooth surface. *Bulletin of the Jsme-Japan Society of Mechanical Engineers*, 18(123):1026–1034, 1975.

[54] Y. Yamada and M. Ito. Frictional resistance of enclosed rotating cones. 2. effects of surface-roughness. *Bulletin of the Jsme-Japan Society of Mechanical Engineers*, 19(134):943–950, 1976.

[55] Y. Yamada and M. Ito. Frictional resistance of enclosed rotating cones with superposed throughflow. *ASME, Transactions, Journal of Fluids Engineering*, 101:259–264, 1979.